THE 4TH INTERNATIONAL CONFERENCE ON INTEGRATED MODELING & ANALYSIS IN APPLIED CONTROL & AUTOMATION

OCTOBER 13-15 2010
FES, MOROCCO

IMAACA 2010

EDITED BY
AGOSTINO BRUZZONE
CLAUDIA FRYDMAN
SERGIO JUNCO
GENEVIÈVE DAUPHIN-TANGUY

PRINTED IN FES, OCTOBER 2010

ISBN 2-9524747-6-1
EAN 9782952474764

THE 4TH INTERNATIONAL CONFERENCE ON INTEGRATED MODELING & ANALYSIS IN APPLIED CONTROL & AUTOMATION

OCTOBER 13-15 2010

FES, MOROCCO

ORGANIZED BY

FACULTAD DE CIENCIAS EXACTAS, INGENIERÍA Y AGRIMENSURA – UNIVERSIDAD NACIONAL DE ROSARIO, ARGENTINA

DIPTEM – UNIVERSITY OF GENOA

LIOPHANT SIMULATION

ECOLE SUPERIEURE D'INGENIERIE EN SCIENCES APPLIQUEES

UNIVERSITY OF AIX-MARSEILLE - LSIS MARSEILLE

MECHANICAL DEPARTMENT, UNIVERSITY OF CALABRIA

MSC-LES, MODELING & SIMULATION CENTER, LABORATORY OF ENTERPRISE SOLUTIONS

MSLS – AUTONOMOUS UNIVERSITY OF BARCELONA

SPONSORED BY

ACADEMIC SPONSORS

FACULTAD DE CIENCIAS EXACTAS, INGENIERÍA Y AGRIMENSURA – UNIVERSIDAD NACIONAL DE ROSARIO, ARGENTINA

CIFASIS: CONICET - UNR - UPCAM

EDITORS

AGOSTINO BRUZZONE
MISS-DIPTEM, UNIVERSITY OF GENOA
VIA MOLINERO 1
17100 SAVONA, ITALY
agostino@itim.unige.it
www.st.itim.unige.it

CLAUDIA FRYDMAN
LSIS - LABORATOIRE DES SCIENCES DE L'INFORMATION ET DES SYSTEMES
UNIVERSITE AIX-MARSEILLE (U3)
DOMAINE UNIVERSITAIRE DE SAINT-JEROME, AVENUE ESCADRILLE NORMANDIE-NIEMEN, 13397 MARSEILLE CEDEX 20
claudia.frydman@lsis.org
www.lsis.org

SERGIO JUNCO
DEPARTAMENTO DE CONTROL, ESCUELA DE INGENIERÍA ELECTRÓNICA – FACULTAD DE CIENCIAS EXACTAS, INGENIERÍA Y AGRIMENSURA – UNIVERSIDAD NACIONAL DE ROSARIO.
RÍOBAMBA 245 BIS, S2000EKE ROSARIO, ARGENTINA
sjunco@fceia.unr.edu.ar
http://www.fceia.unr.edu.ar

GENEVIEVE DAUPHIN-TANGUY
ECOLE CENTRALE DE LILLE
LAGIS, LABORATOIRE D'AUTOMATIQUE, GENIE INFORMATIQUE ET SIGNAL
CITE SCIENTIFIQUE - BP 48 - 59651 VILLENEUVE D'ASCQ CEDEX, FRANCE
gdt@ec-lille.fr
www.ec-lille.fr

THE INTERNATIONAL MEDITERRANEAN AND LATIN AMERICAN MODELING MULTICONFERENCE, I3M 2010

GENERAL CO-CHAIRS

AGOSTINO BRUZZONE, *MISS DIPTEM, UNIVERSITY OF GENOA, ITALY*
MIQUEL ANGEL PIERA, *AUTONOMOUS UNIVERSITY OF BARCELONA, SPAIN*

PROGRAM CHAIR

CLAUDIA FRYDMAN, *LSIS, UNIVERSITY OF AIX-MARSEILLE, FRANCE*
KHALID MEKOUAR, *ESISA, MOROCCO*

THE 4TH INTERNATIONAL CONFERENCE ON INTEGRATED MODELING & ANALYSIS IN APPLIED CONTROL & AUTOMATION, IMAACA 2010

GENERAL CO-CHAIRS

SERGIO JUNCO, *CONTROL SYSTEMS DEPARTMENT,FCEIA, UNR, ROSARIO, ARGENTINA*
GENEVIEVE DAUPHIN-TANGUY,*ECOLE CENTRALE DE LILLE, FRANCE*

PROGRAM CHAIR

SERGIO JUNCO, *CONTROL SYSTEMS DEPARTMENT,FCEIA, UNR, ROSARIO, ARGENTINA*

IMAACA 2010 International Program Committee

FRANÇOIS BATEMAN, LSIS, UNIVERSITÉ PAUL CÉZANNE, FRANCE
WOLFGANG BORUTZKY, BONN-RHEIN SIEG UNIVERSITY, GERMANY
BELKACEM OULD BOUAMAMA, USTL, FRANCE
CARLOS CHRISTOFFERSEN, LAKEHEAD UNIVERSITY, CANADA
PIETER MOSTERMAN, THE MATHWORKS, USA
OSCAR ALBERTO ORTIZ, UNIVERSIDAD NACIONAL DE SAN JUAN, ARGENTINA
MUSTAPHA OULADSINE, LSIS, UNIVERSITÉ D'AIX-MARSEILLE III, FRANCE
RACHID OUTBIB, LSIS, UNIVERSITÉ D'AIX-MARSEILLE III, FRANCE
RICARDO PÉREZ, PONTIFICIA UNIVERSIDAD CATÓLICA, CHILE
XAVIER ROBOAM, INPT-LAPLACE, FRANCE
BRUNO SICILIANO, UNIVERSITÀ DI NAPOLI, ITALY
CHRISTOPHE SUEUR, ÉCOLE CENTRALE DE LILLE, FRANCE
DANIEL VIASSOLO, VESTAS, HOUSTON, TX, USA
KOSTAS TZAFESTAS, NTUA, GREECE

Special Sessions Chairs

MODELING AND CONTROL OF MECHANICAL SYSTEMS, JEAN-YVES DIEULOT, LAGIS-LABORATOIRE D'AUTOMATIQUE GÉNIE INFORMATIQUE ET SIGNAL, LILLE, FRANCE.

HYBRID ENERGY SYSTEMS, MARTA BASUALDO, CIFASIS, UNR, ROSARIO, ARGENTINA and RACHID OUTBIB, LSIS, UNIVERSITÉ D'AIX-MARSEILLE III, FRANCE.

PROGRAM CHAIR'S MESSAGE

WELCOME TO IMAACA 2010
PROGRAM CHAIRS MESSAGE

Sergio Junco

Control Systems
Department
FCEIA-UNR
Rosario, Argentina

Geneviève Dauphin-Tanguy

LAGIS, École
Centrale de Lille,
France

It is our great pleasure to address to all authors, representatives and other participants to IMAACA 2010 in order to welcome everybody to Fez, Morocco, the splendid site of this year's conference.

It is our hope that this 4th edition of IMAACA will be as successful and fruitful to all participants as the previous conferences held in Genoa, Marseille and Buenos Aires have been. The fact of IMAACA being a small conference gives us the opportunity to strongly focuse on our domain of expertise and enough time to interact in order to discuss and exchange our ideas. On the other hand, being IMMACA embedded in the multiconference I3M constitutes also an excellent occasion to have a direct look at the international advances in modeling and simulation understood at the large. This would certainly excite our curiosity, offer us some fun, stimulate our parallel thinking and enrich our own perspectives of the discipline.

The valuable contribution of the International Program Committee in the difficult job of selecting the finally accepted papers is deeply appreciated. Also the input of the general chairs of I3M and the efforts of the local organizers is sincerely acknowledged.

Let us finally augur you a fully enjoyable conference in both its technical and social aspects.

ACKNOWLEDGEMENTS

The general chairs of IMAACA 2010 are deeply indebted to all the authors for their contributions as well as to all the members of the International Program Committee for their help in carefully reviewing the submitted papers. We expect a very successful event based on their efforts.

A special thank to the organizations, institutions and societies that are supporting and technically sponsoring the I3M Multiconference hosting IMAACA: University of Genoa, Liophant Simulation, Ecole Supérieure d'Ingénierie en Sciences Appliquées, University of Aix-Marseille, Autonomous University of Barcelona, University of Calabria, Modeling & Simulation Center – Laboratory of Enterprise Solutions (MSC-LES), McLeod Institute of Simulation Science (MISS), McLeod Modeling & Simulation Network (M&SNet), International Mediterranean & Latin American Council of Simulation (IMCS), Management and Advanced Solutions and Technologies (MAST). Finally, we would like to thank all the Conference Organization Supporters.

Table of Contents

Bond Graph Session

- TRAJECTORY CONTROL OF A THREE DOF DUAL ARM SPACE ROBOT WITH SMALL ATTITUDE DISTURBANCE
  Haresh Patolia, P. M. Pathak, S. C. Jain 1

- SIMULATION AND EXPERIMENTAL STUDIES ON WALKING ROBOT WITH FLEXIBLE LEGS
  V. L. Krishnan, P. M. Pathak, Lokesh Sardana, S. C. Jain 11

- FUEL CONSUMPTION IMPROVEMENT OF VEHICLE WITH CVT BY BOND GRAPHS
  Katsuya Suzuki, Kazuhiro Tanaka, Sho Yamakawa, Fumio Shimizu, Masaki Fuchiwaki 21

- AUTOMATIC HANDLING OF COMMUTATIONS IN BOND GRAPH BASED SIMULATION OF SWITCHED SYSTEMS
  Matías Nacusse, Sergio Junco 27

Modeling and Control of Mechanical Systems

- SWITCHING MULTIMODEL LQ CONTROLLERS FOR VARIABLE SPEED AND VARIABLE PITCH WIND TURBINES
  Nadhira Khezami, Naceur Benhadj Braiek, Xavier Guillaud 37

- DYNAMIC MODELING OF A PARALLEL ROBOT WITH SIX DEGREES OF FREEDOM
  Abdelhakim Chibani, Chawki Mahfoudi, Abdelouahab Zaatri, Achour Amouri 45

- OPTIMAL GRASPING FORCE DISTRIBUTION FOR THREE ROBOTS HOLDING A RIGID OBJECT
  Ammar Khadraoui, Chawki Mahfoudi, Abdelouahab Zaatri, Karim Djouani 53

- DYNAMIC MODEL OF A FLEXIBLE BLADE WIND TURBINE IN AN ELECTRICAL GRID CONTROL STRUCTURE
  Lamine Chalal, Jean-Yves Dieulot, Geneviève Dauphin-Tanguy, Frederic Colas 61

Hybrid Energy Systems

- A PUMPING SYSTEM FED BY HYBRID PV-WIND SOURCES WITHOUT BATTERY STORAGE, BG MODELLING CONTROL AND ENERGY MANAGEMENT
  Amine Ben Rhouma, Jamel Belhadj, Xavier Roboam 67

- PNEUMATIC HYBRIDISATION OF DIESEL ENGINE IN A HYBRID WIND-DIESEL INSTALLATION WITH COMPRESSED AIR ENERGY STORAGE
  Tamman Basbous, Rafic Younes, Adrian Ilinca, Jean Perron 73

- ANALYSIS OF RENEWABLE ENERGY POTENTIAL OF HYBRID SYSTEMS FOR DWELLINGS IN FRANCE
  Philippe Poulet, Rachid Outbib 83

- PSEUDO DYNAMIC MODEL OF A BIO-ETHANOL PROCESSOR FOR A HYBRID VEHICLE PROTOTYPE
  Lucas Nieto Degliuomini, David Zumoffen, Diego Feroldi, Marta Basualdo, Rachid Outbib 93

System Automation and Management

- DEPENDABILITY EVALUATION OF SAFETY INSTRUMENTED SYSTEMS INCORPORATING INTELLIGENT INSTRUMENTS
  Abdelhak Mkhida, Badr Bououlid, Jean Marc Thiriet 99

- DEVELOPING INTEGRATED PERFORMANCE MEASUREMENT SYSTEM - USING MDA APPROACH
  Souhail Sekkat, Jean Luc Paris, Khalid Kouiss, Janah Saadi, Laurant Deshayes 107

- TRAFFIC CONTROL AND QUEUES MANAGEMENT FOR A SINGLE INTERSECTION
  Fadi Motawej, Rachid Bouyekhf, Abdellah EL Moudni 115

Control of Electrical Drives and Process Modeling

- AN ALTERNATIVE WAY TO THE PWM CONTROL OF SWITCHED RELUCTANCE MOTOR DRIVES
  Hedi Yahia, Mohamed Faouzi Mimouni, Rachid Dhifaoui 121

- EXPERIMENTAL ASSESSMENT OF TRAPEZOIDAL COMMUTATION AND FOC PERFORMANCES OF 3-PHASE PERMANENT MAGNET BRUSHLESS MOTOR
  Rachid Askour, Badr Bououlid 129

- IMPLEMENTATION OF IDENTIFICATION ALGORITHM USING RECURRENT RBF NEURAL NETWORKS FOR THE INSIDE TEMPERATURE IN A GREENHOUSE
  Latifa Ezzine, Mohamed Guerbaoui, Youssef El Afou, Abdelali Eddahhak,Abdeslam Lachhab, Lotfi Belkoura, Benachir Bouchikhi 135

- NON-ISOTHERMAL MODEL OF THE YEASTS GROWTH IN ALCOHOLIC FERMENTATIONS FOR HIGH QUALITY WINES
  Pablo M. Aballay, Gustavo J.E. Scaglia, Martha D. Vallejo, Laura A. Rodríguez, Oscar A. Ortiz 143

Authors' Index 152

TRAJECTORY CONTROL OF A THREE DOF DUAL ARM SPACE ROBOT WITH SMALL ATTITUDE DISTURBANCE

Haresh Patolia[(a)], P. M. Pathak[(b)], S. C. Jain[(c)]

[(a)] [(b)] Robotics and Control Laboratory, Mechanical and Industrial Engineering Department,
Indian Institute of Technology, Roorkee, India, 247667
[(c)] Mangalayatan University, Aligarth, India

[(a)] haresh_patolia@yahoo.co.in, [(b)] pushpfme@iitr.ernet.in, [(c)]sjainfme@yahoo.com

ABSTRACT
This work presents a trajectory planning strategy for a three degree of freedom (DOF) dual arm space robot in work space. The strategy is based on the principle of dynamic coupling between the tip motion and the vehicle motion of the space robot. The strategy uses the two arms of three link serial manipulator. One arm called mission arm achieves the trajectory control task while the other arm called balance arm moves in a way to reduce the attitude of the vehicle. A robust overwhelming controller is used for trajectory control of tip of the mission arm. The first and second joint rotations of balance arm are based on the first and second joint rotations of mission arm whereas the third joint rotation of balance arm is carried out such that small attitude disturbance of vehicle takes place. An example of three DOF dual arm space robot is considered to illustrate the methodology. Bond graph has been adopted as modeling tool as it facilitates the system modeling from the physical paradigm itself and it is easy to develop various control strategies by modifying the physical paradigm.

Keywords: dual arm space robot, robust overwhelming controller, attitude control, bond graph modeling

1. INTRODUCTION

In a large number of space applications like maintenance of components, capture of floating objects, removal of debris or old satellites, orbital replacement unit operations, refueling etc., the manipulator motion is required to be controlled precisely. In a free-floating space robotic system, the spacecraft position and the attitude are not actively controlled using external jets or thrusters during manipulator activity. Due to the conserved linear and angular momenta, the spacecraft moves freely in response to the dynamic disturbances caused by the manipulator motion. Such disturbances may result in significant deviation of the end-effector from the desired trajectory, and are particularly significant when the manipulator is holding a heavy payload. Moreover, the angular momentum conservation constraints are non-integrable rendering the system non-holonomic. Hence, it is not possible to cancel this base disturbance using static state feedback. This complicates the motion planning and control issue further (Nakamura and Mukherjee 1991).

The dynamic coupling between space vehicle and manipulators has been a subject of intense investigation since the Space Shuttle RMS went into service in 1982. Due to dynamic coupling, the resulting motion at the shuttle base caused the end-effector to miss its target. This type of problem can be particularly acute during satellite rendezvous in which errors of even a few centimeters could result in a failed capture attempt or even damage to the satellite. Also vehicle attitude disturbance assumes prime importance because any disorientation would affect the communication link of the satellite with the control station. One of the key issues in space robotics is using arms to contact worksite elements safely, quickly, and accurately without accidentally contacting unintended objects or imparting excessive forces beyond those needed for the task. For this purpose trajectory planning assumes importance. A well planned trajectory, taking care of singularities of manipulator arm, is essential for efficient and smooth controlled motion of arm tips.

Control of space robot has been studied by many authors but control studies on multi arm space robot are only few. Dubowsky and Papadopoulos (1993a, 1993b) discussed concepts of virtual Manipulator (VM) model with an application to workspace analysis, path planning using Enhanced Disturbance Map (EDM) as well as effects of dynamic singularities on workspace of free flying manipulator. Moosavian and Papadopoulos (1998) proved the advantage of Direct Path Method over Barycentric vector approach while developing kinematic modeling of rigid multi arm space robots. Papadopoulos and Moosavian (1994) compared by simulation study, the performance of Euler angle and Euler parameter base control law to that of a transposed Jacobian algorithm and showed that the latter gives reasonably good performance with reduced computational burden. Huang, Xu, and Liang (2005) developed a space robot system consisting of two arms, with one arm (mission arm) for accomplishing the capture mission, and the other one (balance arm) compensating for the disturbance of the base. Marchesi

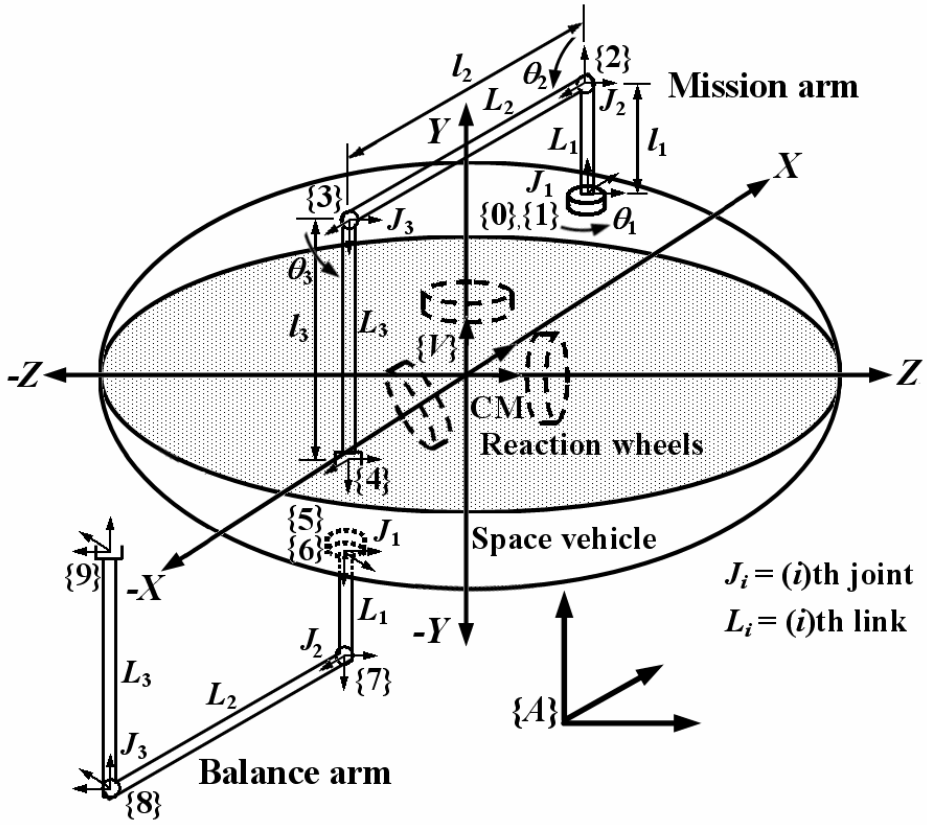

Figure 1: Schematic Diagram of Three DOF Dual Arm Space Robot

and Angrolli (1997) focused on control strategy for a free-flying space manipulator and described the methods used to solve the inverse kinematic problem of a non-redundant robotic arm mounted on a free floating spacecraft for minimal disturbance of spacecraft attitude. Yokokohji, Toyoshima, and Yoshikawa (1993) proposed an efficient computation algorithm for the trajectory control of multi arm free-flying space robot using the generalized Jacobian matrix technique. Chen and Tang (2006) presented the optimal non-holonomic motion planning of free-floating space robot system with dual arms.

Based on the insights developed from bond graph modeling, Ghosh (1990) developed a robust overwhelming controller for the robotic manipulator, which does not require the knowledge of the robot parameters and the payload. Pathak, Kumar, Mukherjee, and Dasgupta (2008) presented a scheme for robust trajectory control of free-floating space robots.

This work presents a strategy for trajectory control of mission arm with small attitude disturbance of vehicle. Trajectory control of mission arm is achieved by using robust overwhelming controller (Ghosh 1990; Pathak, Kumar, Mukherjee, and Dasgupta 2008; Mukherjee, Karmakar, and Samantray 2006). Due to mission arm tip motion, vehicle attitude gets disturbed. A control law is proposed for joint control of balance arm such that when it works with trajectory control of mission arm small vehicle attitude disturbance is obtained. It is assumed that the space vehicle is equipped with three small reaction wheels. A numerical example of free-floating space vehicle carrying two manipulators, each of having three links is presented to demonstrate the efficacy of the proposed control strategy. The complete dynamics is modeled using bond graphs (Karnopp, Margolis, and Rosenberg 2006; Mukherjee, Karmakar, and Samantray 2006; Breedveld and Dauphin-Tanguy 1992). For the purpose of modeling and simulation, the bond graph package SYMBOLS Shakti (Users Manual) has been used.

2. MODELING OF THREE DOF DUAL ARM SPACE ROBOT

To illustrate the control strategy for the space robot, a three DOF free-floating space robot consisting of two serial manipulators each of having three links mounted on a space vehicle is considered and shown in Figure 1.

Joint rotation (θ_i) of manipulator and Euler angle of the base (ϕ, θ, ψ) in 3-2-1 convention are used as generalized coordinates. All joints are assumed to be revolute. The joint between links (i) and (i+1) is numbered as (i+1). In Figure 1, {A} is the absolute frame and {V} is the vehicle frame located at the centre of mass (CM) of the vehicle. The frames {0} and {5} are attached on the vehicle to represent the mission arm and balance arm base location on the vehicle at a position (r_x, r_y, r_z) and (-r_x, -r_y, -r_z) from the origin of frame {V}, respectively. The frames {1} and {6} are attached on the first links of mission arm and balance arm at their bases, respectively. The frames {1} and {6} have relative motion with respect to frames {0} and {5} about Y-axis. Frames {2} and {3} are attached at the

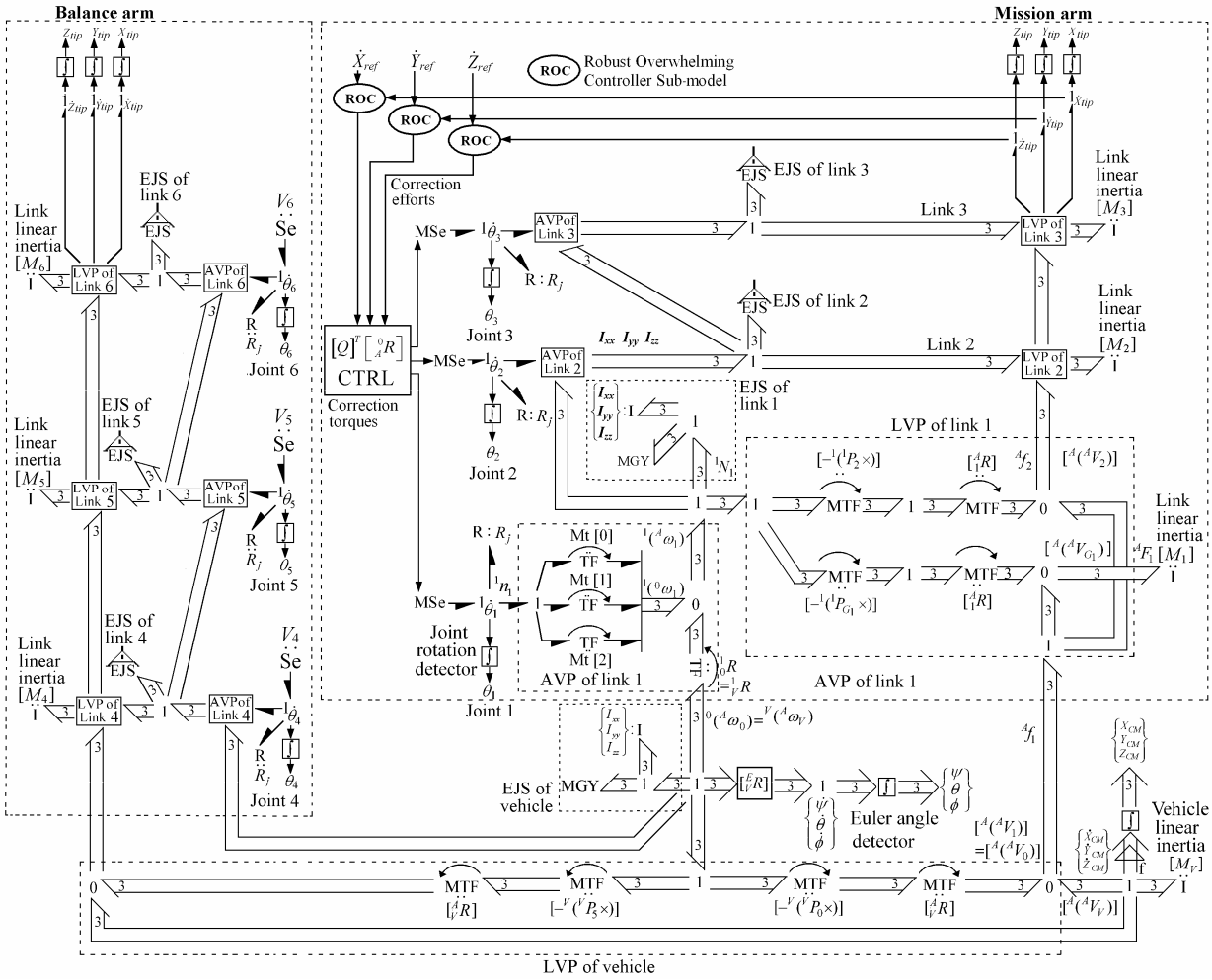

Figure 2: Multi Bond Graph Model of Three DOF Dual Arm Space Robot

base of second and third links of the mission arm whereas frames {7} and {8} are attached at the base of second and third links of the balance arm, respectively. They represent the joint axes for the second and third joints of both the arms and have rotation about their *Z*-axes. The moments of inertia are defined about the body-fixed principal coordinate system. It is assumed that all the links are to be rigid and the specified task space trajectory is within the reachable workspace of the manipulators for simplicity. The frames {4} and {9} represent the tips of mission and balance arm, respectively.

The angular relative velocities of links of the mission arm are defined as,

$$
\begin{aligned}
{}^{1}\omega_1 &= [0 \quad \dot{\theta}_1 \quad 0]^T \\
{}^{2}\omega_2 &= [0 \quad 0 \quad \dot{\theta}_2]^T \\
{}^{3}\omega_3 &= [0 \quad 0 \quad \dot{\theta}_3]^T
\end{aligned} \tag{1}
$$

Here $\dot{\theta}_1$, $\dot{\theta}_2$ and $\dot{\theta}_3$ are the joint velocities of first, second and third joints of the mission arm, respectively.

Modeling of dual arm space robot involves modeling of the linear and angular dynamics of the manipulators as well as the space vehicle on which they are mounted. The complete bond graph model of three DOF dual arm space robot is created and shown in Figure 2. Various sub-models required for drawing bond graph model are briefly presented here.

2.1. Kinematic Relations

A signal structure has been made for transforming the vehicle angular velocity to Euler angle rates using the relation,

$$
\begin{bmatrix} \dot{\psi} \\ \dot{\theta} \\ \dot{\phi} \end{bmatrix} = \begin{bmatrix} 1 & t\theta s\psi & t\theta c\psi \\ 0 & c\psi & -s\psi \\ 0 & s\psi / c\theta & c\psi / c\theta \end{bmatrix} \begin{bmatrix} \omega_x \\ \omega_y \\ \omega_z \end{bmatrix} \tag{2}
$$

where $\dot{\psi}$, $\dot{\theta}$ and $\dot{\phi}$ are the Euler angle rates; ω_x, ω_y and ω_z are the vehicle angular velocities. Also $t\theta = \tan\theta$, $c\theta = \cos\theta$, $c\psi = \cos\psi$ and $s\psi = \sin\psi$. The angular velocity of (i+1)th link with respect to the absolute frame {A}, ${}^{i+1}({}^{A}\omega_{i+1})$ can be computed recursively using the following relation (Craig, 1986),

$$
{}^{i+1}({}^{A}\omega_{i+1}) = {}^{i+1}_{i}R \; {}^{i}({}^{A}\omega_i) + \dot{\theta}_{i+1} \; {}^{i+1}\hat{U}_{i+1} \tag{3}
$$

where ${}^{i+1}_{i}R$ is the rotation matrix of direction cosines relating frame {i} with respect to frame {i+1}, ${}^{i}({}^{A}\omega_i)$ is the angular velocity of (i)th link with respect to the absolute frame {A}, $\dot{\theta}_{i+1}$ is the velocity of (i+1)th joint and ${}^{i+1}\hat{U}_{i+1}$ is a unit vector representing the direction of the joint axis. This computation is implemented through angular velocity propagation (AVP) sub-model of link as shown in Figure 2. This sub-model takes the angular velocity of previous link and the joint velocity between the previous and current link as input and the angular velocity of the current link is given out after calculation. The joint velocity $\dot{\theta}_{i+1}$ is relative between two adjacent links, can be about any one of the axes of the joint coordinate frame. Based on the axis of the joint rotation, one of the transfer moduli (Mt[0], Mt[1] or Mt[2]) connected to the joint velocity junction will be unity, and the remaining will be zero. This is decided by the vector ${}^{i+1}\hat{U}_{i+1}$.

The relation for linear velocity of the tip of the link can be computed as,

$$ {}^{A}({}^{A}V_{i+1}) = {}^{A}({}^{A}V_i) + {}^{A}_{i}R[{}^{i}({}^{A}\omega_i) \times {}^{i}({}^{i}P_{i-1})] \quad (4) $$

where ${}^{i}({}^{i}P_{i+1}) = \begin{bmatrix} 0 \\ l_i \\ 0 \end{bmatrix}$, $[{}^{i}({}^{i}P_{i+1}\times)] = \begin{bmatrix} 0 & 0 & l_i \\ 0 & 0 & 0 \\ -l_i & 0 & 0 \end{bmatrix}$, and

l_i = length of (i)th link.

The linear velocity of the CM of the link can be obtained by using ${}^{i}({}^{i}P_{Gi}) = [0 \quad l_{Gi} \quad 0]^T$ in place of ${}^{i}({}^{i}P_{i+1})$ in Eq. (4). The bond graph sub-model for linear velocity propagation (LVP) of link is created and is shown in Figure 2. This sub-model takes the angular velocity of current link and tip velocity of previous link as input and gives velocity of CM of current link and tip velocity of current link as output. The CM velocities of the space vehicle and links of the manipulators are obtained from the linear inertia of the space vehicle and links, respectively. In Figure 2, $1_{\dot{\theta}_i}$ junctions represent the joint relative velocities and the integrator sub-models used as displacement detectors.

2.2. Euler Junction Structure

A rigid body has translation and angular motion. Thus its dynamics has two parts. The translation dynamics is modeled using Euler's first law and the angular dynamics using the Euler's second law. In order to model the Euler's equations, the gyrator loop commonly known as an Euler Junction Structure (EJS) is used and a sub-model EJS is created to represent the rotational dynamics of the space vehicle and that of the links. The following Euler equations are used to create the sub-model EJS,

$$ N_x = I_{XX}\dot{\omega}_x + (I_{ZZ} - I_{YY})\omega_y\omega_z \quad (5) $$

$$ N_y = I_{YY}\dot{\omega}_y + (I_{XX} - I_{ZZ})\omega_z\omega_x \quad (6) $$

$$ N_z = I_{ZZ}\dot{\omega}_z + (I_{YY} - I_{XX})\omega_x\omega_y \quad (7) $$

here N_x, N_y and N_z represent the moments acting on the vehicle expressed in vehicle frame in X, Y, and Z direction, respectively. I_{XX}, I_{YY} and I_{ZZ} are the moment of inertia of the rigid body about X, Y and Z directions, respectively. The created sub-model EJS is shown in Figure 2.

3. CONTROLLER DESIGN OF SPACE ROBOT

3.1. Trajectory Control of Mission Arm

For the mission arm tip trajectory control, robust overwhelming controller (ROC) presented elsewhere, is used. The bond graph sub-model for ROC is shown in Figure 3. A reference flow input for plant is supplied to sub-model ROC from main bond graph which is shown in Figure 2. This sub-model is also provided with mission arm tip velocity as input from main bond graph

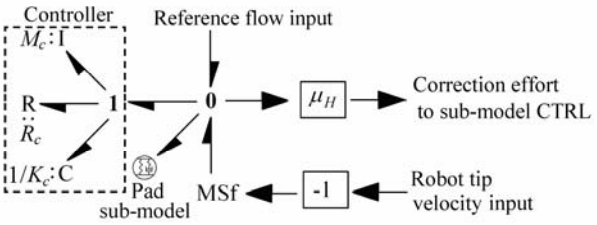

Figure 3: Robust Overwhelming Controller (ROC) Sub-model

and it gives correction efforts as output to sub-model CTRL. In Figure 3, pad sub-model is used to avoid differential causality. Pads are lumped flexibilities with high values of stiffness and damping. Three ROC sub-models (one for each X, Y and Z direction) are used to control the space robot as shown in Figure 2. A signal structure CTRL can be created using forward kinematic relations to convert correction efforts from ROC into correction torques to be supplied to different joints of the mission arm. For creation of this signal structure CTRL, the tip velocity of the mission arm with respect to its base frame {0} expressed in absolute frame {A} can be evaluated as,

$$ {}^{A}({}^{0}V_4) = {}^{A}_{0}R\ {}^{0}({}^{0}V_4) \quad (8) $$

here, ${}^{k}({}^{j}V_i)$ denotes the velocity of the origin of {i}th frame as observed from {j}th frame and expressed in {k}th frame, ${}^{A}_{0}R$ represents the orientation of a frame {0} with respect to a frame {A}. The term ${}^{0}({}^{0}V_4)$ in Eq. (8) can be derived as,

$$ {}^{0}({}^{0}V_4) = \begin{bmatrix} (s_1s_2l_2 + s_1s_{23}l_3) & -(c_1c_2l_2 + c_1c_{23}l_3) & -c_1c_{23}l_3 \\ 0 & -(s_2l_2 + s_{23}l_3) & -s_{23}l_3 \\ (c_1s_2l_2 + c_1s_{23}l_3) & (s_1c_2l_2 + s_1c_{23}l_3) & s_1c_{23}l_3 \end{bmatrix} \begin{Bmatrix} \dot{\theta}_1 \\ \dot{\theta}_2 \\ \dot{\theta}_3 \end{Bmatrix} \quad (9) $$

where $c_i = \cos\theta_i$, $s_i = \sin\theta_i$, $c_{ij} = \cos(\theta_i + \theta_j)$ and $s_{ij} = \sin(\theta_i + \theta_j)$. One can write Eq. (9) in a compact form as,

$$^0(^0V_4) = [Q][\dot{\theta}_1 \quad \dot{\theta}_2 \quad \dot{\theta}_3]^T \tag{10}$$

where [*Q*] is the transformation matrix in Eq. (9). The transformation ${}^A_0R$ is computed as ${}^A_0R = {}^A_V R\ {}^V_0R$ where,

$${}^A_V R = \begin{bmatrix} c\phi c\theta & c\phi s\theta s\psi - s\phi c\psi & c\phi s\theta c\psi + s\phi s\psi \\ s\phi c\theta & s\phi s\theta s\psi + c\phi c\psi & s\phi s\theta c\psi - c\phi s\psi \\ -s\theta & c\theta s\psi & c\theta c\psi \end{bmatrix} \tag{11}$$

and ${}^V_0R$ is identity matrix, $c\phi = \cos\phi$, $s\phi = \sin\phi$, $c\psi = \cos\psi$, $s\psi = \sin\psi$, $c\theta = \cos\theta$ and $s\theta = \sin\theta$. Thus Eq. (8) can be written as,

$$^A(^0V_4) = [{}^A_0R][Q][\dot{\theta}_1 \quad \dot{\theta}_2 \quad \dot{\theta}_3]^T \tag{12}$$

Thus, the relationship between joint correction torques and correction efforts from controller can be expressed as,

$$[{}^1\eta_1 \quad {}^2\eta_2 \quad {}^3\eta_3]^T = [Q]^T [{}^0_A R][F_x \quad F_y \quad F_z]^T \tag{13}$$

where ${}^i\eta_i$ is the torques exerted on link (*i*) by link (*i*-1), expressed in terms of frame {*i*}. F_x, F_y and F_z are corrective efforts in *X*, *Y* and *Z* directions, respectively. The created sub-model CTRL for signal structure for conversion of correction efforts to correction torques is shown in Figure 2.

3.2. Attitude Control of Space Vehicle

The proposed control strategy for attitude control of space vehicle can be worked out as,

(i) Assuming that the motions of actuators at first and second joints of mission arm and balance arm are equal and opposite direction to each other. The control law for the actuators at first and second joints of the balance arm can be given as,

$$\tau_{Bj} = K_p(-\theta_{Mj} - \theta_{Bj}) + K_v(-\dot{\theta}_{Mj} - \dot{\theta}_{Bj}) \text{ for } j = 1, 2. \tag{14}$$

here τ_{Bj} is the torque at (*j*)th joint of balance arm; θ_{Mj} is the position of (j)th joint of mission arm; θ_{Bj} is the position of (*j*)th joint of balance arm; $\dot{\theta}_{Mj}$ is the (*j*)th joint angular velocity of mission arm; $\dot{\theta}_{Bj}$ is the (*j*)th joint angular velocity of balance arm; K_p is proportional gain parameter and K_v is derivative gain parameter.

(ii) The control law for the actuator at third joint of balance arm can be written as,

$$\begin{aligned} \tau_{B3} = {} & K_p(\psi_d - \psi_a) + K_v(\dot{\psi}_d - \dot{\psi}_a) \\ & + K_p(\theta_d - \theta_a) + K_v(\dot{\theta}_d - \dot{\theta}_a) \\ & + K_p(\phi_d - \phi_a) + K_v(\dot{\phi}_d - \dot{\phi}_a) \end{aligned} \tag{15}$$

where τ_{B3} is the torque at third joint of balance arm; ψ, θ and ϕ are the Euler angles; $\dot{\psi}$, $\dot{\theta}$ and $\dot{\phi}$ are the Euler angle rates; suffix 'd' stands for 'desired' whereas suffix 'a' stands for 'actual'. This control law has been devised based on the observation that the body attitude is controllable from the joints of the balance arm (Dauphin-Tanguy, Rahmani, and Sueur, 1999).

4. SIMULATION AND RESULTS

To validate the control strategy discussed in Section 2 and 3, a bond graph model as shown in Figure 2 has been simulated. The parameters used for the simulation are given in Appendix A. It is assumed that initially the absolute frame and vehicle frame are coincident. For the simulation, the reference velocity command for mission arm in absolute frame is taken as,

$$\dot{X}_{ref} = R\omega\sin(\omega t) \quad \text{in } X \text{ direction} \tag{16}$$

$$\dot{Y}_{ref} = A\sin(2\omega t) \quad \text{in } Y \text{ direction} \tag{17}$$

$$\dot{Z}_{ref} = R\omega\cos(\omega t) \quad \text{in } Z \text{ direction} \tag{18}$$

where *R* is the radius of the reference circle in *X*-*Z* plane; *A* is the amplitude of velocity in *Y* direction. It is a circular trajectory in *X*-*Z* plane and parabolic

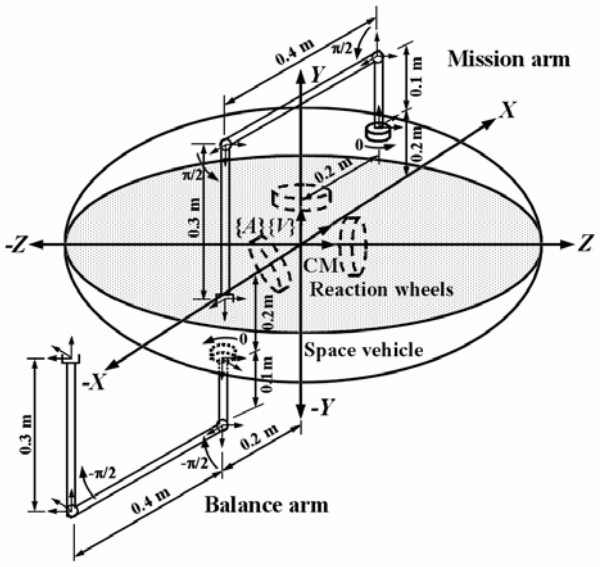

Figure 4: Initial Configuration of Three DOF Dual Arm Space Robot

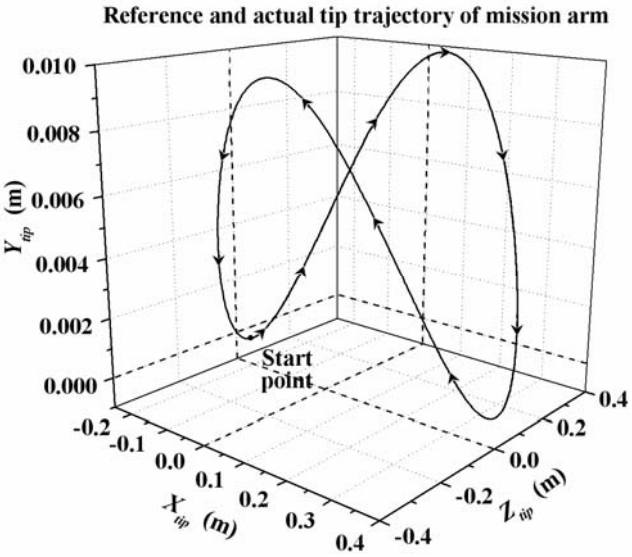

Figure 5: 3-D Plot of Reference and Actual Tip Trajectory of Mission Arm

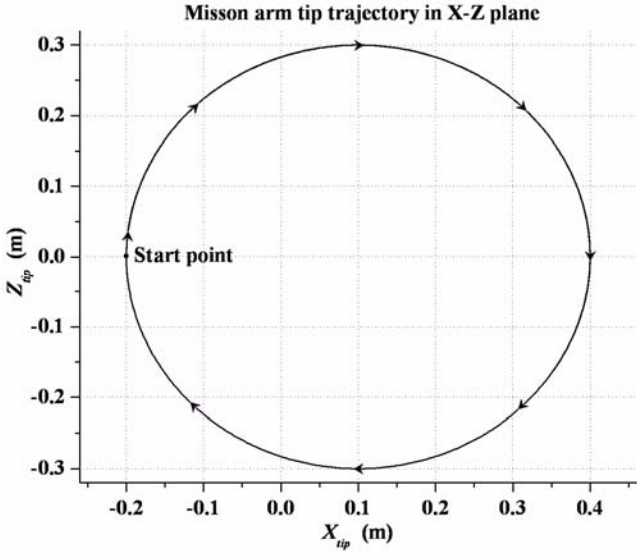

Figure 6: Plot of Reference and Actual Tip Trajectory of Mission Arm in *X-Z* Plane

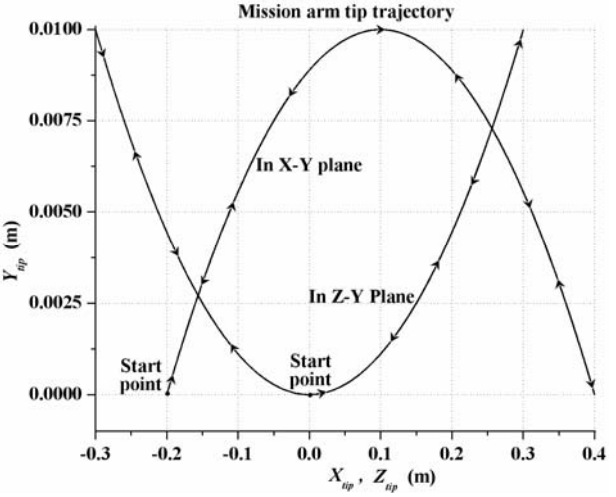

Figure 7: Plot of Reference and Actual Tip Trajectory of Mission Arm in *X-Z* and *Z-Y* Plane

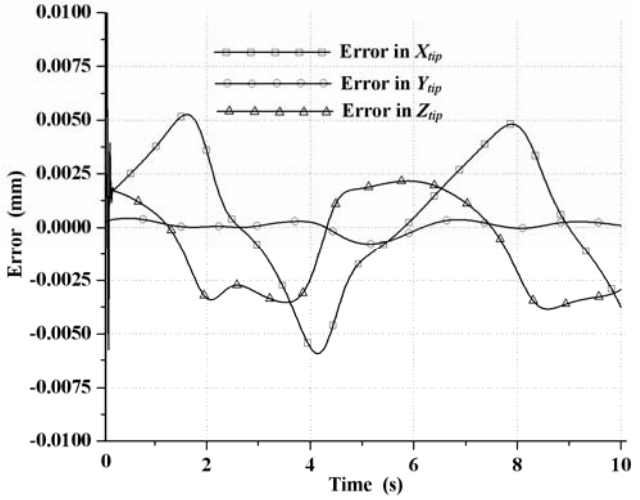

Figure 8: Plot of Mission Arm Tip Position Error versus Time

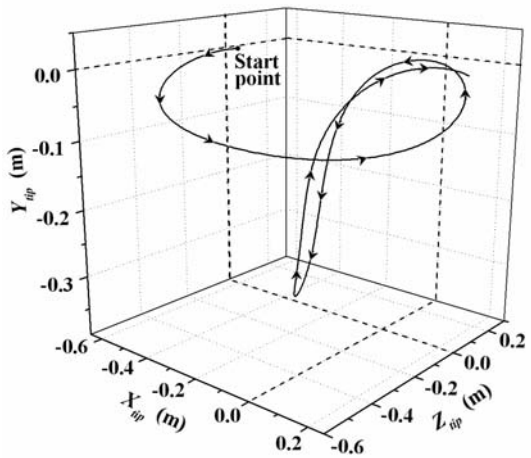

Figure 9: 3-D Plot of Actual Tip Trajectory of Balance Arm

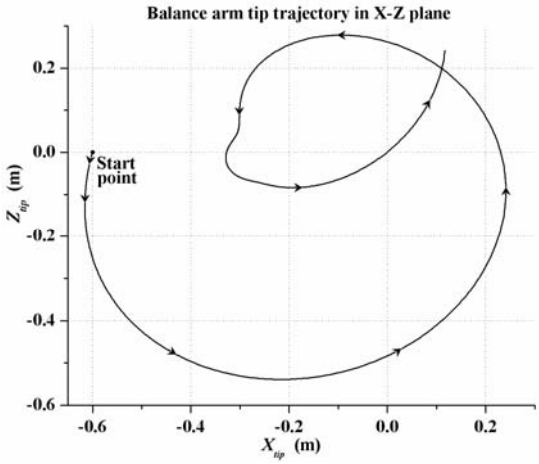

Figure 10: Plot of Actual Tip Trajectory of Balance Arm in *X-Z* Plane

trajectory in *X-Y* plane and *Y-Z* plane. The joint torques for balance arm is given as per control law shown in Eq. 14 and 15. At the beginning of the simulation, the overwhelmer initial position is set to mission arm tip position in order to keep the initial error to be zero.

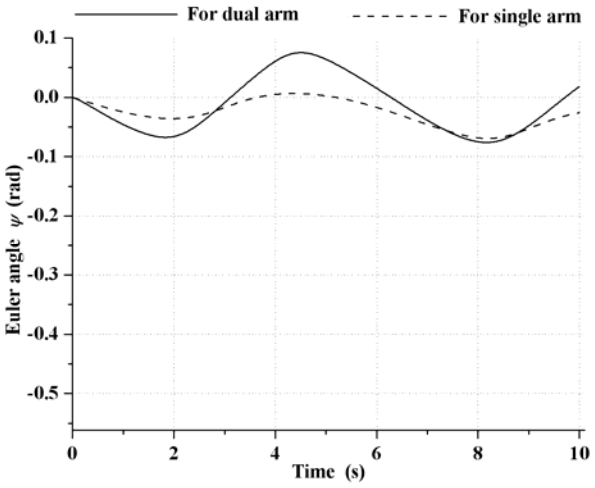

Figure 11: Plot of Variation of Euler Angle ψ for Single and Dual Arm Space Vehicle versus Time

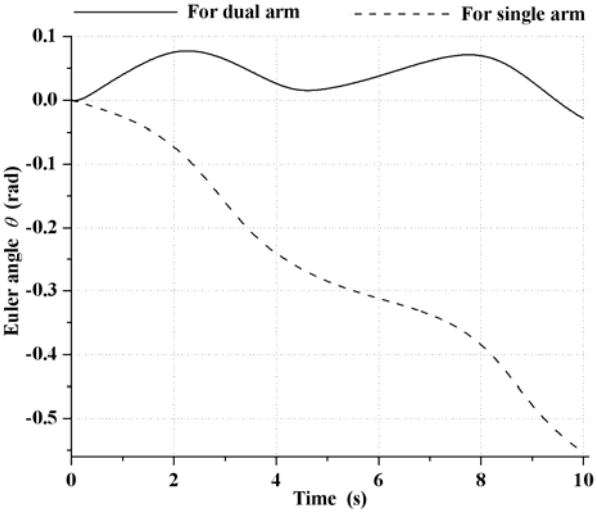

Figure 12: Plot of Variation of Euler Angle θ for Single and Dual Arm Space Vehicle versus Time

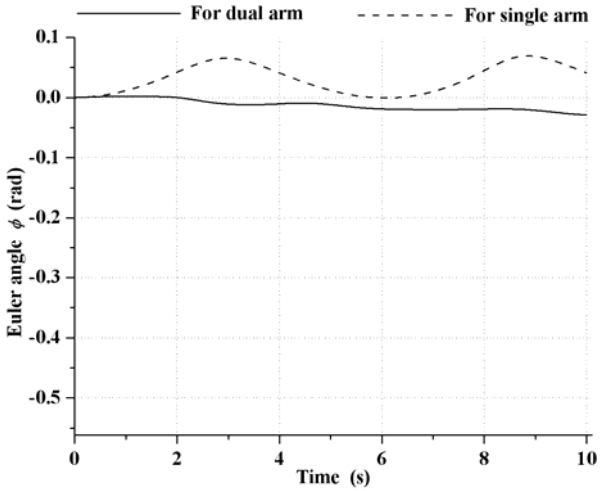

Figure 13: Plot of Variation of Euler Angle ϕ for Single and Dual Arm Space Vehicle versus Time

As the reaction wheels are provided to introduce the redundancy in the system, the input source of voltage to them is kept zero. In this condition, they will only follow the attitude of the vehicle base. However reaction wheels can be actuated by input source of voltage as and when required. The initial configuration of the space robot is shown in Figure 4. The simulation is carried out for 10 seconds.

A three-dimensional plot of reference and actual trajectories of tip of the mission arm are shown in Figure 5. The reference and actual tip trajectories of the mission arm in *X-Z* plane are shown in Figure 6, whereas in Figure 7, the reference and actual tip trajectories of the mission arm in *X-Y* and *Z-Y* planes are shown. Figure 8 shows the plots of error between the reference and actual tip positions with respect to time for mission arm. Here for mission arm, X_{tip} position error varies between -0.0059 to +0.0053 mm, Y_{tip} position error varies between -0.0008 to +0.0004 mm and that of Z_{tip}, it varies between -0.0036 to +0.0021 mm, except the initial phase and it is due to that the tip acquires a velocity from the rest position. From Figure 5 to 8, it is observed that mission arm tip is effectively dragged along the reference trajectory.

Figure 9 shows a three-dimensional plot of the balance arm tip trajectory. The trajectory followed by tip of the balance arm in *X-Z* plane is presented in Figure 10. From Figure 9 and 10, it is seen how the balance arm tip moved while controlling the space vehicle attitude disturbance.

The variations in Euler angles ψ, θ, and ϕ for the space vehicle carrying two arms as well as the space vehicle carrying single arm (mission arm) only with respect to time are shown in Figure 11, 12 and 13, respectively. From these figures, it is observed that for a same set of parameters and reference trajectory that of the dual arm, the space vehicle carrying single arm having a continuous drift in Euler angle θ from 0 to -0.553 radians. The space vehicle carrying two arms, the variation in Euler angle θ is reduced significantly and is between -0.028 to +0.077 radians only. The variation in Euler angle ϕ for single arm space vehicle is 0.0 to +0.065 radians and it is further improved for dual arm space vehicle which varies from 0 to -0.028 radians. However, there is no any improvement in Euler angle ψ but it varies between -0.075 to +0.075 radians for dual arm space vehicle.

5. CONCLUSION

This work contributes a control strategy for small attitude disturbance of space vehicle while mission arm follows the desired trajectory. Here our objective is that the mission arm should follow the desired trajectory but vehicle attitude disturbance should be small. This objective has been achieved with the help of the proposed control laws of balance arm.

ACKNOWLEDGMENTS

We are thankful to Indian Space Research Organization (ISRO) for funding the project vides Grant No. ISRO/RES/3/596/09-10.

APPENDIX A
Parameters used in simulation

Link Parameters	Mass (kg)	Length l_i (m)	Length l_{Gi} (m)	I_{XX} (kg m^2)	I_{YY} (kg m^2)	I_{ZZ} (kg m^2)	Initial Joint angle θ (rad)
For mission arm							
Link 1	6.13	0.1	0.05	0.0300	0.0250	0.0300	0
Link 2	15.69	0.4	0.20	0.2153	0.0126	0.2153	$\pi/2$
Link 3	11.76	0.3	0.15	0.0929	0.0094	0.0929	$\pi/2$
For balance arm							
Link 1	6.13	0.1	0.05	0.0300	0.0250	0.0300	0
Link 2	15.69	0.4	0.2	0.2153	0.0126	0.2153	$-\pi/2$
Link 3	11.76	0.3	0.15	0.0929	0.0094	0.0929	$-\pi/2$
Space vehicle	200.0	-	-	40.000	40.000	40.000	-

Initial Arm Base Position from Vehicle CM		
	Mission Arm	**Balance Arm**
r_x	0.2 m	-0.2 m
r_y	0.2 m	-0.2 m
r_z	0.0 m	0.0 m

Overwhelming Controller Parameters	**Parameter value**
Mass (M_c)	1.0 kg
Stiffnesss (K_c)	1e5 N/m
Rasistance (R_c)	1e3 Ns/m
Feed forward gain (μ_H)	10.0
Attitude Controller Gain Parameters	
Proportional gain of controller (*Kp*)	10
Derivative gain of controller (*Kv*)	5
Reference Trajectory Parameters	
Radius of reference circle (*R*)	0.3 m
Amplitude of velocity in *Y*-direction (*A*)	0.01 m
Angular velocity (ω)	1.0 rad/s
Actuator and reaction wheel Parameters	
Inductance of the armature (I_m)	0.001 H
Resistance of the armature (R_m)	0.2 ohm
Inertia of reaction wheel (I_{RW})	0.5 kg m^2
Bearing resistance for reaction wheel (R_b)	0.02 Nm/rad/s
Pad Parameters	
Stiffness of hard spring (K_h)	2e5 N / m
Stiffness of soft spring (K_s)	1e5 N/m
Damping resistance (R_d)	1e3 Ns/m
Joint Resistance (R_j)	0.1 Nm/rad/s

REFERENCES

Dauphin-Tanguy, G., Rahmani, A., and Sueur, C., 1999. Bond graph Aided Design of Controlled Systems. *Simulation Practice and Theory*, 7(5-6), 493-513.

Dubowsky, S. and Papadopoulos, E., 1993a. The Kinematics, Dynamics, and Control of Free-Flying and Free-Floating Space Robotic Systems. *IEEE Transactions on Robotics and Automation*, 9(5), 531-543.

Dubowsky, S. and Papadopoulos, E., 1993b. Dynamic Singularities in the Control of Free-Floating Space Manipulators. *ASME Journal of Dynamic Systems, Measurement and Control*, 115(1), 44-52.

Huang, P., Xu, Y., and Liang, B., 2005. Dynamic Balance Control of Multi-arm Free-Floating Space Robots. *International Journal of Advanced Robotic Systems*, 2(2), 117-124.

Moosavian, S. A. A. and Papadopoulos, E., 1998. On the Kinematics of Multiple Manipulator Space Free-Flyers and their Computation. *Journal of Robotic Systems*, 15(4), 207-216.

Nakamura, Y. and Mukherjee R., 1991. Non-holonomic Path Planning of Space Robots via a Bidirectional Approach. *IEEE Transactions on Robotics and Automation*, 7(4), 500-514.

Pathak, P. M., Kumar, R. P., Mukherjee, A., and Dasgupta, A., 2008. A Scheme for Robust Trajectory Control of Space Robots. *Simulation Modeling Practice and Theory*, 16(9), 1337-1349.

Yokokohji, Y., Toyoshima, T., and Yoshikawa, T., 1993. Efficient Computational Algorithms for Trajectory Control of Free-Flying Space Robots with Multiple Arms. *IEEE Transactions on Robotics and Automation*, 9(5), 571-579.

Chen, L. and Tang, X., 2006. Optimal Motion Planning of Attitude Control for Space Robot System with Dual-arms, *Proceedings of 6th World Congress on Intelligent Control and Automation*, pp. 8858-8861. June 21-23, Dalian, China.

Marchesi, M. and Angrilli, F., 1997. Control Strategy for a Free-flying Space Manipulator. *Proceedings of 8th International Conference on Advanced Robotics*, pp. 665-670. July 7-9, Monterey, CA.

Papadopoulos, E. and Moosavian, S. A. A., 1994. Dynamics and Control of Multi-arm Space Robots during Chase and Capture Operations. *Proceedings of the International Conference on Intelligent Robots and Systems*, pp. 1554-1561. September 12-16, Munich, Germany.

Breedveld, P. C. and Dauphin-Tanguy, G., 1992. *Bond Graphs for Engineers*, Amsterdam North-Holland, Elsevier.

Craig, J. J., 1986. *Introduction to Robotics–Mechanics and Control*, Addison-Wesley Publishing Co.

Karnopp, D. C., Margolis, D. L., and Rosenberg, R. C., 2006. *System Dynamics: Modeling and Simulation of Mechatronics Systems*, New Jersey, John Wiley and Sons Inc.

Mukherjee, A., Karmarkar, R., and Samantray, A. K., 2006. *Bond graph in Modeling, Simulation and Fault Identification*, India, I.K. International Publishing House Pvt. Ltd.

Ghosh, A. K., 1990. *Dynamics and robust control of robotic system: a bond graph approach*. Thesis (PhD). Department of Mechanical Engineering, Indian Institute of Technology, Kharagpur, India.

Users Manual of SYMBOLS Shakti, 2006. High-Tech Consultants, S.T.E.P., Indian Institute of Technology, Kharagpur. http://www.htcinfo.com/

AUTHORS BIOGRAPHY

Haresh Patolia received the B. E. degree in 1991and M. E. degree in 2001, both in Mechanical Engineering from B. V. Mahavidyalaya, V. V. Nagar, India. He joined the Department of Mechanical Engineering at B. V. Mahavidyalaya, V. V. Nagar, India in 1994. Currently he is a Ph. D. candidate at the Department of Mechanical and Industrial Engineering, Indian Institute of Technology, Roorkee, India.

P. M. Pathak received the B. Tech. degree in 1988 from R. E. College, Calicut, India and M. Tech. degree in 1998 from IIT, Kanpur, India both in Mechanical Engineering. He received Ph. D. degree in 2004 from IIT, Kharagpur, India. He is an Assistant Professor at the Department of Mechanical and Industrial Engineering, Indian Institute of Technology, Roorkee, India. His areas of interest are space robotics, walking robots, dynamics and control.

S. C. Jain received the B. Sc. Engg. degree in 1969 from AMU, Aligarh, India and M. E. degree in 1971 from University of Roorkee, India, both in Mechanical Engineering. He received Ph. D. degree in 1985 from University of Roorkee, India. He is a Vice-Chancellor at Mangalayatan University, Aligarth, India. His areas of interest are tribology, vibration and noise control, CAD, and robotics.

SIMULATION AND EXPERIMENTAL STUDIES ON WALKING ROBOT WITH FLEXIBLE LEGS

V. L. Krishnan[(a)], P. M. Pathak[(b)], Lokesh Sardana[(c)], S. C. Jain[(d)]

Robotics and Control Laboratory
Mechanical and Industrial Engineering Department
Indian Institute of Technology, Roorkee, 247667, India

[(a)]vlk08dme@iitr.ernet.in, [(b)]pushpfme@iitr.ernet.in, [(c)] lokesume@iitr.ernet.in, [(d)]sjainfme@iitr.ernet.in

ABSTRACT
Passive motions caused by the elasticity of the muscles, tendons, and bones help animals in swimming, flying, breathing, running etc. This passive motion can be realized in artificial legged robots by using compliant elements viz. springs etc. Appropriate use of such elements can lead to power autonomous legged robots. Several attempts in exploiting compliance in legged robots are ongoing. Yet the scientific community is far from developing commercially viable flexible legged robots. In this work, simulation and experimental studies of sagittal plane dynamics of a flexible legged quadruped has been carried out. Bond graph is used as a tool for modeling and simulation of robot dynamics. Experimental studies have been carried out to explore the underlying principles and potential challenges in the locomotion of robots with flexible legs.

Keywords: legged robot, passive motion, flexible leg, sagittal plane, bond graph modeling.

1. INTRODUCTION

The most efficient way to create desired locomotion in case of legged robots is to generate it by the passive dynamic motion of a mechanism. Passive dynamics is defined as the unforced response of the dynamic system. Nature has gifted several animals the ability to exploit passive dynamics and thus to reduce the metabolic cost of running by utilizing the elastic properties of their muscles, tendons, and bones. Passive motions caused by the elasticity of the muscles, tendons, and bones help animals in swimming, flying, breathing, running etc. This passive motion can be realized in artificial legged robots by using compliant elements viz. springs etc. Compliant elements viz. different types of springs may be employed to realize coordinated oscillatory and translational motions of various parts of legged robots leading to various gaits viz. hopping, bounding, galloping etc. Appropriate use of such elements can lead to not only energy efficient but power autonomous legged robots. Raibert (1990) pioneered research pertaining to exploitation of passive dynamics for achieving dynamic legged locomotion. He achieved remarkable experimental success in realizing dynamic legged locomotion through his famous three-part controller. Buehler led a series of work (Ahmadi and Buehler 1997; Papadopoulos and Buehler 2000; McMordie and Buehler 2001) in this area leading to development of multi-legged robots demonstrating stable, robust walking and running gaits. Hyon and Mita (2002) developed a single legged robot "Kenken", similar to the hind leg of a dog in design, which successfully executed planar locomotion. They used springs and actuators to imitate tendons and muscles in the leg of a dog. Geyer, Seyfarth and Blickhan (2005) investigated the applicability of simple spring-mass models in analyzing the human and animal locomotion. Iida, Rummel and Seyfarth (2007) studied the role of compliance in bipedal walking and running behavior. Kimura, Fukuoka and Cohen (2007) employed central pattern generators to imitate neural system and reflex response of animals in the quadruped robot "Tekken" series. Zhang and Kimura (2009) further developed an autonomous running robot titled as 'Rush'. However the research in this area is still continuing with the pursuit to develop commercially viable energy efficient (if not power autonomous) legged robots capable of performing stable locomotion at different speeds on various terrains.

In this work a flexible legged walking robot has been modeled by considering the sagittal plane representation of the quadruped robot locomotion. Bond graph is used as a tool for modeling and simulation of the robot dynamics. Robot dynamics in sagittal plane has been tested through the experiment. Experimental result shows the locomotion of the robot. Salient observations from the experiment are presented in this paper. The motive of the work is to use the passive component for force accommodation, and energy efficiency, as passive component can store energy in one step and release in other. Thus it saves the overall energy supplied to actuators.

2. MODELING OF WALKING ROBOT WITH FLEXIBLE LEGS

Modeling of a quadruped robot consists of modeling of translational and angular dynamics of robot legs and body. Figure 1(a) shows the laboratory prototype of the quadruped robot with flexible leg (Mittal, Lohani and Pandey 2009). The legs are made flexible using commercial shock absorber, shown in fig 1(b), in the lower link of the leg. Schematic diagram of the robot is shown in Fig. 1(c). Each leg of the robot has been modeled as an open chain manipulator comprising of two links connected through revolute joints. Thus each leg of the walking robot has three degrees of freedom

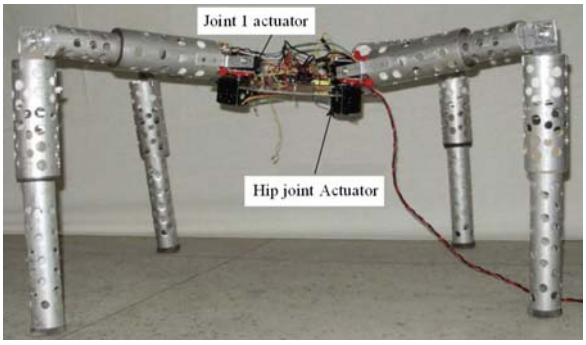

(a)

(b)

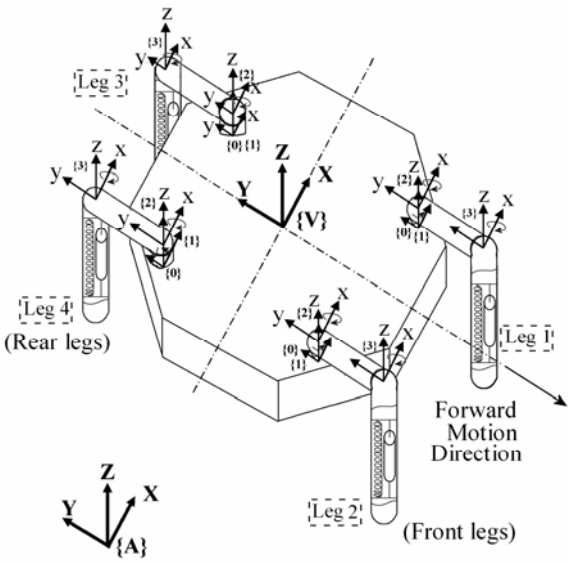

(c)

Fig. 1 (a) Quadruped Laboratory Prototype (b) Shock Absorber by ACE Controls Inc., MI, USA (c) Schematic Diagram of Flexible Legged Robot

and hence the robot has eighteen degrees of freedom (twelve degrees of freedom of legs and six degrees of freedom of body). The lower link mass of each leg is assumed to be concentrated at the leg toe. In the Fig. 1(c), frame $\{A\}$ is an inertial frame of reference and $\{V\}$ is body frame attached at the body CG. A coordinate frame is also attached to each link. The link frames are numbered according to the link to which

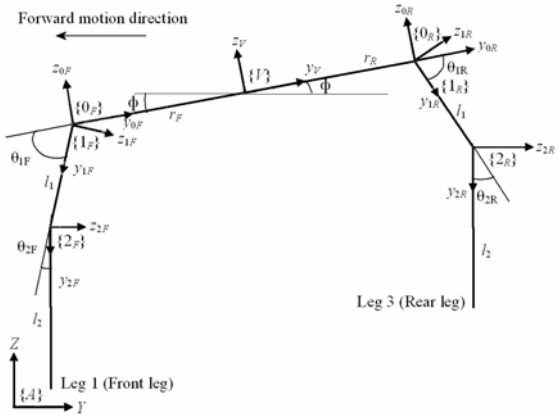

Fig. 2 Sagittal Plane Representation of Quadruped Robot

they are attached i.e. frame $\{i\}$ is rigidly attached to link i. The joint between links i and i+1 is numbered as i+1. The rotational inertia of a body (or link) is defined about a frame fixed at the centre of gravity (CG) of the body (or link). The axis of the CG frame is fixed along the principal directions of the body (or link). The surface on which robot is walking is assumed as a hard surface with no slipping of legs. The forward direction of motion of the robot has been chosen to be the negative Y-axis. The robot dynamics has been analyzed in the sagittal plane of locomotion i.e., YZ plane. It has been considered that the frontal dynamics can be taken care of with the help of an attitude control device viz. moving appendage employed in the transverse direction i.e. along X-axis. Moving appendage is an inertial element in the form of a rack to balance the disturbing moments on the body. The rack is driven through a pinion which in turn is actuated by a servomotor.

The corresponding representation of the kinematics of quadruped robot in the sagittal plane of locomotion is shown schematically in the Fig. 2. The figure shows the view of the robot with two degree of freedom (DOF) legs in a sagittal plane viz. YZ plane. The two DOF referred in fig 2. are in correspondence to joint 2 and 3 of a leg in fig. 1(c). The DOF at the hip joint of each leg (rotation about z axis), i.e. joint 1 in fig. 1 (c) is non-functional with respect to the current analysis and hence considered to be locked. From Fig. 2, the position of the front leg tip can be expressed in y and z-directions as,

$$Y_{Flt} = Y_{CM} + r_F \cos(\pi+\phi) + l_1 \cos\left(\pi+\phi+\theta_{1F}\right) + l_2 \cos\left(\pi+\phi+\theta_{1F}+\theta_{2F}\right) \quad (1)$$

$$Z_{Flt} = Z_{CM} + r_F \sin(\pi+\phi) + l_1 \sin\left(\pi+\phi+\theta_{1F}\right) + l_2 \sin\left(\pi+\phi+\theta_{1F}+\theta_{2F}\right) \quad (2)$$

In Eq. (1) and (2) Y_{CM} and Z_{CM} represents the location of frame $\{V\}$ with respect to frame $\{A\}$; r_f is the distance of $\{0_F\}$ frame from $\{V\}$ frame, ϕ is attitude of body with respect to frame $\{A\}$, θ_{1F} and θ_{2F} are the joint

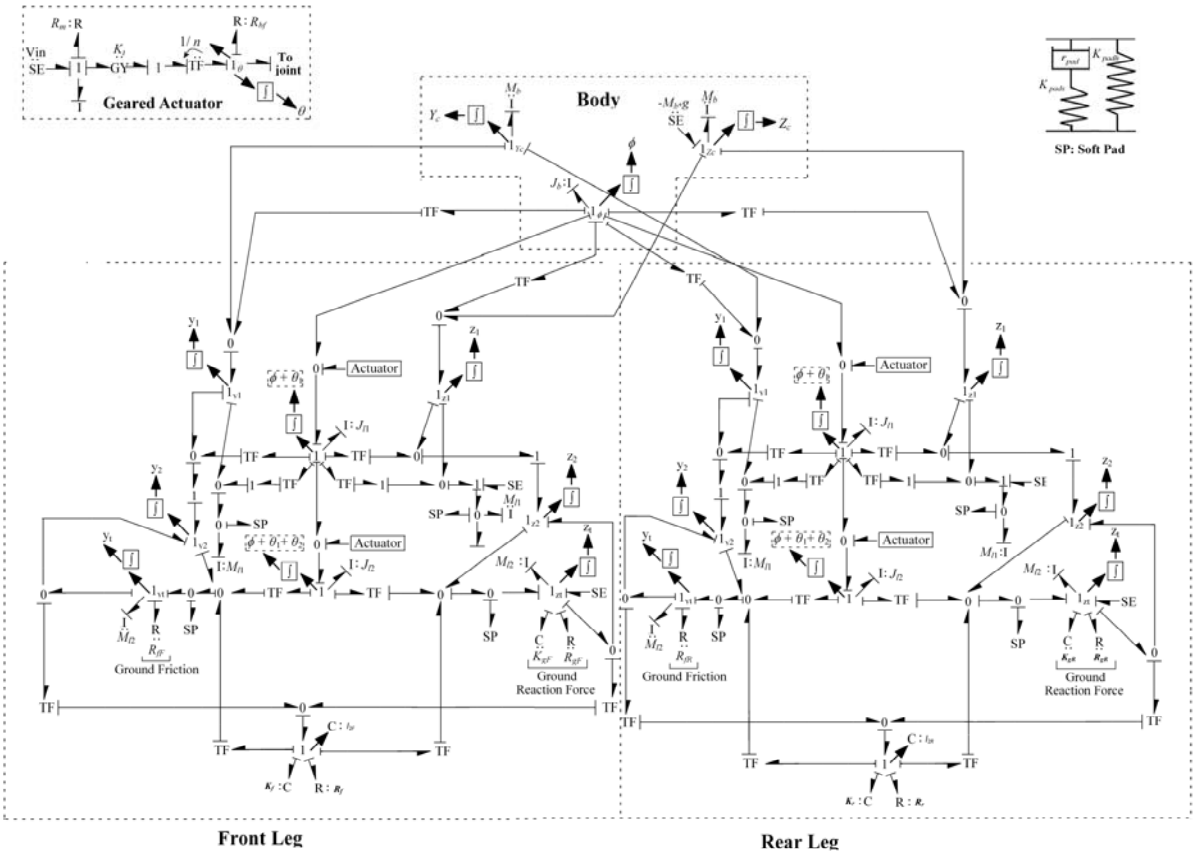

Fig. 3 Bond Graph representation of Sagittal Plane Dynamics of Flexible Legged Robot

angles of first and second joint of front leg, l_1 and l_2 are the lengths of the first and second links of a leg. Differentiating the expressions in Eq. (1) and (2), we get components of the front leg tip velocity in y and z-directions as,

$$\begin{aligned} V_{FtY} &= \dot{Y}_{CM} - r_F \sin(\pi+\phi)\dot{\phi} \\ &-l_1 \sin\left(\pi+\phi+\theta_{1F}\right)\left(\dot{\phi}+\dot{\theta}_{1F}\right) \\ &-l_2 \sin\left(\pi+\phi+\theta_{1F}+\theta_{2F}\right)\left(\dot{\phi}+\dot{\theta}_{1F}+\dot{\theta}_{2F}\right) \\ &+\dot{l}_2 \cos\left(\pi+\phi+\theta_{1F}+\theta_{2F}\right) \end{aligned} \tag{3}$$

$$\begin{aligned} V_{FtZ} &= \dot{Z}_{CM} + r_F \cos(\pi+\phi)\dot{\phi} \\ &+l_1 \cos\left(\pi+\phi+\theta_{1F}\right)\left(\dot{\phi}+\dot{\theta}_{1F}\right) \\ &+l_2 \cos\left(\pi+\phi+\theta_{1F}+\theta_{2F}\right)\left(\dot{\phi}+\dot{\theta}_{1F}+\dot{\theta}_{2F}\right) \\ &+\dot{l}_2 \sin\left(\pi+\phi+\theta_{1F}+\theta_{2F}\right) \end{aligned} \tag{4}$$

Similarly, rear leg tip position with respect to inertial reference frame $\{A\}$ can be represented as,

$$\begin{aligned} Y_{Rlt} &= Y_{CM} + (r_R \cos\phi) + l_1 \cos\left(\phi+\theta_{1R}\right) \\ &+l_2 \cos\left(\phi+\theta_{1R}+\theta_{2R}\right) \end{aligned} \tag{5}$$

$$\begin{aligned} Z_{Rlt} &= Z_{CM} + (r_R \sin\phi) + l_1 \sin\left(\phi+\theta_{1R}\right) \\ &+l_2 \sin\left(\phi+\theta_{1R}+\theta_{2R}\right) \end{aligned} \tag{6}$$

Where r_R is the distance of frame $\{0_R\}$ from frame $\{V\}$, θ_{1R} and θ_{2R} are the joint angles of first and second joint of rear leg. It is assumed that initially rear leg link lengths are equal to the respective front leg link lengths. The rear leg tip velocities can be evaluated from Eq. (5) and (6) as,

$$\begin{aligned} V_{RtY} &= \dot{Y}_{CM} - (r_R \sin\phi)\dot{\phi} - l_1 \sin\left(\phi+\theta_{1R}\right)\left(\dot{\phi}+\dot{\theta}_{1R}\right) \\ &-l_2 \sin\left(\phi+\theta_{1R}+\theta_{2R}\right)\left(\dot{\phi}+\dot{\theta}_{1R}+\dot{\theta}_{2R}\right) \\ &+\dot{l}_2 \cos\left(\phi+\theta_{1R}+\theta_{2R}\right) \end{aligned} \tag{7}$$

$$\begin{aligned} V_{RtZ} &= \dot{Z}_{CM} + (r_R \cos\phi)\dot{\phi} + l_1 \cos\left(\phi+\theta_{1R}\right)\left(\dot{\phi}+\dot{\theta}_{1R}\right) \\ &+l_2 \cos\left(\phi+\theta_{1R}+\theta_{2R}\right)\left(\dot{\phi}+\dot{\theta}_{1R}+\dot{\theta}_{2R}\right) \\ &+\dot{l}_2 \sin\left(\phi+\theta_{1R}+\theta_{2R}\right) \end{aligned} \tag{8}$$

The flexibility of lower links of each leg is modeled on the basis of the following equations.

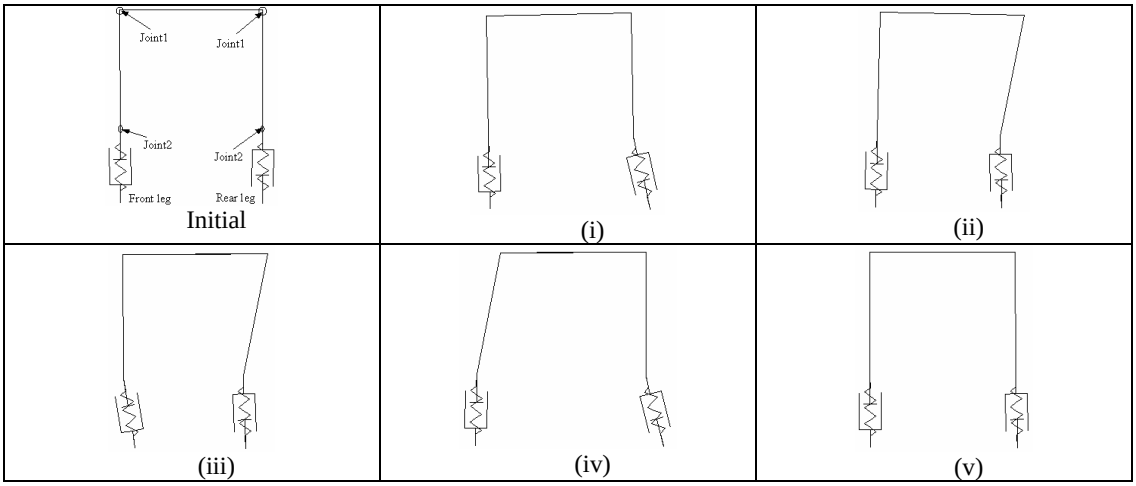

Fig. 4 Phases of gait pattern

$$(l_{2F})^2 = (Y_{Flt} - y_{2F})^2 + (Z_{Flt} - z_{2F})^2 \quad (9)$$

$$(l_{2R})^2 = (Y_{Rlt} - y_{2R})^2 + (Z_{Rlt} - z_{2R})^2 \quad (10)$$

where l_{2F} and l_{2R} are respectively the instantaneous lengths of link 2 of the front and rear legs. Y_{Flt} and Z_{Flt} are respectively the Y and Z coordinates of the toe of front leg and Y_{Rlt} and Z_{Rlt} of the rear leg.
Taking derivative of Eq. (9) and (10), we obtain respectively Eq. (11) and (12) as below:

$$(\dot{l}_{2F}) = \frac{(Y_{Flt} - y_{2F})}{l_{2F}} * (\dot{Y}_{Flt} - \dot{y}_{2F}) + \frac{(Z_{Flt} - z_{2F})}{l_{2F}} * (\dot{Z}_{Flt} - \dot{z}_{2F}) \quad (11)$$

$$(\dot{l}_{2R}) = \frac{(Y_{Rlt} - y_{2R})}{l_{2R}} * (\dot{Y}_{Rlt} - \dot{y}_{2R}) + \frac{(Z_{Rlt} - z_{2R})}{l_{2R}} * (\dot{Z}_{Rlt} - \dot{z}_{2R}) \quad (12)$$

With the help of Eq. (3), (4), (7), (8), (11) and (12) bond graph model is drawn in Fig. 3. It represents the sagittal plane dynamics of a quadruped robot with flexible legs. Further, in order that the robot demonstrates locomotion in the forward direction a gait pattern has been specified. The gait pattern is presented pictorially through fig. 4. The following steps describe the gait pattern:

1. Joint 2 of the rear leg (Leg3) to be rotated by 0.2 radians in *anticlockwise* direction about -x axis.
2. Joint 1 of the rear leg to be rotated by 0.2 radians in *clockwise* direction about -x axis.
3. Joint 2 of the front leg (Leg1) rotated by 0.2 radians in *anticlockwise* direction about -x axis.
4. Joint 1 of the front and rear legs are rotated by 0.2 radians respectively in *clockwise* and *anticlockwise* direction about -x axis.
5. Joint 1 of the front leg is rotated by 0.2 radians in *anticlockwise* direction and joint 2 of the front and rear legs are rotated by 0.2 radians in *clockwise* direction about -x axis.

Table1: Walking Robot Parameters

Parameters	Value
Walking robot Body	Mass: M_b = 0.26Kg; Polar M. I.: J_b = 0.002Kg-m^2
Position of Hip joints from body CG	Front: r_F = 0.04m; Rear: : r_R = 0.04m
Link Lengths	l_1 = 0.068m, l_2 = 0.04m
Link Mass	M_{l1}= 0.07Kg; M_{l2}= 0.06Kg
Polar M. I of links	J_{l1}= 0.00004 Kg-m^2 ; J_{l2} = 0.00002Kg-m^2
Actuator parameters	Inductance: L_m =0.001H; Resistance: R_m =1000Ohms; Motor constant: K_t = 0.2N-m/A; Gear Ratio: n = 254; Bearing resistance: R_{bf} = 0.1N-s/m
Ground Parameters	Stiffness: K_g = 10000N/m; Damping: R_g = 10N-s/m; frictional resistance: R_{fY} = 10N-s/m
Flexible Link parameters	Stiffness: K_f = 350N/m; DampingR_f = 0.35N-s/m

The above steps of a gait together forms a locomotion cycle. This gait is repeated over ten cycles to

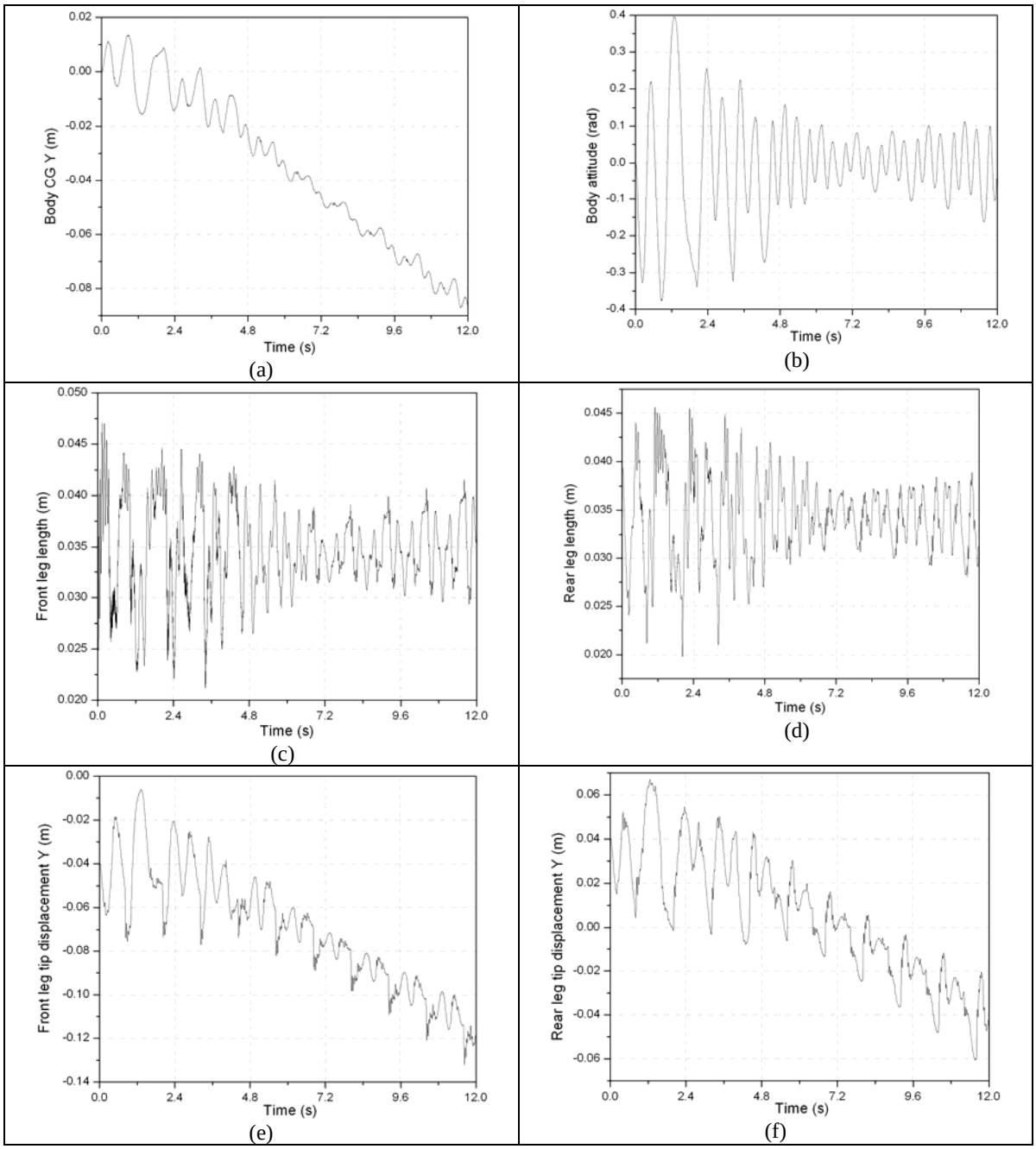

Fig. 5 Simulation results of sagittal plane locomotion of flexible legged robot (a) Body CG Y displacement v/s time (b) Body attitude v/s time (c) Front Leg Length v/s time (d) Rear Leg Length v/s time (e) Front leg tip displacement v/s time (f) Rear leg tip displacement v/s time

demonstrate the body advancement in the forward direction. To take the joint angles to the specified value of joint angles the voltage supplied to motor is based on PD control. One locomotion cycle is assumed to be of 1.2 seconds. The parameters used for simulation are listed in table 1.

Fig. 5 shows the simulation results of sagittal plane locomotion of flexible legged robot over a period of 12s. Fig. 5 (a) shows the body CG Y displacement versus time. It can be noted that the body displacement in -Y direction occurs. Fig. 5 (b) presents the body attitude versus time. Fig. 5(c) shows the variation of instantaneous length of lower link of front leg i.e. l_{2F} versus time. Similarly Fig. 5 (d) shows the variation of l_{2R} versus time. The results indicate the flexibility modeled in the lower link of each leg. Fig. 5 (e) shows the front leg tip displacement versus time. Fig. 5 (f) shows the rear leg tip displacement versus time. These figures show the locomotion of the robot with flexible legs. Fig. 6(a) shows the front leg joint '1' angle

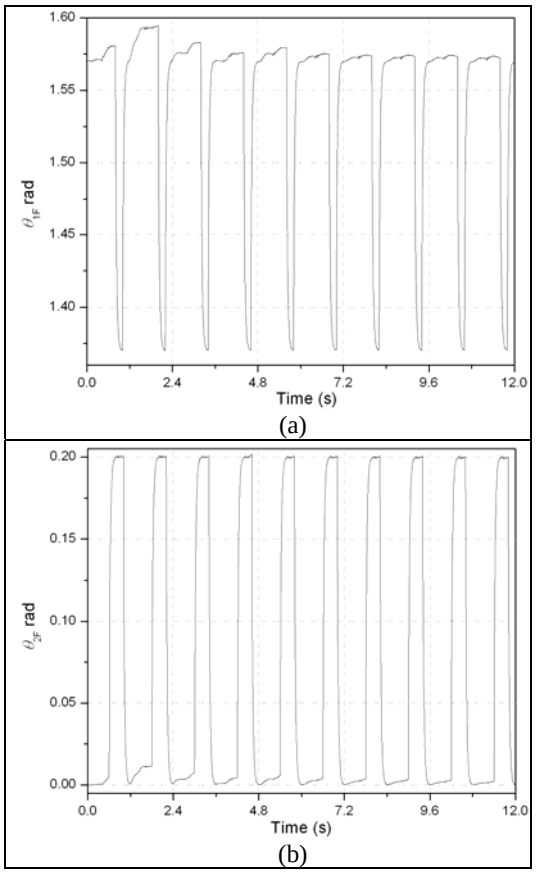

Fig. 6 Simulation results (a) θ_1 Front leg v/s time (b) θ_2 Front leg v/s time

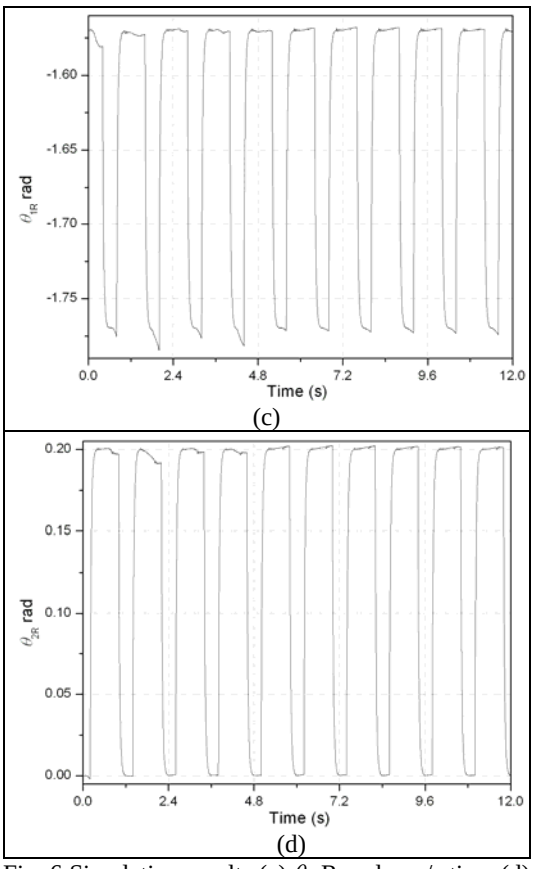

Fig. 6 Simulation results (c) θ_1 Rear leg v/s time (d) θ_2 Rear leg v/s time

displacement versus time. Fig. 6(b) presents the front leg joint '2' angle displacement versus time. Rear leg joint '1' angle displacement versus time is shown in fig. 6(c). Fig. 6(d) presents the rear leg joint '2' angle displacement versus time. Fig. 7 shows the animation result which indicates desired forward motion of the walking robot. Animation has been generated from the simulation results. Here only few frames are shown to have clarity in the figure.

3. EXPERIMENTAL RESULTS

The sagittal plane dynamics of walking robot has been tested through the experimental set up shown in fig. 8.

The experimental setup comprises of a post which supports the planar model of the flexible legged quadruped robot through a horizontal rod. The body of the robot is pivoted about the rod. Thus it is constrained to move along a circular trajectory about the post. Hence, the instantaneous response of robot is restricted to a plane tangential to the circular trajectory. In this way the sagittal plane response of the robot is realized. The planar model of flexible legged robot consists of body, legs and actuators at the two joints in each of the front and rear legs. Hence, in total four AX-12+ motors (Dynamixel make) are used to realize the two link legs. The controller CM5+ housed in a plastic sturdy shell constitutes the body of the robot. Springs are attached to the lower link of each leg to introduce flexibility into the legs.

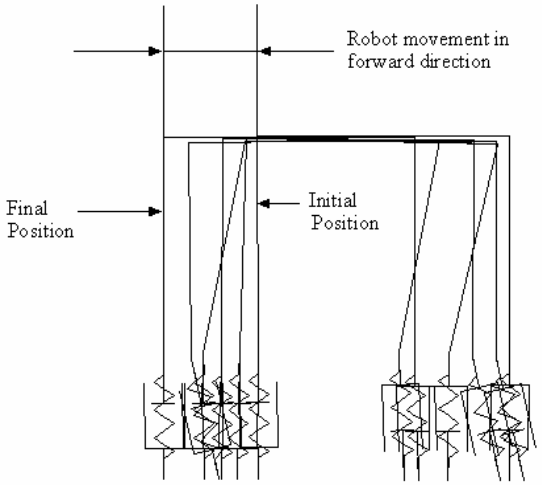

Fig. 7: Animation of Walking Robot Motion

The flow chart corresponding to the gait pattern used for the robot locomotion control is presented in fig. 9. Bioloid control behavior interface of the Robotis

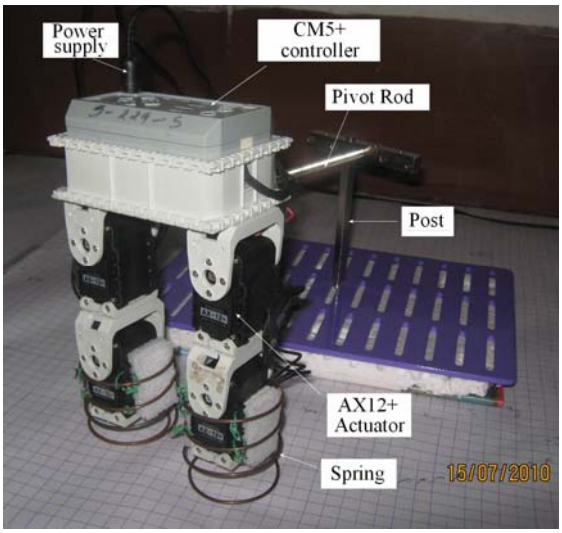

Fig.8: Experimental set up representing saggital plane dynamics of walking robot

Inc. is used for the purpose of controlling robot locomotion. The program is fed to the CM5+ controller through personal computer (not shown in the fig. 8). SMPS is used for supplying required power to the actuators and electronic circuitry.

Fig. 10 presents the snapshots of robot locomotion. It can be noted from the snapshots that the robot is constrained, through the pivot rod connected to post, to trace a semicircular trajectory. Fig. 11 shows the actual joint angle displacement of legs. Fig. 11(a) and (b) respectively shows the front leg first and second joint rotation versus time. Fig. 12(a) and (b) respectively shows the rear leg first and second joint rotation versus time. It can be noted from the plots of joint rotation curves that the specified gait pattern is being followed. The joint rotation curves in fig. 11 and 12 are similar to the simulated results in fig. 6. Fig. 13 presents the front and rear leg tip movement versus time, recorded over first ten locomotion cycles. Front and rear leg tip movement pattern is similar to simulated results presented in Fig. 5(e) and 5(f). It can be noted that simulation is also carried out for ten locomotion cycles i.e for 12 seconds. The leg tip movement values plotted in fig 13 is the arc length translated by the leg tip along a semicircular trajectory versus time. It can be noted that the arc length traced at the end of ten cycles by the front and rear leg tips are respectively about 0.16m and -0.04m which is very close to corresponding simulation results. Thus the robot locomotion in forward direction based on the specified gait pattern is obtained.

4. CONCLUSION AND DISCUSSIONS

Following observations has been made while realizing the sagittal plane locomotion of the robot:

(i) Stiffness of the spring selected should be appropriate. It should be within an optimum range so that it absorbs undesirable impact forces coming from the ground while in locomotion. At the same time less stiffer springs will not generate traction force required for locomotion.

(ii) The clearance between the springs and the leg links should be minimum possible so that the link rotation may carry the spring also along with it.

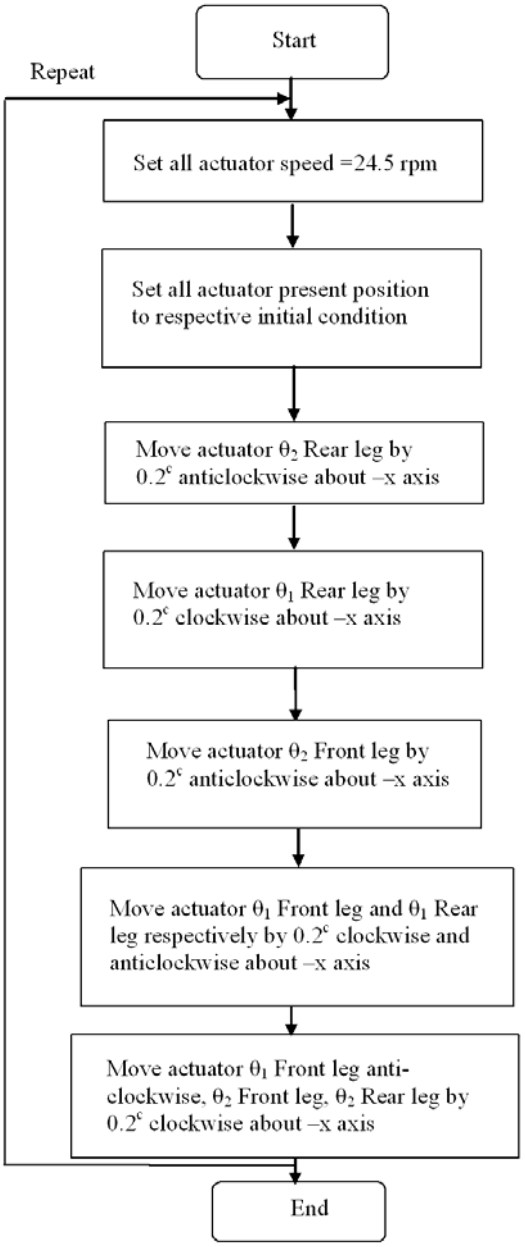

Fig. 9: Flowchart of the program for locomotion control

Fig. 10 Snapshots of sagittal plane locomotion of flexible legged walking robot

(iii) There can be alternative gait patterns leading to faster and stable locomotion which is a matter of further investigation.

In the present experimental setup provision for recording the ground reaction forces and the traction force does not exists. In future, force sensors can be employed at the toe and investigations pertaining to the

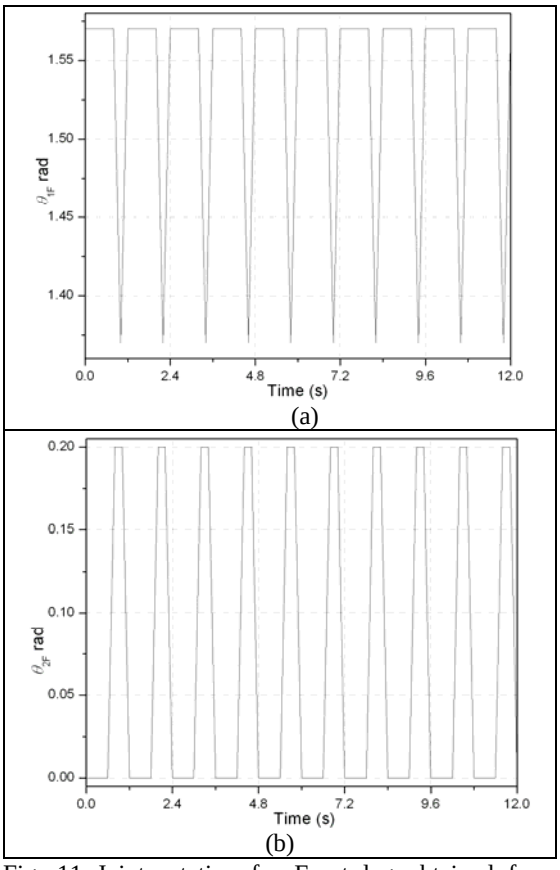

Fig. 11 Joint rotation for Front leg obtained from Experiment (a) θ_1 v/s time (b) θ_2 v/s time

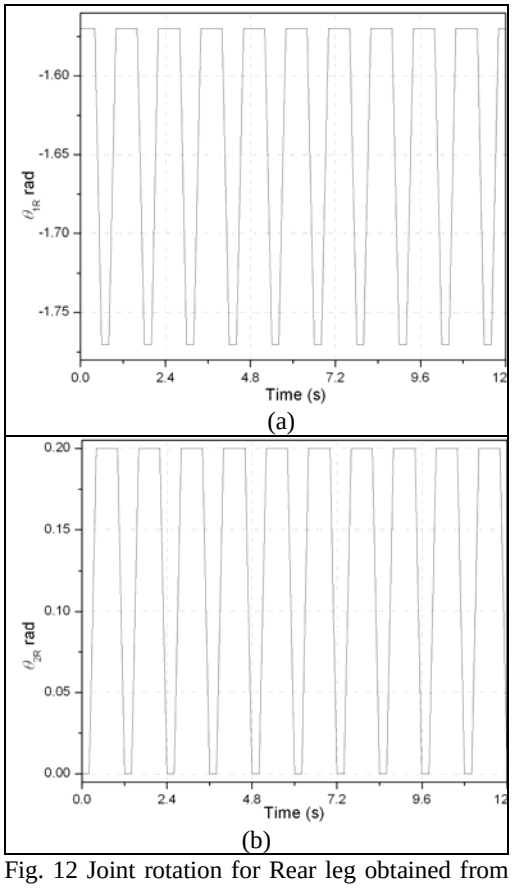

Fig. 12 Joint rotation for Rear leg obtained from Experiment (a) θ_1 v/s time (b) θ_2 v/s time

role of passive elements viz. spring in absorbing impact forces can be carried out. The ultimate aim is to implement the force control strategy with the help of flexible link and to extend the developed strategy to four legged walking robot with flexible legs.

(ii) In future the present setup is proposed to be used for studies aiming at improving the energy efficiency of the robot locomotion.

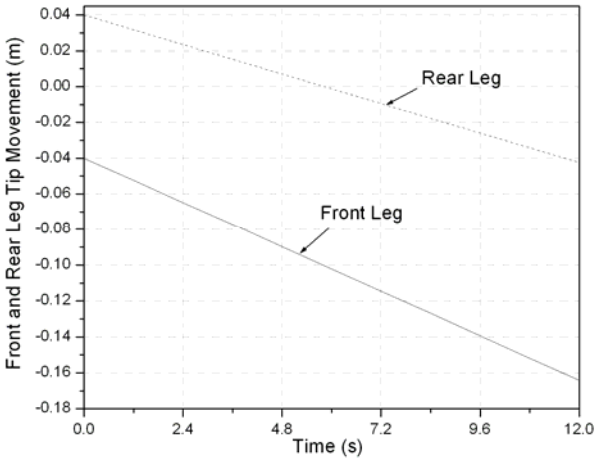

Fig. 13: Front and Rear Leg Tip Forward Movement (m) v/s time (s)

REFERENCES

Ahmadi, M. and Buehler, M., 1997, Stable Control of a Simulated One-Legged Running Robot with Hip and Leg Compliance, *IEEE Transactions on Robotics and Automation,* 13 (1); 96 – 104.

Geyer, H., Seyfarth, A. and Blickhan, R., 2005, Spring-Mass Running: Simple Approximate Solution and Application to Gait Stability, *Journal of Theoretical Biology*, 232(3); 315-328.

Hyon, S. H. and Mita, T., 2002, Development of a biologically inspired hopping robot: Kenken, *Proceedings of IEEE International Conference on Robotics and Automation*, Vol. 4, pp. 3984–3991, 11-15 May, Washington, DC (U.S.A).

Iida, F., Rummel, J. and Seyfarth, A., 2007, Bipedal Walking and Running with Compliant Legs, *Proceedings of IEEE International Conference on Robotics and Automation*, pp. 3970–3975, 10-14 April., Roma, Italy.

Kimura, H., Fukuoka, Y. and Cohen, A. H., 2007, Adaptive Dynamic Walking of a Quadruped Robot on Natural Ground based on Biological Concepts, *Int. Journal of Robotics Research*, 26(5); 475-490.

McMordie, D. and Buehler, M., 2001, Towards Pronking with a Hexapod Robot, *Proceedings of 4th International Conference on Climbing and Walking Robots,* pp. 659-666, 24-26 September, Karlsruhe, Germany.

Mittal A., Lohani H. and Pandey A., 2009, *Dynamic Analysis of a Quadpruped Robot*, B. Tech thesis, IIT Roorkee, Roorkee, India.

Papadopoulos, D. and Buehler, M., 2000, Stable Running in a Quadruped Robot with Compliant Legs, *Proceedings of IEEE International Conference on Robotics and Automation*, Vol. 1, pp. 444–449, 24-28 April, San Francisco (U.S.A).

Raibert, M. H., 1990, Trotting, Pacing and Bounding by a Quadruped Robot, *Journal of Biomechanics*, 23(1); 79-81.

Zhang, Z. G. and Kimura, H., 2009, Rush: A Simple and Autonomous Quadruped Running Robot, *Journal of Systems and Control Engineering*, 223(1), 323-336.

FUEL CONSUMPTION IMPROVEMENT OF VEHICLE WITH CVT BY BOND GRAPHS

Katsuya Suzuki[(a)], Kazuhiro Tanaka[(b)], Sho Yamakawa[(c)], Fumio Shimizu[(d)], Masaki Fuchiwaki[(e)]

[(a)- (e)]Kyushu Institute of Technology

[(a)]kachandesu2002@yahoo.co.jp, [(b)]kazuhiro@mse.kyutech.ac.jp, [(c)]yamakawa@vortex.mse.kyutech.ac.jp, [(d)]shimizu@mse.kyutech.ac.jp, [(e)]futiwaki@mse.kyutech.ac.jp,

ABSTRACT

Dynamic system simulation is important for automotive development and improvement as well as for analyzing mechanism of the system. A vehicle power train with a continuously variable transmission (CVT) was modeled into a simple and a detailed Bond Graph model and the fuel economy and engine power performance was simulated by use of the models according to the Japanese 10 Mode cycle. As a result, it is verified that the proposed Bond Graph models represent the basic dynamic characteristics of vehicle power train system with CVT and it is useful to calculate the optimum gear change pattern for low fuel consumption.

Keywords: Bond Graphs, Vehicle, CVT, Power train

1. INTRODUCTION

Recently environmental problems such as global warming and air pollution become more serious year by year. Car exhaust gas emission of vehicle is one of the causes of the environmental problems, so that in order to solve the problems vehicle industries have been making activities, one of which is to improve fuel economy of car. A simulation method can play an important role to predict and determine parameters necessary to develop and improve a fuel economy, especially. Though simulations on fuel economy were studied in the past (Suzuki and Hosoi 2007; Yokoi 1979), there are few studies of the inverse problem such as running resistance is an input parameter for a vehicle power train system (Togai and Koso 2006).

The objectives of our study are to establish a system Bond Graph model of a power train system with the continuously variable transmission (CVT) (Carbone, Mangialardi, Bonsen, Tursi, and Veenhuizen 2007; Cho and Hedrick 1989; Kong and Parker 2008; Mantriota 2002; Srivastava and Haque 2008; Srivastava and Haque 2009; Srivastava and Haque 2009) as a study of the inverse problem in which running resistance is an input parameter for a vehicle power train system, and a simulation method calculating an optimal gear ratio of CVT suitable for running pattern of a vehicle.

In this study, a one-dimensional system Bond Graph of a vehicle power train including the CVT was established and an engine output power was simulated in the Bond Graph model according to The Japanese 10 Mode cycle. Then it is also clarified that it is possible to calculate the optimal gear ratio suitable for running pattern of a vehicle with CVT.

2. MODELING OF VEHICLE WITH THE CVT

Generally driving power performance is shown by vehicle maximum speed and arrival time for some distance as output variables against engine torque as an input variable. However, fuel consumption can be measured after running according to a legal running mode. In this case, an input variable is power for running resistance connected with vehicle acceleration and an output variable is engine power, from which the fuel consumption can be calculated. Namely, power-flow is quite reverse against the case of calculating driving power performance in a vehicle system model.

2.1. Analysis Object

In this paper, an analysis target is a power train system of vehicle including a belt type CVT with a gasoline engine as a driving source. Figure 1 shows a schematic illustration of the power train system, which consists of an engine, a clutch, a belt-type CVT, a final gear, an axle, and tires. This system can be expressed by Bond

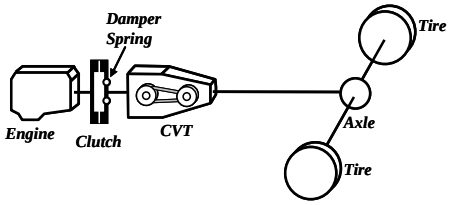

Figure 1: Schematic Illustration of Power Train

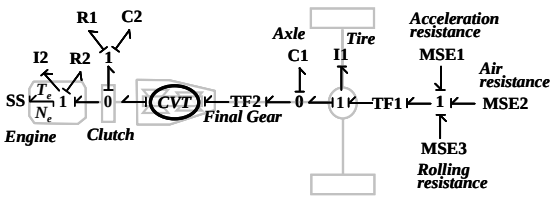

Figure 2: Bond Graph for Power Train

Graphs (Karnopp and Rosenberg 1970; Karnopp, Margolis, and Rosenberg 2006; Thoma 1990), shown in Figure 2 (Hrovat and Tobler 1991).

Each Bond Graph symbol indicates the respective following;

SE elements (effort source elements),

MSE1; the acceleration resistance R_s,

MSE2; the air resistance R_a,

MSE3; the rolling resistance R_r,

R elements (resistance),

R1; the frictional loss in the clutch,

R2; the frictional loss in the engine,

C elements (capacitor),

C1; the stiffness of the axle,

C2; the damper spring of the clutch,

I elements (inertia),

I1; the inertia of tires,

I2; the inertia of the engine,

TF elements (transformer),

TF1; transformer of the tire radius,

TF2; transformer of the final gear.

SS elements (flow and effort sensor in Bicausal Bond Graphs) (Gawthrop 1995)

Using this model, the engine revolution as well as engine torque are calculated as the output variables through the running resistance proportional to vehicle speed as the input variable. A way for calculating fuel consumption is described in Section 2.3.

2.2. Input Variable

The input variable in the simulation is the running resistance which is the sum of the following four resistances, the acceleration resistance, the air resistance, the rolling resistance and the gradient resistance, that are such function of the vehicle speed as expressed by Equation (1), (2), (3), and (4), respectively. Here, as described later, a running mode is supposed running on a level ground, the hill climbing resistance is always zero, 0 [N].

$$R_s = Ma \tag{1}$$

$$R_a = C_D \frac{\rho}{2} AV^2 \tag{2}$$

$$R_r = \mu Mg \ (V > 0) \tag{3}$$

$$R_c = Mg \sin\theta \tag{4}$$

Here, A, a, C_D, g, M, V, μ, θ, and ρ indicate vehicle frontal projected area [m^2], vehicle acceleration [m/s^2], drag coefficient [-], acceleration of gravity [m/s^2], vehicle mass [kg], vehicle speed [m/s], coefficient of rolling resistance [-], up-hill road gradient [deg], and air density [kg/m^3], respectively.

In a simulation of forward power-flow direction, the engine power is delivered to the running resistance (the acceleration resistance, the air resistance and the rolling resistance), the frictional loss dissipated in components and the inertial power. However, in a simulation of reverse power-flow direction, the running resistance (the acceleration resistance, the air resistance and the rolling resistance) calculated in proportional to each running mode is given to the system as an input variable and reverse calculation through the power train system including a CVT component causes the output power transmitted to the engine finally.

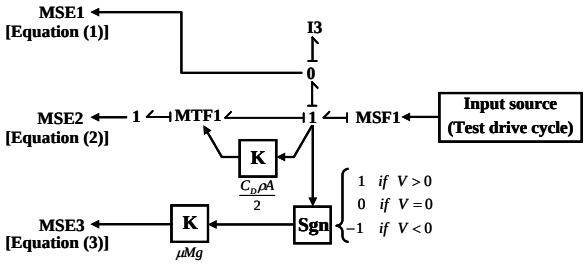

Figure 3: Input Variables

Figure 3 shows the input variables for the system. Each input variable shown by MSE-element is defined as the respectively corresponding Equation (1), (2) and (3). MSF1-element shows flow source (the 10 Mode cycle). In SE3-element, the rolling resistance is active only at $V > 0$. In this model the friction resistance in the clutch and the power lost in the engine are taken into consideration, so that the engine output power and fuel economy can be calculated more precisely.

2.3. Method of Calculating Fuel Economy

Figure 4 shows experimental data for the representative performance curves of vehicle engine. Fuel consumption is calculated using specific fuel consumption (*SFC* [g/(PS*h)]) which is expressed by broken lines in Figure 4. The chain line, the solid line with an arrow and WOT in the Figure indicate the optimum operating line for engine, the constant horse power line and the torque line on condition that the engine throttle valve is fully opened. In order to calculate easily the digital value of *SFC* from Figure 4, Figure 5 as a new diagram of *SFC* is made by the least-square method.

Equations (5), (6), (7), and (8) are used to calculate the sum of fuel consumption (*TFC* [*l*]) and the average fuel consumption (*AFC* [km/*l*]). In Equation (5), an engine output power (P [PS]) is calculated as the product of engine torque (T_e [Nm]) and engine revolution (N_e [rpm]). Fuel consumption (*FC* [*l*/s]) is calculated by Equation (6), in which unit of *SFC* is changed from [g/(PS*h)] to [*l*/(PS*s)] using density of gasoline, 0.783 [g/cm^3] at 15 [^oC]. To integrate *FC* for vehicle running time leads *TFC* in Equation (7). Finally *AFC* is given in Equation (8), where *SM* ([km]) indicates sum of millage for vehicle running time.

$$P = T_e \times N_e \times 1.42 \times 10^{-4} \tag{5}$$

$$FC = [((SFC \div 3600) \div 0.783) \times 10^{-3}] \times P \tag{6}$$

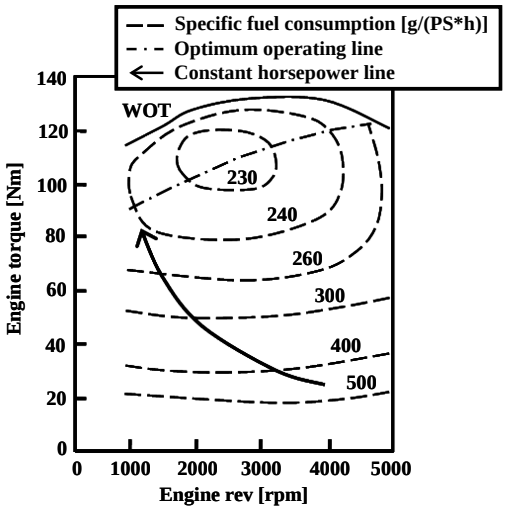

Figure 4: Representative Engine Performance Curves (Experimental Data)

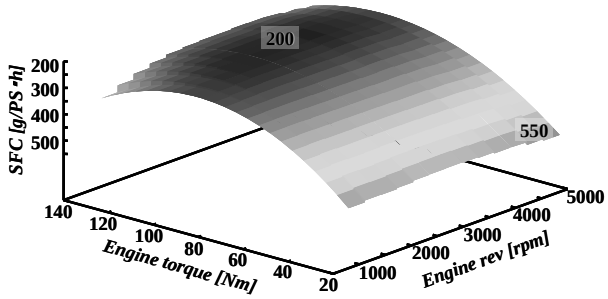

Figure 5: Specific Fuel Consumption (Approximate Value)

$$TFC = \int FC\, dt \tag{7}$$

$$AFC = SM \div TFC \tag{8}$$

The 20-Sim software is used for Bond graph modeling and simulation of vehicle fuel consumption with a CVT component in the present study.

2.4. How to Search for Optimum Gear Ratio in the CVT

A continuously variable transmission (CVT) is a new component expected to improve fuel economy. Especially in vehicle transmissions, the CVT is well suited for more fuel-efficient driving in any driving mode compared with traditional gear transmissions with fixed gear ratio, because it is possible to change the gear ratio continuously and smoothly, to reduce the shock of gear change and to operate at high efficiency domain of engine revolution.

A CVT component, shown in Figure 6, is modeled into two kind systems, CVT-1 in Figure 7 as a simple model and CVT-2 in Figure 9 as a detailed model. The difference between the two models is also studied after simulation of dynamic characteristics.

Figure 6: CVT (Daihatsu Motor Co. 2006)

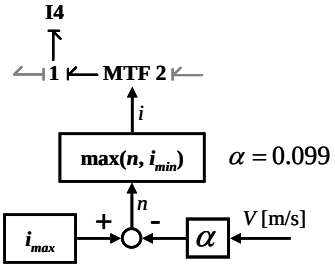

Figure 7: Bond Graph of CVT-1

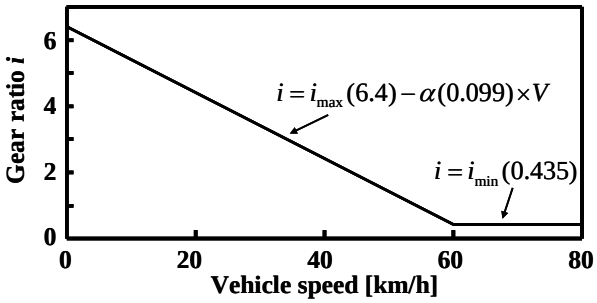

Figure 8: Assumed Gear Ratio of CVT-1

Figure 7 shows the Bond Graph model of CVT-1, where one inertial mass consisting of two pulleys and a belt is expressed by one I-element, I4, and gear ratio by a modulated transformer, MTF2-element, and its variable coefficient is given as CVT gear ratio *i* shown in Figure 8.

In the present case, the coefficient function of MTF2-element is defined to be linearly proportional to vehicle speed. In Figure 8, α indicates the proportional coefficient and is defined as 0.099. The gear ratio *i* is defined as a function $\max(n, i_{\min})$ and is calculated by Equations (9) and (10), where i, n, V, $i_{\max}$, and $i_{\min}$ indicate gear ratio, variable, vehicle speed [km/h], maximum and minimum gear ratio, respectively.

$$n = i_{\max} - \alpha \times V \tag{9}$$

$$i = \max(n, i_{\min}) \tag{10}$$

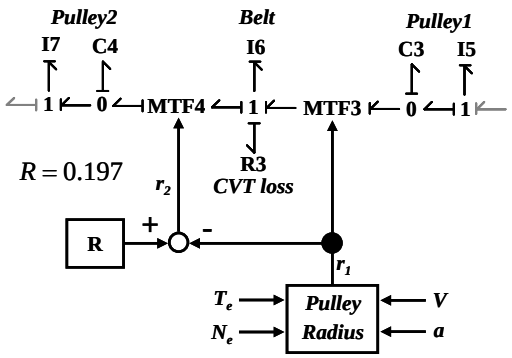

Figure 9: Bond Graph of CVT-2

Figure 9 shows Bond Graph of CVT-2, where the pulley and the belt are expressed independent in the model. Inertial effects of Pulley1 and Pulley2 are expressed by I5- and I7-element, respectively. Stiffness between Pulley1 and the belt and stiffness between Pulley2 and the belt are expressed by C3- and C4-elements, respectively. Belt transforms power between rectilinear motion and rotational motion, and its variable coefficient is given by *r*, which is a pulley radius from the center of pulley shaft to the contact point at the belt and the pulley. Because *r* is variable according to driving condition in CVT, the belt is represented by MTF-element. The inertial effect of the mass of belt is represented by I6-element and the frictional power loss between the belt and the pulleys by R3-element.

Gear ratio is decided as to reduce the torque difference between a point A on the constant horse power line and a point B on the optimum operating line (Figure 10) (Pfiffner, Guzzella, and Onder 2003; Takiyama and Morita 1993). Radius r_1 and r_2, the coefficients of MTF3- and MTF4-elements, are decided from the function of engine torque, engine revolution, vehicle speed and vehicle acceleration force. Radius r_1 is changeable on the arrow direction of solid line. The optimum operating line shown by chain line in Figure 10 is represented as Equation (11) obtained with the least-square method. Radius r_2 is given by Equation (12), where R is constant and is the sum of r_1 and r_2. Then, gear ratio i of CVT-2 is represented by Equation (13).

$$T_e = -1.0\times10^{-6}\times N_e^2 + 1.45\times10^{-2}\times N_e + 79.29 \quad (11)$$

$$r_2 = R - r_1 \quad (12)$$

$$i = r_2 / r_1 \quad (13)$$

3. JAPANESE AUTOMOTIVE TEST DRIVE CYCLES

In the present study, the test driving mode is Japanese test drive cycle, called as the Japanese 10 Mode cycle and shown in Figure 11, which approximates a situation of driving in the city by combining ten kinds of driving patterns such as idling, acceleration, constant speed, and deceleration.

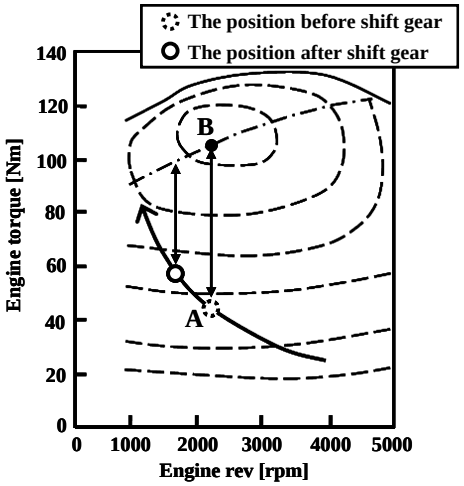

Figure 10: Active Control of CVT-2 (Yokoi 1979)

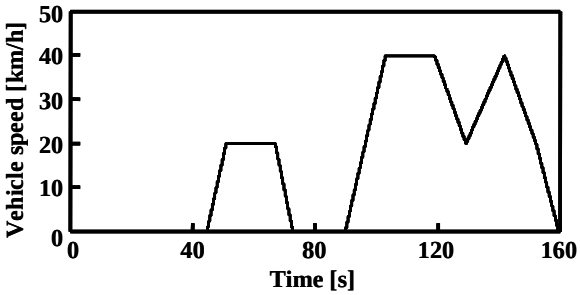

Figure 11: The Japanese 10 Mode cycle

Table 1: Automotive Specifications

CVT gear ratio	0.435 – 6.4
Final gear ratio	5.69
Vehicle weight	1305 [kg]
Frontal projected area	1.8 [m^2]
Coefficient of drag	0.36
Tire radius	0.273 [m]
Coefficient of rolling resistance	0.018
Air density	1.166 [kg/m^3]

4. SIMULATION RESULTS

Table 1 shows automotive specifications of the analysis target in the present study. Time history of the gear ratio of the CVT is shown in Figure 12 which is obtained by Bond Graph simulation. In the Figure a broken line and a solid line indicate the calculated results of CVT-1 and CVT-2, respectively. The different results are caused by the difference of gear change pattern between CVT-1 and CVT-2. Hereafter in all figures the chain line, the broken line and the solid line indicate the 10 Mode cycle, the results of CVT-1 and CVT-2, respectively.

Figures 13, 14, 15, 16, 17, 18, and 19 show time histories of engine revolution, engine torque, engine output power of CVT-1 and CVT-2, sum of mileage according to the Japanese 10 Mode cycle, fuel consumption per unit time, sum of fuel consumption, and average fuel consumption calculated by Equation (7) from Figure 18, respectively.

In Figure 13, engine revolution of CVT-2 is always lower than that of CVT-1. Though engine revolution of CVT-1 is kept constant for constant speed driving mode, engine revolution of CVT-2 always varies even for constant speed driving mode. It is because the gear ratio is continuously-varied to determine engine revolution with high efficiency in CVT-2, as shown in Figure 12.

On the other hand, in Figure 14 the engine torque of CVT-2 is always larger than that of CVT-1, contrary to features of engine revolution shown in Figure 13. As a result, the engine output power is almost same between CVT-1 and CVT-2, as shown in Figure 15, though the gear ratio is different. This is because parameters except for the driving resistance as an input variable and CVT are the same between the simple model of CVT-1 and the detailed model of CVT-2. This result shows the validity of CVT-1 and CVT-2 models.

Both Figures16 and 18 have upward-sloping curves, which are similar tendency in sum of mileage and sum of fuel consumption. It is because vehicle speed late in the Japanese 10 Mode cycle is twice as fast as that early in the 10 Mode cycle and fuel consumption increases rapidly in proportion to vehicle speed especially late in the 10 Mode cycle. At acceleration period, engine torque and revolution increase and fuel consumption increase similarly, though average fuel consumption deteriorates inversely.

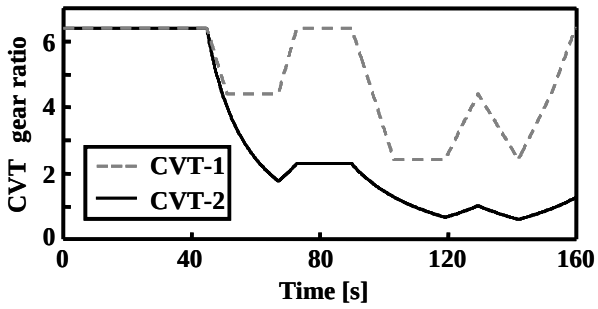

Figure 12: CVT Gear Ratio

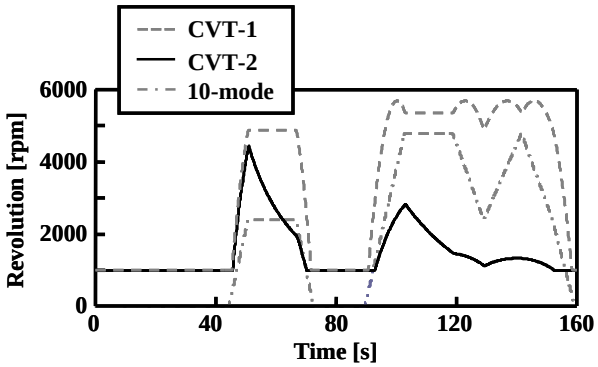

Figure 13: Engine Revolution

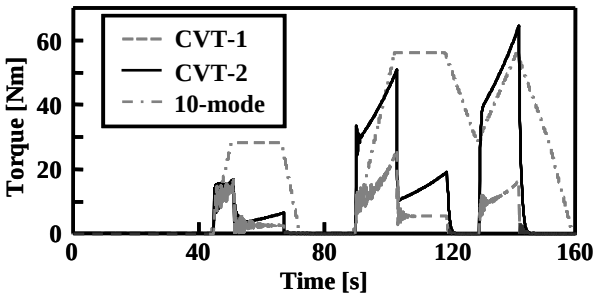

Figure 14: Engine Torque

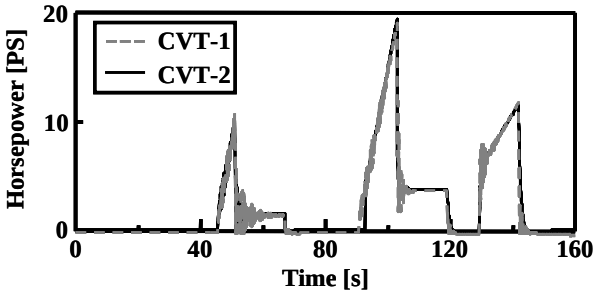

Figure 15: Horse Power

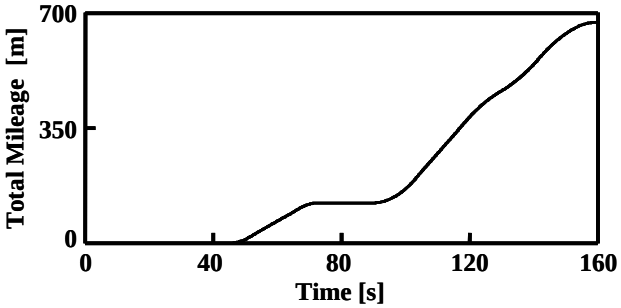

Figure 16: Sum of Mileage (The 10 Mode cycle)

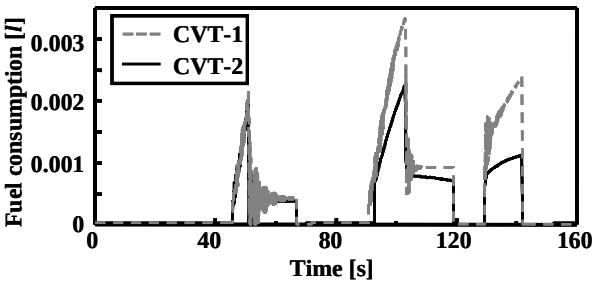

Figure 17: Fuel Consumption

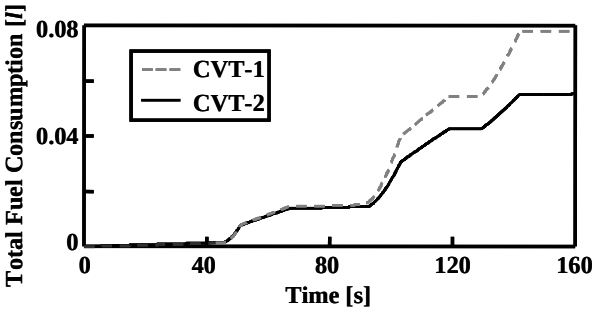

Figure 18: Sum of Fuel Consumption

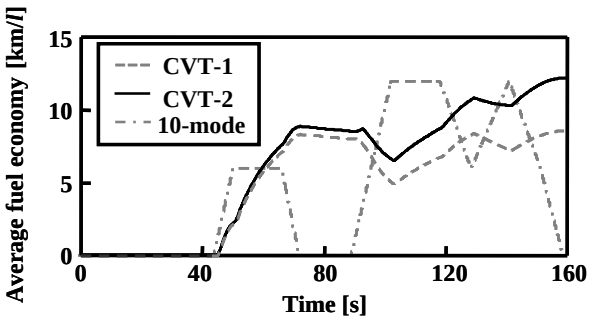

Figure 19: Average Fuel Consumption

In Figure 19 the average fuel consumption for 160 [s] according to the Japanese 10 Mode cycle is finally calculated as 12 [km/*l*] and 8.6 [km/*l*] in CVT-2 and CVT-1 model, respectively. It is caused by controlling the gear change minutely that the average fuel consumption in CVT-2 is better than that in CVT-1.

From the results mentioned above, it is verified that the Bond Graph models represent the basic dynamic characteristics of power train system with CVT and it is possible to calculate the optimum gear change pattern for high fuel-efficiency by combining the above Bond Graph models with some control programs for gear change pattern in CVT.

PC calculating time is 72 [s] for 160 [s] the Japanese 10 Mode cycle and is almost same between the models of CVT-1 and CVT-2.

5. CONCLUSION

The proposed Bond Graph models represent the basic dynamic characteristics of vehicle power train system with CVT and it is useful to calculate the optimum gear change pattern for low fuel consumption.

REFERENCES

Carbone, G., Mangialardi, L., Bonsen, B., Tursi, C., Veenhuizen, P.A., 2007. CVT dynamics: Theory and experiments. *Mechanism and Machine Theory* 42: pp.409-428

Cho, D., Hedrick, J.K., 1989. Automotive Powertrain Modeling for Control. *Transaction of the ASME Journal of Dynamic Systems, Measurement, and Control* Vol. 111: pp568-573.

Daihatsu Motor Co., Ltd.,2006. Continuously Variable Transmission. *Challenge Next Press Information* Vol.4.

Gawthrop, P., 1995. Bicausal Bond Graphs. *International Conference on Bond Graph Modeling and Simulation*, pp. 83-88. January 15-18, Las Vegas (Nevada, USA).

Karnopp, D., Rosenberg, R.C., 1970. Application of Bond Graph Techniques to the Study of Vehicle Drive Line Dynamics. *Transactions of the ASME Journal of Basic Engineering*. June: pp355-359

Karnopp, D.C., Margolis, D. L., Rosenberg, R. C., 2006. *System Dynamics.* New Jersey: John Wiley & Sons, Inc.

Kong, L., Parker, R.G., 2008. Steady mechanics of layered, multi-band belt drives used in continuously variables transmission (CVT). *Mechanism and Machine Theory* 43: pp.171-185

Hrovat, D., Tobler, W.E., 1991. Bond Graph Modeling of Automotive Power Trains. *Journal of the Franklin Institute Pergamon Press plc*: pp. 623-637.

Mantriota, G., 2002. Performances of a parallel infinitely variable transmissions with a type II power flow. *Mechanism and Machine Theory* 37: pp.555-578

Pfiffner, R., Guzzella, L., Onder, C.H., 2003. Fuel-optimal control of CVT powertrains. *Control Engineering Practice* 11: pp.329-336

Srivastava, N., Haque, I., 2008. Transient dynamics of metal V-belt CVT: Effects of band pack slip and friction characteristic. *Mechanism and Machine Theory* 43: pp.459-479

Srivastava, N., Haque, I., 2009. A review on belt and chain continuously variable transmissions (CVT): Dynamics and control. *Mechanism and Machine Theory* 44: pp.19-41

Srivastava, N., Haque, I., 2009. Nonlinear dynamics of a friction-limited drive: Application to a chain continuously variable transmission (CVT) system *Journal of Sound and Vibration* 321: pp.319-341

Suzuki, T., Hosoi, K., 2007. Development of Fuel Economy Simulation for Heavy-Duty Vehicles with Automatic Transmission. *Journal of Automotive Study* Vol.29, No.12: pp15-18.

Takiyama, T., Morita, S., 1993. Study of the Control Algorithm for Engine-CVT Consolidated Control. *JSME Journal Series B* Vol. 59: pp. 377-383.

Thoma, J. U., 1990. Simulation by Bondgraphs. Berlin Heidelberg New York London Paris Tokyo Hong Kong: Springer-Verlag.

Togai, K., Koso, M., 2006. Dynamic Scheduling Control for Engine and Gearshifts: Consolidation of Fuel-Economy Optimization and Reserve Power. *Mitsubishi Motors Technical Review* No.18: pp. 25-32.

Yokoi, T., 1979. Automatic Transmission Optimization for Better Fuel Economy. *Toyota Technology* Vol.100: pp. 24-29.

AUTOMATIC HANDLING OF COMMUTATIONS IN BOND GRAPH BASED SIMULATION OF SWITCHED SYSTEMS

Nacusse, Matías A.[a,b] and Junco, Sergio J.[a]

[a] Departamento de Control, Facultad de Ciencias Exactas, Ingeniería y Agrimensura, Universidad Nacional de Rosario, Ríobamba 245 Bis – S2000EKE Rosario – Argentina.
[b] CONICET – Consejo Nacional de Investigaciones Científicas y Técnicas.

[a,b]nacusse@fceia.unr.edu.ar, [a]sjunco@fceia.unr.edu.ar

ABSTRACT
This paper proposes a Bond Graph based solution to the problems of modeling switched physical systems and automatically handling their commutations during the simulation process, featuring the following properties: simultaneous representation of all the operation modes of the switching system in a unique switched Bond Graph, one-to-one correspondence between physical phenomena and model components, and integral-only causality assignment in the Bond Graph storages. To this aim, the Switched Power Junction formalism is used to manage the switching between the different modes, along with a residual-sink-like concept to avoid derivative causality when constraints among energy storages appear, and conservation principles of generalized momentum and charge to re-initialize the state variables when mode switching induces state discontinuities. The proposed solution is illustrated through modeling and simulation of a mechanical and an electromechanical example.

Keywords: Bond Graph, Switched Power Junction, Residual Sinks, Constrained State Variables.

1. INTRODUCTION

Frequently in engineering problems, abrupt changes in physical systems are considered to occur instantaneously. This is mainly so because the phenomena the engineer is interested in have a time scale much bigger than that of the abrupt changes, and that the details inside the time windows of these changes are not relevant to the behavior under study. Thus, ignoring them results in saving modeling time and computational effort. This practice generates a new class of mathematical model, the switched system, where "a logical rule orchestrates switching between a finite number of dynamical subsystems described by differential or difference equations" (Lin and Antsaklis 2007). This paper particularly considers switching among bond graphs (BG) representing different modes of a physical system. This kind of models may arise when modeling under ideal assumptions natural phenomena like mechanical collisions, saturation phenomena, switching in diodes, etc, or technically imposed limitations for safety or commutations for control purposes.

As this practice departs from the assumptions of continuity and smoothness underlying classical physics, it requires special modeling tools as well as suitable simulation and analysis techniques to handle the mathematical models thus obtained, see (Mosterman and Biswas 1998) for a detailed discussion of modeling and simulation issues related to this problem.

Many formalisms for ideal switching modeling have been proposed in the BG domain: MTFs modulated with gain changing between 0 and 1 (Karnopp and Rosenberg 1992), (Asher 1993), (Dauphin-Tanguy and Rombaut 1997); an ideal switch as a new bond graph element (Strömberg, Top, and Söderman 1993); a switch as an ideal current source and a voltage source (Demir and Poyraz 1997); switching bonds (Broenink and Wijbrans 1993); controlled junctions (Mosterman and Biswas 1995, 1998); Petri nets to represent discrete modes and transition between modes (Allard, Helali, Lin, and Morel 1995); and the SPJ or Switched Power Junction formalism. See (Umarikar and Umanand 2005) for an introduction to the latter modeling technique and a brief description and discussion of the pros and cons of all the others. Out of these formalisms, this paper choses the SPJ concept to model mode switching, i.e., the switching among the different BGs, each one of them corresponding to a continuous mode or dynamical subsystem of the switched system. This concept is based on the introduction of two new junction elements, the $\mathbf{0_S}$ or switched-zero junction, and the $\mathbf{1_S}$ or switched-one junction. Using them it is possible to represent all of the switched system operation modes in a unique (switched) BG.

Modeling and simulation of switched systems is particularly defying when nonlinear dynamics is involved and mode changing implies emergence of new and/or disappearance of existing state variables in certain modes, which in the BG domain implies emergence/disappearance of energy storages in integral (and usually also in derivative) causality. Indeed, this latter fact is usually accompanied by discontinuities in the state variables, which calls for re-initialization of state variables immediately after switching. As it is well

known, when such a discontinuity or state jump occurs, there is an instantaneous lost of a finite amount of energy in the system (violation of the energy conservation principle), to which a power impulse is associated. Because of this fact, the values of the state variables after the jump are obtained invoking principles of conservation of generalized momentum or generalized charge, depending upon the kind of energy storages being involved in the state jumps (Borutzky 2004).

In (Junco, Diéguez, and Ramírez 2007) the SPJs have been interpreted in terms of the classical **0**- and **1**-junctions and MTFs modulated by a gain taking the values 0 or 1. In (Nacusse, Junco, and Donaire 2008) the implementation of the $\mathbf{0_S}$ and $\mathbf{1_S}$ as new standard elements of the 20sim basic library has been presented and used in a case study to automatically manage all the mode changes of the switched system without any need of user intervention during the simulation run. From the standpoint of an Object Oriented Modeling (OOM) approach, that work has the drawback of demanding the duplication of the BG components whose causality change due to the mode switching (having more than an object for the same physical phenomenon is a fact that in a certain way collides with the OOM concept). On the other hand, derivative causality unavoidably appears if an I or C component changes causality. Having in mind both aims, to perform the modeling task with an OOM approach, where to each physical phenomenon corresponds a unique BG component, and to avoid derivative causality, the current paper suggests a solution which involves the use of the residual sink concept (Borutzky 2004). This concept is incorporated in 20Sim as the "constraint" sentence (help manual 20Sim 4.1). Its usage is intended to avoid derivative causality in problems like multibody dynamics, where the OOM approach would otherwise force derivative causality when degrees of freedom are lost because the (permanent) coupling of rigid body models. However, if used in switching problems, this sentence assures the satisfaction of the constraints forcing the derivative causality *only* when before commutations there is no discrepancy between the state values to be matched after commutations. In this paper we propose a solution to this problem via the addition of an additional term to the terms usually employed in conjunction with the residual sinks approach. This additional term is just a model of the above mentioned power impulse responsible for the momentum and/or charge conservation during switching. Summarizing, this paper proposes a BG-SPJ based solution to the problem of modeling switched physical systems and automatically handling their commutations during the simulation process, featuring the following properties: simultaneous representation of all the operation modes of the switching system in a unique switched BG, one-to-one correspondence between physical phenomena and BG elements, and integral-only causality assignment in the storages.

Through simple examples Section 2 addresses the background techniques used in the paper: the basics of modeling switched systems using the SPJ method, the principles of momentum and charge conservation during state jumps, and the use of residual sinks to avoid derivative causality in BG. Section 3 recalls the electromechanical application system dealt-with in (Nacusse, Junco, and Donaire 2008). For the sake of comparison, the solution proposed in that paper is first presented, followed by the new solution contributed in this paper. In order to explore the feasibility of the proposed technique to solve complex mechanical problems, Section 4 addresses a mechanical example where somewhat involved calculations are necessary to re-initialize the state variables. Simulation results are provided all along the case studies. Finally, Section 5 presents some conclusions and points out to further work.

2. BACKGROUND RESULTS

The classical continuous BG representations of the continuous modes of a switched system are augmented with the SPJ formalism in order to have a unique and global representation of the whole switched system, which is called a switched bond graph (SwBG). The SPJ-formalism has been selected out of the many ideas and techniques proposed to handle idealized commutations because of its advantages in order to circumvent some associated modeling drawbacks like varying causality of switching-modeling components, hanging junctions, failure to disconnect subsystems, and other inconsistencies (Umarikar and Umanand 2005).

The modeling task is carried out with an OOM approach in which each physical phenomenon has its own and unique BG component. Mode switching could induce causality changes in certain elements, which is not allowed in some M&S software. A way out of this situation is to duplicate the BG component (Nacusse, Junco, and Donaire 2008). This solution works but it does not seem very elegant nor too consistent with the OOM idea. Instead, adding residual sinks to the BG is proposed here in order to prevent from switching causality. An important benefit of this solution is that it allows keeping the preferred integral causality in all the energy storage elements, independently of any causal constraints on their energy variables.

State discontinuity is another phenomenon frequently associated with mode switching. To continue the simulation after such a mode switching, re-initialization of the state variables is necessary. The background computations employed in this paper are based on momentum and charge conservation principles.

All the previous background results are reviewed next.

2.1. Mode switching using SPJ

There are two kinds of SPJ, the $\mathbf{0_S}$ and the $\mathbf{1_S}$, which are **0**- and **1**-junctions admitting more than one bond *graphically* imposing effort or flow on them,

respectively. In the classic BG formalism this presents a causality conflict, because only one bond can impose effort to a **0**- (or flow to a **1**-) junction. However, this causality conflict can be solved adding a constraint via a control variable witch *selects* only one of the imposed efforts (or flows) (Umarikar and Umanand 2005). See appendix A for the basics of SPJs and (Nacusse, Junco, and Donaire 2008) for a generic 20sim implementation of the $\mathbf{0_S}$ and $\mathbf{1_S}$, available for download at http://www.fceia.unr.edu.ar/dsf/I&D/BG.html.

The following example illustrates how to use the SPJ technique. Figure 1 shows a simple electrical circuit which contains two switching elements, an ideal switch (modeling the on-off behavior of a transistor, for instance) and a free-wheel diode. These elements have the complementary logic states {switch open, diode closed} and {switch closed, diode open}. This means that only one control variable is necessary in the SwBG.

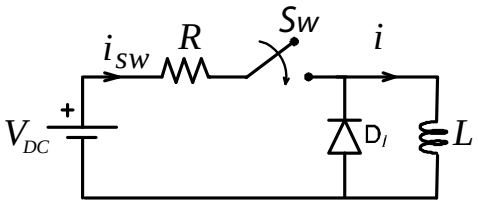

Figure 1: Switched electronic circuit

The current commutations of the ideal switch are modeled with the $\mathbf{1_S}$ and the source $\mathbf{S_f}$ (f≡0), whereas the voltage commutation at the diode is modeled with the $\mathbf{0_S}$ plus the resistor **R** labelled *D1* (it models the diode's conduction state). This yields the SwBG model presented in Figure 2. When the switch is off, the $\mathbf{S_f}$-bond is selected by the $\mathbf{1_S}$ to impose zero current to the submodel to its left, and the $\mathbf{0_S}$ connects the **I** and the **R**(*D1*). When the switch is on, the $\mathbf{1_S}$ disconnects the $\mathbf{S_f}$ and connects the bond on its right side, while the $\mathbf{0_S}$ connects the **I** and disconnects **R**(*D1*).

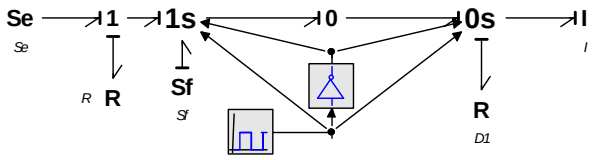

Figure 2: SwBG model

2.2. State variable re-initialization and prevention from derivative causality.

To avoid derivative causality in a BG, a residual sink component is added in order to break the causality constraints (Borutzky 2004). There are two kinds of residual sinks, effort residual sinks *rSe* and flow residual sinks *rSf*. The residual sink injects the necessary effort or flow in order to make vanish the power conjugated variable into the sink. This is *numerically* implemented in 20sim as the *constraint* sentence, but it only works when either the effort or flow is already close to zero.

Here, the need of performing a numerical differentiation is traded against the addition of an algebraic constraint. This constraint is solved off-line in order to also handle the problems associated with state re-initialization when state discontinuities are forced by the system commutations.

The well known electrical example of Figure 3 allows to better see this approach (Borutzky 2004). It shows two electrical RC networks connected by an ideal switch. The ideal switch directly connects two capacitors in parallel.

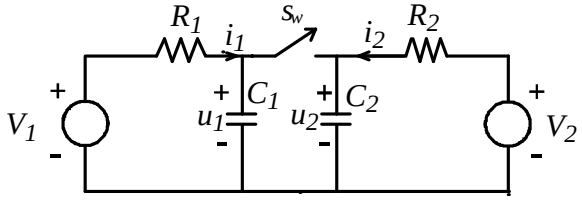

Figure 3: Switched electric circuit

The circuit has two modes of operation, namely mode m_1 and mode m_2, corresponding to open and closed switch, respectively. Switching from m_2 to m_1 does not imply any problem with the initial conditions of the new mode, since there is a smooth transition in the energy variables of the C-elements and the initialization of the new mode is trivial. However, at the instant of a switching from m_1 to m_2, the voltages over the capacitors might be different, so that a state variable re-initialization must be performed. In standard BG modeling two options are available to represent the system in mode m_2: either both C-elements are kept with one of them in derivative causality, or both are combined in a unique equivalent C-element representing the parallel connection. The choice here is the SwBG of Figure 4, a BG where both C-elements are kept in integral causality means the management made by a $\mathbf{1_S}$ junction and an associated switch model featuring a residual sink performing the calculations detailed below in order to inject the current i_S.

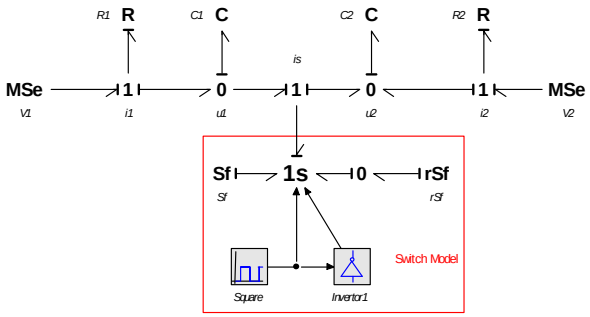

Figure 4: SwBG model.

In mode m_1 the current through the switch is zero and the RC circuits are independent one each other. The SwBG achieves this through the $\mathbf{1_S}$ connecting the flow source with value zero. In mode m_2 the $\mathbf{1_S}$ connects the *rSf* which injects the necessary current to make $u_1=u_2$. This means that the output efforts of both C-elements must be kept equal at all times while the system is in mode m_2. This includes changing instantaneously the (possibly) different efforts in these elements to an equal

and common value when entering this mode. This latter task requires injecting a current impulse, what cannot be done numerically, so that an approximate solution will be provided.

The control law for i_S enforcing the constraint is obtained as follows in terms of the system variables (Borutzky 2004):

$$\begin{aligned} \dot{u}_1 &= \frac{1}{C_1}\left(\frac{V_1-u_1}{R_1} - i_s\right) \\ \dot{u}_2 &= \frac{1}{C_2}\left(\frac{V_2-u_2}{R_2} + i_s\right) \end{aligned} \quad (1)$$

Calling $i_1 = \frac{V_1-u_1}{R_1}$ and $i_2 = \frac{V_2-u_2}{R_2}$ and defining $u_E = u_1 - u_2$ then:

$$\dot{u}_E = \dot{u}_1 - \dot{u}_2 = \frac{1}{C_1}(i_1 - i_s) - \frac{1}{C_2}(i_2 + i_s)$$

$$\dot{u}_E = \frac{1}{C_1}i_1 - \frac{1}{C_2}i_2 - \frac{C_1+C_2}{C_1C_2}i_s \quad (2)$$

So, if:

$$i_s = \frac{C_1C_2}{C_1+C_2}\left(\frac{1}{C_1}i_1 - \frac{1}{C_2}i_2\right) \quad (3)$$

Then

$$\dot{u}_E = 0$$

Equation (3) enforces the constraint $u_1 \equiv u_2$ only if the two voltages are equal at t_C^+, the time instant immediately after commutation. If this condition does not hold –which is the normal situation after a switching from m_1 to m_2–, then a constant error between u_1 and u_2 appears. A remedy to this problem is to add an extra term in equation (3), as shown in (4).

$$i_s = \frac{C_1C_2}{C_1+C_2}\left[\frac{1}{C_1}i_1 - \frac{1}{C_2}i_2 + K_E u_E\right] \quad (4)$$

If K_E is chosen to be the Dirac impulse applied at the commutation instant, i.e., $K_E = \delta(t - t_C)$, then the additional term becomes

$$\frac{C_1C_2}{C_1+C_2}\delta(t - t_C)u_E(t_C^-)$$

which is exactly the impulsive current producing the charge transfer from one capacitor to the other which instantaneously equalizes their voltages, see (Borutzky 2004) for instance. Of course, in a numerical simulation the Dirac impulse can be only approximatively implemented as a square pulse, for instance, of high value and correspondingly short time-base.

Another option would be to let K_E be a high-value constant defining the speed of asymptotic convergence between u_1 and u_2, as the resulting error dynamics $\dot{u}_E = -K_E u_E$ shows. Even if it works, it is easily seen that in the BG domain this amounts to connect a **R**-element with very low resistance value (high admittance K_E), which implies a stiff system when the SwBG is in mode m_2. This is not desirable, as one of the reasons for the choice of the SPJ approach was to avoid alternatives like inserting parasitic elements, precisely because the stiffness induced by them.

An third alternative, exactly equivalent to have the Dirac impulse in the extra term in (4), is provided by 20sim. It involves resetting the integrators associated to each storage whose energy variable jumps. To this aim, the regular integration sentence *int(x, init)* must be replaced by *resint(x,newoutp,reset,init)*, see (Nacusse, Junco, and Donaire 2008) for an application example and also the 20sim manual for more details.

Figure 5 show the results of a simulation implemented in 20sim of the SwBG depicted in Figure 4. The flow residual sink *rSf* is implemented by a modulated flow source with equation (4) as control law, with the impulse approximately realized as a pulse, as above discussed. The simulation scenario is as follows, the switch is commanded by a square signal with period *T=10 s* starting in m_2. The voltages source V_1 is a sine wave with amplitude 100 volts and V_2 is a constant voltage source of 120 volts. The parameters of the circuit are: *R1=2MΩ, C1=0.1μF, R2=1MΩ, C2=1μF* and K_E has amplitude equal to K_E*=1000* during 1ms

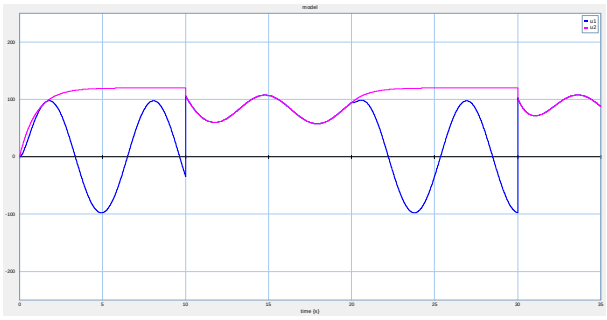

Figure 5: Capacitors voltages u_1 (blue) and u_2 (magenta)

3. APLICATION EXAMPLE: SERIES DC MOTOR WITH SWITCHED CIRCUIT FOR FIELD WEAKENING.

Figure 6 shows the application example presented in this section in order to illustrate the approach explained in the previous sections. The example consists of a series DC motor with switched circuit for field weakening (Leonhard 1997). Equations 5 are the electromechanical conversion relationships, where *K* is a constructive constant and *g(.)* is the nonlinear magnetic characteristic of the excitation field.

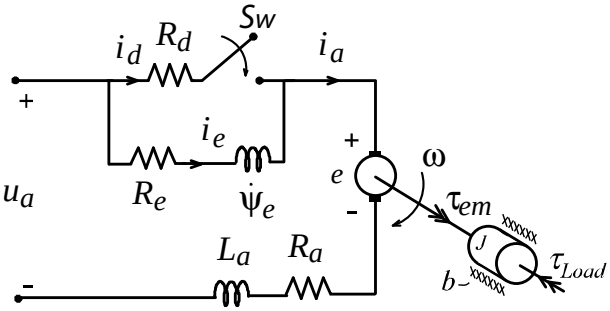

Figure 6: Equivalent circuit of series DC motor.

$$\begin{aligned} \tau_{em} &= K\Psi_e i_a \\ e &= K\Psi_e \omega \\ \Psi_e &= g(i_e) \end{aligned} \tag{5}$$

In this configuration the motor operates in two modes: in the full field (FF) mode when the switch is open and in field weakening (FW) mode when the switch is closed. The FF mode is used when the motor speed is below the base (nominal) speed and the FW mode is used for higher motor speeds.

3.1. Full excitation mode.

Figure 7 shows the BG model in the FF operation mode. In this figure the nonlinear I element representing the excitation winding is in derivative causality. As explained in section 2.2, to avoid derivative causality a residual sink element is properly placed in the BG, see Figure 8.

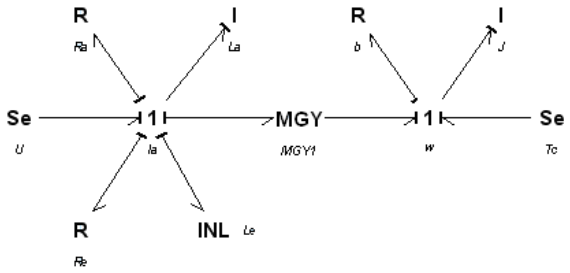

Figure 7: FF BG with derivative causality

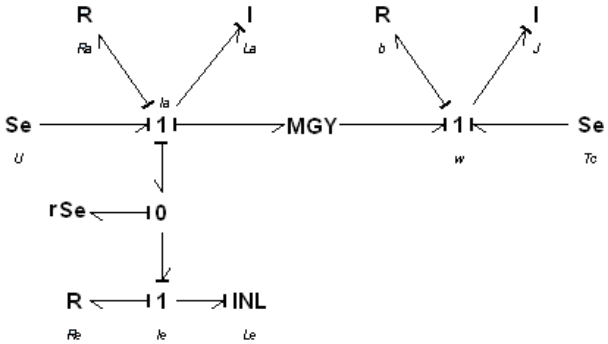

Figure 8: FF BG with all elements in integral causality

3.2. Field weakening mode.

Figure 9 shows the BG model in the FF operation mode. The corresponding state equations are given in (6).

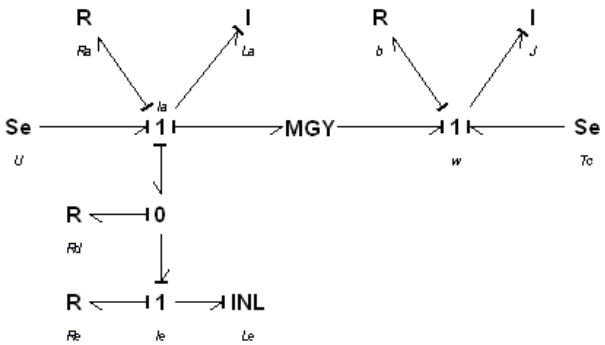

Figure 9: FW BG model

$$\begin{aligned} \dot{\imath_a} &= -\frac{K}{L_a}\Psi_e\omega - \frac{(R_a+R_d)i_a}{L_a} - \frac{R_d}{L_a}g^{-1}(\Psi_e) + \frac{U}{L_a} \\ \dot{\Psi_e} &= R_d i_a - (R_e + R_d)g^{-1}(\Psi_e) \\ \dot{\omega} &= -\frac{b}{J}\omega + \frac{K}{J}\Psi_e i_a - \frac{\tau_c}{J} \end{aligned} \tag{6}$$

Entering in the FW mode does not present any problem because there is no jump in the energy variables. On the contrary, when the system passes from FW mode to FF mode discontinuities appear in the energy variables associated to both electrical I-elements, so that the initial conditions for the simulation of the FF mode must be calculated.

3.3. Switched BG models of Series DC-Motor

Combining the BG of Figures 7 and 9 the SwBG model of Figure 10 is obtained, which has been previously presented in (Junco, Diéguez, and Ramírez 2007). The excitation winding has been duplicated to handle the causality switching caused by the commutation.

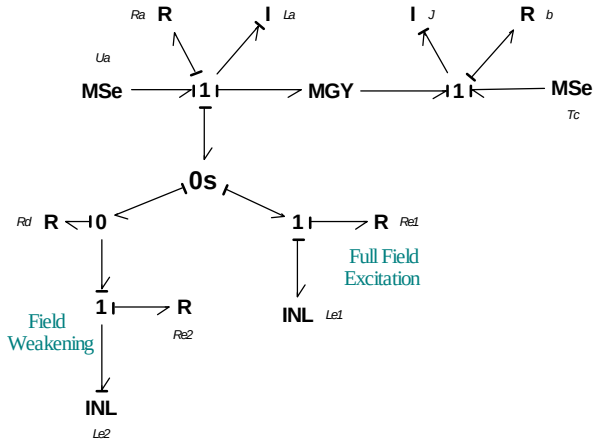

Figure 10: SwBG with derivative causality and duplicated elements: **1**, **INL** (Le1,2) and **R** (Re1,2).

The only differences between Figures 8 and 9 are the residual sink element (FF mode) and the R component labelled *Rd* (FW mode), which represents the field weakening resistance R_d. Both components impose effort to the zero junction. This means that a $\mathbf{0_s}$ SPJ can be used to connect either the residual sink or the field weakening resistor, as shown in the SwBG model of the series DC-motor of Figure 11. Equations 7 show the state equations read from this SwBG. The auxiliary variable U_S impressed by the $\mathbf{0_S}$ has been used.

$$\begin{aligned} \dot{\imath_a} &= \frac{U}{L_a} - \frac{R_a}{L_a}i_a - \frac{K}{L_a}\Psi_e\omega - \frac{U_S}{L_a} \\ \dot{\Psi_e} &= U_s - R_e g^{-1}(\Psi_e) \\ \dot{\omega} &= \frac{K}{J}\Psi_e i_a - \frac{b}{J}\omega - \frac{\tau_c}{J} \end{aligned} \tag{7}$$

When the DC motor is in FW mode, then $U_s = R_d(i_a - i_e)$ and equations 7 coincide with equations 6. For FF operation U_s is calculated as follows:

Be $U_1 = U - R_a i_a - K\Psi_e\omega$ and $U_2 = R_e g^{-1}(\Psi_e)$

Then, rewriting the first two equations of 7 in term of i_a and i_e:

$$\dot{i_a} = \frac{U_1 - U_s}{L_a}$$
$$\dot{i_e} = \frac{U_s - U_2}{g'(i_e)} \qquad (8)$$

Where $g'(i_e) = \frac{\partial g}{\partial i_e}$ .Then, defining $\dot{i_\delta} = \dot{i_a} - \dot{i_e}$ and performing the same steps as in section 2.2 yields:

$$U_s = \frac{L_a g'(i_e)}{L_a + g'(i_e)} \left[\frac{1}{L_a} U_1 + \frac{1}{g'(i_e)} U_2 + K_E i_E \right] \qquad (9)$$

Mutatis mutandis, K_E plays here for the current error the same role as in (4) for the voltage error.

$$\dot{i_E} = -K_E i_E \qquad (10)$$

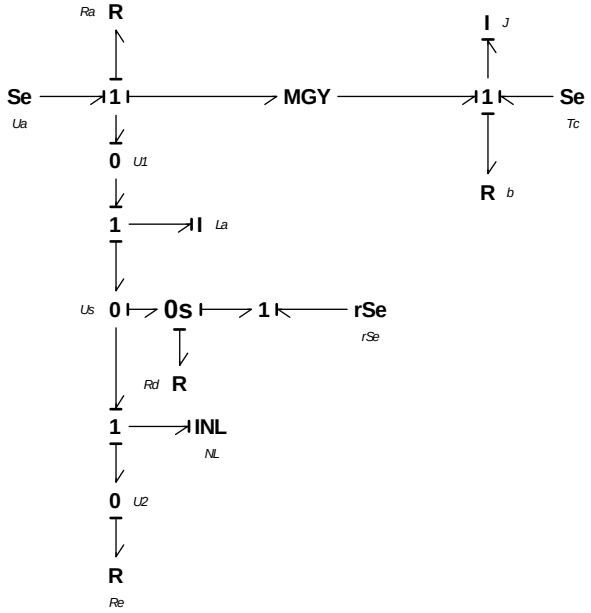

Figure 11: SwBG. All storages in integral causality.

3.4. Simulations Results

To make the simulations more realistic a cascade control system is added, where a PI-speed controller runs a hysteresis-band current controller, see (Leonhard 1997) for details. The block diagram of the cascade control system is shown in Figure 12. Figure 13 shows the internal block diagram of the switch control block, which connects/disconnects the field weakening resistor. The logic signal Switch is one for FF mode and is zero for FW mode. Figure 14 shows the 20sim implementation of overall control scheme. The block called Series DC-Motor contains the SwBG model of Figure 11. The effort residual sink *rSe* is implemented by a modulated effort source with equation 9 as control law. The motor parameters used in the simulation are: U_a=*1000 V*; base speed ω_B = *1910 rpm*, R_a=*9.89 mΩ*, L_a=*1.4 mH*, R_e=*14,85 mΩ*, R_d=*16,96 mΩ*, *K=0.04329 Nm/WbA*, *J=3 Kgm2*, T_{Load}=*1370 Nm*.

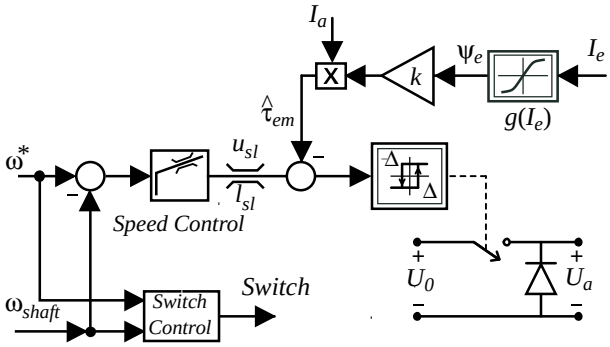

Figure 12: Block diagram SwBG model

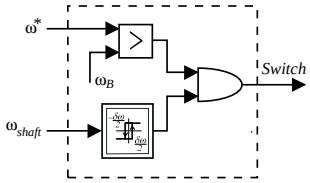

Figure 13: Switch Control Block

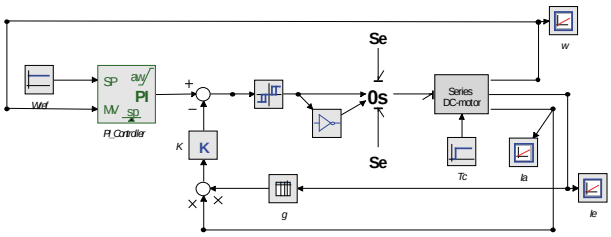

Figure 14: 20sim implementation of the control scheme.

Figure 15 shows the speed profile followed by the motor. The motor speed decrement at time *T=3sec* is produced by the load torque application. Figure 16 shows the armature current i_a, the excitation current i_e and the switch state.

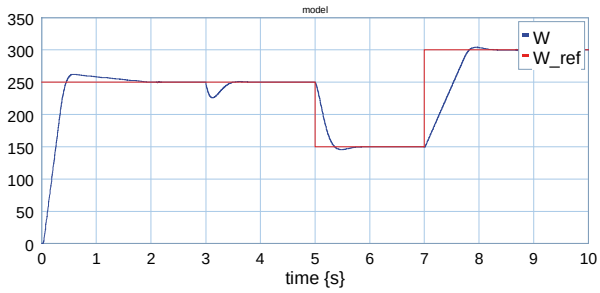

Figure 15: Reference (red) and motor speed (blue).

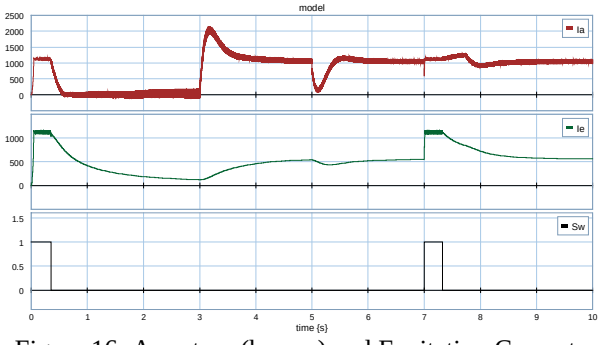

Figure 16: Armature (brown) and Excitation Current (green). Switch state (black).

4. MECHANICAL EXAMPLE:

Figure 17 shows an idealized physical system of a slider crank mechanism. The slider crank mechanism transforms rotational into translational motion, or vice-versa.

The rotation wheel is attached to the mass by means of a rigid and massless bar with longitude *l*. This implies that one of the *I* elements in the BG must be in derivative causality.

Avoiding derivative causality can be performed in different ways. Here, it is achieved splitting in two the MTF-element linking the rotational and translational inertias, as shown in the SwBG of Figure 18. Friction has been modeled associated to both motion coordinates (linear models with coefficients b_1 and b_2).

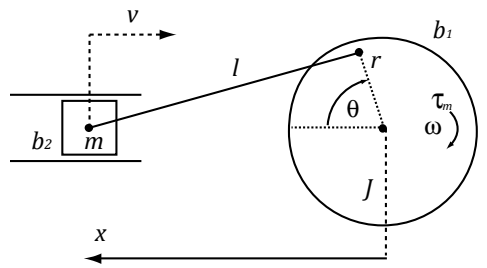

Figure 17: Idealized Physical System of a Slider crank mechanism.

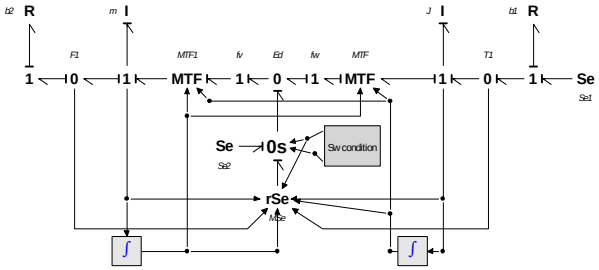

Figure 18: SwBG model of the Slider crank mechanism.

The MTF-elements have the following gains:

$$f_v = \frac{(x - r\cos\theta)}{l} v \qquad (11)$$

$$f_\omega = \frac{(rx\sin\theta)}{l} \omega \qquad (12)$$

Where equation 11 corresponds to the *MTF1* element and equation 12 to *MTF* depicted in Figure 18.

In order to obtain the control law for the residual sink we can write the state equations of the system as:

$$\dot{v} = \frac{1}{m}\left[\frac{(x - r\cos\theta)}{l} E_D - F_1\right]$$

$$\dot{\omega} = \frac{1}{J}\left[\tau_1 - \frac{rx\sin\theta}{l} E_D\right]$$

Where F_1 is the fiction effort in the mass *m*, $\tau_1$is the input torque minus the friction torque and E_D is the effort injected by the residual sink. Defining $f_E = f_w - f_v$ as the flow error, the control law for the residual sink can be obtained performing the same steps as in the previous examples.

$$E_D = \left[\frac{(x - r\cos\theta)^2}{ml^2} + \frac{(rx\sin\theta)^2}{Jl^2}\right]^{-1} \left[\frac{(rx\sin\theta)}{Jl}\tau_1 + \frac{(x - r\cos\theta)}{ml} F_1 + \frac{v^2 + xr\omega^2\cos\theta - 2v\omega r\sin\theta}{l} + K_E f_E\right]$$

The parameters used in the simulation were: $J=0.124Nm^2$, $b_1=0.1Kgm/s$, $r=0.5m$, $l=2$, $m=8Kg$, $b_2=15.Kg/s$ (Rideout and Stein 2003).The simulation starts with the mass at rest in position $x=1.6m$ and disconnected from the wheel. An input torque of constant value $\tau_{in}=250Nm$ is applied to the wheel at time $T=0s$. At time $T=2.368s$ the wheel is connected to the mass. The angle θ at connection time is $\theta=1.192rad$ (68.3degrees).

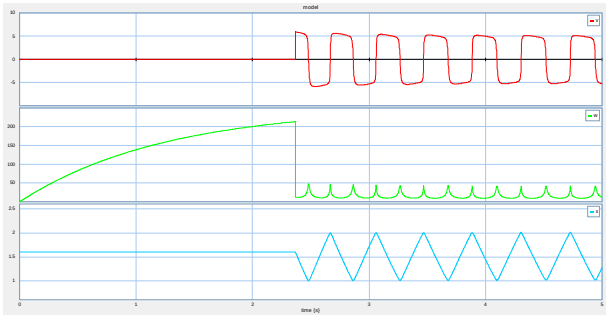

Figure 19: Response of the slider crank mechanism. Mass speed (red) and position (light blue), angular speed (green).

A correct response is observed in the simulation figures, particularly the discontinuities in both the translational and the angular speeds at the collision-like coupling time can be appreciated.

This example has been included in order to test the applicability of the proposed methodology to mechanical problems where the constraints among energy variables often involves nonlinear functions of the state variables, i.e., through much more complex relationships as in the first two examples. This is the case, for instance, when the multibody modeling and simulation approach is employed for mechanical systems subject to collision-like connection of 3D-bodies composing the overall system.

5. CONCLUSIONS.

The problem of modeling and simulation of physical systems undergoing switching and state discontinuities has been addressed in the bond graph domain. A solution has been proposed to automatically handling the commutations during the simulation process, featuring the following properties: simultaneous representation of all the operation modes of the switching system in a unique switched Bond Graph, one-to-one correspondence between physical phenomena and model components, and integral-only causality assignment in the Bond Graph storages. The Switched Power Junction formalism has been used to represent the switching between the different modes, while the residual-sink was the resource employed to avoid derivative causality when constraints among

energy storages appear, and conservation principles of generalized momentum and charge have been resorted to in order to re-initialize the state variables when mode switching induces state discontinuities. The proposed solution has been demonstrated through modeling and simulation of a mechanical and an electromechanical example. Further work aims at applying the method to complex mechanical systems undergoing collision and constrained coupling modeled with the multibody dynamics approach.

ACKNOWLEDGMENTS

The authors wish to thank CONICET (the Argentine National Council for Scientific and Technological Research) and SeCyT-UNR (the Secretary for Science and Technology of the National University of Rosario) for their financial support.

APPENDIX A: SWICHED POWER JUNCTIONS

Figure 20 show the SPJ with causality assignment.

Only one of the control variables is allowed to have the value 1 at a given time instant, the rest are zero.

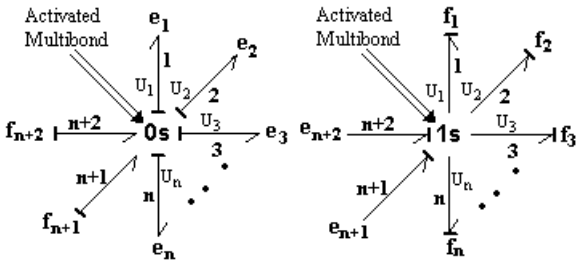

Figure 20: Switch Power Junctions with causality assignment.

Equations 13 and 14 express the mathematical relationship, for the $\mathbf{0_S}$ and the $\mathbf{1_S}$ respectively, between the power variables and the control signals injected to select the appropriate bond.

$$\begin{aligned} &\text{Effort} = U_1 e_1 + U_2 e_2 + \cdots + U_n e_n \\ &f_i = U_i (f_{n+1} + f_{n+2}) \quad ; \; i = 1, \ldots, n \end{aligned} \tag{13}$$

$$\begin{aligned} &\text{Flow} = U_1 f_1 + U_2 f_2 + \cdots + U_n f_n \\ &e_i = U_i (e_{n+1} + e_{n+2}) \quad ; \; i = 1, \ldots, n \end{aligned} \tag{14}$$

APPENDIX B: RESIDUAL SINKS

The residual sink component injects the necessary effort or flow in order to make vanish the power conjugated variable into the sink.

A residual sink element can be interpreted as an energy store where it parameter tend to zero. For example, an effort residual sink can be interpreted a C element in integral causality:

$$C\dot{e} = \Delta f$$

If the parameter C tends to zero, then $\dot{e}$ is determined by the algebraic equation $\Delta f = 0$.

Figure 21 shows the graphical representation of the effort and flow residual sink used in (Borutzky 2009).

Figure 21: Effort and flow residual sink

REFERENCES

Allard, B., Helali, H., Lin, Ch., Morel, H., 1995. Power converter average model computation using the bond graph and Petri Net Techniques. *IEEE Power Electronic Specialist Conference*, pp. 830–836.

Asher, G., 1993. The robust modeling of variable topology circuits using bond graphs. *Proc. Int. Conf. on Bond Graph Modeling and Simulation*. San Diego, CA, pp. 126–131.

Borutzky, W., 2004. *Bond Graphs. A Methodology for Modelling Multidisciplinary Dynamic Systems*. Erlangen, San Diego: SCS Publishing House.

Borutzky, W., 2009. Bond graph model-based fault detection using residual sinks. *Proc. IMechE, Part I: Journal of Systems and Control Engineering*, Vol. 223, pp. 337-352, London: PEP.

Broenink, J. and Wijbrans, K., 1993. Describing discontinuities in bond graphs. *Proceedings of International Conference on Bond Graph Modelling*. San Diego, CA, pp. 120–125.

Controllab Products B.V., 20-sim™, http://www.20sim.com/

Dauphin-Tanguy, G. and Rombaut, C., 1997. A Bond Graph Approach For Modeling Switching Losses of Power Semiconductor Devices. *Proc. Int. Conf. on Bond Graph Modeling and Simulation*. pp. 207-212.

Demir, Y. and Poyraz, M., 1997. Derivation of state and output equations for systems containing switches and a novel definition of switch using the bond graph model. *Journal of the Franklin Institute*. 3343 (2) 191–197.

Lin, H. and Antsaklis, P., 2007. Switching Stabilizability for Continuous-Time Uncertain Switched Linear Systems. *IEEE Transactions on automatic control*. Vol. 52, N°4, April 2007. pp 633-646.

Help 20sim 4.1 Controllab Products B.V., 20-sim™, http://www.20sim.com/webhelp.html

Junco, S., Diéguez, G., Ramírez, F., 2007. On commutation modeling in Bond Graphs, *Proc. Int. Conf. on Bond Graph Modeling and Simulation*, San Diego, CA, pp. 12-19.

Karnopp, D. and Rosenberg, R., 1992. *System Dynamics. A Unified Approach*, 2nd ed., Wiley Interscience, New York.

Karnopp, D., Margolis, D., Rosenberg, R., 2000. *System Dynamics. Modeling and simulation of mechatronic systems*, 3rd edition, Wiley Interscience, New York.

Leonhard, W., 1997. *Control of Electrical Drives*. New York. Springer-Verlag.

Mosterman, P. and Biswas, G., 1995. Behaviour generation using model switching. A hybrid bond graph modeling technique. *Proc. Int. Conf. on Bond Graph Modeling and Simulation*, Las Vegas, pp. 177–182.

Mosterman, P. and Biswas, G., 1998. A theory of discontinuities in physical systems models. *Journal of the Franklin Institute*, 335B (3), 401–439.

Mosterman, P., 1997. *Hybrid Dynamic Systems. A hybrid bond graph modeling paradigm and its application in diagnosis*. Ph.D. Thesis, Vanderbilt University, Nashville, Tennessee, USA.

Nacusse, M., Junco, S., Donaire, A., 2008. Automatizando el Modelado y Simulación con Bond Graph de sistemas Físicos Conmutados. *Mecánica Computacional.* XXVII, pp. 3479-3494.

Rideout, G. and Stein, J., 2003. An Energy-Based Approach to Parameterizing Parasitic Elements for Eliminating Derivative Causality. *Proc. Int. Conference on Bond Graph Modeling and Simulation*, Orlando, FL.

Strömberg, J., Top, J., Söderman, U., 1993. Variable causality in bond graph caused by discrete effects. *Proc. Int. Conf. on Bond Graph Modeling and Simulation*, San Diego, CA, pp. 115–119.

Umarikar, A. and Umanand, L., 2005. Modelling of switching systems in bond graphs using the concept of switched power junctions. *Journal of the Franklin Institute*, Vol. 342, pp. 131-147.

SWITCHING MULTIMODEL LQ CONTROLLERS FOR VARIABLE SPEED AND VARIABLE PITCH WIND TURBINES*

Nadhira KHEZAMI[(a)], Naceur BENHADJ BRAIEK[(b)], Xavier GUILLAUD[(c)]

[(a)] LECAP, École Polytechnique de Tunisie, BP 743 – 2078 La Marsa, Tunisia
[(b)] LECAP, École Polytechnique de Tunisie, BP 743 – 2078 La Marsa, Tunisia
[(c)] L2EP, École Centrale de Lille, Cité Scientifique, 59651 Villeneuve d'Ascq Cedex, France

[(a)] nadhira.khezami@ec-lille.fr, [(b)] naceur.benhadj@ept.rnu.tn, [(c)] xavier.guillaud@ec-lille.fr

ABSTRACT
This paper deals with the design of two gain scheduled linear quadratic (LQ) controllers for variable speed, pitch regulated wind turbines in the whole plant operating area. Depending essentially on the wind speed, the wind turbine operating range can be divided into two different zones. Each LQ controller is then valid in a specific operating zone and has different control objectives. And the system switches between them during the transitions from one operating zone to another in order to ensure a good level of performances in the whole plant operating area. The design of the LQ controllers is based on a multimodel description of the nonlinear plant. The good performances of the proposed approach are illustrated on a 2MW wind turbine.

Keywords: Wind turbines, LQ regulators, multimodel approach, switching system.

1. INTRODUCTION

Variable-speed wind turbines are being more and more popular between the commercial ones. Actually, in contrast to constant-speed turbines, variable-speed wind turbines are designed to follow wind-speed variations in low winds to maximize aerodynamic efficiency (Johnson *et al.*, 06; Bianchi *et al.*, 2007). In this scheme, variable-speed wind turbine controller design has become an area of increasing interest.

The wind turbine operating area can be divided into two different zones: the partial-load zone (PL) and the full load zone (FL). We can define two partial-load zones: PL1 and PL2, corresponding respectively to low and medium wind speed values. The control objectives are different for each zone. Indeed, in the PL operating zone, the turbine operates at fixed pitch and the regulator aims to control the rotor speed and the generated electrical power through acting on the electromagnetic torque. In the FL operating zone – corresponding to high wind speeds- the pitch is variable and the controller uses then two control variables which are: the electromagnetic torque and the pitch angle to regulate the rotor speed and the electric power around their rated values. Other issue can be added to the control objectives: it deals with reducing the dynamic loads of the mechanical structure, which can affect wind turbine lifetime. The control problem is then to ensure a trade-off between these objectives, by taking into account the high nonlinearity of the plant and the stochastic nature of the main component acting on it: the wind speed.

In response to this multi-objective control problem, we propose in this paper two linear quadratic (LQ) controllers (for each operating zone) calculated from a linearization of the model around several operating points depending on the wind speed. Then, a multimodel strategy is considered with the controllers to handle the problem of the nonlinearity of the system.

This paper is organized as follows: the second section deals with the description of the considered plant, then, in the third section, we develop the proposed control laws for the two wind-turbine operating zones, and finally, simulation results are presented for a 2MW wind turbine showing the transition between the different zones.

2. SYSTEM DESCRIPTION

The wind turbines convert a part of the kinetic energy of the wind into mechanical energy first, and then electrical energy. The wind affects the main shaft by a driving aerodynamic torque T_{aero} expressed as:

$$T_{aero} = \frac{\rho \pi R_T{}^5 \Omega_T^2}{2\lambda^3} c_p(\lambda, \beta) \quad (1)$$

where ρ is the air density, R_T is the turbine radius, Ω_T is the turbine rotational speed, and c_p is the power coefficient which is a non linear

* *This work was supported by the CMCU project numbered:* ***08G1120***

function (as presented in Figure 1) of the blade pitch β and the tip speed ratio λ depending on the wind speed value w and given by:

$$\lambda = \frac{\Omega_T \, R_T}{w} \tag{2}$$

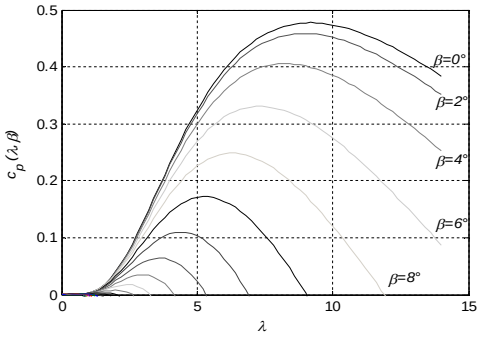

Figure 1: Illustration of the Power Coefficient (c_p) Curves

The aerodynamic torque is an input to the transmission system, modeled as a two mass system. This model considers two inertias (the generator and the turbine inertias respectively J_g and J_T) linked to a flexible shaft with a mechanical coupling damping coefficient d and a mechanical coupling stiffness coefficient k (Bianchi *et al.*, 2004; Camblong *et al.*, 2002). The drive train mechanical behavior is then characterized by the following equations reported to the low speed shaft:

$$\begin{cases} J_T \dot{\Omega}_T = T_{aero} - T_{mec} \\ J_{g-ls} \dot{\Omega}_{g-ls} = T_{mec} - G T_{em} \\ \dot{T}_{mec} = k\left(\Omega_T - \Omega_{g-ls}\right) + d\left(\dot{\Omega}_T - \dot{\Omega}_{g-ls}\right) \end{cases} \tag{3}$$

where T_{mec} and T_{em} are respectively the mechanical and the electromagnetic torques, G is the gearbox ratio, J_{g-ls} and Ω_{g-ls} are respectively the generator inertia and rotational speed reported to the low speed shaft, defined as:

$$\begin{cases} \Omega_{g-ls} = \dfrac{\Omega_g}{G} \\ J_{g-ls} = G^2 . J_g \end{cases} \tag{4}$$

The interconnection between the previously mentioned wind turbine components is illustrated in the block diagram of the Figure 2.

The pitch actuator dynamic is described by a first order system:

$$\dot{\beta} = \frac{1}{\tau_\beta}\left(\beta_{reg} - \beta\right) \tag{5}$$

β_{reg} is the control value of the blade-pitch angle β and τ_β is the time constant of the pitch actuator.

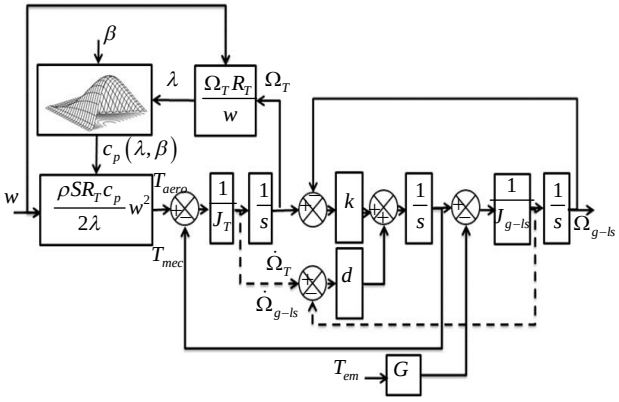

Figure 2: Block Diagram of Wind Turbine Model

The plant model, as it has been described, is highly nonlinear, mostly because of the nature of the wind seed and the coupling through the aerodynamics. It seems then appropriate to use linearized models where the wind is the gain scheduling variable. The linearization of the expression (1) of T_{aero} around an operating point (*o.p*) defined by the wind speed value w_i (Munteanu *et al.*, 2005; Bianchi *et al.*, 2007; Khezami *et al.*, 2009) leads to:

$$\begin{aligned} \Delta T_{aero} &= \left.\frac{\partial T_{aero}}{\partial \Omega_T}\right|_{o.p} \Delta\Omega_T + \left.\frac{\partial T_{aero}}{\partial \beta}\right|_{o.p} \Delta\beta \\ &= a_i \Delta\Omega_T + b_i \Delta\beta \end{aligned} \tag{6}$$

The symbol Δ presents the deviation from the chosen operating point.

3. MULTIMODEL APPROACH

The multimodel approach is an effective method to solve the control problem of strong nonlinear and parameter varying systems. For this reason, a multimodel strategy is considered in this study to describe the wind turbine. The core idea is to represent the nonlinear dynamical system by a set of locally valid sub-models across the whole operating range (Kardous *et al.*, 2006, 2007; Chedli *et al.*, 2002). The equivalent model is obtained by a weighted sum of these valid sub-systems. We will only valid two successive local models at once as described in Figure 3.

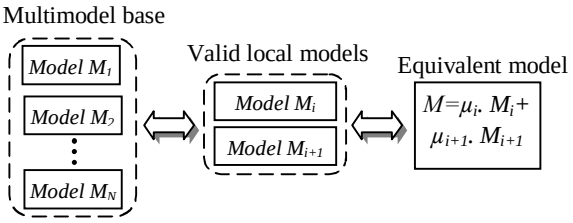

Figure 3: Wind Turbine Multimodel Description

The weighting coefficient μ_i is the validity value of the local model M_i and is calculated using the residue method as expressed in the following equation (Khezami *et al.*, 2009):

$$\mu_i = 1 - r_i \tag{7}$$

where r_i is a normalized residue measuring the error between w and w_i which are the wind speed values of respectively the instantaneous model and the valid local model (respectively M and M_i). When M_i and M_{i+1} are the valid models, the residue can be expressed as:

$$r_i = \frac{|w_i - w|}{w_i + w_{i+1}} \tag{8}$$

4. CONTROL TASK

The control objectives are to ensure good performances of the selected outputs, i.e. energy conversion and alleviation of the mechanical loads affecting the plant structure. The wind turbine operating area can be divided into two partial load zones and one full load zone as defined in the Figure 4.

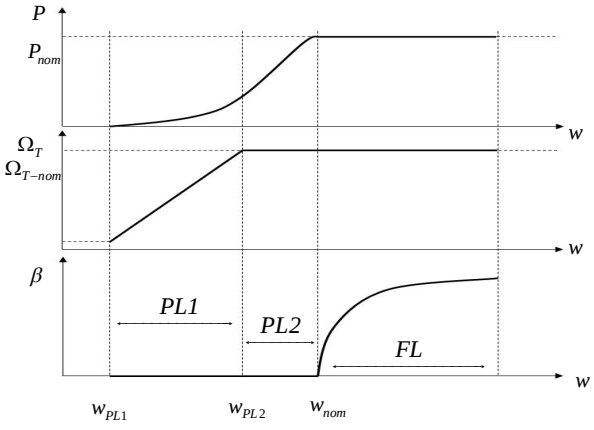

Figure 4: Evolution of the Plant Main Variables (Power P, rotor speed Ω_T and pitch angle β) in function of the wind speed

4.1. PL zone control law

In the partial load zones, the wind turbine operates at variable speed, fixed pitch in PL1 zone and at fixed speed, fixed pitch in PL2 zone. For low wind speeds ($w \le w_{PL2}$: PL1 zone), the main objective is to maximize the system energy conversion by maintaining the power coefficient at its optimal value $\left(c_p = c_{p-opt} = c_p\left(\lambda_{opt}, 0\right)\right)$. This supposes to regulate the rotor around a given reference Ω_{T-ref} calculated as follows:

$$\Omega_{T-ref} = \frac{\lambda_{opt} w_i}{R_T}; \forall w_i \le w_{PL2} \tag{9}$$

For medium wind speeds ($w_{PL2} \le w \le w_{nom}$: PL2 zone), the turbine speed reaches its nominal value and the control aim is to regulate it around this rated value.

The PL zones control objectives could be satisfied by acting on only the electromagnetic torque.

We define:

$$\begin{cases} \Omega_{T-ref} = \begin{cases} \dfrac{\lambda_{opt} w_i}{R_T}; \forall w_i \le w_{PL2} \\ \Omega_{T-nom}; \forall w_i \ge w_{PL2} \end{cases} \\ T_{aero-ref} = \begin{cases} \dfrac{1}{2}\rho\pi R_T^5 \Omega_T^2 \dfrac{c_{p-opt}}{\lambda_{opt}}; \forall w_i \le w_{PL2} \\ \dfrac{1}{2}\rho\pi R_T^5 \Omega_{T-nom}^2 \dfrac{c_{p-i}}{\lambda_i}; \forall w_i \ge w_{PL2} \end{cases} \\ T_{em-ref} = \dfrac{T_{aero-ref}}{G} \\ T_{mec-ref} = T_{aero-ref} \end{cases} \tag{10}$$

with:

$$\forall w_i \ge w_{PL2} : \begin{cases} \lambda_i = \dfrac{\Omega_{T-nom} R_T}{w_i}; \\ c_{p-i} = c_p\left(\lambda_i, 0\right) \end{cases} \tag{11}$$

The linearization of the aerodynamic torque as presented in equation (6), leads to write:

$$\begin{cases} \Delta T_{aero} = a_{1i} \Delta\Omega_T \\ a_{1i} = \dfrac{-\rho\pi R_T^4 w_i\, c_{p-opt}}{2\lambda_{opt}^2}; \forall w_i \le w_{PL2} \\ a_{1i} = \dfrac{\rho\pi R_T^4 w_i^2}{2\Omega_{T-nom}} \left[\dfrac{\partial c_p\left(\lambda, 0\right)}{\partial\lambda} - \dfrac{c_{p-i}}{\lambda_i} \right]; \forall w_i \ge w_{PL2} \end{cases} \tag{12}$$

The system could be now presented in the following state space representation:

$$\begin{cases} \dot{\widehat{\Delta x_1}} = A_{1i}\Delta x_1 + B_{1i}\Delta u_1 \\ \Delta y_1 = \Delta x_1 \end{cases} \quad (13)$$

where:

$$\begin{cases} \Delta x_1 = \begin{pmatrix} \Delta\Omega_T \\ \Delta\Omega_{g-ls} \\ \Delta T_{mec} \end{pmatrix}; \Delta u_1 = \left(\Delta T_{em}\right); B_{1i} = \begin{pmatrix} 0 \\ -\dfrac{G}{J_{g-ls}} \\ \dfrac{dG}{J_{g-ls}} \end{pmatrix} \\ A_{1i} = \begin{pmatrix} \dfrac{a_{1i}}{J_T} & 0 & -\dfrac{1}{J_T} \\ 0 & 0 & \dfrac{1}{J_{g-ls}} \\ k + \dfrac{a_{1i}d}{J_T} & -k & -d\left(\dfrac{1}{J_T} + \dfrac{1}{J_{g-ls}}\right) \end{pmatrix} \end{cases} \quad (14)$$

The proposed control law aims to minimize the following quadratic criterion (Boukhezzara *et al.*, 2007; Hammerum et al., 2007; Cutululis *et al.*, 2006):

$$J_1 = 1/2 \int_0^{\infty} \left[\Delta x_1^T Q \Delta x_1 + \Delta u_1^T R \Delta u_1 \right] dt \quad (15)$$

where Q and R are diagonal positive definite matrices.

By solving a Riccati equation, an optimal gain is calculated such that:

$$\Delta u_1 = -K_1 \Delta x_1 \quad (16)$$

Then, we can write:

$$\begin{cases} u_1 = \left(T_{em}\right) = -K_1\left(x_1 - x_{1-ref}\right) + u_{1-ref} \\ x_1 = \begin{pmatrix} \Omega_T \\ \Omega_{g-ls} \\ T_{mec} \end{pmatrix}; x_{1-ref} = \begin{pmatrix} \Omega_{T-ref} \\ \Omega_{g-ls-ref} = \Omega_{T-ref} \\ T_{mec-ref} \end{pmatrix} \\ u_{1-ref} = \left(T_{em-ref}\right) \end{cases} \quad (17)$$

The Figure 5 presents the block diagram of the controlled system.

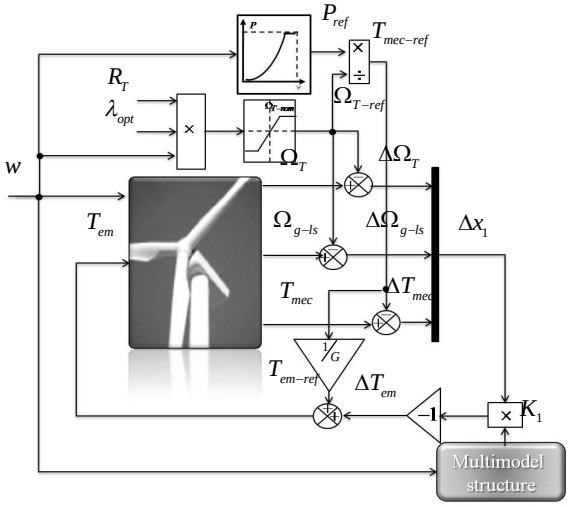

in PL Operation

To illustrate the good performances of the proposed control law, simulations have been runned on the basis of a dynamic model implemented on Matlab-Simulink of a three blades 2MW wind turbine.

The wind is generated with the method elaborated by C. Nichita in (Nichita *et al*, 2002).

For a variable wind with a speed mean value of 8m/s, the evolution of the different wind turbine variables are represented in Figure 6.

A preferential choice was taken on the regulation of the generated power with regard to the rotor speed regulation.

As shown in Figure 6, all the wind turbine variables follow nearly perfectly their reference signals while the wind varies and that by acting only on the electromagnetic torque (the pitch angle is maintained null).

4.2. FL zone control law

In the FL operation, the electrical power reaches its rated value. The main objective of the controller is then to regulate the generated power and the rotor speed at their rated values.

The linearization of the aerodynamic torque as presented in equation (6), leads to write:

$$\begin{cases} \Delta T_{aero} = a_{2i}\Delta\Omega_T + b_{2i}\Delta\beta \\ a_{2i} = \dfrac{1}{2}\rho\pi R_T^3 \dfrac{w_i^2}{\Omega_{T-nom}}\left[\dfrac{\partial c_p\left(\lambda,\beta\right)}{\partial\lambda} - \dfrac{c_{p_{i-nom}}}{\lambda_{i-nom}}\right] \\ b_{2i} = \dfrac{1}{2}\rho\pi R_T^2 \dfrac{w_i^3}{\Omega_{T-nom}} \dfrac{\partial c_p\left(\lambda,\beta\right)}{\partial\beta} \end{cases} \quad (18)$$

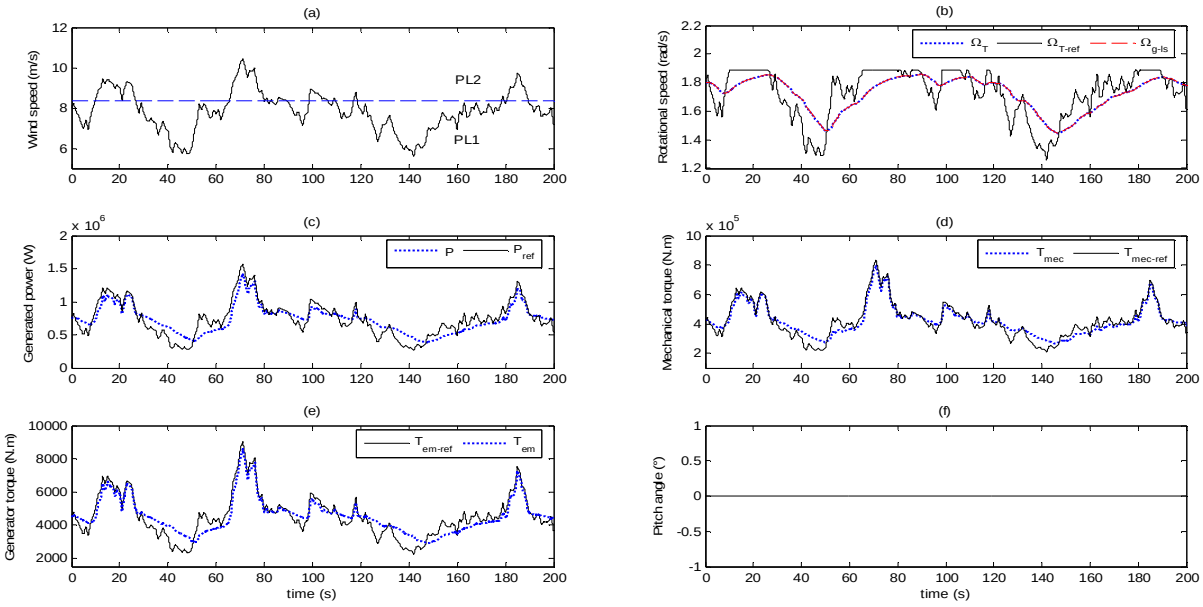

Figure 6: Evolution of the Wind Turbine Variables for a Partial Load Operation

where:

$$c_{p_{i-nom}} = c_p\left(\lambda_{i-nom}, \beta_{i-nom}\right) = \frac{2\Omega_{T-nom} T_{aero-nom}}{\rho \pi R_T^2 w_i^3} \tag{19}$$

For the wind turbine FL operation, we choose to use a linear quadratic controller combined to reference model and an integral action. With two control variables: the electromagnetic torque and the regulating pitch angle, the state space representation is as follows:

$$\begin{cases} \dot{\Delta x_2} = A_{2i}\Delta x_2 + B_{2i}\Delta u_2 \\ \Delta y_2 = C_{2i}\Delta x_2 + D_{2i}\Delta u_2 \end{cases} \tag{20}$$

where Δx_2, Δy_2 and Δu_2 represent the deviation of respectively the state vector x_2, the output vector y_2 and the input vector u_2 from the operating point at the wind speed w_i characterized by x_{2i-ref}, y_{2i-ref} and u_{2i-ref}:

$$\begin{cases} \Delta x_2 = x_2 - x_{2i-ref}\,; \Delta y_2 = y_2 - y_{2i-ref}\,; \\ \Delta u_2 = u_2 - u_{2i-ref} \\ x_2 = \begin{pmatrix} \Omega_T \\ \Omega_{g-ls} \\ \beta \\ T_{mec} \end{pmatrix}; u_2 = \begin{pmatrix} \beta_{reg} \\ T_{em} \end{pmatrix}; y_2 = \begin{pmatrix} \Omega_T \\ P \end{pmatrix} \\ x_{2i-ref} = \begin{pmatrix} \Omega_{T-nom} \\ \Omega_{g-ls-nom} = \Omega_{T-nom} \\ \beta_{i-nom} \\ T_{mec-nom} \end{pmatrix} \\ y_{2i-ref} = \begin{pmatrix} \Omega_{T-nom} \\ P_{nom} \end{pmatrix}; u_{2i-ref} = \begin{pmatrix} \beta_{i-nom} \\ T_{em-nom} \end{pmatrix} \end{cases} \tag{21}$$

The matrices of this state representation are given by:

$$\begin{cases} A_{2i} = \begin{pmatrix} \frac{a_{2i}}{J_T} & 0 & \frac{b_{2i}}{J_T} & -\frac{1}{J_T} \\ 0 & 0 & 0 & \frac{1}{J_{g-ls}} \\ 0 & 0 & -\frac{1}{\tau_\beta} & 0 \\ k+\frac{a_{2i}d}{J_T} & -k & \frac{db_{2i}}{J_T} & -d.\left(\frac{1}{J_T}+\frac{1}{J_{g-ls}}\right) \end{pmatrix} \\ B_{2i} = \begin{pmatrix} 0 & 0 \\ 0 & -\frac{G}{J_{g-ls}} \\ \frac{1}{\tau_\beta} & 0 \\ 0 & \frac{dG}{J_{g-ls}} \end{pmatrix}; D_{2i} = \begin{pmatrix} 0 & 0 \\ 0 & G.\Omega_{T-nom} \end{pmatrix} \\ C_{2i} = \begin{pmatrix} 1 & 0 & 0 & 0 \\ 0 & G.T_{em-nom} & 0 & 0 \end{pmatrix} \end{cases} \quad (22)$$

The proposed approach is developed in (Khezami *et al*, 2010), and the derived control law has the following form:

$$u_2 = -\gamma_1 x_2 - \gamma_2 v - \gamma_3 s + \gamma_4 \eta_i + \gamma_5 \xi_i + \gamma_6 y_o \quad (23)$$

where:

- v is the integral action,
- s is the reference model on the outputs,
- y_o is the order signals (the input of the reference model),
- η_i and ξ_i give information on the chosen operating point, they are given by:

$$\begin{cases} \xi_i = \dot{x}_{2i-ref} - A_{2i} x_{2i-ref} - B_{2i} u_{2i-ref} \\ \eta_i = y_{2i-ref} - C_{2i} x_{2i-ref} - D_{2i} u_{2i-ref} \end{cases} \quad (24)$$

The Figure 7 presents the block diagram of the system with the proposed control law.

To illustrate the good performances of the proposed controller, simulations have been carried on a 2MW wind turbine operating at a variable wind with a speed mean value of 18m/s. the Figure 8 presents the evolution of the wind turbine variables in a full load operation.

As one can see in Figure 8, the main control objectives are satisfied: the generated power and the rotor speed are maintained very close to their rated values with admissible control signals.

To prevent the mechanical fatigue damage, the alleviation of the drive train loads has been taken into consideration. Indeed, the mechanical torque keeps an almost constant value with acceptable fluctuations.

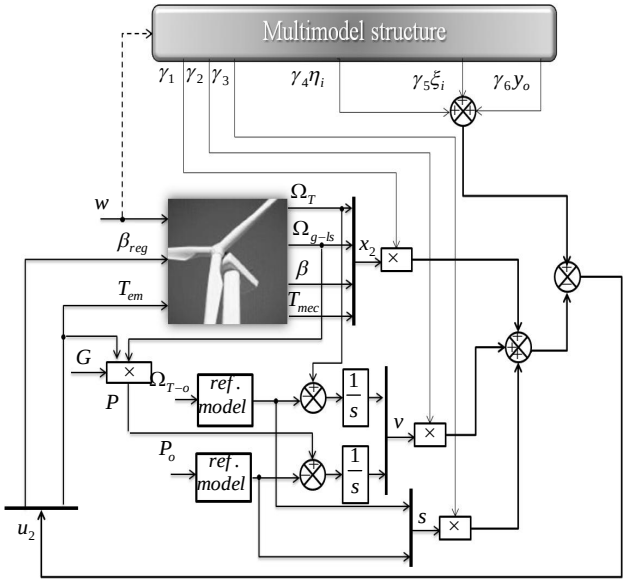

Figure 7: Block Diagram of the Controlled System in FL Operation

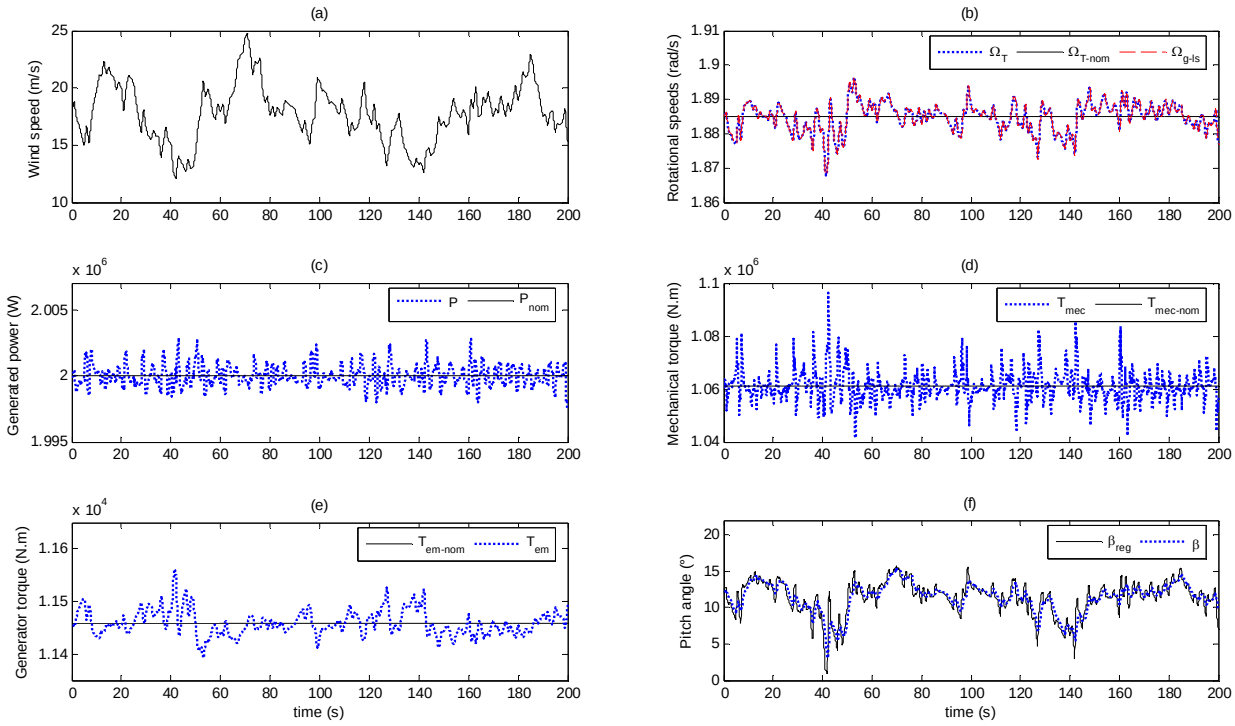

Figure 8: Evolution of the Wind Turbine Variables for a Full Load Operation

4.3. Switching controllers

On the basis of the measured wind speed, an algorithm allows to switch from one multimodel base to another during the transitions between the wind turbine operating zones. This is explained in Figure 9.

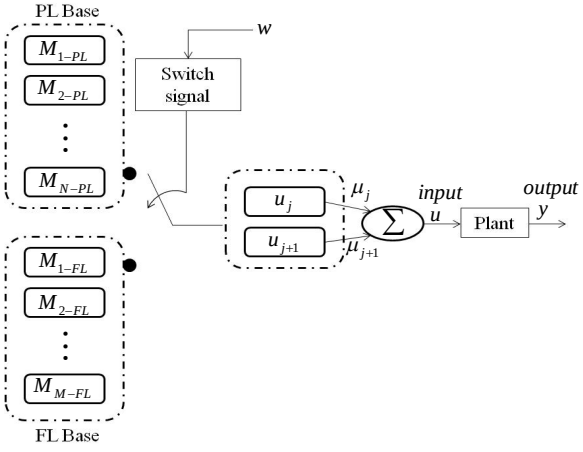

Figure 9: General Structure of a Multimodel Switching System

The efficiency of the proposed approach has been illustrated in the sight of simulation results obtained for a variable wind with a speed mean value of 11m/s, and transients between the three wind turbine operating zones: PL1, PL2 and FL zones as shown in Figure 10.

The transitions between these different operating zones have been efficiently handled by the control system in a smooth manner, which avoids the generation of large transients that could have damaging effects on the plant structure.

The rotor speed was kept slightly over its reference characteristic in order to get a better regulation and a better quality of the generated electrical power.

5. CONCLUSION

In this paper, two LQ controllers have been proposed for the whole operating range of a variable speed, pitch regulated wind turbine. The proposed strategy presented a compromise between different control objectives. The simulation results showed good performances of the controllers with acceptable mechanical stress. Furthermore, the presented approach handled successfully and efficiently the transitions between the different operating zones.

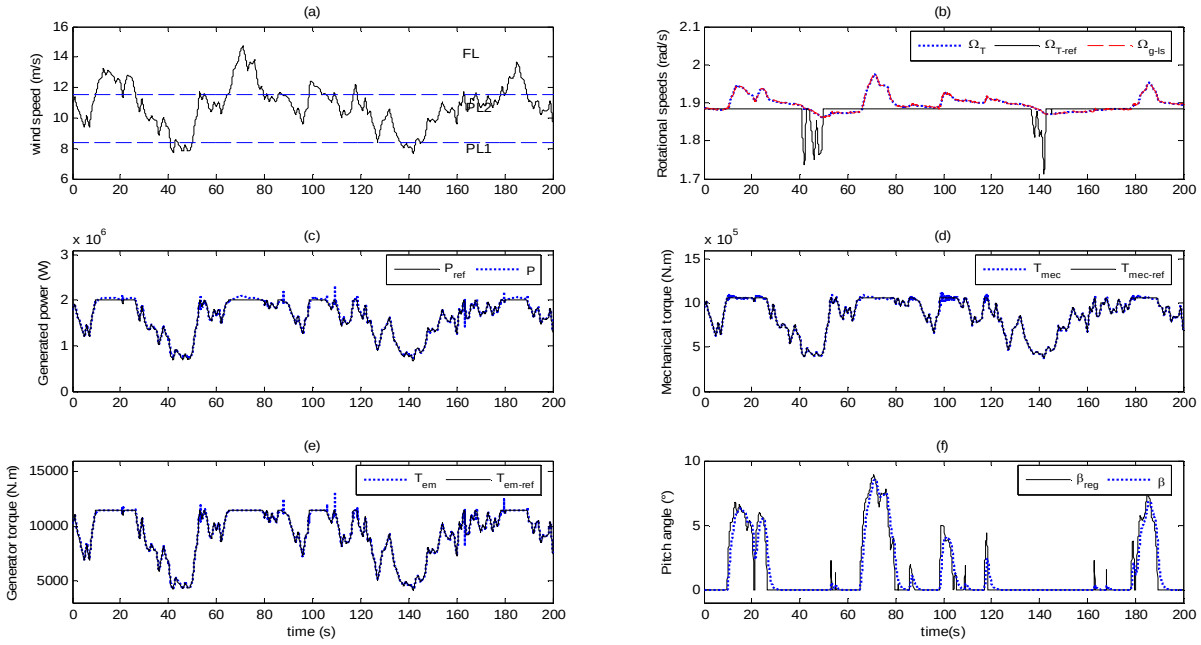

Figure 10: Evolution of the Wind Turbine Variables in Case of Switching Controllers Between PL and FL Operations

REFERENCES

Bianchi, F. D., Mantz, R. J. and Christiansen, C. F., 2004, Control of Variable-speed Wind Turbines by LPV Gain Scheduling. In *Wind Energy*, vol. 7, issue 1, pp: 1-8.

Bianchi, F. D., De Battista, H. and Mantz, R. J., 2007. *Wind turbine control systems: principles, modeling and gain scheduling design*, Springer-Verlag. London, 1st edition.

Boukhezzara, B., Lupua, L., Siguerdidjanea, H. and Hand, M., 2007. Multivariable control strategy for variable speed, variable pitch wind turbines. In *Science Direct, Renewable Energy*, vol. 32, pp: 1273–1287.

Camblong, H., Rodriguez, M., Puiggali, J. R. and Abad, A., 2002, Comparison of different control strategies to study power quality in a variable-speed wind turbine. *In 1st world wind energy conference proceeding, Berlin.*

Chedli, M., 2002. *Stabilité et commande de systems décrits par des multimodèles.* PhD thesis, Institut National Polytechnique de Lorraine.

Cutululis, N. A., Bindner, H., Munteanu, I., Bratcu, A., Ceanga, E., and Soerensen, P., 2006. LQ Optimal Control of Wind Turbines in Hybrid Power Systems. In *European Wind Energy Conference and Exhibition*, Athens.

Hammerum, K., Brath1, P. and Poulsen, N. K., 2007. A fatigue approach to wind turbine control. In *Journal of Physics*: Conference Series 75.

Johnson, K. E., Pao, L. Y, Balas, M. J. and Fingersh, L. J, june 2006, Control of variable speed wind turbines: Standard and adaptive techniques for maximizing energy capture, In *IEEE Control systems magazine*, pp 70-81.

Kardous, Z. , Benhadj Braiek, N. and Al Kamel, A., 2006. On the multimodel stabilization control of uncertain systems – Part 1, In *International Scientific IFNA-ANS Journal: Problems on Nonlinear Analysis in Engineering Systems,* No 2.

Kardous, Z., Benhadj Braiek, N. and Al Kamel, A., 2007. On the multimodel stabilization control of uncertain systems – Part 2. In *Int. J. of Problems of Nonlinear Analysis in Engineering Systems*, No.1(27), pp: 76-87, vol. 13.

Khezami, N., Guillaud, X., and Benhadj Braiek, N., 2009. Multimodel LQ controller design for variable-speed and variable pitch wind turbines at high wind speeds. In *IEEE International Multi-conference on Systems, Signals and Devices*, Djerba.

Khezami, N., Benhadj Braiek, and Guillaud, X., N., 2010. Wind turbine power tracking using an improved multimodel quadratic approach. In *ISA Transactions*, to be published.

Munteanu, I., Bratcu, A. I., Cultululis, N. A. and Ceanga, E., 2005. A two loop optimal control of flexible drive train variable speed wind power systems, *16th Triennial World Congress-IFAC*, Prague.

Nichita, C., Luca, D., Dakyo, B. and Ceanga, E., 2002, Large band simulation of the wind turbine simulators *IEEE Transactions on Energy Conversion*, 523-529.

DYNAMIC MODELING OF A PARALLEL ROBOT WITH SIX DEGREES OF FREEDOM

A. Chibani[(a)] ; **C. Mahfaudi**[(b)] ; **A. Zaatri**[(c)] ; **A. Amouri**[(d)]

[(a)] , [(b)] , [(d)] University Larbi Ben M'hidi Oum El Bouaghi, Faculty of Science and Technology.

[(c)] University Mantouri of Constantine.

[(a)]: chibaniabdelhakim@yahoo.fr
[(b)]: c_mahfoudi_dz@yahoo.fr
[(c)]: azaatri@yahoo.com

ABSTRACT

Parallel robots seem to be the most suitable spots requiring high performance such as speed and accuracy. Such performances sought now are that the dynamics of parallel structures is no longer negligible.
This work represents a contribution in this latter context; it deals in the whole dynamic study of a parallel robot with six degrees of freedom constituting the so-called Gough Stewart platform. In determining the direct and inverse geometric model, we use a setup based on Khalil and Kleinfinger ratings [7] for structures with closed loops. The kinematical modeling, using the calculation of the Jacobian matrix and its inverse, were deduced from the joint velocities of the six cylinders in order to follow a desired trajectory for the platform.
The Newton Euler formalism is used to model the dynamics of the robot and the first to consider each kinematics chain (legs) as a serial structure, and then by considerations of balance and closed chain, we determine the dynamics of the platform.

Keywords: Gough-Stewart platform, parallel robot, dynamic modeling, Newton Euler formalism.

1. INTRODUCTION

The complex architecture of parallel robots makes it increasingly necessary to improve their dynamic performance, this is especially motivated by the proven qualities recognized by the research community [2] and industrial robotics, addressing the very high speed, driving simulators, machine - tools, medical applications, etc.. Parallel robots in comparison with serial robots, have special characteristics, stiffness and dynamic load capacity higher still, actuators, high precision guidance and stable operation.
To obtain the dynamics of parallel robots, many methods have used the classical procedure of computing dynamic model of an equivalent tree structure; Principle of virtual works has been used in [4]; work [3] and [5] have used the Euler-Lagrange formalism. On the other hand, the equations of Newton - Euler have been used by [10], [13] and [14]. Through the establishment of iterative matrix relations for kinematics and dynamic analysis of parallel robot Gough - Stewart [17] used the principle of virtual work to derive the fundamental equations of dynamics.
This paper presents a method for obtaining the inverse dynamic model of parallel robot with six degrees of freedom consisting of a mobile platform attached to a fixed base by six identical kinematics chains using an universal joint (on base), a spherical joint (on the mobile platform) and an active prismatic joint. The model based on the formalism of Newton – Euler is obtained in terms of the dynamic models of the legs. It concludes with a simulation of kinematics and dynamics of the robot.

2. DESCRIPTION OF PARALLEL ROBOT.

The proposed parallel robot to look like a platform composed of six identical kinematics chains linked to a mobile platform through ball and connected with a fixed base by universal joints. A prismatic actuator used to vary the length of the kinematics chains (Fig. 1), the platform provides six degrees of freedom. Geometric modeling, kinematics and dynamics of parallel robots require the knowledge descriptions robots closed structure, description of tree structure robots as well as open-chain robots. It defines two headers one R_0 attached to base its origin is the point O, the other set at R_p mobile platform with O_2 as the origin.

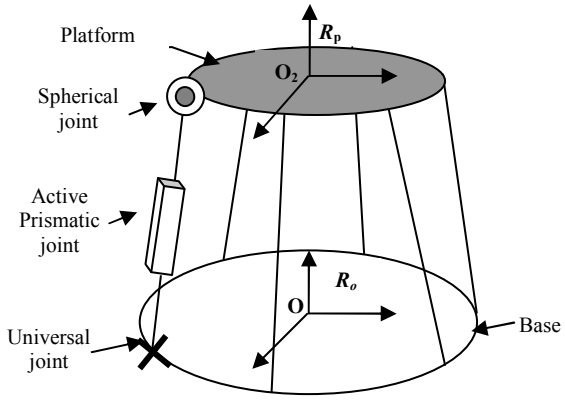

Fig. 1: Description of parallel robot with six degrees of freedom

The center of each drive shaft and the center of each ball are denoted by Bi and Pi (i = 1 to 6).
The robot consists of 5 loops space motorized prismatic joints 6 and 30 passive revolute joints. The tree structure equivalent minimum [3] is obtained by isolating the platform. It is composed of 6 prismatic joints and 12 motorized passive revolute joints. In this structure the joints were removed.
Each kinematics chain to a structure consisting of 3 bodies with 3 joints [11]. The situation of the first revolute axis of each kinematics chain is shown in Figure 2.

1.1. Geometrical parameters of the kinematics chain i (i=1…6)

Table 1. : Setting geometric chain *i*.

J_i	$a(ji)$	μ_{ji}	σ_{ji}	γ_{ji}	b_{ji}	α_{ji}	d_{ji}	θ_{ji}	r_{ji}
$1i$	0	0	0	γ_{1i}	b_{1i}	$-\pi/2$	d_{1i}	q_{1i}	0
$2i$	$1i$	0	0	0	0	$\pi/2$	0	q_{2i}	0
$3i$	$2i$	1	1	0	0	$\pi/2$	0	0	q_{3i}

for i=1…6; $\gamma_{11} = b_{11} = \gamma_{12} = b_{12} = b_{16} = 0$

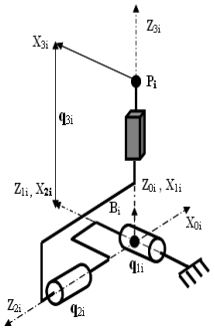

Fig.2: Location frame joints of each kinematics chain.

The geometric parameters of the structure are given in Table 1, we note:
- $\mu(j)$ and $\sigma(j)$ that describe the type of joint; $\mu(j) = 1$ if the joint j is motorized and $\mu(j) = 0$ if it is passive.
$\sigma(j) = 1$ if the joint is prismatic and $\sigma(j) = 0$ if it is revolute. (γ_j, b_j, a_j, d_j, θ_j, r_j)
The parameters (γ_j, b_j, a_j, d_j, θ_j, r_j) are used to set the frame *Rj* in reference of its antecedent *Ri*.
The transformation matrix (T) consists of these parameters is given by:

$$ {}^{i}T_{j} = \begin{vmatrix} {}^{i}\mathrm{A}_{j} & {}^{i}P_{j} \\ 0_{(1*3)} & 1 \end{vmatrix} $$

Where to:
${}^{i}\mathrm{A}_{j}$: is the matrix (3 * 3) which defines the direction of the coordinate *Rj* in the coordinate *Ri* .

$$ {}^{i}A_{j} = \left| {}^{i}s_{j} \quad {}^{i}n_{j} \quad {}^{i}a_{j} \right| $$

${}^{i}P_{j}$: is the position vector (3 * 1) which defines the origin of the coordinate *Rj* in the coordinate *Ri*.

2. GEOMETRICAL MODEL OF THE ROBOT.

2.1. Direct geometrical Model of chain i

The direct geometric model of a leg *i* robot expresses the operational coordinates (X) of point P_i in frame R_0 according to the joint variables ($q_i = [q_{1i}\, q_{2i}\, q_{3i}]^T$ for i = 1 to 6).

$$ X = f(q) \tag{1} $$

We use the transformation matrices to define the coordinate R_{3i} origin P_i, which is the frame of the chain i in the reference base of the robot R_0:

$$ {}^{0}T_{3i} = {}^{0}T_{1i}\, {}^{1i}T_{2i}\, {}^{2i}T_{3i} \tag{2} $$

The geometric model solution of the parallel robot is not unique since for a given joint configuration variables, the platform can take several different situations.

2.2. Inverse geometric model

The Inverse geometric model is to calculate the joint coordinates (q_i) corresponding to a given situation of the terminal body (platform) based on operational details.

$$ q_i = f(X) \tag{3} $$

This model is easily calculated using some basic elementary geometric relationships (Fig. 3).

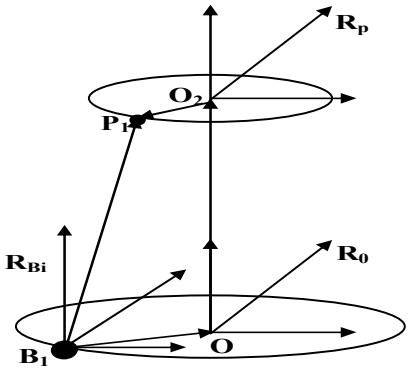

Fig.3: Representation vector $\overrightarrow{BP_{(i)}}$

$$ \overrightarrow{BP_{(i)}} = R\overrightarrow{O_2P_{(i)}} + \overrightarrow{OO_2} + \overrightarrow{B_{(i)}O} \tag{4} $$

R: matrix orientation of the platform.

$$ R = rot(Z,\phi) * rot(Y,\theta) * rot(X,\psi) \tag{5} $$

Let ${}^{Bi}P_{xi}$, ${}^{Bi}P_{yi}$, ${}^{Bi}P_{zi}$ coordinates vectors *BP(i)* from a frame R_{Bi}. The prismatic variables q_{3i} are obtained by the following equation:

$$q_{3i} = \sqrt{{}^{Bi}P_{xi}^2 + {}^{Bi}P_{yi}^2 + {}^{Bi}P_{zi}^2} \tag{6}$$

The variables relating to passive joints q_{1i} and q_{2i} are given by equations (7), obtained using the method of Paul [1]:

$$-{}^{Bi}P_{xi}S_{1i} + {}^{Bi}P_{yi}C_{1i} = 0 \tag{7}$$

Note: $Sqj_i = Sj_i$ et $Cqj_i = Cj_i$

$$\begin{cases} {}^{Bi}P_{xi}C_{1i}C_{2i} + {}^{Bi}P_{yi}S_{1i}C_{2i} + {}^{Bi}P_{zi}S_{2i} = 0 & (8) \\ -{}^{Bi}P_{xi}C_{1i}S_{2i} - {}^{Bi}P_{yi}S_{1i}S_{2i} + {}^{Bi}P_{zi}C_{2i} = 0 & (9) \end{cases}$$

$$\begin{cases} q_{1i} = \operatorname{atan2}\left({}^{Bi}P_{yi}, {}^{Bi}P_{xi}\right) & (10) \\ \text{ou} \\ q'_{1i} = q_{1i} + \pi & (11) \end{cases}$$

and:

$$q_{2i} = \operatorname{atan2}\left(\frac{-q_{3i}\left({}^{Bi}P_{1i}C_{1i} + {}^{Bi}P_{1i}S_{1i}\right)}{Det}, \frac{-q_{3i}\,{}^{Bi}P_{3i}}{Det}\right) \tag{12}$$

with:

$$Det = {}^{Bi}P_{3i}^2 + \left({}^{Bi}P_{1i}C_{1i} + {}^{Bi}P_{2i}S_{1i}\right)^2 \neq 0$$

The condition $Det \neq 0$ is verified as ${}^{Bi}P_{zi}$ is strictly positive and not zero (practically zero means that the chain is collinear with the plane of the base which is impossible), the variable is physically q_{1i} joint between zero and π.

3. KINEMATIC MODEL OF THE ROBOT.

3.1. Direct Kinematics model of the chain i:

The direct kinematics model of the chain *i* gives the linear velocity of point P as a function of velocity joints of the chain *i* $\left(\dot{q}_{1i}, \dot{q}_{2i}, \dot{q}_{3i}\right)$ for i = 1..6. This model is identical to the direct kinematics model of a serial structure with three joints (RRP).

$${}^0V_{pi} = {}^0J_{3i}\dot{q}_i \tag{13}$$

Vpi: linear velocity of point *Pi;*
${}^0J_{3i}$: Jacobian matrix of the kinematics chain *i*.

3.2. Inverse Kinematics model:

The inverse kinematics model allows expressing the linear speed of the motorized joint variables *q* as a function of kinematics torsor mobile platform is given by the following equation:

$$\dot{q} = {}^0J_p^{-1}\begin{pmatrix} {}^0V_p \\ {}^0\omega_p \end{pmatrix} \tag{14}$$

${}^0V_p$, ${}^0\omega_p$: translational speed and angular velocity of the mobile platform;
°J_p^{-1}: inverse Jacobian matrix (6 * 6) of the robot.

3.3. Calculating the inverse Jacobian J^1_p:

The calculation of the inverse of the Jacobian matrix platform is based on determining the speed q_{3i} with the projection of the speed of point *Pi* on the axis z_{3i}.
We have for a prismatic joint (σ_k=1):

$$\dot{q}_{3i} = {}^0\mathrm{a}_{3i}^T\,{}^0V_{pi} \tag{15}$$

${}^0V_{pi}$ linear speed of point P_i, is computed according to V_p and ω_p by modeling of kinematics chains. ${}^0\mathrm{a}_{3i}$: unit vector carried by the axis of articulation z_{3i} prismatic.

$${}^0V_{pi} = {}^0V_p + {}^0\omega_p \times {}^0L_i \tag{16}$$

${}^0L_i$: vector representing the components of P_1P_i vector expressed in the frame R_0.
It comes as:

$$\dot{q}_{3i} = {}^0\mathrm{a}_{3i}^T\,{}^0V_P + {}^0\mathrm{a}_{3i}^T\left({}^0\omega_p \times {}^0L_i\right) \tag{17}$$

and then:

$$\dot{q}_{3i} = {}^0\mathrm{a}_{3i}^T\,{}^0V_P + \left({}^0L_i\,{}^0\mathrm{a}_{3i}\right)^T\,{}^0\omega_p \tag{18}$$

$$\dot{q}_{3i} = {}^0\mathrm{a}_{3i}^T\left(\left({}^0\hat{L}_i\mathrm{a}_{3i}\right)^T\begin{pmatrix} {}^0V_p \\ {}^0\omega_p \end{pmatrix}\right) \tag{19}$$

$${}^0J_p^{-1} = \begin{pmatrix} {}^0\mathrm{a}_{31}^T & \left({}^0\hat{L}_1\,{}^0\mathrm{a}_{31}\right)^T \\ \cdot & \cdot \\ \cdot & \cdot \\ \cdot & \cdot \\ \cdot & \cdot \\ {}^0\mathrm{a}_{36}^T & \left({}^0\hat{L}_6\,{}^0\mathrm{a}_{36}\right)^T \end{pmatrix} \tag{20}$$

In section five, a MATLAB simulation is required to view and verify the results obtained from the Jacobian matrix inverse ${}^0J_p^{-1}$. (Fig.4)

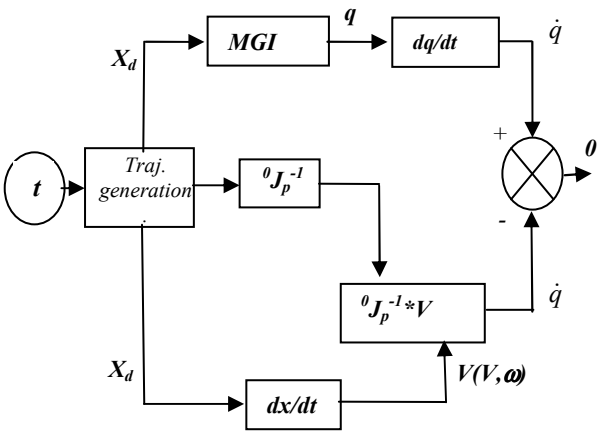

Fig.4: Global Scheme used to validate the analytical kinematics model.

4. INVERSE DYNAMIC MODEL

The inverse dynamic model is the relationship between the forces of the motorized joint and positions, velocities, accelerations of the platform. The inverse dynamic model is intended to control robots.

$$\Gamma = f\left({}^0T_p, {}^0V_p, {}^0\dot{V}_p\right) \tag{21}$$

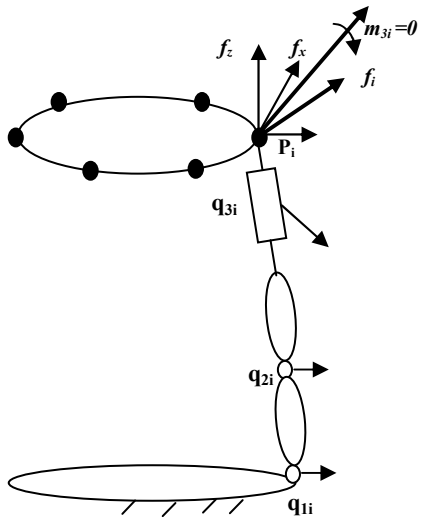

Fig. 5: Forces and moments applied on the platform by the forces of reaction chains.

For the dynamic model we decompose the system into two subsystems: the platform that is linked to the kinematics chain of joints, the torque reaction transmitted to the chain at a platform is zero, the effect of chain i kinematics on the platform is represented by reaction forces f_i (i = 1 to 6).
The tree structure (the second subsystem) consists of the base and legs with two pairs of revolute joints (Γ_{1i} , Γ_{2i}) are zero.

In this problem the unknowns are the 18 components of reaction forces ${}^of_i = [{}^of_{xi}\ {}^of_{yi}\ {}^of_{zi}]^T$ and the 6 forces motorized joints Γ_{3i} (i =1 à 6). Each dynamic model of a kinematics chain is composed of three equations, giving a total of 18 equations. The Newton-Euler equations of the platform gives 6 equations, we obtain a system of 24 equations in 24 unknowns.
This system will be solved sequentially as follows:
- calculation of ${}^of_i$ based Γ_{3i} using the dynamic model of the kinematic chain i
- Γ_{3i} forces will be obtained from Newton-Euler equations of the platform.

4.1 Calculating the reaction force ${}^of_i$

The general form of the dynamic model of the kinematics chain i, is written:

$$\Gamma_i = \mathrm{H}_i\left(q_i, \dot{q}_i, \ddot{q}_i\right) + {}^0J_{3i}\,{}^0f_i^T \tag{22}$$

With:
H_i : vector (3 * 3) containing the inertial forces, Coriolis, centrifugal and gravity.
Γ_i : is composed of forces / torques of the joints of the chains where Γ_{1i} and Γ_{2i} are zero;

$$\Gamma = \left[\Gamma_{1i} \quad \Gamma_{2i} \quad \Gamma_{3i}\right]^T = \left[0 \quad 0 \quad \Gamma_{3i}\right]^T \tag{23}$$

From equation (22) of the general form, the reaction force of the kinematics chain i can be written:

$${}^0f_i = -{}^0J_{3i}^{-T}\,\mathrm{H}_i\left(q_i, \dot{q}_i, \ddot{q}_i\right) + {}^0J_{3i}^{-T}\,\Gamma_i \tag{24}$$

4.2 Dynamic of platform

The Newton Euler equations around the origin of the platform are written:

$${}^0F_p = {}^0\mathrm{II}_p\,{}^0\dot{V}_p + \begin{pmatrix} {}^0\omega_p \times \left({}^0\omega_p \times {}^0MS_p\right) \\ {}^0\omega_p \times \left({}^0I_p \times {}^0\omega_p\right) \end{pmatrix} - \begin{pmatrix} M_pI_3 \\ {}^0M\hat{S}_p \end{pmatrix} {}^0g \tag{25}$$

With :
${}^0F_p$: external forces and moments applied on the platform.

${}^0f_i = [{}^0f_{xi}, {}^0f_{yi}, {}^0f_{zi}]^T$ reaction force of the chain i and 6 forces motorized joints Γ_{3i} (i= 1à 6).
${}^\circ\mathrm{II}_p$: space inertia matrix (6 * 6) of the platform, we have :

$${}^0\mathrm{II}_p = \begin{pmatrix} M_pI_3 & -{}^0M\hat{S}_p \\ {}^0M\hat{S}_p & {}^0I_p \end{pmatrix} \tag{26}$$

${}^0I_p$: inertia tensor (3 * 3) of the platform expressed in the frame R_0, which is expressed by:

$${}^0I_p = {}^0A_p\,{}^pI_p\,{}^0A_p^T \tag{27}$$

${}^{p}I_{p}$: inertia tensor (3 * 3) of the platform expressed in the coordinate R_p and ${}^{0}A_{p}$ matrix orientation that expresses the frame R_p in the frame R_0.

$$ {}^{p}I_{p} = \begin{pmatrix} XX_p & XY_p & XZ_p \\ XY_p & YY_p & YZ_p \\ XZ_p & YZ_p & ZZ_p \end{pmatrix} \tag{28} $$

${}^{0}MS_{p}$: first moment of inertia of the platform around the origin of the frame R_p.

$$ {}^{p}MS_{p} = \begin{bmatrix} MX_p & MY_p & MZ_p \end{bmatrix}^{T} \tag{29} $$

$$ {}^{p}MS_{p} = {}^{0}A_{p}\,{}^{p}MS_{p} \tag{30} $$

I_3: Identity matrix (3*3) ; M_p: mass of the platform ; ${}^{0}g$: acceleration of gravity.

4.3. Relationship between $^{\circ}F_p$ and $^{\circ}f_i$:

The forces and moments applied on the origin of the platform by the reaction forces of kinematics chains are given by the following equation:

$$ {}^{0}F_{p} = \sum_{i=1}^{6} \begin{pmatrix} I_3 \\ {}^{0}\hat{L}_i \end{pmatrix} {}^{0}f_i \tag{31} $$

Equation (24) allows to write:

$$ {}^{0}F_{p} = \sum_{i=1}^{6} \left(\begin{pmatrix} I_3 \\ {}^{0}\hat{L}_i \end{pmatrix} \left(-{}^{0}J_{3i}^{-T}\mathrm{H}_i(q_i,\dot{q}_i,\ddot{q}_i) + {}^{0}J_{3i}^{-T}\Gamma_i \right) \right) \tag{32} $$

Let $\mathrm{H_{xi}}$ expressing the vector $\mathrm{H}_i(q_i,\dot{q}_i,\ddot{q}_i)$ in cartesian space to the point $\mathrm{P_i}$:

$$ \mathrm{H}_{xi} = {}^{0}J_{3i}^{-T}\mathrm{H}_i(q_i,\dot{q}_i,\ddot{q}_i) \tag{33} $$

With:

$$ {}^{0}J_{3i}{}^{-T}\Gamma_i = {}^{0}A_{3i}\,{}^{3i}J_{3i}\Gamma_i \tag{34} $$

$$ {}^{0}J_{3i}^{-T}\Gamma_i = {}^{0}A_{3i}\begin{vmatrix} 0 \\ 0 \\ \Gamma_{3i} \end{vmatrix} = {}^{0}a_{3i}\Gamma_{3i} \tag{35} $$

With: $ {}^{3i}J_{3i}^{-T} = \begin{bmatrix} 0 & 1/q_{3i}\sin(q_{2i}) & 0 \\ 1/q_{3i} & 0 & 0 \\ 0 & 0 & 1 \end{bmatrix} $

Equation (34) can be written:

$$ \sum_{i=1}^{6} \left(\begin{pmatrix} I_3 \\ {}^{0}\hat{L}_i \end{pmatrix} {}^{0}a_{3i}\Gamma_{3i} \right) = {}^{0}F_{p} + \sum_{i=1}^{6} \left(\begin{pmatrix} I_3 \\ {}^{0}\hat{L}_i \end{pmatrix} \mathrm{H}_{xi}(q_i,\dot{q}_i,\ddot{q}_i) \right) \tag{36} $$

Using the equation of the Jacobian inverse, we can deduce that:

$$ \sum_{i=1}^{6} \left(\begin{pmatrix} I_3 \\ {}^{0}\hat{L}_i \end{pmatrix} {}^{0}a_{3i}\Gamma_{3i} \right) = {}^{0}J_{p}^{-T}\Gamma \tag{37} $$

With:

$$ \Gamma = [\Gamma_{31} \ldots\ldots\ldots \Gamma_{36}] \tag{38} $$

Substituting equation (38) in equation (30), we obtain:

$$ \Gamma = {}^{0}J_{p}{}^{T}\left({}^{0}F_{p} + {}^{0}F_{chaine} \right) \tag{39} $$

With:

$$ F_{chaine} = \sum_{i=1}^{6} \left(\begin{pmatrix} I_3 \\ {}^{0}\hat{L}_i \end{pmatrix} \mathrm{H}_{xi}(q_i,\dot{q}_i,\ddot{q}_i) \right) \tag{40} $$

Equation (39) represents the inverse dynamics model of the robot without friction and inertia of the actuators. To complete this model, we introduce the friction and inertia of the actuators. The expression (39) becomes:

$$ \begin{aligned} \Gamma = \mathrm{diag}(\dot{q}_{\mathrm{a}})F_s + \mathrm{diag}(\mathrm{sign}(\dot{q}_{\mathrm{a}}))F_v + \\ \mathrm{diag}(\ddot{q}_{\mathrm{a}})M_{\mathrm{a}} + {}^{0}J_{p}^{T}F_{robot} \end{aligned} \tag{41} $$

Where:

diag(.) : represents a matrix (6 * 6) with the terms in parentheses on the diagonal non-zero and other zero;

$$ diag(\dot{q}_a) = \begin{bmatrix} \dot{q}_{31} & 0 & 0 & 0 & 0 & 0 \\ 0 & \dot{q}_{32} & 0 & 0 & 0 & 0 \\ 0 & 0 & \dot{q}_{33} & 0 & 0 & 0 \\ 0 & 0 & 0 & \dot{q}_{34} & 0 & 0 \\ 0 & 0 & 0 & 0 & \dot{q}_{35} & 0 \\ 0 & 0 & 0 & 0 & 0 & \dot{q}_{36} \end{bmatrix} \tag{42} $$

sign(.) : represents the sign function;

F_s : vector (6 * 1) composed of dry friction parameters of the actuators;

F_v :vector (6*1)composed of viscous friction parameters of the actuators.

H_i (q_i, $\dot{q}_i$, $\ddot{q}_i$) representing the inverse dynamics model of the chain i is calculated by Newton's - Euler method [8].

Equation (42) represents the inverse dynamics model. For the calculation, in addition to the calculation of Jacobian matrices, we must determine $\mathrm{H}_i(q_i,\dot{q}_i,\ddot{q}_i)$ which is simply the inverse dynamic model of the chain i expressed in cartesian space.

It summarizes the steps of calculating the inverse dynamics model as follows:

- Resolution of geometric and kinematics direct models ;
- Calculation of dynamic model of each kinematics chain : $\mathrm{H}_i\left(q_i, \dot{q}_i, \ddot{q}_i\right)$;
- Calculation of the Cartesian dynamic model of each kinematics chain : H_{xi} ;
- Calculation of forces and moments ${}^0\mathbb{F}_{\text{chaine}}$ that match all H_{xi} ;
- Determine the forces and / or moments required to move the platform, ${}^0\mathbb{F}_{\text{p}}$;
- Calculation of forces and / or desired moments: $\Gamma = {}^0J_p^T\,({}^0\mathbb{F}_{\text{p}} + {}^0\mathbb{F}_{\text{chaine}})$.

Physical interpretation

We note from equations (38) (39) and (40), the effect of kinematics chains on the platform is equivalent to a force equal to $-\mathrm{H}_{xi}\left(q_i, \dot{q}_i, \ddot{q}_i\right)$ at each point P_i. The corresponding total force is equal to $\sum \mathrm{H}_{xi}\left(q_i, \dot{q}_i, \ddot{q}_i\right)$.

The parallel robot we just studied can be represented by a single body with the same parameters as the inertial platform on which is applied to each point P_i a force $-H_{xi}$.

5. SIMULATION AND RESULTS

The overall pattern of the simulation (figure 4) reflects the summary of the method developed for the kinematics analysis. Indeed, the inverse jacobian matrix of the robot (equation 20) allows deducing the velocities of the segments (cylinders). By direct derivation of active joint variables (results of inverse geometrical Model) yields the same vector velocity $\dot{q}_{3i}$. The estimate of the error term is used to validate the results of the analytical method.

To this end, using a trajectory generator whose parameters reflect the position and orientation (rotations about the base z-axis φ, y-axis θ and x-axis Ψ) of the platform at any time *t* (desired situation). The numerical values of parameters used in the simulation reveal two important factors:

- General form and dimensions adopted for the structure of the robot. A conceptual study of a robot type Gough-Stewart CAD (Solid Works) at identified all the dimensional parameters and inertial i.e. mass, center of gravity, inertia, and dimensions.
- Singularities. The values given to the angles (φ, θ, Ψ) must lead to positions available (joint limits).

In order to validate simulation models proposed considering the following physical data:

a. Movement of the platform.

$t = 0 : 10$ sec.

Position and orientation of the origin of the frame R_p

$$P_{x0} = 10 * t \qquad \varphi = 0.07 * \mathrm{t}$$
$$P_{y0} = 0 \qquad \theta = 0.04 * \mathrm{t}$$
$$P_{z0} = 800 + 50 * t \qquad \psi = 0$$

b. Masses.

Platform M= 24.45 kg

Kinematics chains *m =[0.11818 ; 7.27885 ; 3.15325]*

c. Moments of the 2nd order of chains [kg.m^2].

K (:,:,1)=[18822.31 0 0 ; 0 11453.35 0 ; 0 0 11343.03]

K(:,:,2) =[95191796 2745801 31799761.94; 2745801 106222355.34 13430543; 31799761.94 13430543 34166734]

K(:,:,3)=[136247234.57 0 0 ; 0 136234387.21 0 ; 0 0 693106.67].

d. Moments of inertia of the platform around the origin of the coordinate R_p [kg.m^2].

Ixx =6246766024.15; *Iyy*=612114662.55; *Izz*=1222025614.27;

For a simple configuration chosen in advance, we can see the corresponding movement of the platform (Fig.6).

It is shown in Figures 7, 8, 9 and 10 the change of variables and joint velocities q_{3i}, $\dot{q}_{3i}$, and the different speeds of the platform *Vp*.

Figure 11 shown for the same physical data, the variation of active forces in joints obtained from the equations of Newton - Euler governing the dynamics of the platform.

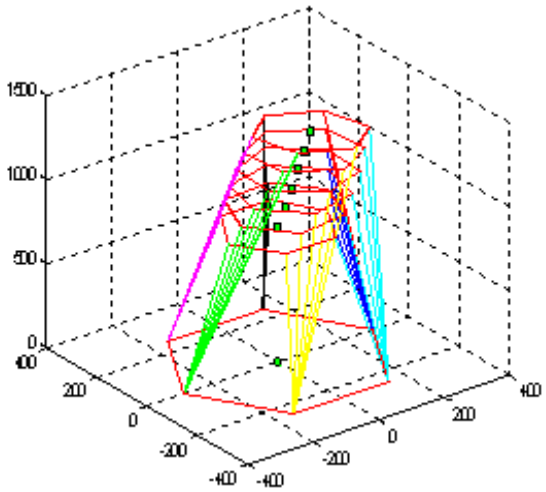

Fig.6: Matlab simulation of a space trajectory's robot.

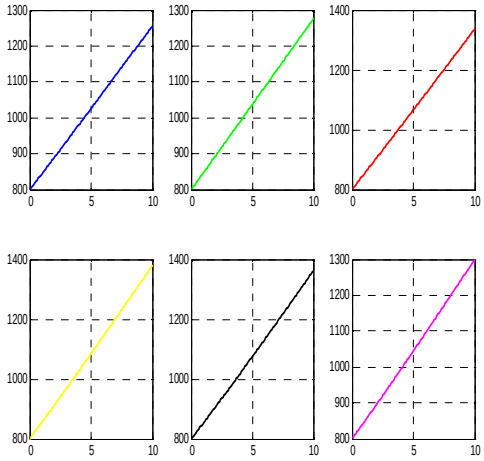

Fig. 7: Displacement of active joints q_{3i} [mm].

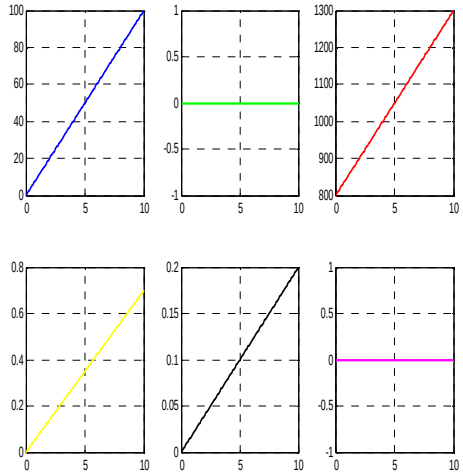

Fig.8: Displacement and orientation of the platform in [mm] and [rd].

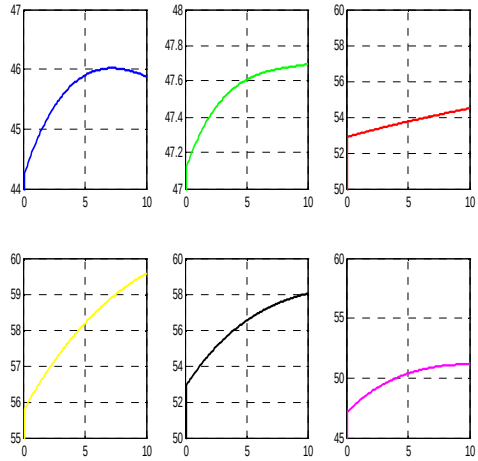

Fig. 9: Speed actuators " $\dot{q}_{3i}$ " [mm/sec.].

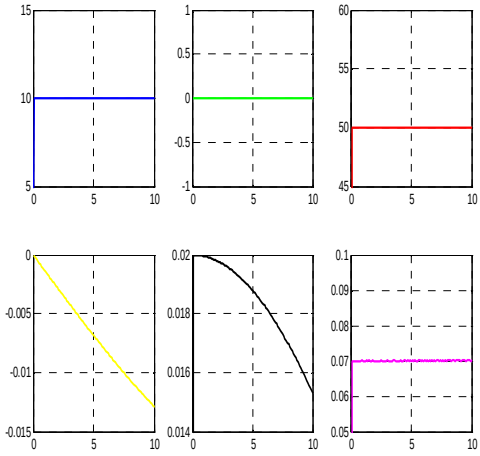

Fig. 10: Linear and angular velocities of the Platform" V_{0p}" [mm/sec.] and [rd/sec.].

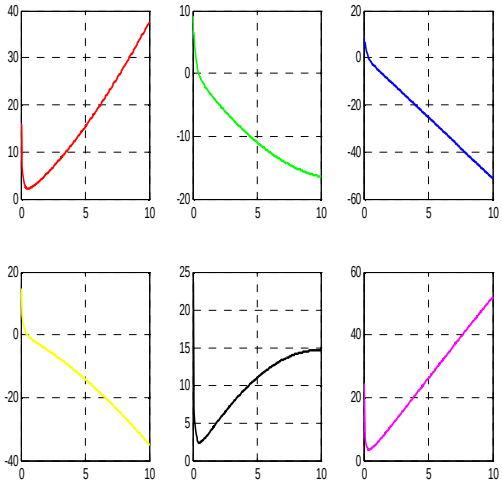

Fig. 11: Change Γ_{3i} forces at the actuators [N].

CONCLUSION:

In this paper, a dynamic model of the parallel robot with six degrees of freedom has been made. A description based on the decomposition of the robot into two parts: the mobile platform and chains (legs) attached to the base forming a tree structure, to permit application of the methods known and used for robot series, branching or closed loop.
Geometric modeling and kinematics of the robot was developed on the basis of previous work [7], [10] and [14]. The proposed models take into account the dynamics of the robot type Gough - Stewart. The calculation of these models is facilitated by being able to apply the techniques developed for serial robots. The value of modeling dynamic developed is that it allows to deduce directly a physical interpretation of the model. Indeed the one body equivalent to the robot has the same parameters as the inertial platform which is applied a force vector whose points of application are connections to the chains. There is therefore a compact algorithm capable of solving the dynamic a parallel robot in view of its adaptation to dynamic control laws.
It plans to use and extend this approach to what we call the hybrid structure [10], serial – parallel robots.

BIBLIOGRAPHY

[1] Wissama Khalil**,** "modélisation identification et commande des robots"
[2] Merlet .J-P.," parallel robots ", Kluwer Academic Publ., Dortdrech, the Neterland, 2000
[3] Ait Ahmed M., "Contribution à la modélisation géométrique et dynamique des robots parallèles", Thèse de doctorat, LAAS, Toulouse, 1993.
[4] Tsai L-W., "Solving the inverse dynamic of Gough – Stewart manipulator by the principle of virtual work" , J. of Mechanical design, Vol. 122, P. 3-9, mars 2000.
[5] Liu M. J.,Li C-X, Li C-N "dynamic analysis of the Gough – Stewart platform manipulator" ,IEEE Transaction on robotics and Automation, Vol. 16(1), P. 94-48, Février 2000.
[6] Borojéni D**.**," Modélisation cinématique et dynamique des système polyarticulés à chaînes ouvertes ou fermées". Cas des robots parallèles, Thèse de doctorat, Université Paris XII- Val de Marne, 2006.
[7] Guegan S**.**,"Contribution à la modélisation et identification dynamique des robots parallèles", Thèse de doctorat, ECN, Nantes, 2003.
[8] Gautier M**.**, " Contribution à la modélisation et à l'identification des robots", Thèse d'état, Université de Nantes, ENSM, Mai 1990.
[9] Khalil W., Kleinfinger J.-F**.**, »A new geometric notation for open and closed-loop robots», Proc.IEEE conf .on Robotics and Automation, San Fransisco, avril 1986, p1174-1180.
[10] Ourda Ibrahim, "Contribution à la modélisation dynamique des robots parallèles et des robots hybrides", Thèse de doctorat, année 2006
[11] Pierre Renaud, "Kinematic and dynamic identication of parallel mechanisms; Article, Control engeneering practice 14 (2006) 1099-1109
[12] Oscar Andrés V. A**.**, "Contribution à l'identification et à la commande des robots parallèles", Thèse de doctorat, Univ. Monpelier II, novembre 2004.
[13] Guegan S., Khalil W**.,** "Modélisation dynamique d'un robot parallèle à trois degrés de liberté : l'Orthoglide", Article année 2004, IRCCyN.
[14] Ibrahim O., Khalil W., Guegan S., "Dynamic modeling of some parallel robots", 35th International Symposium on robotics, Villepinte, France, 23-26 Mars, 2004.
[15] C. Mahfoudi , K. Djouani, M. Bouaziz and S. Rechak, "General method for dynamic modeling and control of an hexapod robot including optimal force distribution", J. WSEAS, Transaction on signal processing, Vol. 2, P. 323-330, 2006.
[16] C. Mahfoudi , K. Djouani, S. Rechak and M. Bouaziz, "Optimal force distribution for the legs of an hexapod robot", IEEE Conference on control Application CCA, Istanbul, Vol. 1, P. 65-670, 2003.
[17] Stefan Staicu, "Modèle matriciel en dynamique du robot parallèle Stewart - Gough", Rev. Roum., sci. Tech. -Méc. -Appli., Tome 54, No 3, Bucarest : 2009.

Optimal grasping force distribution for three robots holding a rigid object

A. Khadraoui [(a)] ***, C. Mahfoudi*** [(a)]***, A. Zaatri*** [(b)]***, K. Djouani*** [(c)]

[(a)] *University Larbi Ben M'Hidi , Institute of Mechanics, Ain Beida, Algeria*
omar.khadraoui@gmail.com
[(b)] *University Mentouri Constantine,Institute of Mechanics, ,Algeria*
azaatri@yahoo.com
[(c)] *LISSI Lab/University Paris 12, France*
djouani@univ-paris12.fr

Abstract

In this paper we present a methodology for optimal force distribution calculation for the multiple manipulators system grasping an object.We consider for this case three robots holding a common rigid object with three contact points , where the object can translate and rotate in any directions. This approach is used in the case of real time dynamics object force control. The force distribution problem is formulated in terms of a nonlinear programming problem under equality and inequality constraints. Then, according to [1],[2],[3] and [4] the friction constraints are transformed from non linear inequalities into a combination of linear equalities and linear inequalities. The original non linear constrained programming problem is then transformed into a quadratic optimization problem. Some simulation results are given to show the efficiency and accuracy of the proposed methodology and perspectives on multiple manipulators system grasping an object control are discussed.
Keywords : Multiple Manipulators System, Grasping, Optimal Force Distribution, Quadratic Programming, Friction Constraints.

1 Introduction

Cooperative system is generally understood as several coordinated robots simultaneously performing a given task. The main objective of a multi-robots cooperative system in robotics is to manipulate an object. Manipulation is performed with the aim of, for example , changing the space position of an object,grasping an object in contact with environment , gripping,lifting, lowering, releasing, withdrawing...

The object force control need calculation of real-time force distribution on the robot's efectors. Due to the existence of more than three actuated joints in each robot , the manipulators system has redundant actuation leading to more active joints than the object degree-of-freedom (6 dof). Thus, when formulating the force distribution problem, we find fewer force moment balancing equations than unknown variables. So, the solution of these equations is not unique. Moreover, some physical constraints, that concern the contact nature, friction, ...etc , must be taken into account in the calculation of force distribution. In addition, joints torque saturation must also be considered. Several approaches in the literature have been proposed to address robot coordination problem in [5],[6] Contact and friction constraints for grasp conditions are considered and a optimization algorithm is developed by minimizing the total energy E consumed by the actuators of the planar dual-arm manipulators system.A new approach for computing force-closure grasps of two-dimensional and three-dimensional objects was proposed in [7]-[8]and [9] then a new necessary and sufficient condition for n-finger grasps to achieve force-closure property are developed.in [10] The analysis of grasping and manipulation of deformable objects by a three finger robot hand has been carried out.Thus the Force Distribution Problem (FDP) can be formulated as a nonlinear constrained programming problem under nonlinear equality and inequality constraints.

- Linear-Programming (LP) Method [3],[11]
- Compact-Dual LP (CDLP) Method [12],[13]
- Quadratic Programming (QP) Method [14], [15]
- Analytical Method [16],[17],[18],[19]

A comparative study for the cited methods can be found in [20]. Some researchers proposed the optimal force distribution scheme of multiple cooperating robots by combining the Dual Method with the

QP [21]. In FDP solving, according to some criteria, physical aspects of the multiple cooperating robots have to be considered. In this paper we propose an approach to solve the problem of real-time force distribution for a multiple manipulators system, based on the approach proposed in [22],[23] for an hexapod robot.

This approach consists of the combination of the QP Method with the reduction technique of problem size. The main idea concerns the transformation of the original nonlinear constrained problem into a linear one, by reducing the problem size and transforming the nonlinear constraints into a linear ones, respecting some physical considerations.

The rest of the paper is organized as follows. The direct and inverse geometrical models of the robot manipulator are presented in section 2. Section 3 concerns the force distribution problem. Problem reduction and optimal solution are presented in section 4. Before presenting some remarks and perspectives, a Matlab simulation results of two cooperating manipulators is presented in section 5 to show the efficiency of this approach.

2 Geometrical Modelling

Before presenting the direct and inverse geometrical models, let us consider the robot architecture. As all the robot are identical, only one robot modelling is considred, the robot j architecture is given in figure (2). Every robot "j" j=1,...,n is grasping the object, located at a_j distance from the center of gravity of the object. The angle ϕ_j represents the orientation of the coordinate frame $(x_{1,j}, y_{1,j}, z_{1,j})$ fixed at the first articulation of the robot and the world ground coordinate frame (X, Y, Z). Multiple Manipulators System is considerated as an arborescent robot comporting some closed loops. So to study this kind of robots we use the method defined by Khalil and Kleinfinger [24].

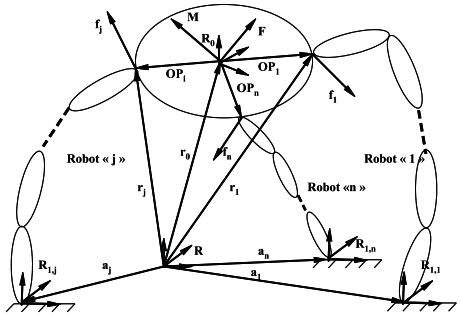

Figure 1: **Geometrical parameters of multiple manipulators system**

The transformation matrix from ith joint's attached coordinate frame to the (i-1)th joint's attached coordinate frame is given by figure (3):

$$^{i-1}\boldsymbol{T}_i = R(Z,\gamma)T(Z,b)R(X,\alpha)T(X,d)R(Z,\theta)T(Z,r) \quad (1)$$

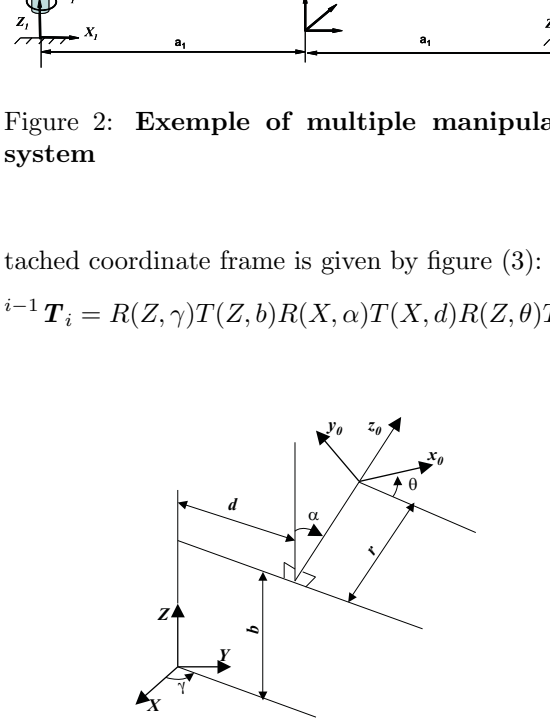

Figure 2: **Exemple of multiple manipulators system**

Figure 3: **geometrical model**

The table (1) describes the transformation from the world ground coordinate frame (X, Y, Z) to the coordinate frame at the contact point "6" of each robot.

frame	α	d	θ	r	b	γ
object	α	d	θ	r	h	β
Joint"1"	0	OP_1	$\theta_{1,1}$	0	0	0
Joint"j"	0	OP_j	$\theta_{1,j}$	0	0	0
Joint"n"	0	OP_n	$\theta_{1,n}$	0	0	0

Table 1: **Geometrical parameters of the object**

The transformation providing the exact position of the contact point"6" of any robot in the absolute coordinate frame fixed at the ground is given by :

$$^{R}\boldsymbol{T}_6 = ^{R}\ \boldsymbol{T}_0^0\boldsymbol{T}_1^1\boldsymbol{T}_2^2\boldsymbol{T}_3^3\boldsymbol{T}_4^4\boldsymbol{T}_5^5\boldsymbol{T}_6 \quad (2)$$

When the position and the orientation of the last coordinate frame fixed to the end of each robot"j" are known ,We apply the method proposed by Paul [25]. It provides the values of the joints coordinates $\theta_{i,j}\,(i = 1, 2, 3, 4, 5, 6)\,(j = 1, .., n)$ as follow:

frame	α	d	θ	r	b	γ
Joint"1"	0	a_j	θ_1	0	0	ϕ_j
Joint"2"	0	0	$\theta_2 + \pi/2$	0	0	0
Joint"3"	$\pi/2$	0	0	r_3	0	0
Joint"4"	0	0	θ_4	r_4	0	0
Joint"5"	$-\pi/2$	0	θ_5	0	0	0
Joint"6"	$\pi/2$	0	θ_6	0	0	0

Table 2: **Geometrical parameters of the jth robot**

$$\begin{cases} \theta_{1,j} = \arctan(Py/(-Px + d_1)) \\ \theta_{2,j} = \arctan(Pz - r_1)/(C1(Px - d_1) + S1Py)) \\ r_{3,j} = C2(C1(Px - d_1) + S1Py) + S2(Pz - r_1) - \\ \quad -R4 - l_2 \\ \theta_{4,j} = \arctan((S1ax - C1ay)/(S2(C1ax + S1ay) - \\ \quad -C2az)) \\ \theta_{5,j} = \arctan((C4S2(C1ax - S1ay) - C4C2az \\ \quad +S4(C1ay - C1sy))/(C2(C1ax + S1ay) + \\ \quad +S2az)) \\ \theta_{6,j} = \arctan((-S4(-S2(C1ax - S1ay) + C2sz + \\ \quad C4S1sx - C1sy))/(C5(-C4S2C1sx - S2S1sy + \\ \quad +C2sz) + S4(S1sx - C1sy) - S5(C1C2sx + \\ \quad +S1C2sy + S2sz)) \end{cases} \tag{3}$$

Remark : S*=sin(*); C*=cos(*); ($Px = P_{x,j}, Py = P_{y,j}, Pz = P_{z,j}$), are the coordinates of the point "6" of the jth robot expressed in (X, Y, Z).

3 Force Distribution Problem

3.1 problem Formulation

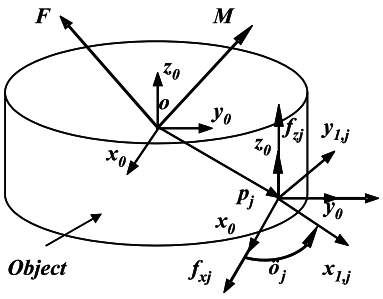

Figure 4: Orientation of coordinate frame

The force system acting on the object is shown in figure (4). For simplicity, only the force components on the contact point are presented here. In the general case, rotational torques at the contact are neglected. Let (x_0, y_0, z_0) be the coordinate frame in which the object is located and $(x_{6,j}, y_{6,j}, z_{6,j})$ denote the coordinate frame fixed at the contact point of the jth robot. The $(x_{6,j}, z_{6,j})$ plane which is assumed to be parallel to the (x_0, y_0, z_0) plane and its z axis is normal to the surface of the object. $\boldsymbol{F} = [F_X F_Y F_Z]^T$ and $\boldsymbol{M} = [M_X M_Y M_Z]^T$ denote respectively the object force vector and moment vector, which results from the gravity and the external force acting on the object [26],[27],[28] and [29]. Define $f_{x,j}, f_{y,j}$, and $f_{z,j}$ as the components of the force acting on the supporting robot "j" in the directions of x_0, y_0 *and* z_0, respectively. The number of supporting robot, n, can vary between 2 and 3 for this studies. The object's quasi-static force/moment equation can be written as

$$\begin{cases} \sum_{j=1}^{n} \boldsymbol{f}_j = \boldsymbol{F} \\ \sum_{j=1}^{n} \boldsymbol{OP}_j \wedge \boldsymbol{f}_j = \boldsymbol{M} \end{cases} \tag{4}$$

where $\boldsymbol{OP}_j$ is the position vector joining contact point of the robot "j" and the gravity center of the object. The general matrix form of this equation can be written as :

$$\boldsymbol{A}\,\boldsymbol{G} = \boldsymbol{W} \tag{5}$$

with:

$$\begin{cases} \boldsymbol{G} = [\boldsymbol{f}_1^T\, \boldsymbol{f}_2^T\, \cdots\, \boldsymbol{f}_n^T]^T & \in \Re^{3n} \\ \boldsymbol{f}_j^T = [f_{x,j}\, f_{y,j}\, f_{z,j}]^T & \in \Re^3 \\ \boldsymbol{W} = [\boldsymbol{F}^T\, \boldsymbol{M}^T]^T & \in \Re^6 \end{cases}$$

$$\boldsymbol{A} = \begin{pmatrix} \boldsymbol{I}_3 & \cdots & \cdots & \boldsymbol{I}_3 \\ \boldsymbol{B}_1 & \cdots & \cdots & \boldsymbol{B}_n \end{pmatrix} \quad \in \Re^{6\times 3n}$$

$$\boldsymbol{B}_j \equiv \widehat{\boldsymbol{OP}}_j \equiv \begin{pmatrix} 0 & -P_{z,j} & P_{y,j} \\ P_{z,j} & 0 & -P_{x,j} \\ -P_{y,j} & P_{x,j} & 0 \end{pmatrix} \quad \in \Re^{3\times 3}$$

where $\boldsymbol{I}_3$ is the identity matrix and $\mathbf{G}$ is the robots force vector, corresponding to three ($\boldsymbol{G} \quad \in \Re^9$) . $\boldsymbol{A}$ is a coefficient matrix which is a function of the positions of the robot supporting, and $\boldsymbol{B}_j$ is a skew symmetric matrix consisting of $(P_{x,j}, P_{y,j}, P_{z,j})$, which is the position coordinate of

contact point of the supporting robot "j" in (x_0, y_0, z_0). $\boldsymbol{W}$ is a total body force/moment vector. It is clear that (5) is an underdetermined system and its solution is not unique. In other words, the robots forces have many solutions according to the equilibrium equation. however, the robot forces must meet the needs for the following physical constraints,

otherwise they become invalid :

[3]Supported object should not slip when the robots move. It results in the following constraint:

$$\sqrt{f_{x,j}^2 + f_{y,j}^2} \le \mu\, f_{z,j} \tag{6}$$

where μ is the static coefficient of friction of the surface of the object Since the robots forces are generated from the corresponding actuators of joints, the physical limits of the joint torques must be taken into account. It follows that :

$$-\tau_{jmax} \le \boldsymbol{J}_j^{T\,j} \boldsymbol{A}_{0j} \begin{pmatrix} f_{x,j} \\ f_{y,j} \\ f_{z,j} \end{pmatrix} \le \tau_{jmax} \tag{7}$$

for $(j = 1, ..., n)$, where $\boldsymbol{J}_j \in \Re^{3\times 6}$ is the Jacobian of the robot "j", $\tau_{jmax} \in \Re^{6\times 1}$ is the maximum joint torque vector of the robot "j", and $\boldsymbol{A}_{0j} \in \Re^{3\times 3}$ is the orientation matrix of $(x_{6,j}, y_{6,j}, z_{6,j})$ with respect to (x_0, y_0, z_0). In order to have definite contact with the object, there must exist a $f_{z,j}$ such that :

$$f_{z,j} \geq 0 \tag{8}$$

In the following, we propose an approach for problem size reduction, linearisation and solving for the three manipulators case. Clearly, it is difficult to solve such a nonlinear programming problem for real-time multi-robots force distribution with complex constraints.

3.2 Problem Size Reduction

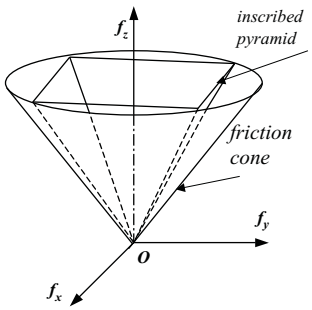

Figure 5: conservative inscribed pyramid

The equation (6) is a formulation of the friction cone figure(5). In order to overcome the non linearities induced by the following equations, most researches substitute this friction cone by the inscribed pyramid [11],[30],[14],Thus, the nonlinear friction constraints are approximately expressed by the following linear inequalities :

$$f_{x,j} \geq \acute{\mu}\, f_{z,j}, \quad f_{y,j} \geq \acute{\mu}\, f_{z,j}, \quad j = 1, ..., n \tag{9}$$

where $\acute{\mu} = \frac{\sqrt{2}\mu}{2}$ is for the inscribed pyramid. Thus, the initial non linear constrained programming problem, substituting the non linear constraint Eq(6) by the linear one of Eq(9), becomes a linear programming problem [11],[12]and [14]. The possibility of slipping can be minimized, by optimizing the ratio of tangential to normal forces at the robot. In [31], the authors have shown that, for multi-robots, all ratios (at the contacts points) are equal to the global ratio. This leads Liu and Wen [17] to find the relationship between the robot forces and transform the initial friction constraints from the nonlinear inequalities into a set of linear equalities. Let us define the global ratio by the ratio of the tangential to normal forces at the object. The advantage of the existing methodes lies in the fact that part of component of the robots forces satisfy the global ratio relation ship and lets the other components satisfy the linear inequality constraints as Eq (9). For example, defining $f_{x,j} \quad (j = 1;;n)$ and $f_{y,j} \quad (j = 1;;n)$, for a robot j Chen et al [1], show that :

$$f_{x,j} = k_{xz} f_{z,j} \quad , (i = 1, ..., n) \tag{10}$$

$$f_{y,j} \leq \mu^{\star} f_{z,j} \quad , (i = 1, ..., n) \tag{11}$$

where $k_{xz} = \frac{F_X}{F_Z}$ is the global ratio of forces at the object in direction of x_0 and z_0. $\mu^{\star}$ is the given coefficient for friction constraints. According to Eq(6), we have $\mu^{\star} = \sqrt{\mu^2 - k_{xz}^2}$. Finally, the force distribution problem is transformed into a linear one by replacing Eq (6) with Eqs (10) and (11).

3.3 Problem transformation and Continuous solution

In modelling this systems, we consider that three robots support the object at a time. so $\boldsymbol{G}$ and $\boldsymbol{A}$ become a vector of 9×1 and a matrix of 6×9, respectively. Equation (5) contains nine unknown variables with six equations. By adding the Eq (10) to the Eq (5) we obtain nine equations.

$$\overline{\boldsymbol{A}}\, \boldsymbol{G} = \overline{\boldsymbol{W}} \tag{12}$$

with :

$$\overline{\boldsymbol{A}} = \begin{pmatrix} \boldsymbol{I}_3 & & & \boldsymbol{I}_3 & & & \boldsymbol{I}_3 & & \\ \boldsymbol{B}_1 & & & \boldsymbol{B}_2 & & & \boldsymbol{B}_3 & & \\ 1 & 0 & -k_{xz} & 0 & 0 & 0 & 0 & 0 & 0 \\ 0 & 0 & 0 & 1 & 0 & -k_{xz} & 0 & 0 & 0 \\ 0 & 0 & 0 & 0 & 0 & 0 & 1 & 0 & -k_{xz} \end{pmatrix}$$

$$\boldsymbol{G} = \begin{pmatrix} \boldsymbol{f}_1 \\ \boldsymbol{f}_2 \\ \boldsymbol{f}_3 \end{pmatrix} \qquad \overline{\boldsymbol{W}} = \begin{pmatrix} \boldsymbol{F} \\ \boldsymbol{M} \\ 0 \\ 0 \\ 0 \end{pmatrix}$$

Using some rows combination of the matrix $\overline{\boldsymbol{A}}$, Eq (12) can be written as :

$$\widehat{\boldsymbol{A}}\, \boldsymbol{G} = \widehat{\boldsymbol{W}} \tag{13}$$

With: $\widehat{\boldsymbol{A}} =$

$$\begin{pmatrix} 1 & 0 & 0 & 1 & 0 & 0 \\ 0 & 1 & 0 & 0 & 1 & 0 \\ 1 & 0 & -k_{xz} & 0 & 0 & 0 \\ 0 & 0 & 0 & 1 & 0 & -k_{xz} \\ -P_{y,1} & P_{x,1} & 0 & -P_{y,2} & P_{x,2} & 0 \\ P_{z,1} & 0 & -P_{x,1} & P_{z,2} & 0 & -P_{x,2} \\ 0 & 0 & 0 & 0 & 0 & 0 \\ 0 & -P_{z,1} & P_{y,1} & 0 & -P_{z,2} & P_{y,2} \end{pmatrix}$$

$$\begin{pmatrix} 1 & 0 & 0 \\ 0 & 1 & 0 \\ 0 & 0 & 0 \\ 0 & 0 & 0 \\ 1 & 0 & -k_{xz} \\ -P_{y,3} & P_{x,3} & 0 \\ P_{z,3} & 0 & -P_{x,3} \\ 0 & -P_{z,3} & P_{y,3} \end{pmatrix} \quad \widehat{\boldsymbol{W}} = \begin{pmatrix} F_X \\ F_Y \\ 0 \\ 0 \\ M_Z \\ M_Y \\ 0 \\ M_X \end{pmatrix}$$

where $\widehat{\boldsymbol{A}} \in \Re^{8\times 9}$ is the resulting matrix of $\overline{\boldsymbol{A}}$ after combination. $\boldsymbol{G} \in \Re^8$ is the robots force vector. $\widehat{\boldsymbol{W}} \in \Re^8$ is the resulting vector of $\boldsymbol{W}$ after combination. Thus, the force distribution problem is subjected to the inequality constraints expressed by (7), (8) (11).

4 Quadratic Problem Formulation and Solution

The solution to the inverse dynamic equations of this system is not unique, but it can be chosen in an optimal manner by minimizing some objective function. The approach taken here is to minimize the sum of the weighted torque of the robot, which results in the following objective function [15] and [21]:

$$f_{\boldsymbol{G}} = \boldsymbol{p}^T \boldsymbol{G} + \frac{\boldsymbol{G}^T \boldsymbol{Q} \boldsymbol{G}}{2} \tag{14}$$

with:

$$\boldsymbol{p}^T = [\widehat{\tau}_1^T \boldsymbol{J}_1^T \ldots\ldots, \widehat{\tau}_n^T \boldsymbol{J}_n^T] \quad \in \Re^{3n}$$

$$\boldsymbol{Q} = \begin{pmatrix} \boldsymbol{J}_1 \boldsymbol{q}_1 \boldsymbol{J}_1^T & \ldots & 0 \\ \vdots & \ddots & \vdots \\ 0 & \ldots & \boldsymbol{J}_n \boldsymbol{q}_n \boldsymbol{J}_n^T \end{pmatrix} \quad \in \Re^{3n\times 3n}$$

where $\widehat{\tau}_j$ is the joint torque vector due to the weight and inertia of the robot "j", $\mathbf{J}_j$ is the Jacobian of the robot "j", and $\mathbf{q}_j$ is a positive definite diagonal weighting matrix of the robot j. This objective function is strictly convex. Because the time for obtaining a solution does not depend on an initial guess, a quadratic programming is superior to linear programming in both speed and quality of the obtained solution [15]. The general linear-quadratic programming problem of the force distribution on robot is stated by :

$$\boldsymbol{p}^T \boldsymbol{G} + \frac{\boldsymbol{G}^T \boldsymbol{Q} \boldsymbol{G}}{2} \tag{15}$$

$$\widehat{\boldsymbol{A}}\,\widehat{\boldsymbol{G}} = \widehat{\boldsymbol{W}} \tag{16}$$

$$\boldsymbol{B}\widehat{\boldsymbol{G}} \leq \boldsymbol{C} \tag{17}$$

where $\mathtt{G} \in \Re^9$ is a vector of the design variables. It should be pointed out that, Eq. (19) denotes Eq (13), and Eq(20) is the resulting inequality constraints for the combination of Eq (7), Eq (8) and (11) where

$$\boldsymbol{B} = [\boldsymbol{B}_1^T\ \boldsymbol{B}_2^T\ \boldsymbol{B}_3^T\ \boldsymbol{B}_4^T]^T \quad \in \Re^{9\times 24}$$
$$\boldsymbol{C} = [\tau_{1max} .. \tau_{6max}\ -\tau_{1max} .. -\tau_{6max}\ \boldsymbol{0\,0\,0\,0\,0\,0}]^T \quad \in \Re^{24}$$

with

$$B_1 = \begin{bmatrix} \boldsymbol{J}_1^T \boldsymbol{R}_1 & 0 & 0 \\ 0 & \boldsymbol{J}_2^T \boldsymbol{R}_2 & 0 \\ 0 & 0 & \boldsymbol{J}_3^T \boldsymbol{R}_3 \end{bmatrix} \quad \in \Re^{9\times 9}$$

$$\boldsymbol{B}_2 = \begin{bmatrix} -\boldsymbol{J}_1^T \boldsymbol{R}_1 & 0 & 0 \\ 0 & -\boldsymbol{J}_2^T \boldsymbol{R}_2 & 0 \\ 0 & 0 & -\boldsymbol{J}_3^T \boldsymbol{R}_3 \end{bmatrix}$$

$$B_3 = \begin{bmatrix} 0 & 0 & -1 & 0 & 0 & 0 & 0 & 0 & 0 \\ 0 & 0 & 0 & 0 & 0 & -1 & 0 & 0 & 0 \\ 0 & 0 & 0 & 0 & 0 & 0 & 0 & 0 & -1 \end{bmatrix}$$

$$B_4 = \begin{bmatrix} 0 & 1 & -\mu^\star & 0 & 0 & 0 & 0 & 0 & 0 \\ 0 & 0 & 0 & 0 & 1 & -\mu^\star & 0 & 0 & 0 \\ 0 & 0 & 0 & 0 & 0 & 0 & 0 & 1 & -\mu^\star \end{bmatrix}$$

In Eq (19), we have eight linear independent equations with nine unknown variables. By using Gauss algorithm, this equation is transformed as follow :

$$[\boldsymbol{I}_8 \quad \widehat{\boldsymbol{A}}_r] \begin{bmatrix} \widehat{\boldsymbol{G}}_b \\ \widehat{\boldsymbol{G}}_r \end{bmatrix} = \widehat{\boldsymbol{W}}_r, \tag{18}$$

where $\boldsymbol{I}_8 \in \Re^{8\times 8}$ identity matrix, $\widehat{\boldsymbol{A}}_r \in \Re^8$ is the remaining column of the matrix $\widehat{\boldsymbol{A}}$ after transformation. $\widehat{\mathbf{G}}_b \in \Re^8$ is the partial vector of $\boldsymbol{G}$. $\widehat{\boldsymbol{G}}_r \in \Re$ is the unknown element of $\widehat{\boldsymbol{G}}$ which denotes the design variable. $\widehat{\boldsymbol{W}}_r \in \Re^8$ is the resulting vector of $\widehat{\boldsymbol{W}}$ after transformation. Equation(21) may be rewritten by the following form

$$\boldsymbol{I}_8 \widehat{\boldsymbol{G}}_b + \widehat{\boldsymbol{A}}_r \widehat{\boldsymbol{G}}_r - \widehat{\boldsymbol{W}}_r = 0, \tag{19}$$

Which yields to

$$\widehat{\boldsymbol{G}}_b = \widehat{\boldsymbol{W}}_r - \widehat{\boldsymbol{A}}_r \widehat{\boldsymbol{G}}_r. \tag{20}$$

Finally, it results in

$$\boldsymbol{G} = \begin{bmatrix} \widehat{\boldsymbol{G}}_b \\ \widehat{\boldsymbol{G}}_r \end{bmatrix} = \begin{bmatrix} \widehat{\boldsymbol{W}}_r \\ 0 \end{bmatrix} + \begin{bmatrix} -\widehat{\boldsymbol{A}}_r \\ 1 \end{bmatrix} \widehat{\boldsymbol{G}}_r. \tag{21}$$

Now let $\widehat{\boldsymbol{G}}_0 = [\widehat{\boldsymbol{W}}_r^T \quad 0]^T \in \Re^8$ *and* $N = [-\widehat{\boldsymbol{A}}_r^T \quad 1]^T \in \Re^9$, then Eq (24) becomes

$$\boldsymbol{G} = \widehat{\boldsymbol{G}}_0 + \boldsymbol{N}\widehat{\boldsymbol{G}}_r. \tag{22}$$

Substituting Eq (22) into Eqs (15) and (17), the linear quadratic programming problem can be expressed by :

$$minimize \quad f(\widehat{\boldsymbol{G}}_r), \tag{23}$$

$$subject\,to \quad \boldsymbol{B}\boldsymbol{N}\widehat{\boldsymbol{G}}_r \leq \boldsymbol{C} - \boldsymbol{B}\widehat{\boldsymbol{G}}_0. \tag{24}$$

where

$$f(\widehat{\boldsymbol{G}}_r) = \boldsymbol{p}^T \widehat{\boldsymbol{G}}_0 + \tfrac{1}{2}\widehat{\boldsymbol{G}}_0^T Q \widehat{\boldsymbol{G}}_0 + \boldsymbol{p}^T \boldsymbol{N}\widehat{\boldsymbol{G}}_r + \tfrac{1}{2}\widehat{\boldsymbol{G}}_0^T \boldsymbol{Q}\boldsymbol{N}\widehat{\boldsymbol{G}}_r + \tfrac{1}{2}\widehat{\boldsymbol{G}}_r^T \boldsymbol{N}^T \boldsymbol{Q}\widehat{\boldsymbol{G}}_0 + \tfrac{1}{2}\widehat{\boldsymbol{G}}_r^T \boldsymbol{N}^T \boldsymbol{Q}\boldsymbol{N}\widehat{\boldsymbol{G}}_r$$

Since $\widehat{\boldsymbol{G}}_r$ is a single variable denoted by x, the optimal force distribution can be written as :

$$minimize \quad a_0x^2+a_1x+a_2 \qquad subject\,to \quad x \in [b_1\, b_2] \tag{25}$$

With

$$a_0 = \tfrac{1}{2}\boldsymbol{N}^T\boldsymbol{Q}\boldsymbol{N}$$
$$a_1 = \boldsymbol{p}^T\boldsymbol{N} + \tfrac{1}{2}\widehat{\boldsymbol{G}}_0^T\boldsymbol{Q}\boldsymbol{N} + \tfrac{1}{2}\boldsymbol{N}^T\boldsymbol{Q}\widehat{\boldsymbol{G}}_0$$
$$a_2 = \boldsymbol{p}^T\widehat{\boldsymbol{G}}_0 + \tfrac{1}{2}\widehat{\boldsymbol{G}}_0^T\boldsymbol{Q}\widehat{\boldsymbol{G}}_0$$

Where $[b_1\, b_2]$ denotes the bound resulted from Eq(24). Since it is clear that $a_0 \geq 0$ because of the positive-definite matrix Q, There must be an optimal solution for the force distribution problem.

5 Simulations

The basic mechanism, size and parameters of the object and one robot are shown in Figure (1) and (2), where a = 0.25 [m], b = 0.61 [m], $l_1 = 0.05$ [m], $l_2 = 0.20$ [m], $l_3 = 0.30$ [m] and $l_4 \simeq 0$ [m]. There are six actuated joints $\theta_{1,j}$, $\theta_{2,j}$, ...*and* $\theta_{6,j}$ in the robot "j", whose torques are denoted as $\tau_{1,j}\, \tau_{2,j}$ ...*and* $\tau_{6,j}$, for (j=1,2,3), respectively. The Jacobian of the robot "j" can be expressed by.

$$\boldsymbol{J}_j^T = [\boldsymbol{J}_{j,1} \quad \boldsymbol{J}_{j,2} \quad \boldsymbol{J}_{j,3}] \tag{26}$$

for (j=1,2,3), where

$$\boldsymbol{J}_{j,1} = \begin{bmatrix} -S(\theta_{1,j})C(\theta_{2,j})(R4+l_2+r3) \\ -C(\theta_{1,j})S(\theta_{2,j})(R4+l_2+r3) \\ C(\theta_{1,j})C(\theta_{2,j}) \\ 0 \\ 0 \\ 0 \end{bmatrix}$$

$$\boldsymbol{J}_{j,2} = \begin{bmatrix} C(\theta_{1,j})C(\theta_{2,j})(R4+l_2+r3) \\ -S(\theta_{1,j})S(\theta_{2,j})(R4+l_2+r3) \\ S(\theta_{1,j})C(\theta_{2,j}) \\ 0 \\ 0 \\ 0 \end{bmatrix}$$

$$\boldsymbol{J}_{j,3} = \begin{bmatrix} 0 \\ -C(\theta_{2,j})(R4+l_2+r3) \\ S(\theta_{2,j}) \\ 0 \\ 0 \\ 0 \end{bmatrix}$$

From Figure (4) the orientation matrix of $(x_{6,j}, y_{6,j}, z_{6,j})$ with respect to the frame (x_0, y_0, z_0) can be obtained by,

$$\boldsymbol{A}_{0j} = \begin{pmatrix} Cos\,\phi_{1,j} & Sin\,\phi_j & 0 \\ -Sin\,\phi_j & Cos\,\phi_j & 0 \\ 0 & 0 & 1 \end{pmatrix} \tag{27}$$

5.1 Simulation results

In order to show the effectiveness of proposed approach,we consider three identical 6-DOF manipulators grasping a rigid object ,the base of each robot is located at a distance of a_1 see figure(6),We denote $X_i \in \Re^6$ where : $X_i = [P_{xi}, P_{yi}, P_{zi}, \theta_i, \phi_i, \psi_i]^T$ represents the vector Cartesian position and orientation of the end-effector of robot i . Furthermore the load vector coordinates (force tensor) at the object is $F = [-5, 10, -250, 3, 1, 2]^T$, $\mu = 0.05$ the static coefficient of friction
some simulations were conducted under Matlab. We consider that the object rotate on the axis and simultaneous deplaced on Z_0.

For the objective function Eq (14), the weighting matrix are choosen as follow : $\boldsymbol{p} = \boldsymbol{0}$ and $\boldsymbol{Q} = \boldsymbol{I}$ (the identity matrix).
The figure 6 shows the trajectory of the object in the X-Y-Z suported with the three robots. The associated joints coordinates are obtained by using the direct and inverse geometric model (Eq (2)and Eq (3)). In the figures 7-9, the force distribution of the object are given. We can show that, this distribution validate the following force equilbrium equation :

$$\Sigma fx_j = Fx, \quad ,\Sigma fy_j = Fy, \quad \Sigma fz_j = Fz$$

Elsewhere, the z-force components fz_j are never negative, respecting the contact constraint. We can also show that the constraint Eq (6) are always satisfiyed as shown in figure 10 for the robot(j) ,j=1,2,3 where the curve $fx_j^2 + fy_j^2$ is always under the curve $\mu^2 fz_j^2$

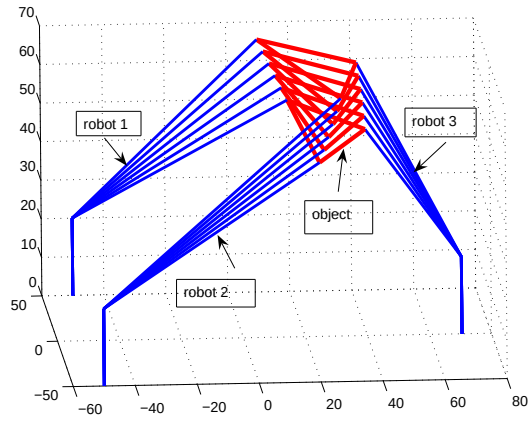

Figure 6: **View of the object suported by three robots**

Figure 7: **Forces on the first robot**

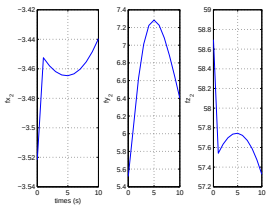

Figure 8: **Forces on the second robot**

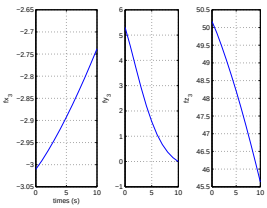

Figure 9: **Forces on the third robot**

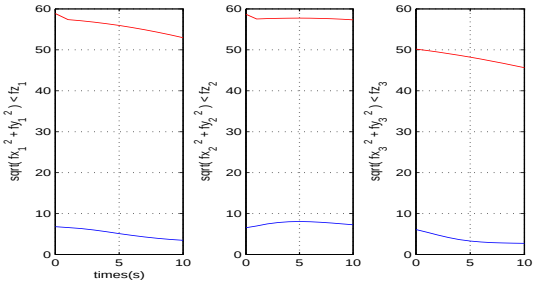

Figure 10: Constraint $fx_j^2 + fy_j^2 \leq \mu^2 fz_j^2$ satisfaction

6 Conclusion

In this paper, the authors have presented the force distribution problem in the case of multiple manipulators system. First, the robot inverse and direct geometric models where presented. Then, the real time force distribution problem where formulated in terms of non linear programming problem. After problem size reduction and transformation, the initial problem is solved in terms of quadratic programming problem. Simulations results where presented. Actually, we are working on the generalisation of this approach at $n > 3$ robots case. Finaly, a new learning approach is under developpment for real-time operationnal space control of the system.

References

[1] S.Ito Y. Mizukoshi and K.Ishihara. The optimal object posture that minimizes contact forces in grasping. *" Journal of the Franklin Institute*, 346:969–979, 2009.

[2] Y.ZHENG and W.H.QIAN. Limiting and minimizing the contact forces in multifingered grasping. *" Mechanism and machine theory*, 41:1243–1257, 2006.

[3] D. E. Orin and S. Y. Oh. Control of force distribution in robotic mechanisms containing closed kinematic chains. *" Trans. of the ASME, J. of Dynamic Systems, Measurement, and Control*, 102:134–141, 1981.

[4] L.Hongyi and w.Bangchun. Force distribution for the legs of a quadruped walking vehicle. *Journal of robotic systems*, (1996).

[5] Jin-Fan Liu Karim Abdel-Malek1. Robust control of planar dual-arm cooperative manipulators. *Robotics and Computer-Integrated Manufacturing.*, pages 109–120, (2000).

[6] Jorge Gudino and Marco A. Arteaga. Dynamic model and simulation of cooperative robots: a case study. *Robotica*, (2005).

[7] A. Zaatri B. Bounab, D. Sidobre. On computing multi-finger force closure grasps of 2d objects. *ICINCO Int. Conf. Informatics in Control, Automat. Robot.*, (2007).

[8] A. Zaatri B. Bounab, D. Sidobre. Central axis approach for computing n-finger force-closure grasp. *in Proc. IEEE Int. Conf. Robot. Automat.*, pages 1169–1174, (2008).

[9] Saito N ; Satoh T ; Okano H. Grasping force control in consideration of translational and rotational slippage of an object by a flexible contact sensor. *" Electrical Engineering in Japan*, 165:51–57, 2008.

[10] Sohil Garg1 Ashish Dutta2. Grasping and manipulation of deformable objects based on internal force requirements. *International Journal of Advanced Robotic Systems*, 3:107–114, (2006).

[11] C. A. Klein and S. Kittivatcharapong. Optimal force distribution for the legs of a walking machine with friction cone constraints. *IEEE Trans. on Robotics and Automation*, 6:73–85, 1990.

[12] F. T.Cheng and D. E. Orin. Efficient formulation of the force distribution equations for simple closed-chain. *IEEE Trans. on Systems, Man, and Cybernetics*, 21:25–32, 1991.

[13] J.Cornella R.Suarez and R.Carloni. Dual programming based approach for optimal grasping force distribution. *" Mechatronics (Oxford)*, 165:348–356, 2008.

[14] M. A. Nahon and J. Angeles. Optimization of dynamic forces in mechanical hands. *Trans. of the ASME, J. of Mechanical Design*, 113:167–173, 1999.

[15] M. A. Nahon and J. Angeles. Real-time force optimization in parallel kinematic chains under inequality constraints. *IEEE Trans. on Robotics and Automa.*, 12:87–94, 1999.

[16] KOO Patrick. An analytical expression for the generalized forces in multibody lagrange equations. *IEEE transactions on robotics and automation*, 20:340–343, 2004.

[17] H. Liu and B. Wen. Force distribution for the legs of quadruped robot. *Journal of Robotique Systemes*, 14:1–8, 1997.

[18] V. Kumar and K. J.Waldron. forces distribution in walking vehicules. *Trans. of the ASME, J. of Mechanical Design*, 112:90–99, 1990.

[19] G.Lin D.Wang and LI. The analytical dynamic model of six-dof industrial robotic manipulators of containing closed chain. *Mechanism and machine theory*, 40:385–393, 2005.

[20] X. Chen and K.Watanabe. Optimal force distribution for the legs of quadruped robot. *Machine inteligence and robotique control*, 1:87–94, 1999.

[21] W. Kwon and B.C. Wen. A new optimal force distribution scheme of multiple cooperating robots using dual method. *J. of Intelligent and Robotic Systems*, 21:301–326, 1998.

[22] C. Mahfoudi K. Djouani S. Rechak and M.Bouaziz. Optimal force distribution for the legs of an hexapod robot. *IEEE Conference on Control Application CCA Istambul*, 1:651670, 2003.

[23] C. Mahfoudi K. Djouani M.Bouaziz and S. Rechak. General method for dynamic modeling and control of an hexapod robot including optimal force distribution. *WSEAS, Transaction on Signal Processing*, 2:323330, 2006.

[24] W. Khalil and E. Dombre. *Modélisation identification et commande des robots*. Hermes sciences, Paris, 1999.

[25] R. C. Paul. *Robots manipulators, mathematics, programing and control*. MIT press, 1981.

[26] T.WATANABE and T.YOSHIKAWA. Grasping optimization using a required external force set. *IEEE transactions on automation science and engineering*, 4:52–66, 2007.

[27] S.Daniel ; EDIN Benoni B. Prediction of object contact during grasping. *Experimental brain research*, 3:265–277, 2008.

[28] X.Zhu and H.Ding. Computation of force-closure grasps. *IEEE Trans. Robot. Autom.*, 22(1):172–179, (2006).

[29] J.Gerardo and S.Mendez. *Sensors, Focus on Tactile, Force and Stress Sensors*. I-Tech, Vienna, Austria, Austria, December 2008.

[30] F. T. Cheng and D. E. Orin. Efficient algorithm for optimal force distribution-the compact-dual lp method. *IEEE Trans. on Robotics and Automation*, 6:178–187, 1990.

[31] J.F. Gardner. Force distribution in walking machines over rough terrain. *Trans. of the ASME, J. of Dynamic Systems, Measurement, and Control*, 113:754–758, 1991.

DYNAMIC MODEL OF A FLEXIBLE BLADE WIND TURBINE IN AN ELECTRICAL GRID CONTROL STRUCTURE

Lamine CHALAL [(a)], Jean Yves DIEULOT[(b)], Genevieve DAUPHIN-TANGUY[(a)] , Frederic COLAS[(c)]

[(a)] LAGIS FRE CNRS 3303, Ecole Centrale de Lille, BP 48, 59651 Villeneuve d'Ascq Cedex, France
[(b)] LAGIS FRE CNRS 3303, Polytech'Lille, Cité Scientifique, 59655 Villeneuve d'Ascq Cedex, France
[(c)] L2EP, ENSAM, 8 Bd Louis XIV, 59000 Lille

[(a)]laminechalal@gmail.com, [(b)]jean-yves.dieulot@polytech-lille.fr , [(c)]genevieve.dauphin-tanguy@ec-lille.fr, [(d)]Frederic.COLAS@ensam.eu

ABSTRACT

It has already been reported that one-mass or lumped model of wind turbine system is insufficient to analyze the transient behaviour of wind turbine. For the sake of exact analysis of transient stability of wind turbines, it is needed to consider two-mass shaft system model. This model of drive train doesn't take into account the flexibility of blades. But it is usually used to calculate the electromagnetic torque reference allowing a Maximum Power Point Tracking (MPPT) strategy at low wind speed. In this paper we will compare the behavior of the controlled system, when the blades are supposed to be rigid and when their flexibility is taken into account using the Blade Element Momentum theory (BEM).

Keywords: Wind turbine, Blade element momentum theory, flexible mechanical systems.

1. INTRODUCTION

Electrical energy generation using wind power has recently received considerable interest and attention all over the world due to growing environmental concern.

In most cases, wind turbines are modeled as a one mass lumped model having combined constant inertia.

As the one-mass lumped model is too simple for representing the dynamics of a wind turbine and wind generator connected to each other through a shaft, stability analysis based on the one-mass shaft model may give significant errors (Muyeen, Hasan Ali, Takahashi,Murata,Tamura,Tomaki, Sakahara and Sasano 2007).

The size of commercial wind turbines has increased dramatically in the last 25 years from approximately a rated power of 50kW and a rotor diameter of 10–15m up to today's commercially available 5MW machines with a rotor diameter of more than 120 m. Since the stiffness is not increasing proportionally, structures of that magnitude are severely dynamical sensitive.

Moreover, very large displacements of the blades may occur, for which reason non-linear effects cannot be ignored (Hansen, Sørensen, Voutsinas and Sørensen 2006).

Usually only the drive-train shaft flexibility is considered, but such other issues should be addressed such as the inherent flexibility of blades and tower while modeling a wind turbine system. While the latter phenomenon is well identified, wind turbines with flexible blades are reported in fewer studies (see Agarwal, Dauphin-Tanguy, and Guillaud, 2009). For wind turbine generation system, control laws are usually designed from steady state equations. The objective of this paper is to point out the consequences of such strategy in the transient phases due to the flexible modes of the blades. It will be shown the overrating and the underrating of the aerodynamic power which can be extracted from the wind turbine.

This paper is organized as followed. After the introduction, section 2 presents the procedure for determining the reference electromagnetic torque used in the control structure. The dynamic model of the wind turbine blade is presented in section 3. In section 4 we present some simulations results. Concluding remarks are given in section 4.

2. CONTROL LOOP AT LOW WIND SPEED:

The aerodynamic efficiency is the ratio of turbine power to wind power and is known as the turbine's power coefficient, C_p. C_p can be computed as:

$$C_p = \frac{P}{P_{wind}} \cdot \quad (1)$$

where P is the power captured by the turbine and P_{wind} is the power available in the wind for a turbine of that size. The power P_{wind} is given by:

$$P_{wind} = \frac{1}{2}\rho S v^3 . \quad (2)$$

where ρ is the air density, S is the rotor swept area, and v is the wind speed.

Variable-speed wind turbines have three main operating regions. The first one, region 1, consists of the turbine startup routine. Region 2 is an operating mode during which it is desirable that the turbine captures as much power as possible from the wind.

Region 3 is encountered when the wind speed is high enough for the power to be held constant by the use of wind turbine controls. The turbine rotational speed is maintained at the desired rotational speed through the use of blade pitch angle. Figure 1 shows the overall control system in region 2 and region 3. The grid control system is not shown in the figure.

In this paper, we focus on region 2 operation, which accounts for more than 50% of yearly energy capture for a typical modern turbine (Johnson, Fingersh, Balas and Pao 2004).

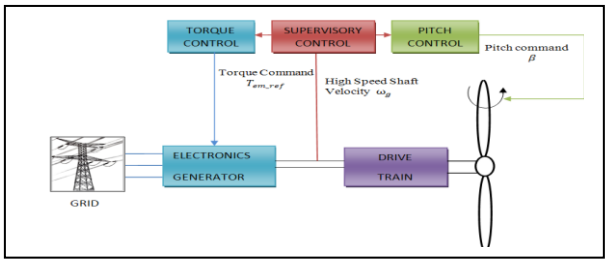

Figure1: Basic turbine control

In region 2, the wind speed and the generator torque are below "rated". Blade pitch is held constant at the optimal value that gives maximum aerodynamic torque. Each wind speed has a corresponding rotor speed at which the greatest possible aerodynamic torque is generated. It turns out that when the blade pitch is held at the optimal β_{opt}, there is a constant value tip-speed ratio λ, that maximizes aerodynamic torque . The tip-speed ratio λ, is defined as :

$$\lambda = \frac{\omega_t R_t}{v} \ . \qquad (3)$$

where ω_t is the wind turbine rotor-speed, R_t is the wind turbine rotor radius, and v is the wind velocity.

So, the control objective in Region 2 is to command electromagnetic torque so that the rotor speed ω_t tracks the wind speed v and gives an optimal tip-speed ratio λ_{opt}.

For modern HAWTs (Horizontal-Axis Wind Turbine), the relationship between the power coefficient C_p and the tip-speed ratio λ is a turbine-specific nonlinear function. C_p also depends on the blade pitch angle in a nonlinear fashion, and these relationships have the same basic shape for most modern HAWTs (Pao and Johnson 2009). So the turbine is considered as an aerodynamic torque generator.

In this work, we will use a two-mass model of the drive train. This is motivated by the fact that one mass-model cannot report the flexibility of the low speed shaft (Boukhezzar and Siguerdidjane 2009).

The masses used in the model correspond to a large turbine rotor inertia J_r, and a small inertia J_g representing the induction generator shaft (figure 2). The dynamic nature of the shaft is illustrated by damping b_{ls} and the spring K_{ls} . The gear ratio G is illustrated by the discs in the middle. Friction coefficients for the turbine and generator are represented by b_r and b_g respectively.

The equations which govern the model are given by:

$$\begin{cases} J_r\dot{\omega}_t = T_a - T_{ls} - b_r\omega_t \ . & (4) \\ \dot{\theta}_{K\_ls} = \omega_t - \omega_{ls} \ . & (5) \\ J_g\dot{\omega}_g = T_{hs} - T_{em} - b_g\omega_g \ . & (6) \end{cases}$$

with:

$T_{ls} = K_{ls}(\theta_t - \theta_{ls}) + b_{ls}(\omega_t - \omega_{ls}),\ T_{hs} = \frac{T_{ls}}{G}$ and $\omega_{ls} = \frac{\omega_g}{G}$

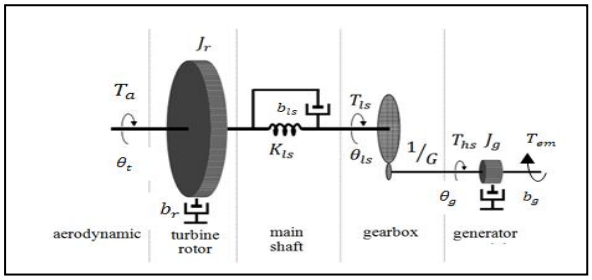

Figure 2: Two-mass Wind Turbine Scheme

In steady state, the previous set of equations becomes:

$$\begin{cases} 0 = T_a - T_{ls} - b_r\omega_t. & (7) \\ 0 = \omega_t - \omega_{ls} \ . & (8) \\ 0 = T_{hs} - T_{em} - b_g\omega_g \ . & (9) \end{cases}$$

From equation (8), we can deduce that:

$$\omega_t = \omega_{ls} = \frac{\omega_g}{G}. \qquad (10)$$

Multiplying (9) by G, and summing with (7) we obtain:

$$T_a - T_{ls} - b_r\omega_t + G\,T_{hs} - GT_{em} - Gb_g\omega_g = 0. \qquad (11)$$

After some rearranging, the electromagnetic torque is given by:

$$T_{em} = \frac{T_a}{G} - \left(b_g + \frac{b_r}{G^2}\right)\omega_g \ . \qquad (12)$$

For determining the optimal electromagnetic torque T_{em_ref} from equation (12), it is usually assumed that:

$$T_a = K_{opt}\,\omega_t^2 \ . \qquad (13)$$

where K_{opt} is derived from equations (1),(2) and (3) as:

$$K_{opt} = \frac{1}{2}\rho\pi R_t^5\ \frac{C_{p\_max}}{\lambda_{opt}^3}$$

The reference electromagnetic torque is obtained by replacing equation (13) in (12),which gives:

$$T_{em\_ref} = K_{opt\_hs}\,\omega_g^2 - K_{t\_hs}\omega_g \ . \qquad (14)$$

where:

$K_{opt\_hs} = \frac{K_{opt}}{G^3}$ and $K_{t\_hs} = b_g + \frac{b_r}{G^2}$

Equation (14) requires the knowledge of K_{opt_hs} and K_{t_hs} , which may be supplied by the turbine manufacturer.

It is reasonable to assume that the generator with a good current control system responds rapidly and accurately when tracking the reference torque produced by the torque controller.

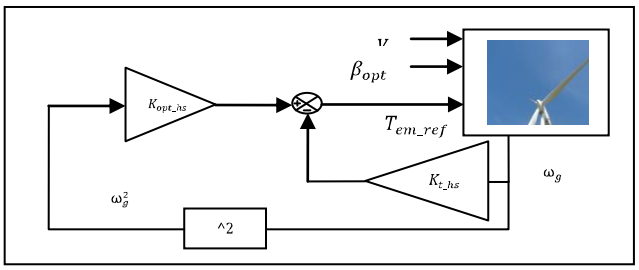

Figure 3 Generation of T_{em_ref}

3. DYNAMIC MODEL OF A WIND TURBINE BLADE:

In this paper structural model of wind turbine blade is based on Rayleigh beam model **(**Mukherjee , Karmakar, and Samantaray 2000**)**. The blade can be assumed as a twisted beam composed of a number of sections (Figure 4) submitted to aerodynamic forces calculated using the blade element momentum (BEM) theory (Agarwal, Dauphin-Tanguy, and Guillaud 2009).

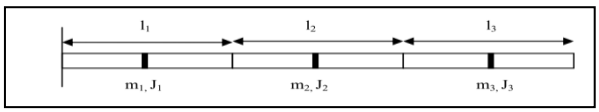

Figure 4: Blade considered as a beam (3 sections)

The forces exerted on an element of the beam are: elastic forces, damping forces, inertial forces and external forces. The bond graph model of each section can be built (figure 5):

- The stiffness matrix is modeled as a 4 – port C – field storage
- The structural damping matrix is modeled as R-field
- The inertia effects are modeled as I element

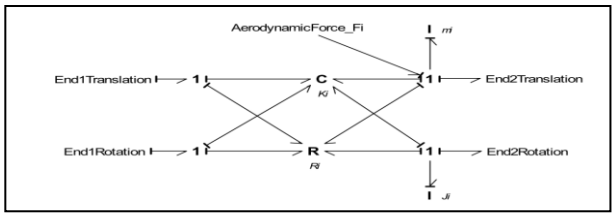

Figure 5: bond graph model of a section of the turbine blade with aerodynamic force

The mathematical model most frequently used by scientific and industrial communities is based on the blade element momentum (BEM) theory (Lanzafame and Messina 2007). Blade element theory assumes that each blade can be divided into a number of radial blade elements, where local aerodynamic loads can be calculated independently, reducing it into a 2D-problem. Then these loads are integrated in order to determine the total aerodynamic load on each blade (Pournaras, Riziotis and Kladas 2008).

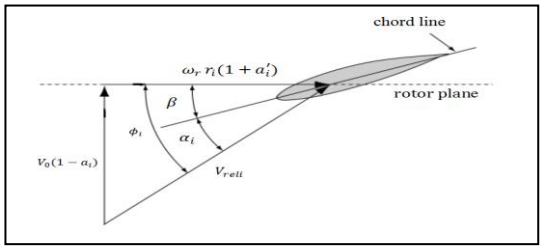

Figure 6: Local element velocities and flow angles

The relationships between the lift and drag forces and the normal and tangential forces are purely vectorial as determined by the angle of attack of the incoming flow stream α_i, defined as the angle between the incoming flow stream and the chord line of the airfoil at the i^{th} section, as shown Figure 6.

The inflow angle is for section *i* obtained from Figure 6 as:

$$\phi_i = tan^{-1}\left(\frac{V_0(1-a_i)}{\Omega_{ri}(1+a_i')}\right) . \qquad (15)$$

Figure 7 shows the resultant aerodynamic forces on the element and their components perpendicular and parallel to the rotor plane. The dF_n is normal to the plane of rotation (contributing to thrust force) while dF_t is the force tangential to the rotor plane creating the useful torque. The aforementioned forces are the dominating ones in turbine design(Moriarty and Hansen 2007).

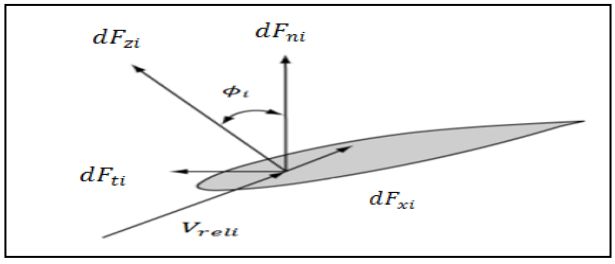

Figure 7: Local forces on a blade

The aerodynamic forces (dF_{zi} and dF_{xi}), per blade unit length, are calculated by means of the corresponding aerodynamic coefficients C_{zi} (lift coefficient) and C_{xi} (drag coefficient) which are known for each blade element , as follows:

$$dF_{zi} = \frac{1}{2}\rho c_i C_{zi} {V_{rel}}^2. \qquad (16)$$

$$dF_{xi} = \frac{1}{2}\rho c_i C_{xi} {V_{rel}}^2. \qquad (17)$$

where ρ is the air density ,c_i the chord of each blade element and V_{rel} is the relative velocity. The lift (C_{zi}) and drag (C_{xi})coefficient are calculated by using

look-up tables which are functions of the angle of attack α_i.

The local force components for each blade element, per unit length, as shown in Figure 7 are calculated normal to and tangential to the rotor plane as follows:

$$dF_{ni} = dF_{zi}\cos\phi_i + dF_{xi}\sin\phi_i. \quad (18)$$
$$dF_{ti} = dF_{zi}\sin\phi_i - dF_{xi}\cos\phi_i. \quad (19)$$

One of the major limitations of the original BEM theory is that there is no influence of vortices shed from the blade tips into the wake on the induced velocity field. This tip vortex creates multiple helical structures in the wake, and they play a major role in the induced velocity distribution at the rotor, so a correction factor F_i, named Prandtl tip-loss factor, is introduced for the calculation of the corrected induction factors a_i and a_i' and is computed as follows :

$$F_i = \frac{2}{\pi} cos^{-1}\left(e^{\left[\frac{-B(R_t - r_i)}{2\, r_i \sin\phi_i}\right]}\right). \quad (20)$$

where B is the number of blades, R_t is the overall radius of rotor and r_i is the local radius of blade element.

The corrected values for the induction factors a_i and a_i', are given by the following equation (Moriarty and Hansen 2007) :

$$a_i = \frac{1}{\frac{4F_i \sin\phi_i{}^2}{\sigma_i C_{ni}} + 1}. \quad (21)$$

$$a_i' = \frac{1}{\frac{4F_i \sin\phi_i \cos\phi_i}{\sigma_i C_{ti}} - 1}. \quad (22)$$

where

- $\sigma_i = \frac{Bc_i}{2\pi r_i}$
- $C_{ni} = C_{zi}\cos\phi_i + C_{xi}\sin\phi_i$
- $C_{ti} = C_{zi}\sin\phi_i - C_{xi}\cos\phi_i$

The aerodynamic force F_{a_i} exerted on each blade section, is calculated using the following equation:

$$F_{a\_i} = \left(\frac{1}{2}\rho V_0 \frac{(1-a_i)^2}{\sin\phi_i{}^2}(C_{zi}\sin\phi_i - C_{xi}\cos\phi_i)c_i\, l_i\right)V_0 . \quad (23)$$

Now that all of the equations for BEM theory have been established, the iteration procedure used to calculate the exerted force F_{a_i} on each section is implemented in gyrator element GY_i (Agarwal, Dauphin-Tanguy, and Guillaud 2009).

Figure 8 shows a bond graph model of the blade (three sections), where:

- Sf: V_0 represents the wind mean velocity
- Sf: represents the angular velocity of the rotor ω_t.
- Sf: *Vbound* and Se define the boundary conditions.
- Gyrators have two input modulating signals; one is the pitch of the blade β, which is a control variable, and the other is the angular velocity of the rotor ω_t.
- J_{whole} is the rigid body inertia of the whole blade.

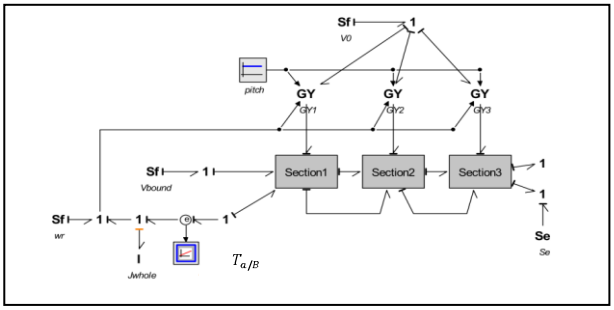

Figure 8 : Bond graph Model of turbine blade (three sections)

The resultant aerodynamic torque T_a is calculated by multiplying the aerodynamic torque, obtained from the bond graph model of single blade, by the number of blades B.

4. SIMULATION RESULTS

The numerical simulations were performed on a wind turbine whose characteristics are given in Table I.

For simulating the controlled wind turbine system, we will use two different models of the wind turbine as shown in figure 8, the first one including a dynamic model of flexible blades, the second one corresponding to an algebraic model of blades supposed rigid. The bond graph model of flexible blades (Figure 8) is connected to the two mass model described in section 2.

The inertia of each blade, which is represented by J_{whole} in figure 8, is lumped with the other wind turbine components: hub inertia and low shaft inertia, to form J_r.

Number of blades B	3
Blade rotor R_t	23.5 m
Turbine rotor inertia J_r	222963 Kg.m²
Friction coefficient for the turbine b_r	743,21 N.m.s
Spring constant K_{ls}	2854 N.m/rad
Damping b_{ls}	1200 N.m.s
Gearbox ratio G	52,63
Generator inertia J_g (asynchronous machine)	12,68 Kg.m²
Friction coefficient b_g	0,2675 N.m.s

Table 1 Wind turbine characteristics

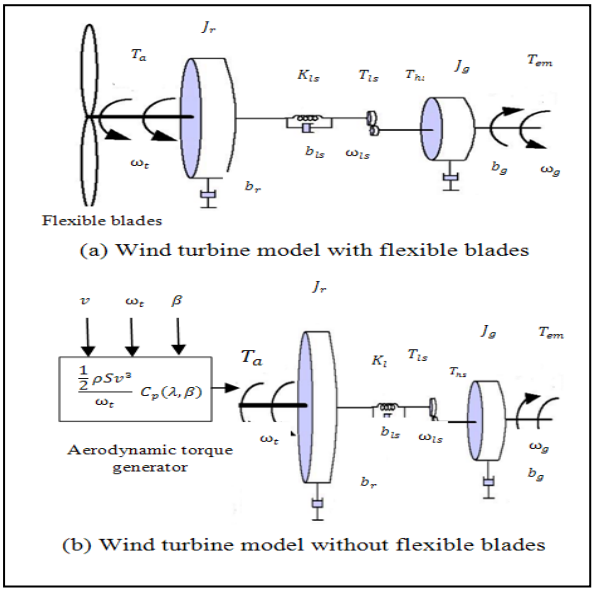

Figure 9: the two models of wind turbine

As explained in section 3, the whole aerodynamic torque is three times the aerodynamic torque obtained from the bond graph model of single blade. Figure 9(a) shows the wind turbine with flexible blade.

The second model of wind turbine is shown in Figure 9(b). In this case, hub inertia, shaft inertia and blades are lumped to form J_r, assuming that blades are rigid.

Usually, wind turbine rotor is considered as an aerodynamic torque generator. This aerodynamic torque is given by an algebraic relation (24):

$$T_a = \frac{1}{2}\rho S \frac{v^3}{\omega_t} C_p(\lambda,\beta). \qquad (24)$$

where the characteristic $C_p(\lambda,\beta)$,given in figure 10, is stored in a look up table.

Some simulations were run to verify the relevance of the generation of electromagnetic torque shown in Figure 3. In the two models, tip-speed ratio at the steady state sticks to the optimal value λ_{opt} which corresponds to the maximum power.

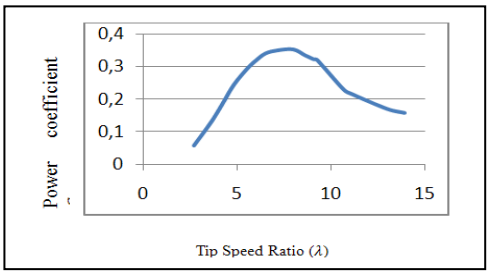

Figure 10: Typical $C_p$curve as a function of λ for $\beta = 1$ deg .

In order to compare the two models, a constant wind speed is applied (6 m/s). The relative error between the two aerodynamic torques at steady state is 0.0012 %.

Now, the wind speed increases from 6 m/s to 8 m/s as a step at t =300 s, and decreases from 8 m/s to 6 m/s at t = 350 s. The aerodynamic torque is shown in figure 11. As it can be seen, in steady state the aerodynamic torque is the same in the two models of wind turbine. However, the model of wind turbine which takes into account the flexibility of the blades, induces oscillations in the transient response.

Figure 12 and figure 13 show respectively the aerodynamic power P_{aer} and the absolute error between the aerodynamic powers of each model of wind turbine. The aerodynamic power is given by equation (25):

$$P_{aer} = T_a \omega_t. \qquad (25)$$

In steady state the absolute error is too small, however in transient state the absolute error is very important. When the wind speed increases from 6 m/s to 8 m/s, the aerodynamic power of the wind turbine model obtained from equation (25), is different for the two cases. Not taking into account the blade dynamics overestimates or underestimates the extractable power, depending on the rising or decreasing phase of the wind speed.

From figure 13,it appears that the specific case that the transient behavior here is 40s long, which involves a big amount of mechanical energy badly estimated ($\Delta E = 520Kj$) when using rigid model of the wind turbine blades.

So, neglecting blades flexibility, in transient state may induce significant error. The rigid model is too simplified to represent the whole turbine accurately, particularly in transient states.

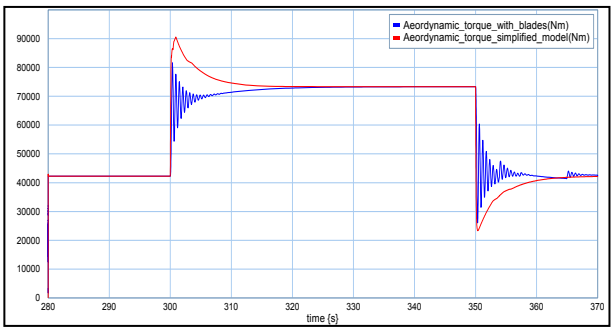

Figure 11: Aerodynamic torque

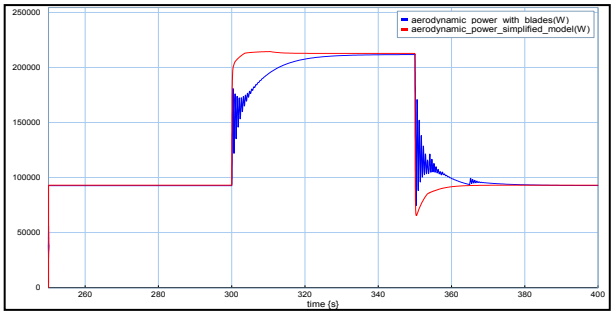

Figure 12: Aerodynamic power

Figure 14 shows the frequency spectrum for the mentioned wind velocity. This fast Fourier transform of the two aerodynamic torques shows the dominant frequency 1.7 Hz for the wind turbine model with flexible blade, which is very closed to the dominant frequency of the blades.

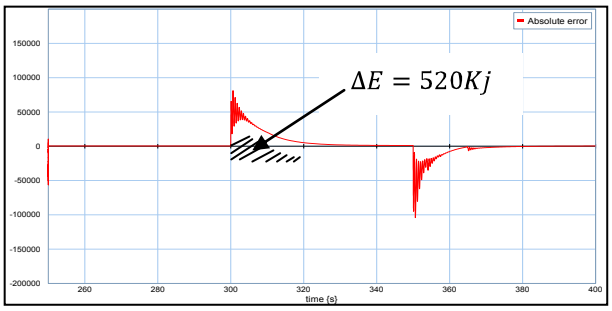

Figure 13: Absolute error between the two aerodynamic powers, ($P_{aero_{simplified}} - P_{aero_{blades}}$)

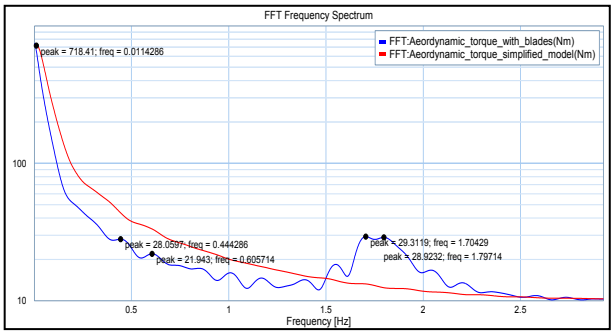

Figure 14: Frequency spectrum ($v = 6\ m/s$)

Conclusion

In this paper wind turbine models and control loop at low wind speed have been presented. Two models of wind turbine have been used. The first model is a two mass model, represented by a large inertia (turbine) and a small inertia (generator) assuming the rigidity of the blades. The second model takes into account the flexibility of blades. Aerodynamic loads are calculated using blade element momentum theory. Simulation results showed that neglecting blade flexibility may give significant error at transient sate. In steady state, wind turbine model can be expressed by the simple two-mass shaft model with reasonable accuracy.

REFERENCES

Agarwal,S.,Dauphin-Danguy,G.,Guillaud,X.,2009.Bond Graph Model of Wind Turbine Blade. Submitted to a journal.

Boukhezzar, B., Siguerdidjane ,H., 2009. Comparison Between Linear and Nonlinear Control Strategies for Variable Speed Wind Turbine Power Capture Optimization. *Proceedings of Fourth International Conference and Exhibition on Ecological Vehicles and Renewable Energies*, March 26-29, Monte-Carlo (Monaco,France).

Hansen, M.O.L., Sørensen , J.N, Voutsinas, S., Sørensen, N., Madsen, H.A., 2006. State of the art in wind turbine aerodynamics and aeroelasticity, *Progress in Aerospace Sciences*, Vol. 42, pp. 285-330.

Johnson,K.E., Fingersh,L.J., Balas,M.J., Pao,L.Y.,2004. Methods for Increasing Region 2 Power Capture on a Variable-Speed Wind Turbine. *Journal of solar energy engineering*, vol. 126**:** pp. 1092-1100.

Lanzafame, R., Messina, M., 2007. Fluid dynamics wind turbine design: Critical analysis, optimization and application of BEM theory. *Renewable Energy*, vol.32: pp. 2291- 2305.

Moriarty, P.J., Hansen, A.C.,2005, AeroDyn Theory Manual. National Renewable Energy Lab., Golden, CO (USA).

Mukherjee, A., Karmakar, Samantaray ,R., A.K., 2000. *Modelling and Simulation of Engineering Systems through Bond Graphs*. India:Narosa Publishing House.

Muyeen , S.M., Hasan Ali, Md. , Takahashi, R. ,Murata, T., Tamura, J., Tomaki , Y., Sakahara, A. , Sasano, E., 2007. Comparative study on transient stability analysis of wind turbine generator system using different drive train models. *IET Renewable Power Generation*, vol. 1: pp. 131–141.

Pao ,L.Y., Johnson ,K.E., 2009. A Tutorial on the Dynamics and Control of Wind Turbines and Wind Farms. *American Control Conference* ,pp. 2076- 2089. June 10-12, St. Louis (USA).

Pournaras, C., Riziotis,V., Kladas,A., 2008.Wind turbine control strategy enabling mechanical stress reduction based on dynamic model including blade oscillation effects. *Proceedings of the 2008 International Conference on Electrical Machines*. September 6-9, Vilamoura (Portugal).

A PUMPING SYSTEM FED BY HYBRID PHOTOVOLTAIC-WIND SOURCES WITHOUT BATTERY STORAGE
BOND GRAPH MODELING, CONTROL AND ENERGY MANAGEMENT

A. BEN RHOUMA[(a)], J. BELHADJ[(b,a)], X. ROBOAM[(c)]

[(a)] LSE-ENIT B.P 37 Le Belvédère, 1002 Tunis Tunisia
[(b)] ESSTT, BP 56 Monfleury 1008 Tunis, Tunisia
[(c)] Université de Toulouse - LAPLACE (CNRS-INPT-UPS), ENSEEIHT-2 Rue Camichel 31071 Toulouse, France.

[(a)] benrhouma.amine@yahoo.fr , [(a, b)] Jamel.Belhadj@esstt.rnu.tn , [(c)] Xavier.Roboam@laplace.univ-tlse.fr

ABSTRACT
This paper studies an original energy management system with control strategy dedicated to an autonomous pumping system fed by a hybrid (photovoltaic and wind) generator without battery storage. A systemic approach is developed to reduce complexity and to analyze the system which involves multi-domains with strong couplings. The Bond Graph formalism is then used for the system modeling. In order to validate the simulation model, an experimental system has been set up and tested under various conditions. A power based analysis is developed to understand the system behavior. Finally, control strategies are deduced allowing a "storageless" energy management of the pumping system fed along given sun and wind conditions.

Keywords: hybrid source, centrifugal pump, Bond Graph, energy management.

1. INTRODUCTION
Hybrid photovoltaic and wind source has become one of several promising alternative to produce electrical energy. The exploitation of this system is relevant and attractive especially for remote area and for small-scale applications such as water pumping and/or desalination [1-3]. Exploitation of drilling water finds a particular interest in arid regions which are neither connected to the hydraulic network nor to the electric grid. In this work, we chose to operate the hybrid source in maximum power point tracking (MPPT) mode. That allows increasing sources efficiency and to extract the maximum of power. The DC bus, on which power sources are coupled is equivalent to a finite and variable "given power source".

Majority of pumping systems operate with the use of batteries which simplify energy management, decoupling, under a certain level, production and consumption but reducing system reliability and increasing its price along the life cycle of the installation. In order to design robust and "low cost" systems for rural applications, we have then removed battery storage, only taking advantage of natural hydraulic storage offered in such devices. In fact, hydraulic tanks play the role of energy buffer between water demand and production. Without battery storage, the DC bus power is imposed directly to the pumping unit through the motor-pump inverter(s). Thus, we may obtain a bad adaptation between the source and the load which would cause efficiency loss.

The main objective of our paper is then firstly to analyze the pumping unit under variable "given DC bus power" without storage. Secondly, original energy management and control strategy are proposed to face particular constraints of this "storageless" structure. We finally proposed a control strategy which allows controlling the DC bus voltage with optimized power transfer towards two motor pumps in parallel. This study requires a convenient modeling of the pumping unit which must reflect main physical and energetic behavior. The experimentation is useful as a reference for the model validation. Bond graphs offer graphical description for dynamic behavior of multi-physical systems. It describes the power flow and models the transformation across domains (electrical, mechanical, and hydraulic). In addition, it provides uniform representation which offers a unified and understandable way to process physical modeling of such system.

2. SYSTEM STRUCTURE

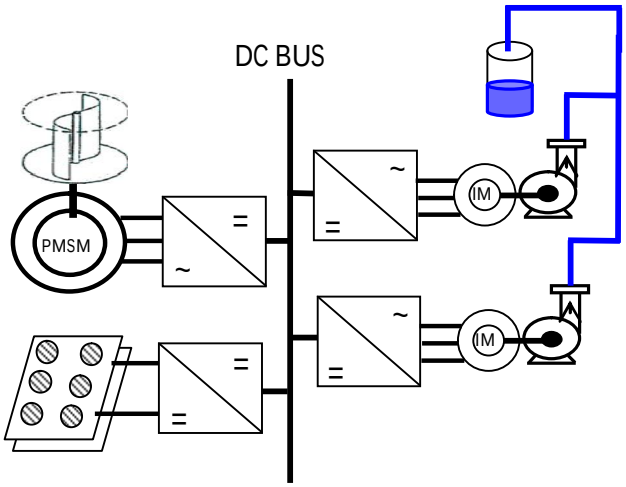

Figure 1: Scheme of the pumping system fed by the hybrid source without battery storage

The pumping system mainly consists on the hybrid source and the pumping unit. The pumping unit can be based on a single motor-pump, [1] or multi-motor pumps. In this paper we have chosen the second configuration with two pumping devices even if development can be generalized. The hybrid source can be composed of wind and photovoltaic generators coupled to the DC bus through static converters ([4-5]) but this part is not focused in this paper in which we have only considered "given power source" for given climatic conditions. The pumping unit is composed of two identical 2HP motor pumps. Each one is driven by a voltage source inverter. Both pumps are associated in parallel with hydraulic pipes (see Figure 1).

3. SYSTEM ANALYSIS

3.1. The Hybrid system

The wind generator is a direct drive technology based on a multi-poles permanent magnet synchronous generator associated with a PWM rectifier, the photovoltaic panel is connected to the DC link via a boost chopper. To increase the energy availability, MPPT techniques are used to maximize the power transfer (these sources are power controlled if the maximum power of the pumping system is reached): degrees of freedom offered by sources power converters are then used for MPPT control.This principle is presented in preceding works as in [2].

3.2. Experimental set up

Figure 2: experimental test bench of the pumping unit

Experiments were conducted to evaluate energy management performance of the pumping system and to validate models. Induction motors driving pumps are connected to Frequency Converter Drive (FCD) devices. We can measure water flow and pressure at the output of the pump. The FCD gives an estimation of the load torque. The hydraulic load variation is possible thanks to a valve setting.

Hydraulic characteristics are given in Figure 3 and 4. These curves are obtained for constant given speeds by setting the valve position VP. Figure 3 shows the centrifugal pump characteristics for various frequencies imposed to the variable speed drive. According to these characteristics we notice that these curves follow the affinity laws.

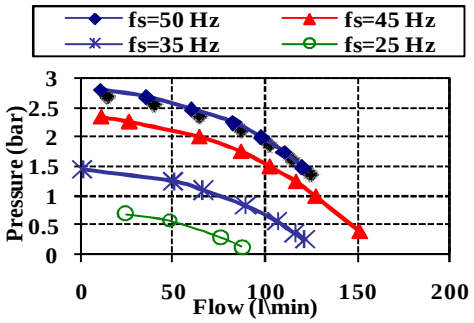

Figure 3: pressure-flow characteristics for several frequencies

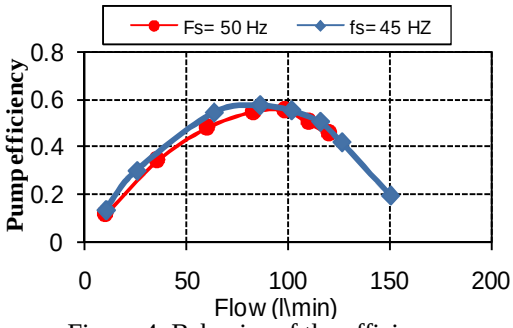

Figure 4: Behavior of the efficiency

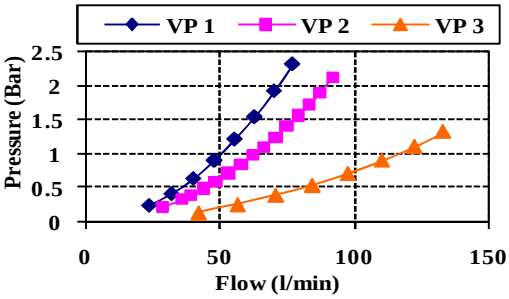

Figure 5: Behavior of the hydraulic load

The hydraulic operating point is fixed by the intersection of the pump (Figure 3) and the hydraulic load curves (Figure 5).

The bell shape characteristic obtained on Figure 4 for motor-pump efficiency shows that an adequate power management is required to avoid energy waste. According to the experimental tests, it exists a tradeoff between efficiency and flow maximization. Indeed, for this application, maximizing the pump flow to obtain a maximum quantity of water is "the" prime objective. This latter factor is linked but not equivalent with efficiency maximization for systems fed by given generated powers.

3.3. The pumping unit modeling

The centrifugal pump is directly coupled to a three phase squirrel cage induction motor (IM) which pumps water from a storage tank. The mechanical power is transformed into hydraulic power through the impeller. This power transformation can be expressed as [7]:

$$T_l = a.\Omega.Q + b.Q^2 \quad (1)$$

$$P = a.\Omega^2 + b.\Omega.Q \quad (2)$$

Where:

- T_l is the load torque of the pump.
- P is the fluid pressure
- Ω is the rotation speed of the induction machine.
- (a,b) are the parameters of the pump.
- Q is the water flow

Hydraulic losses occur throughout the hydraulic network and depend on the static head, on the nature of the flow due to the Reynolds number as well as the characteristics of pipelines (relative roughness and restrictions).
The expression of losses is given by :

$$P_l = \rho.g.Hs + k.Q^2 \quad (3)$$

where :

- k is a parameter due to the losses in the pipeline.
- ρ is the water density.
- g is the gravity.
- Hs is the static head.

The knowledge of pressure losses in the hydraulic pipeline is very important in order to choose a pump well adapted to its hydraulic load then ensuring good efficiency. Practically, efficiency of such system can be strongly degraded if the pump "is not conveniently adapted" to its hydraulic load: this efficiency should be identified and taken into account for the energy management of the system. Indeed, by considering the whole system, it is useless to optimize the power sources (MPPT) if the consumed power is wasted by a bad adaptation with the hydraulic load which would cause a very weak efficiency of the global system. Figure 6 presents the Bond graph model of the centrifugal pump associated with the hydraulic pipe.

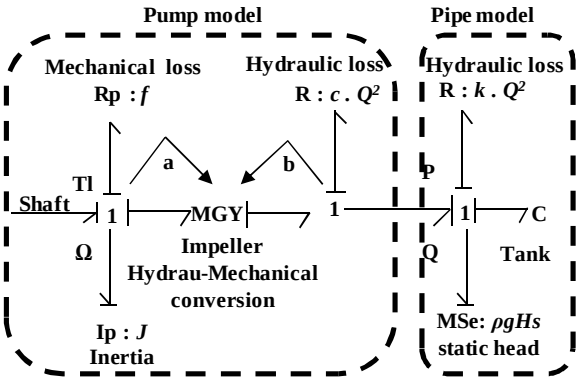

Figure 6: Bond graph model of the centrifugal pump

In this model the hydraulic power is transferred to the pipe of which a part is lost ($c \times Q^2$) by the shocks and frictions of the water between the volute and the pump's impeller. From the experimental study we have the possibility to aggregate the modeling. Indeed, we have identified three parameters (a, b, c) of the pump model starting from experimental curves.

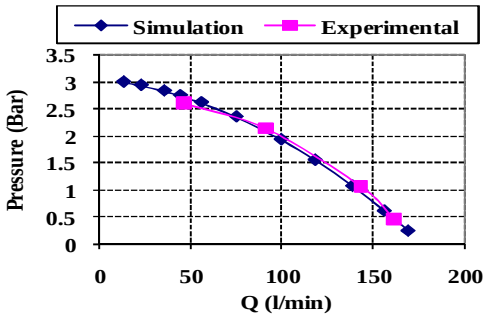

Figure 7: Performance curve of the pump

4. SYSTEM ENERGY MANAGEMENT STUDY

Due to the absence of power storage, this class of system deals with a non classical issue in terms of control and energy management strategy. In fact, without battery storage and with a given generated power, the full generated power is transmitted to the load via the DC link, as shown on figure 8.

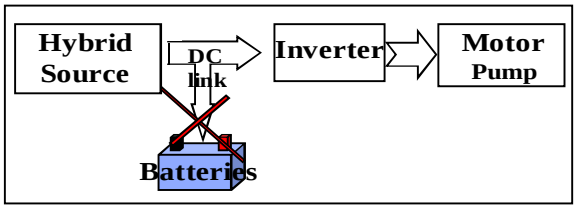

Figure 8: Principle of power/energy transfer into the conversion chain without storage

Before establishing the energy management and the control of the pumping system, a preliminary static study is necessary. The sources operating in MPPT modes are coupled through the DC bus which must be previously regulated to ensure a convenient MPPT control. The DC bus control cannot be achieved thanks to power converters on generators sides which are dedicated to MPPT control. Given climatic conditions, powers are imposed on the DC bus; which then behave as a power sources. A static study of this particular system shows that for a given generated power and for a particular hydraulic load, the hydraulic characteristic of the pump is really different from the one obtained in the case of a traditional grid connected source with "infinite" power [2]. In our case, the operating point of the system is fixed by the source power and the hydraulic load. So, changing the operation in the hydraulic plan leads to change the input power or to modify the hydraulic load. Then, it is not possible to regulate the pump flow by using a conventional control strategy. In this device, the system efficiency will depend on the power of the DC bus.
Figures 9 and 10 respectively show the evolution of the flow and the global (motor + pump) efficiency according to the DC bus power. These curves are obtained from different static heads (ie different hydraulic network characteristics). Note that the efficiency is affected by the static head: then the energy management strategy has to take into account the hydraulic load characteristic. For a given power, the

optimal efficiency is obtained for a high head, not for a maximum flow which emphasizes the tradeoff efficiency-flow.

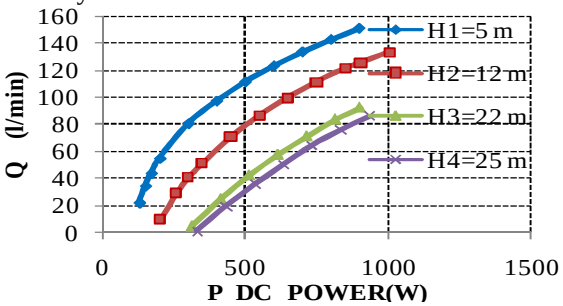

Figure 9: Water flow rate for different static heads

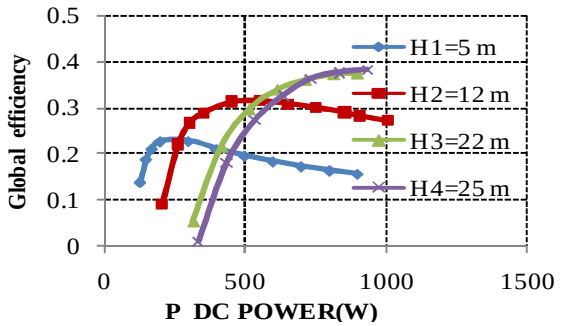

Figure 10: Global efficiency for different static head

Basic conclusions can be put forward:

- Efficiency evolution strongly depends on the hydraulic load characteristics.
- With very low or, at the opposite, with very high powers, efficiency can be so degraded that it becomes inadequate to exploit the motor- pump inside this zone: in this case, *we may prefer to store power in a battery (if any) or to exploit system "modularity"* by using several pumps which would operate sequentially with better efficiencies.

In our case study, without any storage device (except of hydraulic tanks), exploiting modularity of a "multi motor-pump system" is our goal which also constitutes an original way in terms of energy management [6].

5. CONTROL STRATEGIES

Following the previous analysis, we have developed a management strategy in the simplified case of a parallel association of two motor pumps. Both motor pumps are fed by voltage source inverters that offer two degrees of freedom for each: the first one is used to control the magnetic state of the induction machine, and the second one is useful for the management strategy according to the control mode:

- DC bus voltage control: the motor current is set at the output of a voltage bus regulator. This loop allows stabilizing the DC bus voltage to permit the correct operation of all sources especially in MPPT mode.
- Power transfer control: the DC bus being previously controlled (from another motor pump), a power variable operation control can be achieved on the considered motor pump. In particular, it is possible to optimize the power transfer (then the flow) through the motor pump by taking into account efficiencies. Controlling power means that an optimal control of the water flow may be achieved in the considered pump.

This original system management is illustrated by the Figure 11.

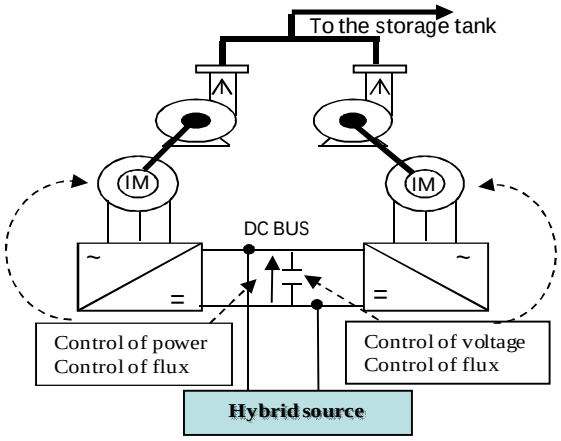

Figure 11: Principle of the energy management of the system with two parallel pumps

The induction motor can be represented using the (d,q) Park's reference frame. In order to generate references for DC bus voltage, power and magnetic flux, a Field Oriented Control (F.O.C) is used to decouple flux and torque. The rotor flux is regulated along the "*d*" axis. The torque is then controlled through the "*q*" axis current. The torque current reference (I_{sq}^{ref}) is set following the control mode (power, or DC bus voltage). Finally, three control loops are proposed for flux, power and DC voltage [1,3].

5.1. DC voltage control

In the case of Figure 14, the voltage control loop is inserted along the "q" axis of the left induction motor (index '*1*') to maintain the voltage constant whatever the power transfer between the hybrid source and the motor- pumps. To keep the power balance, we must fulfill:

$$V_{bus}.I_{e1} = E_{d1}.I_{sd1} + E_{q1}.I_{sq1} \quad (5)$$

(E_{d1},E_{q1}) are the "*d*" and "*q*" axis back emf.

(I_{sd1},I_{sq1}) are the "*d*" and "*q*" axis stator current for the induction machine in the left part of figure 14.

From the previous equation and by considering that the motor current loop is fast with respect to the bus voltage dynamic, the cascaded structure of figure 12 is proposed. Finally with the inverter '*1*', we can control the rotor flux of the induction machine and the voltage of the DC bus.

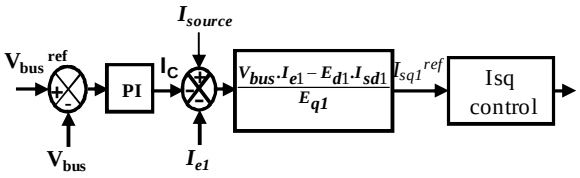

Figure 12: DC voltage control loop

5.2. Power control

The DC voltage being established by the inverter '*1*', a power optimized control is possible by controlling the torque current (I_{sq2}) at the input of the second inverter. The reference current (I_{sq2}^{ref}) is set to maintain the power balance (see Figure 13):

$$I_{sq2}^{ref} = \frac{V_{bus}.I_{e2} - E_{d2}.I_{sd2}}{E_{q2}} \quad (6)$$

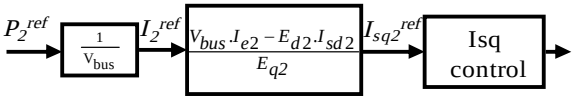

Figure 13: Diagram block of the current regulation.

The general control scheme of the two induction motors is presented on the Figure 14.

Note that the control mode (bus voltage or power control) may by inversed following operating conditions of the whole device. The PI parameters are adjusted using the pole placement method to eliminate all overshoot.

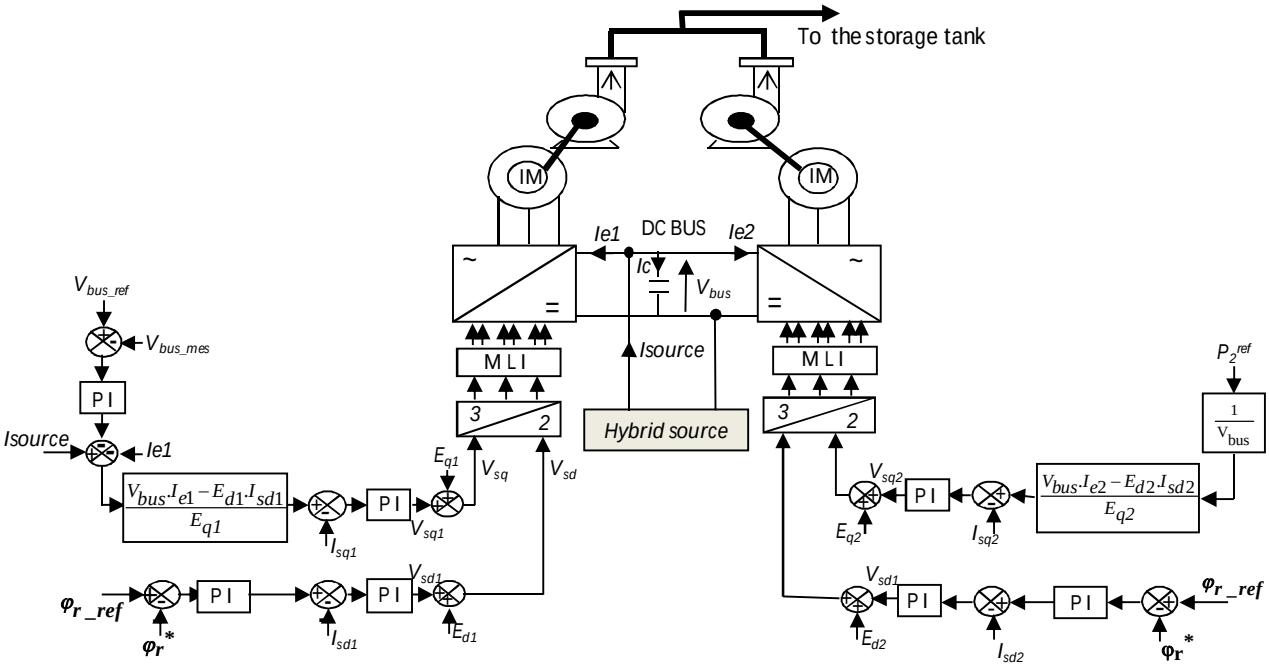

Figure 14: block diagram of the system with two parallel motor pumps

5.3. Simulation results and analysis

Different scenarios allow testing performance of both control and system management. The actual hybrid source is emulated by a "given" power source. The DC voltage is regulated through the motor '*1*'.

The input power imposed on the DC bus is limited between a minimum power (which makes it possible to turn one of the two pumps) and a maximum power (that doesn't exceed rated powers of both pumps)In the first case, from 0 to 10 seconds, a constant input power of 1500W has been applied before increasing to 1800W after 10s.

A constant 600W power reference is applied to the inverter of the pump '*2*' from 0 to 5 seconds then it is increased to 900W. One can see that the system follows the references, the power in inverter '*1*' being set consequently to the bus voltage regulation.

Note that after 10 seconds, the power surplus is imposed to the first inverter.

It is emphasized that, for a given power of the DC bus, the energy management of the second motor pump automatically leads us to set the power in the motor pump '*1*'.

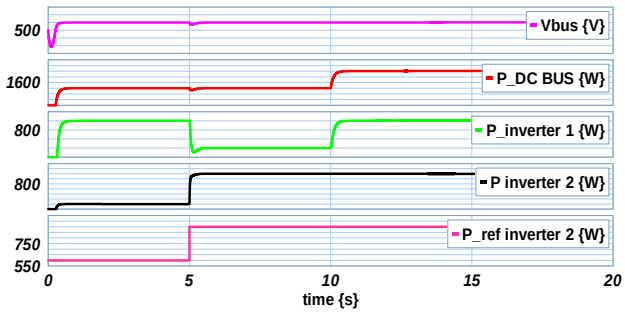

Figure 15: performance of the system control.

In the simulation test of Figure 16, the system is fed with a variable power profile which reflects the response to wind variations.

For a constant reference imposed on the motor-pump '2', the fluctuation of the power will be completely

transmitted to the motor-pump '1', consequently to the bus control which balances powers.

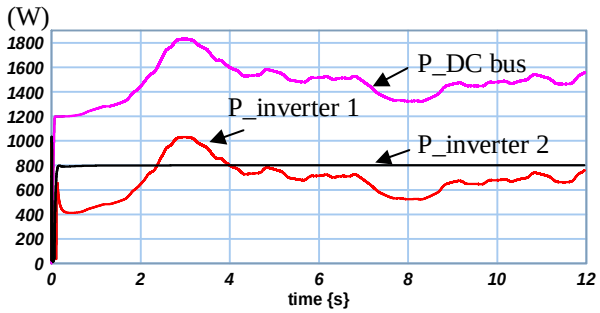

Figure 16: performance of the power control with fluctuating input power conditions

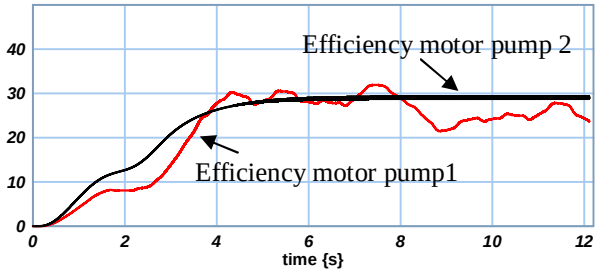

Figure 17: efficiencies of both motor pumps.

Figure 17 shows that efficiency of the voltage controlled motor pump ('*1*') is imposed by the power conditions (P_{DCbus}-P_{inv2}^{ref}) given the hydraulic load characteristics while the power controlled motor pump '2' efficiency depends on the imposed power reference and may be optimized by a system management strategy: it emphasizes the need of a system management for two or, more generally, for 'n' pump devices that will be the aim of future development.

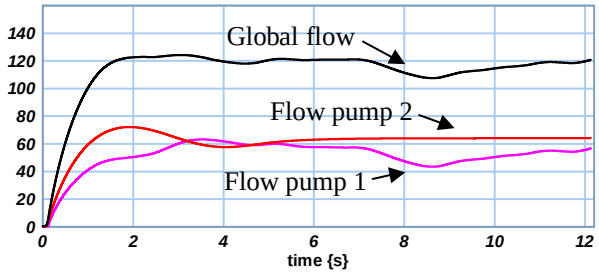

Figure 18: Evolution of the water flow.

By coupling the two pumps in parallel with the hydraulic pipe, the total flow will be the sum of both flows from the two pumps (Figure 18). The system management can be set by solving a real time optimization problem. Indeed, the issue is to optimize water quantity along sun and wind conditions by fulfilling system (technological, rating) constraints.

6. CONCLUSION

A pumping system fed by hybrid source without battery storage was presented in this paper. A special attention was focused on the centrifugal pump's model. Regarding this multi field (electrical, hydraulic, mechanical) device, the Bond graph formalism was proposed to model power exchanges. Experimental tests were carried out for the characterization of the pumping unit and the identification of the bond graph model parameters. Power/energy based analysis has been proposed to evaluate performance of the pumping unit for different 'given' input powers and hydraulic heads. This analysis shows that the input power level and the hydraulic network (here the water head) play an important role in terms of system efficiency. For given water head, we can manage the power to ensure a good efficiency and then to maximize water production. For that purpose, we have developed a control strategy allowing the power management through the two pumps. This study makes it possible in the future to develop a system supervisor which would allow managing the optimal level of pumped water whatever the input power provided to the DC bus along wind and sun conditions at the environment of this "sensorless" hybrid renewable energy generator.

REFERENCES

[1] Ben rhouma, A., Belhadj, J., and Roboam, X., 2007. Design and control of a pumping system fed by hybrid Photovoltaic-Wind source without battery storage. *International conference on Electrical Engineering Design and Technologies (ICEEDT)* November 5-6, Hammamet, Tunisia.

[2] Ben rhouma, A, Belhadj, J, and Roboam X, 2008 Control and energy management of a pumping system fed by hybrid Photovoltaic-Wind sources with hydraulic storage: - Static and dynamic analysis - "U/f" and "F.O.C" controls methods comparisons. *Journal of electrical system (JES) volume 4 issue 4*, December 2008.

[3] Turki, M., Belhadj, J., Roboam, X., 2007. Design and Energy management of a small-scale reverse osmosis desalination unit powered by PV-Wind hybrid system without battery storage. *International conference on Electrical Engineering Design and Technologies (ICEEDT)*, November 5-6, Hammamet, Tunisia.

[4] Dali, M., Belhadj, J., Roboam, X., Blaquiere, J.M., 2007. Control and Energy Management of a Wind photovoltaic Hybrid System", *EPE conference*, Aalborg, Danemark.

[5] Borowy, B. S. and Salameh, Z. M., 1994. Optimum Photovoltaic Array Sizing in a Wind/PV Hybrid System, *IEEE Transactions on Energy Conversion* Vo1.9, No.3**,** pp.482-488.

[6] F, Qing., C, Xiaogao Xie Lei., 2007. High Efficiency Photovoltaic Pump System with Double Pumps, Power Electronics,. ICPE '07. 7th International Conference, pp.493-497

[7] Tanaka, K., Rong, W., Suzuki, K., Shimizu, F., Hatakenaka, K., and Tanaka, H., 2000. Detailed Bond Graph of Turbomachinery. *IECON proceedings*, IEEE, 1550-1555.

PNEUMATIC HYBRIDIZATION OF DIESEL ENGINE IN A HYBRID WIND-DIESEL INSTALLATION WITH COMPRESSED AIR ENERGY STORAGE

Tammam Basbous [(a)], Rafic Younes [(b)], Adrian Ilinca [(c)], Jean Perron [(d)]

[(a)] Anti-icing Materials International Laboratory. Université du Québec à Chicoutimi, Canada
[(b)] Engineering Faculty, Lebanese University, Beirut, Lebanon
[(c)] Wind Energy Research Laboratory, Université du Québec à Rimouski, Canada
[(d)] Anti-icing Materials International Laboratory. Université du Québec à Chicoutimi, Canada

[(a)] tammam.basbous@uqac.ca, [(b)] ryounes@ul.edu.lb, [(c)] adrian_ilinca@uqar.qc.ca, [(d)] jean_perron@uqac.ca

ABSTRACT

In this paper, we are studying an innovative solution to reduce fuel consumption for electricity production in remote areas. Historically, in these areas electricity is provided by Diesel generators. The cost of energy is therefore very high not only because of inherent cost of technology but also because of transportation costs. On the other hand, use of fossil fuels for electricity generation is a significant source of Greenhouse Gas emissions. The use of hybrid systems that combine renewable sources and diesel generators, allows reducing fuel consumption, improves the operation cost and creates therefore environmental benefits. Adding a storage element to the hybrid system above increases fuel saving as it allows an increased penetration of the wind power in the overall system capacity. In a previous work, we demonstrated that Compressed Air Energy Storage (CAES) is a serious solution thanks to its low cost, high power density and reliability. Pneumatic Hybridization of the Diesel engine consists to introduce the CAES through the admission valve. We have proven that we can improve the combustion efficiency and therefore the fuel consumption by optimizing Air/Fuel ratio thanks to the CAES assistance. As a continuation of these previous analyses, we studied the effect of controlling the pressure at the inlet and the exhaust of the Diesel engine on the thermodynamic cycle and evaluated the potential on fuel consumption reduction.

Keywords: Pneumatic Hybridization, Wind Energy, Diesel Engine, Wind-Diesel Hybrid System, Compressed Air Energy Storage.

1. INTRODUCTION

Most of the remote and isolated communities or technical installations (communication relays, meteorological systems, tourist facilities, farms, etc.) that are disconnected from national electric distribution grids rely on diesel engines to generate electricity (Ibrahim 2007). Diesel generated electricity is more expensive in itself than large electric production plants (gas, hydro, nuclear, wind), even prior to taking into account the transport and environmental costs associated with this type of energy.

In Canada, approximately 200,000 people live in more than 300 remote communities (Yukon, Northwest Territories, Nunavut, etc.) that use diesel generated electricity, which is responsible for the emission of 1.2 million tons of greenhouse gases annually (Ibrahim 2007). In Quebec alone, there are over 14,000 subscribers scattered in about forty communities that disconnected from the main grid. Each community constitutes an autonomous network that uses diesel generators.

In Quebec, the total production of diesel power generating units is approximately 300 GWh per year. The operation of these diesel generators is extremely expensive due to the high oil price and transportation costs. Indeed, as the fuel has to be delivered to remote locations, some of them only reachable during the summer by boat, the cost of electricity in 2007 reached more than 50 cent/kWh in some communities, while in the rest of the province the electricity tariff was approximately 6 cent/kWh (Ibrahim 2007). The resulting deficit, which is shared among all Quebecers, is far from being negligible. In 2004, the autonomous networks accounted for 144 MW of installed power, and the consumption was established at 300 GWh. Hydro-Quebec, the provincial utility, estimated at approximately CAD $133 million the annual loss resulting from the difference between the diesel electricity production cost and the uniform electricity tariff (Ibrahim 2007).

Moreover, diesel electricity production is considered ineffective, presents significant environmental risks (spilling), pollutes local air and contributes to global warming. Overall, we estimate at 140,000 tons the annual GHG emission resulting from the use of diesel generators for the autonomous networks in Quebec. This is equivalent to the GHG emitted by 35,000 cars during one year.

While they require relatively little investment, diesel power generating units are generally expensive to operate and maintain, particularly when they function regularly with a partial load (Ibrahim 2007). The use of diesel power generators under weak operating factors

accelerates wear and increases fuel consumption (Ibrahim 2007).

The use of Hybrid Wind-Diesel Generators solves a part of the problems listed above, but its efficiency is limited by wind intermittency. Highly fluctuating wind energy requires the Diesel engine running on idle most of the time and dissipates a part of the wind power in order to control the balance between the energy production and the energy demand. Energy storage is the key to solve this issue, because it allows storing otherwise wasted energy and recover it later, when the Wind power is not sufficient to cover the demand. The use of storage allows an increased penetration of the wind power in the overall system capacity. The high penetration of wind energy means that the installed wind power exceeds the maximum load and, during periods of strong winds, diesel generators may be stopped while surplus of wind energy is stored. The overall energy provided by the Diesel generator is significantly decreased with beneficial economic and environmental results. In a previous work, we demonstrated that Compressed Air Storage (CAES) is a serious solution thanks to its low cost, high power density and reliability. Pneumatic Hybridization of the Diesel engine consists to introduce the CAES in the combustion chamber. We have proven that we can improve the combustion efficiency and therefore the fuel consumption through optimisation of Air/Fuel ratio. As a continuation of these previous analyses, we studied the effect of controlling the pressure at the inlet and the exhaust of the Diesel engine on the thermodynamic cycle and evaluated the potential on fuel consumption reduction

2. IMPROVING INDUSTRIAL DIESEL ENGINES EFFICIENCY

Due to their superior efficiency when compared to other thermal engines especially Spark Ignition engines, Diesel Engines are widely used for applications where high power concentration is required. For this reason, a great deal of research is conducted worldwide to reduce their pollutant emissions and to further improve their efficiency. Taking into account the green house effect that has been recognized the last years caused by increased CO2 emissions, it seems that they offer a reasonable solution for the minimization of this problem. The efficiency of the direct injection diesel engine has been considerably improved during the last decade mainly due to turbo-charging and downsizing technique.

Downsizing Diesel engines consists to reduce its displacement while providing the same maximum power. This is possible thanks to turbo-charging that increases the air filling and thus the specific power (i.e: maximum power per unit displacement) of the engine. Smaller engines have better efficiency than bigger engines, when working under the same load, thanks to better mechanical efficiency and reduced heat losses.

3. PNEUMATIC HYBRIDIZATION OF DIESEL ENGINES

Since the late 1990s, pneumatic hybridization of Internal Combustion Engines has been discussed, but mainly focusing for automotive application. The key idea is to use the engine also as a pump to recuperate the vehicle's kinetic energy during braking phases, and as an expansion motor for propulsion. This can be realized by connecting an air pressure tank to all cylinders via electronically controlled charge valves (Dönitz 2008) as shown in figure 1 – right (ibrabim 2010).

In addition to the recuperation capability, the idea offers the possibility of a rapid start/stop and permits to shift the engine's operating point to high efficiency zones. The latter can be achieved by operating half of the cylinders conventionally while the other half of the cylinders work in the *pump mode*. Previous concepts assumed two-stroke pump and pneumatic motor modes which is possible only if all valves of the cylinders can be variably actuated (Higelin 2002).

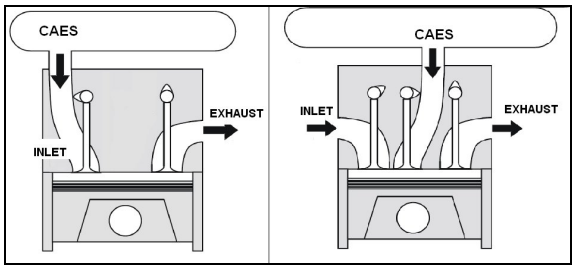

Figure 1: Pneumatic Hybrid ICE Engine through inlet valve (left), and through additional valve (right).

In our current study, we have focused on a more simple technique of Hybridizing Diesel engine. This technique consists in introducing the compressed air through the initial intake valve as shown in figure 1 – left (Ibrahim 2010). The main reason for this choice is to suggest a practical adaptation of existing Diesel power plants installations.

The compressed air is supposed to be previously generated by independent electric air compressor whose energy is provided by wind turbines, during periods of high Wind Power Penetration Rate (WPPR>1), as shown in figure 2 (Ibrahim 2010).

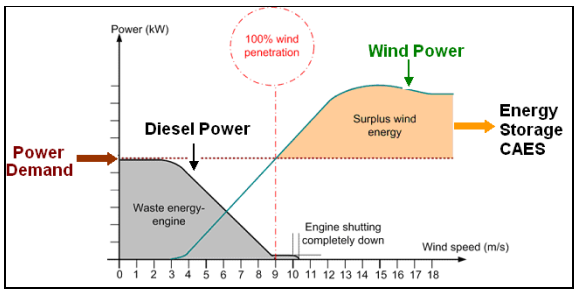

Figure 2: Variation of wind and diesel power with wind speed for a high-penetration Wind Diesel system

4. MATHEMATICAL MODEL

A zero dimensional mathematical model of the thermodynamic Diesel cycle has been developed to and used to conduct our parametric study. The mathematical models used are found in literature review (Heywood 1988; Lopes Correia da Silva 2007; Higelin 2002; Ibrahim 2007). We did not conduct any tests to calibrate and fit our model . We have used parameters that are found in literature review (Guibert 2002). The purpose actually of our study was to give orientations to our conception. In the future, a one dimensional modelling will be conducted to simulate the whole system in steady state mode and in transient mode.

Figure 3 shows the system considered to calculate the evolution of the thermodynamic characteristics (pressure, temperature, specific heat constant, etc…).

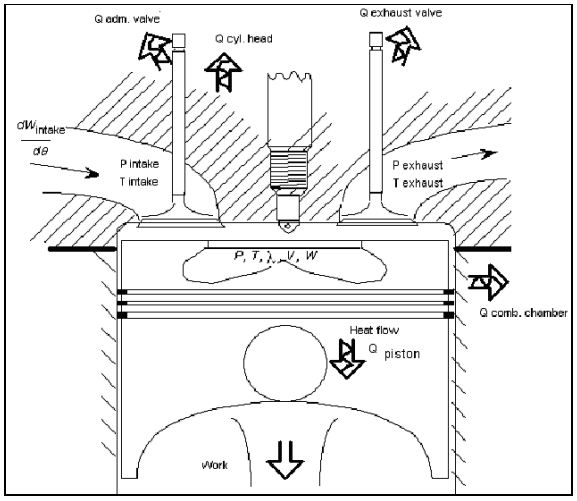

Figure 3: Direct injection Diesel engine simplified model

The hypotheses considered are the following:

1. The thermodynamic equilibrium is established for each step of calculation
2. The mass of gas is a homogeneous mixture of perfect gas. Its thermodynamic characteristics (enthalpy, intern energy, molar mass, etc…) are calculated by interpolation in JANAF thermo-chemical tables (third edition, 1985)
3. The mass transfers occur only through the admission and exhaust valves. The blow-by flow is neglected.
4. The admission back-flow is calculated and taken in consideration. The exhaust flow transferred back to the admission is readmitted in the cylinder at the exhaust temperature.
5. The fuel is injected in the combustion chamber at a constant temperature and it is immediately burned following Wiebe law.
6. The heat transfers occur through the five boundary limits (cylinder head, piston, cylinder wall, exhaust valve and admission valve) that are at a constant and uniform temperature.

4.1. Main equations

Main equations are issued from the mass and heat conservation equations as well as the ideal gas equations review (Heywood 1988).

$$\frac{dW}{dt} = \frac{dW_{intake}}{dt} + \frac{dW_{exhaust}}{dt} + \frac{dW_{inj}}{dt} \quad (1)$$

$$\frac{dW_{air}}{d\theta} = \frac{\frac{dW_{intake}}{d\theta}}{1+\frac{\lambda_{intake}}{\lambda_{st}}} + \frac{\frac{dW_{exhaust}}{d\theta}}{1+\frac{\lambda}{\lambda_{st}}} \quad (2)$$

$$\frac{d\lambda}{d\theta} = \frac{\frac{dW}{d\theta} - \left(1+\frac{\lambda}{\lambda_{st}}\right)\times\frac{dW_{air}}{d\theta}}{W_{air}} \times \lambda_{st} \quad (3)$$

$$\frac{dT}{d\theta} = \frac{A_1 - \frac{\frac{\partial u}{\partial P}}{A_2}\times\left(\frac{\frac{dW}{d\theta}}{W} + \frac{\frac{\partial r}{\partial \lambda}}{r}\times\frac{d\lambda}{d\theta} - \frac{\frac{dV}{d\theta}}{V}\right) - \frac{\partial u}{\partial \lambda}\times\frac{d\lambda}{d\theta}}{\frac{\partial u}{\partial T} + \frac{\partial u}{\partial P}\times\frac{A_2}{A_3}} \quad (4)$$

$$\frac{dP}{d\theta} = \frac{\frac{\frac{dW}{d\theta}}{W} + \frac{\frac{\partial r}{\partial \lambda}}{r}\times\frac{d\lambda}{d\theta} - \frac{\frac{dV}{d\theta}}{V} + A_3\times\frac{dT}{d\theta}}{A_2} \quad (5)$$

Where *A1*, *A2* and *A3* are calculated with equations 6, 7 and 8 (Heywood 1988)..

$$A_1 = \frac{\left(-P\times\frac{dV}{d\theta} + \frac{dQ}{d\theta} + h_{intake}\times\frac{dW_{intake}}{d\theta} + \cdots \right.}{W} \quad \left. \cdots h_{ech}\times\frac{dW_{exhaust}}{d\theta} + h_{inj}\times\frac{dW_{inj}}{d\theta} - u\times\frac{dW}{d\theta}\right) \quad (6)$$

$$A_2 = \frac{1}{P} - \frac{\frac{\partial r}{\partial P}}{r} \quad (7)$$

$$A_3 = \frac{1}{T} + \frac{\frac{\partial r}{\partial T}}{r} \quad (8)$$

4.2. Kinematic model

The volume delimited by the piston, the cylinder wall and the cylinder head can be calculated function of the angular position of the crankshaft θ as shown in equations 9 and 10.

$$V(\theta) = \frac{\pi D^2}{8}\times L\left(1+\frac{R}{L} - cos\,\theta - \sqrt{\left(\frac{R}{L}\right)^2 - sin^2\,\theta} + \frac{2}{\varepsilon - 1}\right) \quad (9)$$

$$\frac{dV(\theta)}{d\theta} = \frac{\pi D^2}{8} \times L \times \sin\theta \times \left(\frac{\cos\theta}{\sqrt{\left(\frac{R}{L}\right)^2 - \sin^2\theta}} + 1 \right) \quad (10)$$

The mean piston velocity is calculated as shown in equation 11.

$$VMP = 2 \times L \times \frac{N}{60} \quad (11)$$

4.3. Intake and exhaust flow models

The first principle of thermodynamics leads to the Baré Saint-Venant model of flow through the admission intake valve as shown in equation 12.

$$\frac{dW}{dt} = A_{intake} \times P_{intake} \times \ldots \sqrt{\frac{2.\gamma_{intake}}{(\gamma_{intake} - 1) \times r_{intake} \times T_{intake}} \times \left[X^{\frac{2}{\gamma_{intake}}} - X^{\frac{\gamma_{intake}+1}{\gamma_{intake}}} \right]} \quad (12)$$

Where X is the maximum found between two values as shows equation 13.

$$X = max\left(\frac{P}{P_{intake}} ; \left(\frac{2}{\gamma_{intake} + 1} \right)^{\frac{\gamma_{intake}}{\gamma_{intake} - 1}} \right) \quad (13)$$

4.4. Backflow model

Backflow is an undesirable phenomenon that reduces the amount of the amount of fresh air admitted in the engine. It occurs during the intake phase and during the exhaust phase.

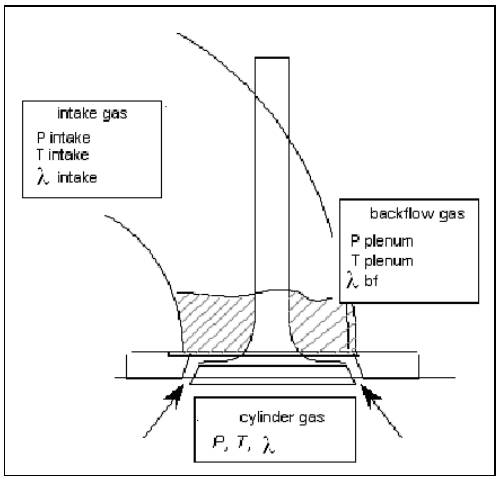

Figure 4: intake backflow phenomena illustration

As shown in figure 4 (case of admission backflow), the exhaust gas that backflow to the admission through intake valve are readmitted in the cylinder in the next cycle. The hypothesis taken for modelling the backflow are the following:

1. the exhaust gas is a homogeneous mixture
2. the temperature of the backflow gas is constant and is equal to the exhaust gas temperature
3. the pressure of the exhaust gas is equal to the intake pressure

The mass conservation laws applied to the admission can be written as shown in equation 14:

$$dW_{bfl} = -dW(\theta) \quad (14)$$

If *P>Pintake*, gas is backflow and *dW(θ)* is calculated with equation 12 after inverting in and out.

If *P<Pintake,* backflow gas are readmitted and *dW(θ)* is calculated with equation 12 in its standard form, until W_{bfl} equals to zero.

4.5. Combustion model

The accurate description of the combustion process in the Diesel engines requires the knowledge of different phenomena that occur starting with the fuel injection and ending with its transformation into combustion products. This knowledge needs the study of the aerodynamic motion in the combustion chamber, the penetration and the vaporization of the fuel as well as the self ignition delay and the combustion itself. Those phenomena cannot be modelled without a three dimensional study.

In our study, we have decided to simplify the modelling work in order to demonstrate a first order potential of our technical solution. A global approach of the combustion process has been modelled considering four phases:

1. The phase of the delay of self ignition: the injected fuel does not start burning before this delay ends
2. The phase of the pre-mixed combustion, where the fuel injected during the delay of self ignition is burned.
3. The phase of the diffusion combustion: while the injection is still ongoing and the combustion chamber is already hot, the combustion happens almost instantly and its speed is limited by the injection flow rate.
4. The final combustion phase: After the fuel injection ends, the remaining unburned fuel (relatively small quantity) burns slowly depending on the diffusion phenomena.

The global combustion model can be simplified by the combination of two Wiebe laws (Wiebe 1970). The first one describes the *pre-mixed combustion* and the second one describes the *diffusion combustion.* Each Wiebe law allowing the calculation of the burned fuel ratio is written as shown in equation 15.

$$xb = \frac{1 - exp\left(-w \times \left(\frac{\theta - \theta_{phase}}{\Delta\theta_{phase}}\right)^{m+1}\right)}{1 - exp(-w)} \quad (15)$$

Where m and w are constants verifying the equations 16 and 17.

$$w = \frac{m}{m+1} \times \frac{1}{\left(\frac{\theta_{HLC} - \theta_{phase}}{\Delta\theta_{HLC}}\right)^{m+1}} \quad (16)$$

$$HLC = \frac{m}{\left(\frac{\theta_{HLC} - \theta_{phase}}{\Delta\theta_{HLC}}\right)} \times \frac{\exp\left(-\frac{m}{m+1}\right)}{1 - \exp(-w)} \times \frac{1}{\Delta\theta_{phase}} \quad (17)$$

The contants above should be calibrated in order to fit with the studied engine performance. As mentioned previously, no test was conducted to fit those constants with a specific engine. All the parameters were taken from literature review (Guibert 2002).

4.6. Heat transfers model

Heat transfers through boundary limits are described with equation 18.

$$\frac{dQ}{d\theta} = \sum_{j=boundary} \varphi . A_j . (CT1 \cdot (Tj - Tsc) + CT2 \cdot (Tsc - T)) \quad (18)$$

Where the thermal exchange coefficient φ is calculated with Woschni (Woschni 1967) model illustrated in equation 19.

$$\varphi = 12.986 \times 10^{-3} \times D^{-0,2} \times P^{0.8} \times T^{-0,53} \times ... \\ ... \left(2.28 \times VMP + 0.00324 \times \frac{Vs \times T0}{V0 \times P0} \times (P - Psc)\right)^{0.8} \quad (19)$$

5. RESULTS AND DISCUSSIONS

5.1. Parametric study conducted

In order to demonstrate the potential of the pneumatic hybridization of the Diesel engine, we have conducted a parametric study varying simultaneously the intake and exhaust pressure. The intake temperature is considered constant and equals to 293 K.

Unfortunately, increasing intake pressure is constrained by stress levels in critical mechanical components. These maximum stress levels limit the maximum cylinder pressure which can be tolerated under continuous operation, though the thermal loading of critical components can become limiting too. As boost pressure is raised, unless engine design and operating conditions are changed, maximum pressures and thermal loadings will increase almost in proportion (Heywood 1988).

Reliability criteria of most common Diesel engines specify 200 bars and 1100 K as limits not to be exceeded. Those limits were taken in consideration in our parametric study.

5.2. Operating at low loads (BMEP = 5 bars)

Figure 5 shows the variation of the specific fuel consumption of the Diesel engine function of the intake and exhaust pressure for a fixed mechanical output equivalent to a BMEP of 5 bars. Natural aspirated engines have an inlet and exhaust pressure close to 1 bar, thus the specific consumption is about 250 g/kWh. Turbocharged Diesel engines has higher intake pressure but also higher exhaust pressure as well. At low loads, exhaust pressure are slightly higher than intake pressure because the exhaust gas enthalpy is relatively low. Previous work (Ibrahim 2007) has showed that intake pressure and exhaust pressure at BMEP of 5 bars for the same engine, are respectively 1.7 bar and 1.9 bar.

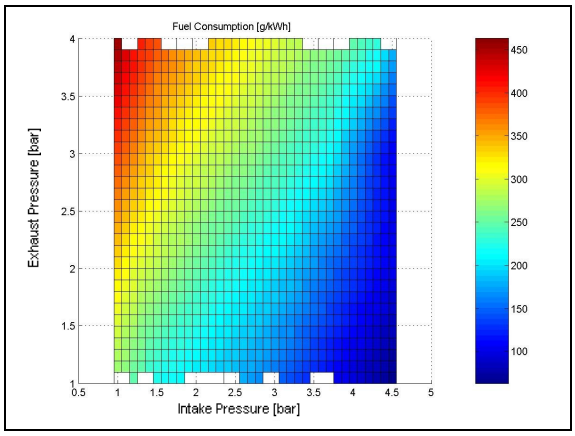

Figure 5: Fuel consumption at BMEP of 5 bars, function of intake and exhaust pressures

As we can see in figure 12, the maximum cylinder pressure increases directly and significantly with intake pressure and it is relatively independent from exhaust pressure. The maximum allowed pressure is reached at an intake pressure of 4.5 bars.

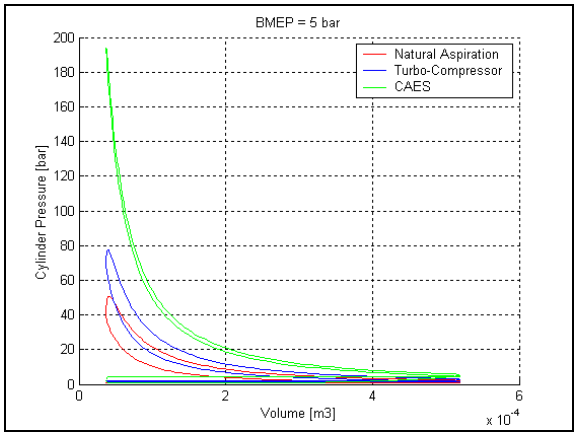

Figure 6: P-V Diagram of Thermodynamic Diesel cycle for Natural Aspirated engine (red), Turbocharged

engine (blue) and pneumatic hybrid engine (green), at BMEP of 5 bars

According to figure 5, the specific consumption for the turbocharged engine working will be close to 275 g/kWh. Now if the CAES is used to increase the inlet pressure until the peak cylinder pressure reaches its maximum allowed and the turbine is removed, the optimal operating point will be for an inlet pressure of 4.5 bars and an exhaust pressure of 1 bar. The specific consumption will be 75 g/kWh; witch is an improvement of about 70% comparing to natural aspirated engines and turbocharged engines. The reasons of this apparently huge improvement are explained as follows.

Figure 6 shows the thermodynamic Diesel cycle for the three operating types above. The three cycles develop the same area. We can observe that the more the intake pressure is, the higher is the peak pressure and the thinner is the shape high pressure cycle.

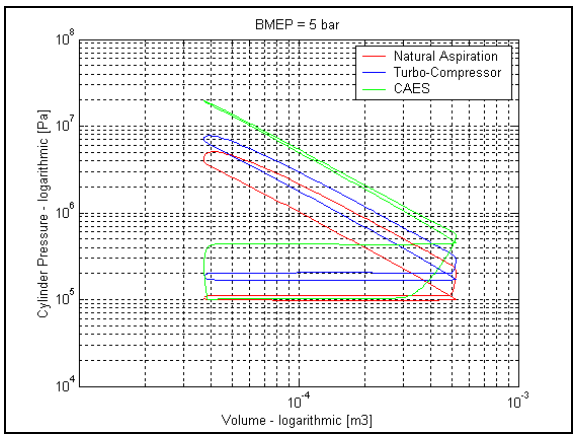

Figure 7: Log (P)-Log (V) Diagram of Thermodynamic Diesel cycle for Natural Aspirated engine (red), Turbocharged engine (blue) and pneumatic hybrid engine (green), at BMEP of 5 bars

Figure 7 is the same as figure 6 but drawn with a logarithmic scale. We can notice the difference in the low pressure cycle. For both Natural aspirated and Turbocharged operation, the low pressure cycle does not contribute significantly in the BMEP; at the opposite, for operation with CAES, the positive gap between inlet pressure and exhaust pressure generates work that contributes significantly in BMEP, as shown also in figure 9. This work is purely pneumatic and does not result from any combustion.

Figure 9 shows the contribution of the pneumatic *green* power in the total power generated by the engine. We can observe that for the highest allowed intake pressure and lowest exhaust pressure, the contribution is positive and can reach 40% witch means 40% of direct fuel saving. On the other hand, increasing intake pressure and reducing exhaust pressure make this contribution negative and thus increases the fuel consumption.

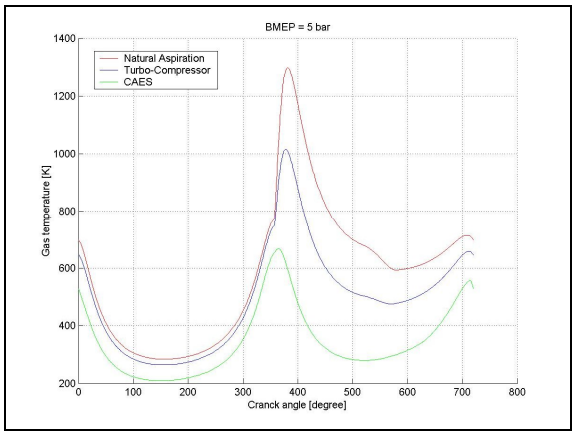

Figure 8: Instant cylinder gas temperature for Natural Aspirated engine (red), Turbocharged engine (blue) and pneumatic hybrid engine (green), at BMEP of 5 bars

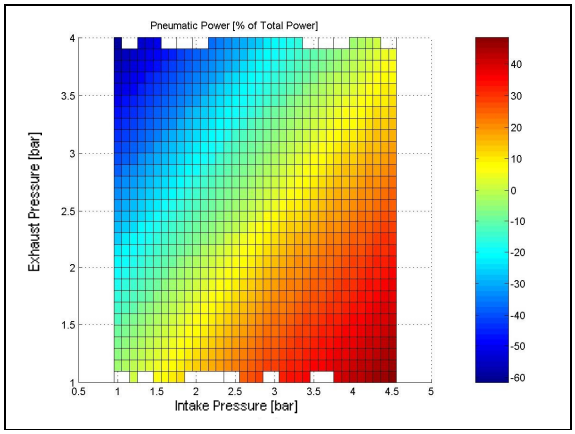

Figure 9: Contribution of the pneumatic power in the total power at BMEP of 5 bars, function of intake and exhaust pressure

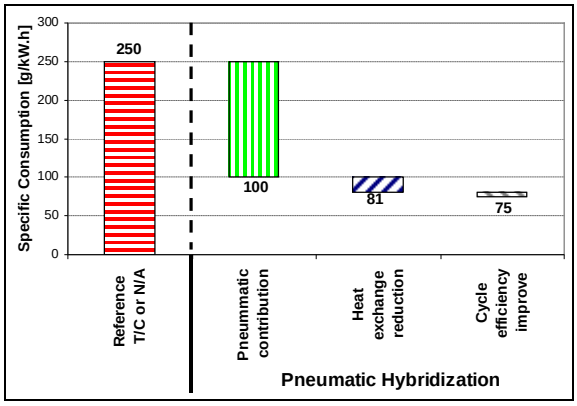

Figure 10: Fuel reduction contribution at BMEP of 5 bars, for Inlet pressure and exhaust pressure of 5 bars and 1 bar respectively

As shown in figure 10, the improvement in fuel consumption is not only the due to pneumatic power contribution, but also to two other phenomena:

1. The first phenomenon is the significant reduction of the heat exchange thanks to two reasons:
   (a) less fuel burned because less high pressure BMEP is needed to provide the target BMEP
   (b) higher air density and therefore high calorific capacity

   The heat exchange is responsible of about 25% according to figure 11 (Heywood 1988; Wanhua 2009) of the total loss in the engine. The gas temperature decrease from a Turbocharged engine to CAES assisted engine, reaches up to 300 K as shows figure 8. The thermal loss reduction is therefore around 30%.
2. The second phenomenon responsible of the remaining improvement is the increase of the combustion velocity thanks to the increase of air density and therefore the *cycle efficiency*.

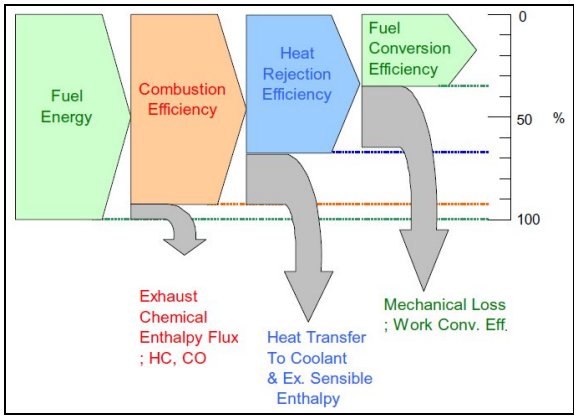

Figure 11: Typical fuel energy flow and efficiencies and losses in internal combustion engines (Heywood 1988; Wanhua 2009)

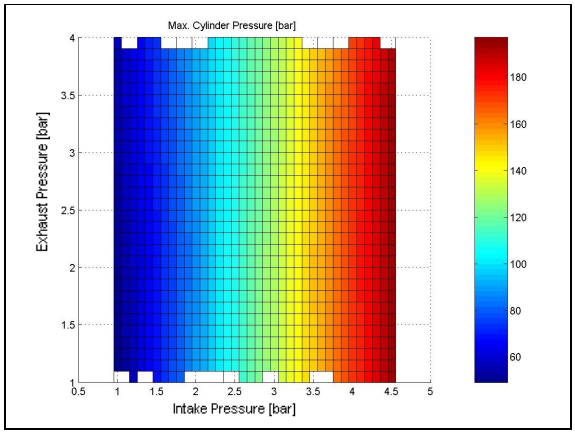

Figure 12: Peak cylinder pressure at BMEP of 5 bars, function of intake and exhaust pressures

The main limitation for fuel economy is the maximum allowed pressure in the combustion chamber. Increasing the admission pressure causes a much higher increase of the maximal pressure in the cylinder. For the Diesel engine specified above, 200 bars in the combustion chamber is reached when the admission pressure is about 5 bars at low engine load and 3.5 bars at high load.

5.3. Operating at medium loads (BMEP = 10 bars)

Operating at a BMEP of 10 bars is considered a medium load for turbocharged engine but is a full load for Natural Aspirated engine.

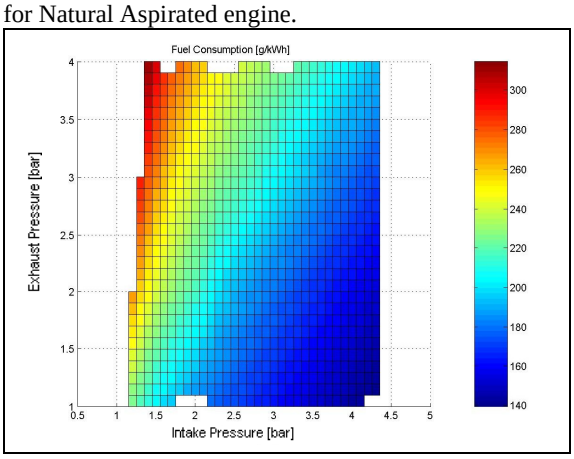

Figure 13: Fuel consumption at BMEP of 10 bars, function of intake and exhaust pressures

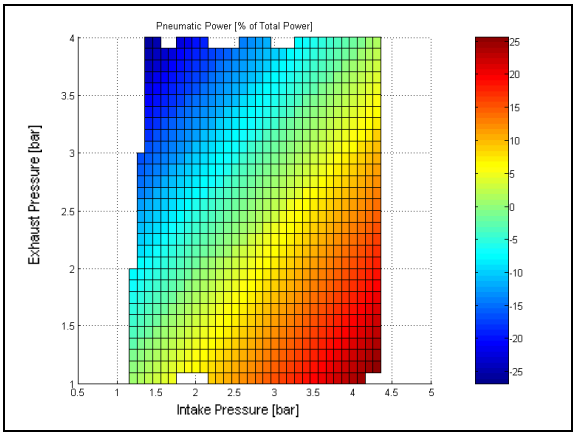

Figure 14: Contribution of the pneumatic power in the total power at BMEP of 10 bars, function of intake and exhaust pressure

For both turbocharged engine where the intake pressure and the exhaust pressure are both around 2.5 bars (Ibrahim 2007) and Natural aspirated engine where the intake pressure and the exhaust pressure are both around 1 bar, the fuel consumption is around 210 g/kWh, as shows figure 13.

Working under CAES assistance, at the limit of stress acceptance, intake pressure is 4.4 bars and exhaust pressure is 1 bar, therefore the fuel consumption is 140 g/kWh as shows figure 13, witch corresponds to an improvement of 33%. The pneumatic

power contribution in the total power reaches 20% as shown in figure 14.

As shown in figure 15, heat loss reduction improve contribute significantly in the global fuel economy, thanks to a great temperature drop of the gas in the cylinder chamber, that reaches up to 200 K.

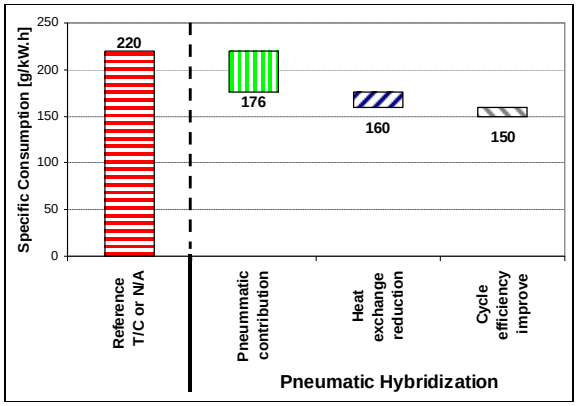

Figure 15: Fuel reduction contribution at BMEP of 10 bars, for Inlet pressure and exhaust pressure of 4 bars and 1 bar respectively

5.4. Operating at high loads (BMEP = 15 bars)

Natural Aspirated Engines cannot provide a torque equivalent to BMEP of 15 bars, while Turbocharged engines can do that. For turbocharged engine where the intake pressure and the exhaust pressure are both around 3 bars (Ibrahim 2007), the fuel consumption is around 210 g/kWh, as shows figure 16.

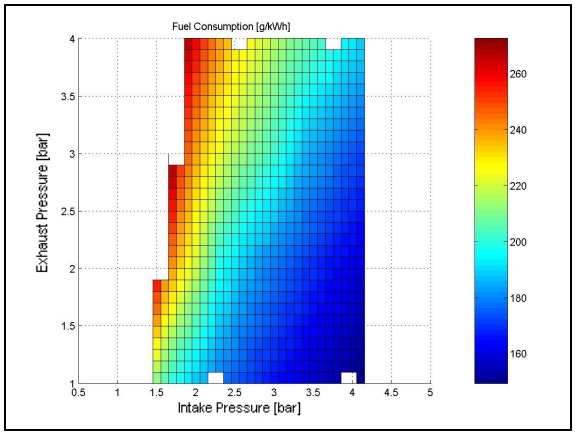

Figure 16: Fuel consumption at BMEP of 15 bars, function of intake and exhaust pressures

Working under CAES assistance, at the limit of stress acceptance, intake pressure is 4 bars and exhaust pressure is 1 bar, therefore the fuel consumption is 150 g/kWh as shows figure 15, witch corresponds to an improvement of 28%. The pneumatic power contribution in the total power reaches 15% as shown in figure 17.

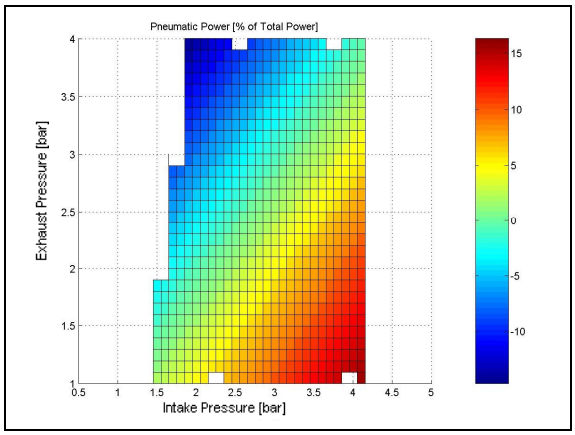

Figure 17: Contribution of the pneumatic power in the total power at BMEP of 15 bars, function of intake and exhaust pressure

Figure 18 shows the contribution of different phenomenon in fuel economy under CAES assistance at the maximum intake pressure allowed and the minimum exhaust pressure.

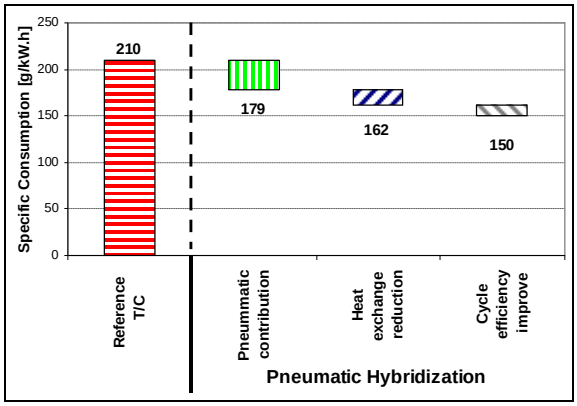

Figure 18: Fuel reduction contribution at BMEP of 15 bars, for Inlet pressure and exhaust pressure of 4 bars and 1 bar respectively

6. IMPACT OF PNEUMATIC HIBRIDIZATION ON POLLUTANT EMISSIONS

As mentioned in the previous paragraph, working under CAES assistance reduces significantly the temperature of gas in the combustion chamber. Previous work indicates that the lowered combustion temperature in diesel engines is capable of reducing soot and nitrogen oxides (NOx) simultaneously (Zheng 2006). CAES has therefore the same effect as Exhaust gas recirculation used in most Diesel applications in order to reduce NOx emissions. Figure 19 shows the impact of local temperature and equivalence ratio in the combustion chamber on the soot and NOx formation.

Operating with a high admission pressure and low exhaust pressure moves the local conditions in the combustion chamber to the right bottom side of Pischinger Diagram and therefore minimizes the

chances of NOx and soot formation and maximizes the chances of soot oxidation. Therefore the pneumatic hybridization of Diesel engines is expected to have a positive effect on pollutant emissions as well as greenhouse gas emissions.

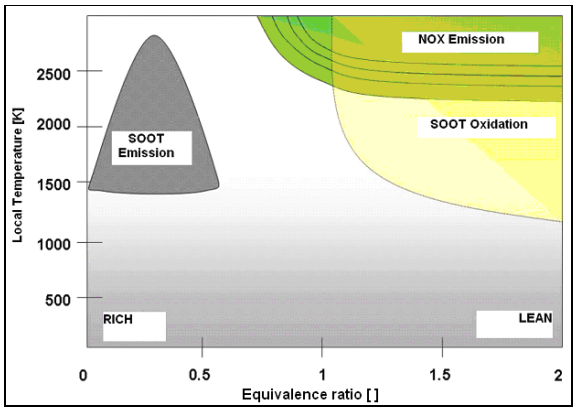

Figure 19: Pischinger Diagram (Pischinger 1988)

7. CONCLUSION

Increasing up to 4.5 bars the pressure at intake and decreasing down to 1 bar the pressure at exhaust of the Diesel engine results in increasing the power produced by the engine for the same fuel quantity and therefore improving the Diesel efficiency considering that the Compressed Air is free of charge. This improvement can reach up to 70% for the low loads (BMEP = 5 bar) and up to 40% for the high loads (BMEP = 15 bar), for a Diesel engine whose compression ratio is 14 and maximum allowed cylinder pressure is 200 bars.

This improvement is a combination of three phenomena:

1. The Low Pressure BMEP usually slightly negative for Turbo-Compressed engines and Natural Aspirated Engines becomes positive and therefore generates pure pneumatic power. The ratio of this pneumatic power to the total power can reach up to 40% for low loads and 10% for high loads.
2. The increase of intake air density reduces significantly the temperature in the cylinder and therefore reduces the thermal loss with the cylinder borders. This thermal loss is usually responsible of about 25% of the total loss in the engine. The gas temperature reduction due to increasing of air pressure can reach up to 200 K for low loads, and 350 K for high loads; the thermal loss reduction is therefore around 30% for low loads and 60% for high loads.
3. The increase of the combustion velocity thanks to the increase of air density and therefore the *cycle efficiency* is responsible of the remaining improvements.

In addition to its potential in fuel economy and greenhouse gas emission reduction, Diesel pneumatic hybridization is expected to have positive effect on pollutants emissions such as nitrogen oxides and soot.

NOMENCLATURE AND ABREVIATIONS

A	Effective area [m^2]
Aj	Boundary areas involved in heat transfer [m^2]
Cp	Specific heat capacity at constant pressure [J/kg/K]
$CT1$	Multiplicative coefficient
$CT2$	Multiplicative coefficient
Cv	Specific heat capacity at constant volume [J/kg/K]
D	Bore [m]
h	Enthalpy [J/kg]
HLC	Maximum heat release rate [1/deg]
L	Stroke [m]
N	Engine angular speed [RPM]
P	Pressure [Pa]
Psc	Gas pressure in the chamber if there was no combustion [Pa]
$P0$	Pressure of combustion chamber at the intake valve close [Pa]
Q	Heat transfer [j]
R	Manivelle radius [m]
T	Absolute temperature [K]
Tj	Mean temperatures of the boundary areas involved in heat transfer [K]
Tsc	Gas temperature in the chamber if there was no combustion [K]
$T0$	Temperature of combustion chamber at the intake valve close [K]
u	Internal specific energy [J/kg]
V	Volume [m^3]
VMP	Mean piston velocity [m/s]
Vs	Combustion chamber volume at Bottom Dead Centre [m3]
$V0$	Volume of combustion chamber at the intake valve close [Pa]
W	mass of gas [kg]
$WPPR$	Wind power penetration rate [%]
xb	Proportion of burned fuel [ ]
$_{air}$	Refers to fresh air conditions
$_{bfl}$	Refers to Backflow conditions
$_{exhaust}$	Refers to exhaust conditions
$_{inj}$	Refers to injected fuel conditions
$_{intake}$	Refers to intake conditions
$_{phase}$	Refers to the combustion phase start
$_{stoch}$	Refers to stoichiometry conditions
ε	Compression ratio [ ]
Θ	Crankshaft angle [deg], where 360° refers to combustion phase Top Dead Center
Φ	Thermal exchange coefficient [J/m^2K]
λ	Equivalence ratio
r	Perfect gas constant [J/kg/K]
γ	Specific or molar volume [ ]

REFERENCES

Dönitz, C., Vasile, I.C., Onder, C.H., and Guzzella, H., 2009, Modelling and optimizing two- and four-stroke hybrid pneumatic engines, *IMechE*.

Guibert, P., 2002, *Etude des cycles thermodynamiques des moteurs thermiques et modélisation*, Rueil Malmaison, Ecole Nationale Supérieure du Pétrole et des Moteurs.

Heywood, J.B., 1988, *Internal Combustion Engine Fundamentals*, New York, McGraw Hill.

Higelin, P., Charlet, A., Chamaillard, Y., 2002, Thermodynamic Simulation of a Hybrid Pneumatic-Combustion Engine Concept, Int.J. *Applied Thermodynamics*, Vol.5, (No.1), p.1-11,

Ibrahim H., Ilinca A., Younes R., Basbous T., 2007, Study of a Hybrid Wind-Diesel System with Compressed Air Energy Storage, *IEEE Canada*,

Ibrahim H., Ilinca A., Younes R., Basbous T., 2007, Study of a Hybrid Wind-Diesel System with Compressed Air Energy Storage*, Renewable and Alternative Energy Ressources*.

Ibrahim H., 2010, *Etude et conception d'un générateur hybride d'électricité de type Eolien-Diesel avec élément de stockage d'air comprimé*, PHD, Université du Québec à Chicoutimi.

Lopes Correia da Silva, L., 2007, Simulation of the Thermodynamic Processes in Diesel Cycle Internal Combustion Engines, *SAE*, 931899.

Pischinger, F., Schulte, H., and Hansen J., 1988, *Grundlagen und Entwicklungslinien des dieselmotorischen Brennverfahren*, Düsseldorf, VDI-Berichte, p. 61-93.

Wiebe, I., 1970, Brennverlauf und Kreisprozess von Verbrennungsmotoren. Berlin, Verlag Technik, p. 286.

Wanhua, S., Yingying, L., Wenbin, Y., Changqing W., and Yiqiang, P., 2009, Density-Low Temperature Combustion in Diesel Engine Based on Technologies of Variable Boost Pressure and Intake Valve Timing, *SAE*, 2009-01-1911.

Woschni, G., 1967, A universally applicable equation for the instantaneous heat transfer coefficient in the internal combustion engine, *SAE*, 670 931.

Zheng, M., and Reader, G.T. Reader, Adaptive Control to Improve Low Temperature Diesel Engine Combustion, *12th Diesel Engine-Efficiency and Emission Reduction Conference*, 2006

ANALYSIS OF RENEWABLE ENERGY POTENTIAL OF HYBRID SYSTEMS FOR DWELLINGS IN FRANCE

Philippe POULET[(a)], Rachid OUTBIB[(b)]

[(a,b)]LSIS UMR CNRS 6168
Domaine Universitaire de Saint-Jérôme, Avenue Escadrille Normandie-Niemen, 13397 Marseille Cedex 20, France

[(a)]philippe.poulet@lsis.org, [(b)]rachid.outbib@lsis.org

ABSTRACT
In this study, the renewable energy potential for dwellings in France is analyzed. Generally, conventional solution consists in using solar panels and wind generator as energy resource. More precisely, the solar thermal panels are used to produce the thermal energy needs, and electricity is provided by wind generator and photovoltaic solar panels.

The goal of this work is to explore an alternative strategy based on an original hybridation of sources. In this alternative solution, a large part of the solar thermal panels is replaced by photovoltaic panels and a heat pump is introduced to ensure a crossover between the thermal energy flow and the electrical energy flow. The simulation results during one year for representative sites in France demonstrate a significant decrease of the missing energy.

This clearly establishes that a higher hybridation level improves the capacity of a renewable energy system to become autonomous.

Keywords: Renewable energy, Wind turbine, Photovoltaic array, Hybrid; Heat pump

1. INTRODUCTION

The main energy resources used in the world for more than one century have major drawbacks. They are fossils for almost 90% and the most optimistic projections about the depletion of oil and gas do not exceed one century (World Energy Council 2007).

They are also considered as the cause of global warming due to the release of carbon dioxide in the atmosphere. Moreover, their production is far away from the consumer because of their geographical distribution. Europe for example has no significant resources of oil, gas and uranium that are yet its main primary energy (World Energy Council 2007). Concerning France, the dwelling sector alone accounts for 25% of the total consumption of primary energy. In these 25%, more than 20% meet the thermal needs (hot water, cooking), and 4% the specific electrical needs (lights, electrical devices) (Ademe 2007).

Nowadays, in France, nuclear energy represents 40% of the primary energy consumption and provides 80% of electricity. This was and still presented as a gage of energetic autonomy. France is less oil dependant than other occidental countries, but its economic needs are dependent on uranium. Notice that, in the first hand, the uranium is also a limited resource, and in the other hand, France imports all its needs concerning uranium. Finally, Frances faces a similar problem than with oil.

Moreover, despite the excellent mastery of nuclear technology, the probability of a nuclear catastrophe is not null. This fact has to be seriously considered to develop green energies. Among the possible solution International Thermonuclear Experimental Reactor (ITER) project, a mass energy production system is now explored. ITER's mission is to demonstrate feasibility of fusion power, and prove that it can work without negative impact. Until the hypothetical success of this project, other solutions have to be explored.

These other solutions mainly consist of a better use of local energies. These local energies are solar energy and its derivative such as wind energy and biomass energy. Therefore, due to the variability of each local energy source, hybridation in sources and storage systems is necessary to meet the needs.

Therefore the configuration of the hybrid system will necessarily depend on geographical and socio-economic considerations. Thus, studies have been conducted on such energies potential in countries like Turkey (Ucar and Figen 2009), Tunisia (Elamouri and Ben-Amar 2009), Egypt (Ahmed-Shata and Hanitsch 2006), Syria (Al-Mohamad 2004), Saudi Arabia (Rehman and Al-Abbadi 2007), Kuwait (Al-Nassar, Al-Hajraf, Al-Enizi and Al-Awadhi 2007), Nigeria (Ngala, Alkali and Aji 2007), Cameroon (Tchindaa, Kendjioa, Kaptouoma and Njomob 2000), Hungary (Radics and Bartholy 2008), Lithuania (Marciukaitis and Katinas 2008), Greece (Bagiorgas, Assimakopoulos, Theoharopoulos, Matthopoulos and Mihalakakou 2007), Netherlands (Schenk, Moll, Potting and Benders 2007), Guadalupe- France (Tarkowski and Uliasz-Misiak 2003), Spain (Ordonez and Jadraque 2010) and Lebanon (Moubayed, El-Ali and Outbib 2009).

Generally speaking, in conventional renewable energy systems, thermal solar panels with water tanks are the most common solution to provide heat from solar radiations. To provide electricity, photovoltaic

NOMENCLATURE

η_0	Rated efficiency for the EN 12975 thermal solar panel model
τ	Time constant of the house (s)
a_{1a}	Coefficient of heat losses for the EN 12975 thermal solar panel model ($W.m^{-2}.K^{-1}$)
a_{2a}	Coefficient of heat losses for the EN 12975 thermal solar panel model ($W.m^{-2}.K^{-2}$)
a_i	Coefficient of the model of the heat pump rated absorbed power
b_i	Coefficient of the model of the heat pump rated produced power
G_h	Global solar radiation on horizontal surfaces ($W.m^{-2}$)
G_i	Global solar radiation on inclined surfaces for the EN 12975 thermal solar panel model ($W.m^{-2}$)
G_v	House global Coefficient of heat exchange ($W.K^{-1}$)
K_{PV}	Coefficient of temperature of the cells for the photovoltaic panels model ($K.W^{-1}.m^{-2}$)
K_u	Charge Coefficient of the heat pump
K_{wpv}	Temperature Coefficient of the maximum power for the photovoltaic panel ($W.K^{-1}$)
P_{ec}	Electrical consumption (kW)
P_{ehp}	Electrical consumption of the heat pump (kW)
P_{epv}	Electrical power of the photovoltaic panels (kW)
P_{erhp}	Rated electrical consumption of the heat pump (kW)
P_{ewg}	Electrical power of the wind generator (kW)
P_e	Electrical power sent or extract from the electrical storage (kW)
P_{thp}	Thermal energy production of the heat pump (kW)
P_{trhp}	Rated thermal energy produced by the heat pump (kW)
P_{ttsp}	Thermal power of the solar thermal panels (kW)
Q_{max}	Thermal storage capacity (kWh)
Q_s	Thermal storage level (kWh)
t_a	Ambient temperature of the air for the EN 12975 thermal solar panel model (K)
t_{in}	Inlet temperature of the water for the EN 12975 thermal solar panel model (K)
t_m	Medium temperature of the water for the EN 12975 thermal solar panel model (K)
t_w	Heat pump outlet water temperature (°c)
t_{out}	Outlet temperature of the water for the EN 12975 thermal solar panel model (K)
t_{PV}	Temperature of the cells for the photovoltaic panels model (K)
t_{sp}	House temperature set point (°c)
t_{STC}	Temperature of the cells of the photovoltaic panels in Standard Test Conditions (K)
W_{emax}	Electrical storage capacity (kWh)
W_e	Electrical storage level (kWh)

panels and wind generators are the most common solutions, and the storage solution is chemical batteries. Finally, the systems are composed by two independent systems. The first one meets the thermal needs and the second one meets the electrical needs.

The goal of this work is to explore an alternative strategy for energy production in France based on an original hybridation of sources and way of storage. To this hand, a local analysis of energy potential in France is necessary. Hence, the paper is dedicated to an analysis of energy autonomy of dwellings powered by renewable energy systems in France. This is done by introducing a cross over between the thermal energy flow and the electrical energy flow, using a heat pump. The electricity provided by photovoltaic panels and/or wind generator can also be converted into thermal energy by the heat pump. Thus, the energy management in this alternative solution is improved since one system manages the energy for all the needs.

The paper is organized as follows. In the second section, the configuration of the considered dwelling and two energy systems to power it are presented, and the characterizations of the system components are developed. This work is done under the hypothesis that the storage capacity for the thermal energy and electrical energy are similar for the two solutions. In the third section, results of the simulation are presented and compared. Finally, in the last part, a conclusion with perspectives is discussed.

2. DESCRIPTION OF SYSTEM COMPONENTS

The goal of this section is to present the models used for the simulation of the whole system.

2.1. Weather data

In renewable energy systems for dwellings, the difficulty is the hazardous energy production that is not synchronous with the needs, not only during the day but also throughout a year. Seasonal variations on solar radiation, wind potential and heating requirements are presented in this section for three different sites (see fig. 1).

The data (from Météofrance statistics, Météofrance is the French national meteorological organism)

conducted over the period 1970-2000 are expressed as a percentage of the maximum to bring out seasonal fluctuations. Overall, the evolution of the solar radiation is not in phase with heating requirements quantified here by the Degree Day method, while wind power for these three areas the most populated in France shows a more regular evolution during one year, even in phase with the heating requirements.

In this simulation, the hourly weather data are provided by the software METEONORM 6.1 (Edition 2009), which is a comprehensive meteorological reference, incorporating a catalogue of meteorological data and calculation procedures for solar applications and system design at any desired location in the world (Remund, Kunz, Schilter and Müller 2009). Hourly data for radiation on inclined surfaces, air temperature and wind speed are generated from meteorological statistics. These data are used to calculate the energy potential of different sites in France.

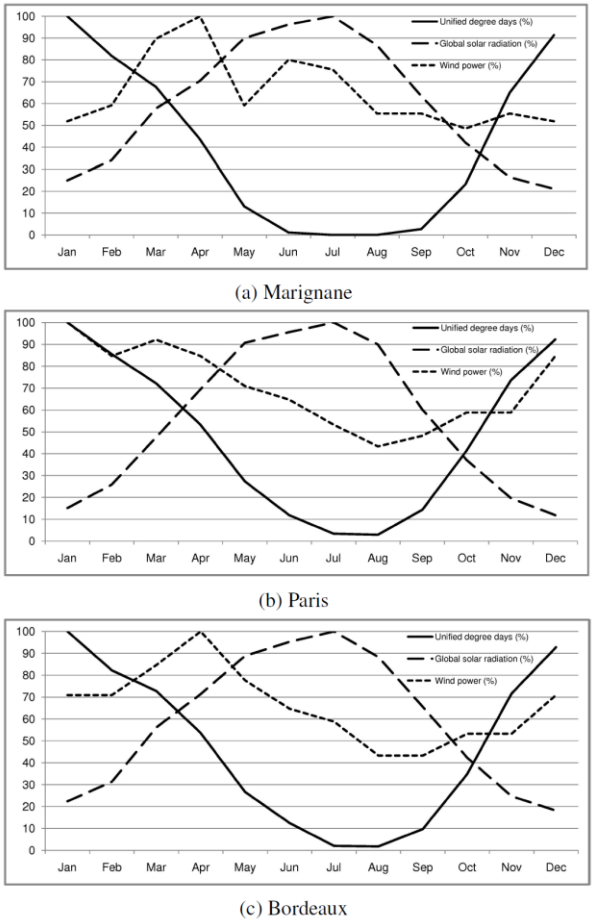

(a) Marignane

(b) Paris

(c) Bordeaux

Figure 1: Seasonal Fluctuation of Heating Needs and Energy Potentials

2.2. House under consideration

In this study, the building is a standard house of 100m2. This house has a global coefficient of heat exchange G_V (Flach-Malaspina 2004) and a time constant τ = 8h = 28800s.

The temperature set point inside house is assumed to be T_{sp} = 19°c (292,15K) for every time. Then, the thermal needs for heating can be expressed :

$$\frac{G_{v\times(T_a-T_{sp})}}{1+\tau p}$$

with T_a the outside temperature of the air (K)

The house is south oriented, and has a A_{gs} = 6m^2 glass surface south exposed. The efficiency of glass surfaces concerning the solar radiations is given to be 80%. In that condition, the energy provided by glass surfaces is equal to $0.8 \times G_{90}$ (the global solar radiation on vertical surfaces [W.m^{-2}]).

The daily electrical consumption is 17kWh (see fig. 2). Forty percent of the electrical energy consumed is Joule losses which heat the house. A part of the losses of the storage tank, due to its localization in the house, also heat the house. The area available for roof integrated solar systems is 60m^2. A garden can receive a wind turbine without major embarrassment for the neighborhood.

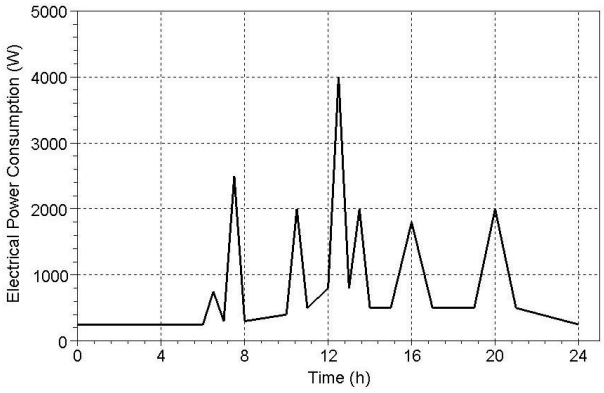

Figure 2: Profile of Daily Electrical Consumption

The usable area of roof is facing south and has a slope of 30°. The air volume to heat is 250m^3 and the air change rate is 0.3 volume per hour. The heating system is a low temperature heating floor, with a maximal temperature of 35°c (308,15K).

2.3. First configuration

The first configuration is as in figure 3 and figure 4. In that configuration, 40m^2 of useful surface for panels are used for photovoltaic panels, and 20m^2 for the thermal panels.

A 10kW heat pump (for a 7°c air temperature and a

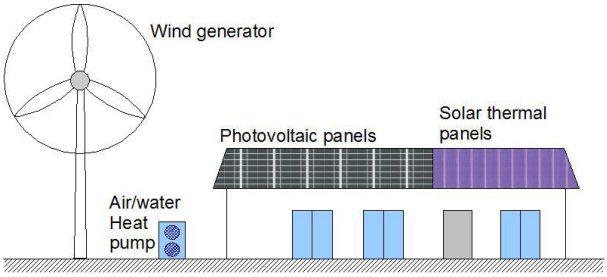

Figure 3: Implantation of the Hybrid System

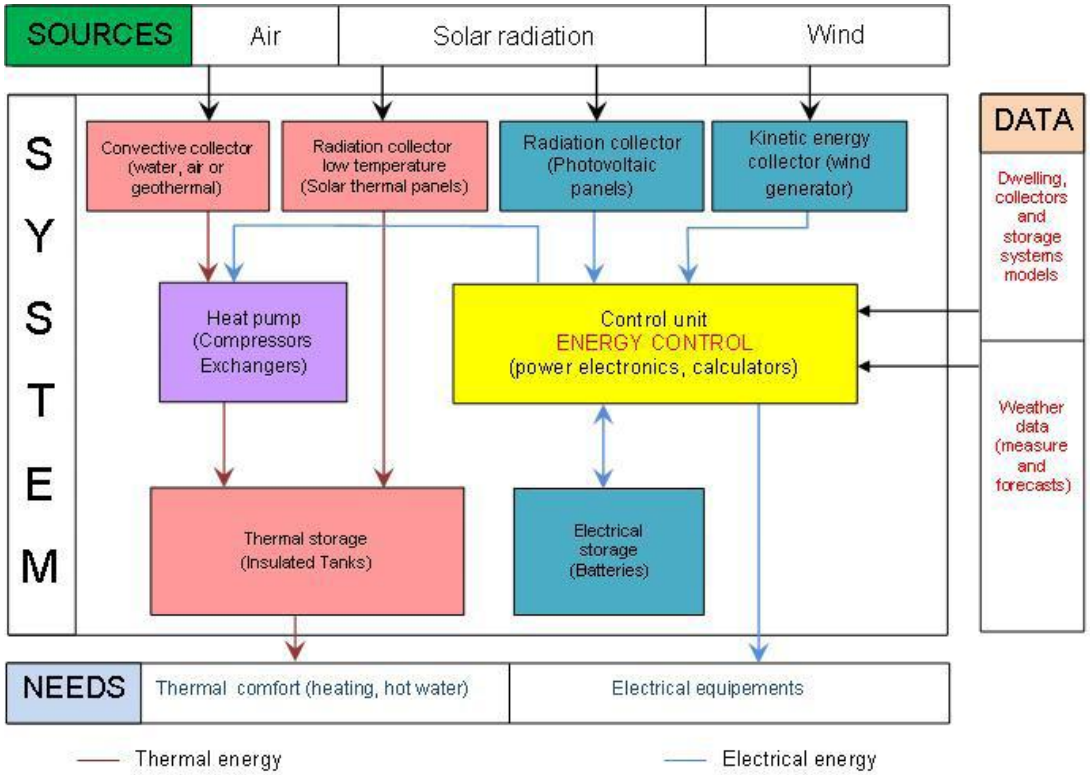

Figure 4: Configuration of the Hybrid System

35°c water temperature) is used to produce heat from the electricity provided by photovoltaic panels and wind generator. Then, this configuration produces heat from thermal panels, photovoltaic panels or from wind generator. Electricity is assumed to be produced by both photovoltaic panels and wind generator.

2.4. Second configuration

The second configuration is as in figure 3 and figure 4, except there is no heat pump and no photovoltaic panels. So, the 60m^2 of useful surface for panels are integrally used for thermal panels. Then, this configuration produces heat only from thermal panels and electricity only from wind generator.

2.5. The solar energy collectors

2.5.1. The thermal solar panels

The model used is the standard EN 12975. The functional dependence of the collector efficiency on the meteorological and system operation values can be expressed by the following mathematical equation :

$$\eta_{(G,(t_m-t_a))} = \eta_0 - a_{10}\frac{t_m - t_a}{G_i} - a_{2a}\frac{(t_m - t_a)^2}{G_i}$$

with $t_m = \frac{t_{in}-t_{out}}{2}$.

The coefficients η_0, a_{10}, a_{2a} have the following meaning:

- η_0: efficiency without heat losses, which means that the mean collector fluid temperature is equal to the ambient temperature
- Coefficients a_{10} and a_{2a} describe the heat loss of the collector. The temperature dependency of the collector heat loss is described by:

$$a_{10} + a_{2a}(t_m - t_a)$$

The parameters used for the simulation are determined from the absorber area of a commercial solar panel (Teknoenergy 2008):

- $\eta_0 = 0.721$
- $a_{10} = 4.4\, W.m^{-2}.K^{-1}$
- $a_{2a} = 0.018\, W.m^{-2}.K^{-2}$

2.6. The solar photovoltaic panels

The solar photovoltaic panels are also modeled by an efficiency rate. In fact, associated with a MPPT controller (Maximum Power Point Tracking), 95% of maximum power can be assumed to be always available (Lucque and Hegedus 2005).

It is also assumed that the power provided by the association of photovoltaic panels and regulator is then nearly proportional to solar radiation. The efficiency of the panel used in this study decreases of 5.8% when the solar radiations decrease from 1000W.m^{-2} to 200W.m^{-2}.

We must also take into account the temperature of photovoltaic cells has a significant influence on performance.

To estimate the temperature t_{PV} of the cells, the approximation to be made is to consider that the difference between ambient temperature t_a and the cell

is proportional to solar radiation G_i (Lucque and Hegedus 2005):

$$t_{PV} = t_a + K_{PV}.G_i$$

For the characteristics of the panels included in the model (Kyocera 2010), the reference used in this estimate is that for an irradiation of 800W.m^{-2} and a air temperature of 20°c, the temperature of the cell under these conditions (NOCT: Normal Operating Cell Temperature) is 47.9°c. The power was then supplied to 95W, and $K_{PV} = 3.49 \times 10^{-3}$. Then, the energy P_{epv} supplied by the association photovoltaic panels together and MPPT regulator can then be expressed for one square meter of installed panel:

$$P_{epv} = \eta_0.G_i - (t_a + K_{PV}.G_i - t_{STC})K_{WPV}$$

The value of K_{WPV} is given to be 0.614W.K^{-1} and the value of t_{STC} is given to be 20°c. The value of η_0 is given to be 0.12.

2.7. The wind energy and the wind generator model

To collect the kinetic energy of air, the use of wind turbines has grown since the middle Ages with the mills to grind grain. Currently, if wind turbines are still relevant, they are predominantly coupled to an alternator to produce electricity. This make the energy collected portable and usable for more applications.

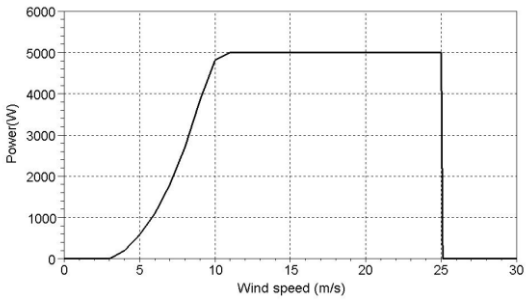

Figure 5: The Wind Generator Power Curve

In this simulation, a typical wind generator curve (see fig. 5) was implemented in the simulation model (Burton, Sharpe, Jenkins and Bossanyi 2001).

2.8. The geothermal energy and the heat pump model

The principle of a heat pump is to transfer calories from a cold source to a warm source, reversing the natural cycle of heat transfer. In the case of heating a home with a heat pump, the pump collects the calories in the environment outside the house and returns inside. These calories can be collected in either the groundwater or in soil or in the air.

The transfer of heat is done using a coolant which undergoes a cycle of compression and relaxation, and it is just necessary to provide compression energy to initiate the transfer.

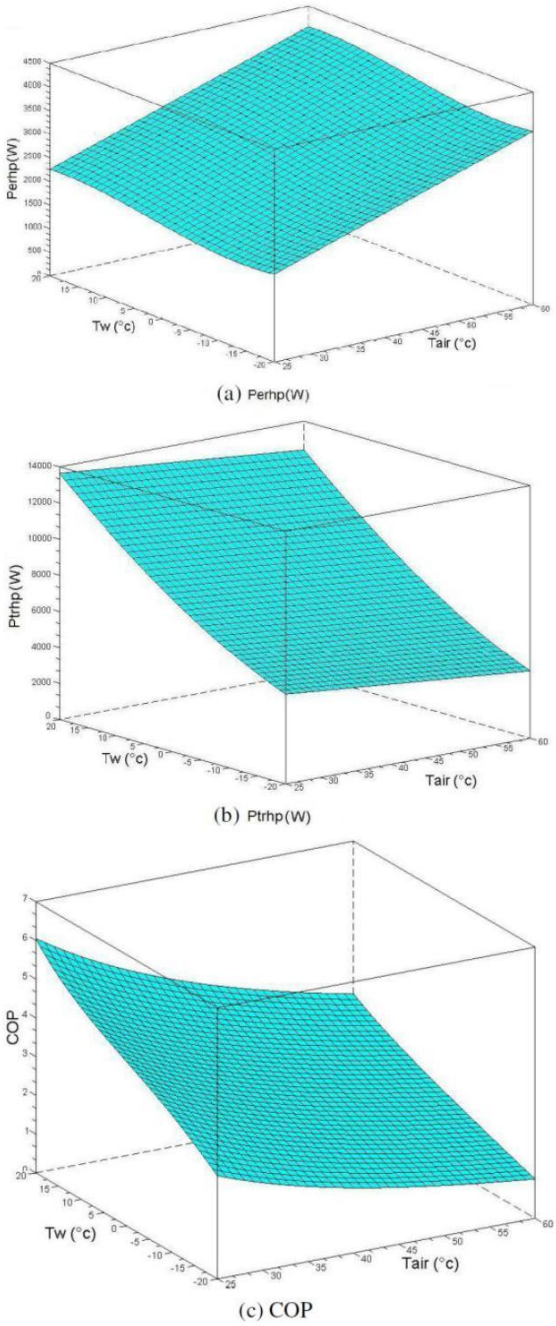

Figure 6: Heat Pump Characteristics

The coefficient of performance (COP) of a air/water heat pump, for air temperature of 7°C and an outlet temperature of water of 35°C for floor heating must be present at 3.5 minimum in order to qualify this equipment for a tax credit in France. This means that under these conditions, for 1 kW of electricity consumed on the electricity network, the pump returns 3.5 kW of heat into the building. The 2.5 kW of variance are collected in the air or soil. Even in winter, outdoor air, water and soil contain enough calories to heat a building.

However, the COP of a heat pump decreases as the temperature difference between the hot source and cold source increases (Auzenet and Clerc-Renaud 2004). Heat pumps in this process collect an indirect solar energy (the heat of the air or the ground) and concentrate that energy in the reduced volume of the house. These systems can be reversible concerning the heat transfer, and they can be used to heat in winter and cool in summer. The heat pumps have long been regarded as not forming part of renewable energy systems, since the primary energy needed to produce the electricity they need are overwhelmingly fossil. The development of electricity generation by renewable resources has nevertheless helped to change this opinion and it is now accepted that heat pumps are an integral part of renewable energy systems.

In the simulation, the heat pump is used as the "energy amplifier" of the energy provided by photovoltaic panels and the wind generator. The model implemented for the simulation is as in Flach-Malaspina (2004):

$$P_{trhp} = a_0 + a_1 t_a + a_2 t_w + a_3 {t_w}^2 + a_4 {t_w}^3$$
$$P_{erhp} = b_0 + b_1 t_a + b_2 t_w + b_3 {t_w}^2 + b_4 {t_w}^3$$

The coefficients a and b are here correlated from the characteristics of a commercial heat pump (CIAT 2009) (see fig. 10) as follow:

$$P_{trhp} = 9345.1127 - 35.247773 t_a + 219.69055 t_w + 2.0963582 {t_w}^2 - 0.00667885 {t_w}^3$$
$$P_{erhp} = 703.03721 + 51.719762 t_a + 21.123712 t_w + 0.1548888 {t_w}^2 - 0.0282035 {t_w}^3$$

The heat pump selected for this study is a variable pump power, with a power variation range from 40 to 100%. This allows operating over a wide range of electrical energy supplied by wind generator and solar photovoltaic panels. The operation at lower power improves the COP, but this fact is neglected in the model. Indeed, the exchangers of the heat pump are sized for full power, and they end up oversized when operating at reduced power.

2.9. The energy storage

Due to the intermittent nature of solar radiations and wind, development of renewable energy systems is intimately linked to the development of reliable and economic energy storage systems. Solar energy is stored spontaneously in nature through the phenomenon of photosynthesis and biomass. To store it in a usable form, several technologies exist: thermal energy

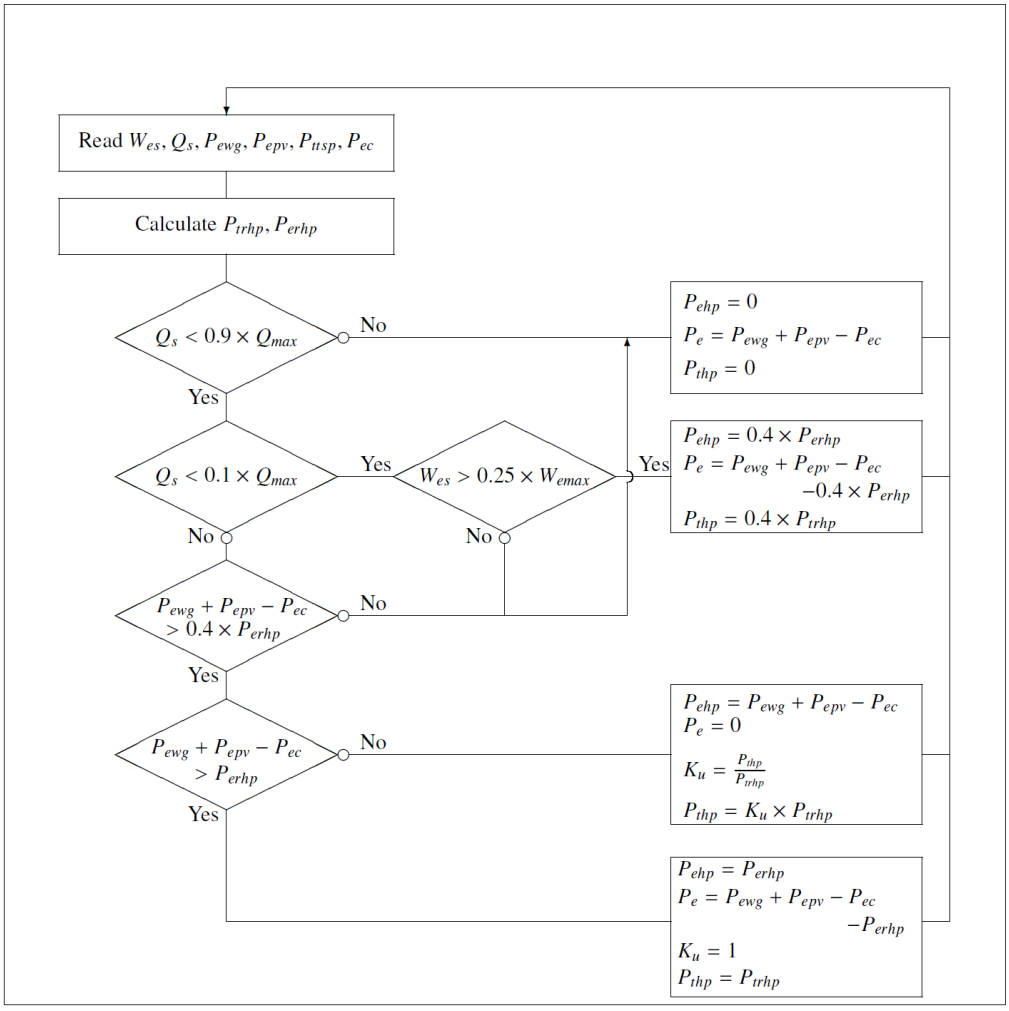

Figure 7: Algorithm of the Electrical Energy Management

storage, electrochemical batteries, supercapacitors, flywheels, hydrogen, compressed air, two-phase materials, etc. Some processes are well mastered and widely used, but for others it remains to be done.

2.9.1. Thermal storage

This is the most used and easiest way to store solar energy. In the case of systems of hot water, it is simply an insulated water tank which uses the heat capacity of water (4185J.kg^{-1}.K^{-1}). For this application, water is indeed a material which has one of the best characteristic and is cheaper. For comparison, the heat capacity of steel is nearly ten times lower than the water's one.

2.9.2. Chemical batteries

Different technologies exist: lead-acid, nickel cadmium, lithium, zinc air, etc. Their main interest is due to their high energy density (up to 150kWh.kg^{-1} for lithium) and their technological maturity, at least for a few kWh of capacity. Their main disadvantage is their short lifespan of around 1000 cycles of high amplitude cycling. The main application is embedded systems and emergency systems such static uninterruptible power supply (UPS).

When performing a charge-discharge cycle, the energy efficiency of a battery varies from 70% to 90% depending on the technology (Multon and Ben Ahmed 2007).

2.9.3. The energy storage in the simulation

The thermal energy storage (W_{ths}) consists of insulated water tanks. The energy level is considered to be empty when the water temperature is 35°c, and to be high when the water temperature is 55°c. The storage capacity is 150kWh; this represents a volume of 6.45m^3. The energy losses are for the simulation are 5W.K^{-1}.

The electrical energy storage (W_{es}) consists of typical lead-acid batteries, with a charge efficiency of 85% and a discharge efficiency of 85% too. This means that when the electrical production is in excess (Pe > 0), $\frac{dW_{es}}{dt} = 0.85P_e$, and when there is not enough electrical energy produced (Pe < 0), $P_e = 0.85\frac{dW_{es}}{dt}$.

The storage capacity W_{esmax} for the simulation is 50kWh. This kind of electrical storage is probably not the best way to store electricity in a large scale, so other way will be discussed in the fourth part.

3. RESULTS OF THE SIMULATIONS

The algorithm implemented to manage the electrical energy is described in figure 7. Globally, the priority is the thermal needs. When the thermal level storage is under 10% of its maximum capacity, the electrical storage is used to produce heat with the heat pump, and this until the electrical storage level is over 25%.Thermal energy production

Considering the total duration on one year of missing thermal energy, the first configuration provides more better results than the second one (table 1) . Even in less sunny regions as Macon or Clermont-Ferrand, a

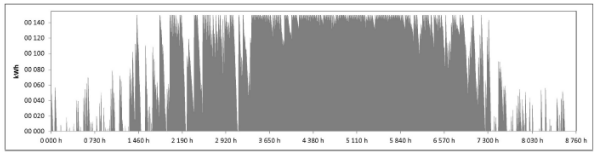

(a) Evolution of the thermal storage level for the site of Trappes in configuration 2

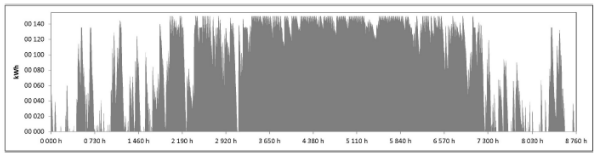

(b) Evolution of the thermal storage level for the site of Trappes in configuration 1

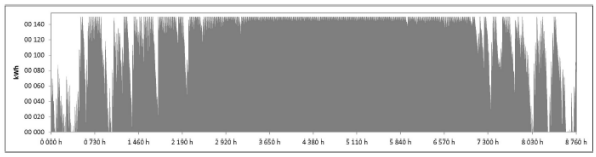

(c) Evolution of the thermal storage level for the site of Marseilles in configuration 2

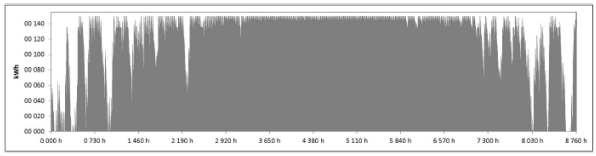

(d) Evolution of the thermal storage level for the site of Marseilles in configuration 1

Figure 8: Evolution during a Typical Year of the Thermal Energy Storage Level for the Configuration 1 and 2 for the Sites of Trappes and Marseille

significant decrease of the total duration of missing thermal energy is observed. The missing thermal energy decreases significantly with the configuration 1 (table 2). The gain estimated is up to 50% for sites as Caen, Millau and Perpignan.

Tableau 1: Total Duration of Missing Thermal Energy for some Sites in France (hours)

Site	Config.1	Config.2	Variation
BORDEAUX	788	860	-8%
BREST	820	1535	-47%
CAEN	765	1601	-52%
CLERMONT	1159	1263	-8%
LIMOGES	1118	1487	-25%
MACON	1812	1894	-4%
MARSEILLE	242	303	-20%
MONTPELLIER	232	347	-33%
NANTES	1013	1399	-28%
NICE	119	173	-31%
PARIS	1415	2352	-40%
PERPIGNAN	108	249	-57%
RENNES	1021	1703	-40%
STRASBOURG	2225	2356	-6%
TRAPPES	1293	1898	-32%

Tableau 2: Total of Missing Thermal Energy for some Sites in France (kWh)

Site	Config.1	Config.2	Variation
BORDEAUX	2417	2633	-8%
BREST	2414	4186	-42%
CAEN	2455	4957	-50%
CLERMONT	4052	4426	-8%
LIMOGES	3688	4800	-23%
MACON	6036	6363	-5%
MARSEILLE	759	952	-20%
MONTPELLIER	785	1066	-26%
NANTES	3185	4316	-26%
NICE	313	456	-32%
PARIS	4512	7065	-36%
PERPIGNAN	330	735	-55%
RENNES	3295	1021	-37%
STRASBOURG	8406	9054	-7%
TRAPPES	4382	6247	-30%

Then, from the thermal point of view, replacing 66% of the thermal solar panels by photovoltaic panels associated with a air/water heat pump has beneficiary consequences on the thermal energy production. The figure 8 shows the evolution of the thermal energy storages level for the two configurations and the sites of Trappes and Marseilles.

3.1. Electrical energy production

Considering the total duration on one year of missing thermal energy, the first configuration provides better results than the second one (table 3). A spectacular decrease of the total duration of missing electrical energy is observed for all the localizations. The best gain is obtained during the summer season. The configuration 2 is thermally oversized during this season, whereas the configuration 1 provides really more electricity during that period.

Tableau 3: Total Duration of Missing Electrical Energy for some Sites in France (hours)

Site	Config.1	Config.2	Variation
BORDEAUX	937	4819	-81%
BREST	686	3263	-79%
CAEN	386	2253	-83%
CLERMONT	1378	5301	-74%
LIMOGES	1081	4481	-76%
MACON	2004	5934	-66%
MARSEILLE	199	1650	-88%
MONTPELLIER	254	2788	-91%
NANTES	725	3788	-81%
NICE	98	2923	-97%
PARIS	1013	3408	-70%
PERPIGNAN	52	1942	-97%
RENNES	674	3269	-79%
STRASBOURG	2335	5858	-60%
TRAPPES	986	3766	-74%

Tableau 4: Total of missing Electrical Energy for some Sites in France (kWh)

Site	Config.1	Config.2	Variation
BORDEAUX	464	3219	-86%
BREST	347	2167	-84%
CAEN	190	1469	-87%
CLERMONT	685	3563	-81%
LIMOGES	526	3000	-82%
MACON	1045	4038	-74%
MARSEILLE	90	1046	-91%
MONTPELLIER	112	1771	-94%
NANTES	359	2513	-86%
NICE	47	1882	-97%
PARIS	509	2278	-78%
PERPIGNAN	25	1231	-98%
RENNES	325	2157	-85%
STRASBOURG	1219	3956	-69%
TRAPPES	528	2493	-79%

The gain for the non-used electricity can reach more than 5000% for a site such Strasbourg. The figure 9 shows the evolution of the electrical energy storages level for the two configurations and the sites of Trappes and Marseilles.

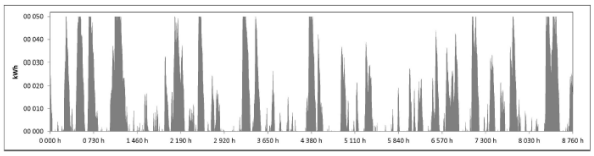

(a) Evolution of the electrical storage level for the site of Trappes in configuration 2

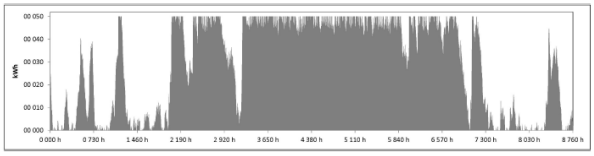

(b) Evolution of the electrical storage level for the site of Trappes in configuration 1

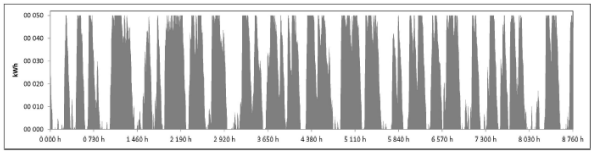

(c) Evolution of the electrical storage level for the site of Marseilles in configuration 2

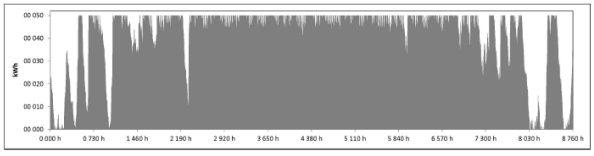

(d) Evolution of the electrical storage level for the site of Marseilles in configuration 1

Figure 9: Evolution during a Typical Year of the Electrical Energy Storage Level for the Configuration 1 and 2 for the Sites of Trappes and Marseille

The gain is essentially obtained during the summer time, where the configuration 2 is thermally oversized.

The missing electrical energy decreases significantly with the configuration 1 (table 4). The gain estimated is up to 90% for sites as Marseille, Montpellier, Nice or Perpignan.

4. DISCUSSION

The configuration of the studied hybrid system was the same for all the studied sites. The aim was to prove that whatever is the chosen site, a higher level of hybridation improves the energy management in renewable energy systems. The choice of the configuration can be adapted to the site meteorological characteristics to improve the exploitation of local energies. This will be the aim of another article. The electrical storage chosen should evolute up to a reversible fuel cell or compressed air system. In renewable energy systems, hydrogen is produced by electrolysis and then compressed to be stored in tanks, like compressed air. Energy efficiency is about 70%. The hydrogen is stored to power a fuel cell that produces the reverse of electrolysis and can therefore restore the energy stored as hydrogen into electrical energy. The fuel cell itself can not constitute a renewable energy system; it is just a way of stored energy release. The performance of a fuel cell is also close to 70%, the yield of chain-electrolyzer stack is about 50%.

Research has already shown that a simple hybrid battery-electrolyser-fuel cell storage for electric refund reduces the overall cost of storage by 91% compared to a solution based entirely on batteries (Vosen and Keller 1999). Other studies (Santarelli, Cali and Macagno 2004; Onar 2008) show about the site significance on the choice of elements of a hybrid system of energy production by renewable sources, given the specific climate of each site.

Thus, it is certain that the explosion risk of hydrogen remains a major obstacle to developing this technology. Strict regulations should be established to oversee the development and dissemination of such technology. The security problem is less critical with compressed air. Investigation and optimization of hybrid electricity storage systems based on compressed air and supercapacitors have been conducted and seem to be full of promises (Lemofouet-Gatsi 2006).

5. CONCLUSION AND PERSPECTIVES

In this study, a configuration of a renewable energy system was proposed. A part of the solar thermal panel surface is covered with photovoltaic panels, and a heat pump is installed to create a crossover between the electrical energy flow and the thermal energy flow. It can be concluded as follows concerning the configuration with a heat pump:

1. The thermal needs of a dwelling on one year are as well met than for a full thermal solar panel configuration. An improvement up to 50% is estimated for some sites.
2. The electrical needs of a dwelling on one year are as really better met than for a full thermal solar panel configuration. An improvement up to 90% is estimated for some sites of the study.
3. The improvement of the unused electrical energy is significant, and is a perspective of a better autonomy when the storage technologies will enable to use that energy. That energy could be used per example to produce hydrogen with electrolysers, and so to power hydrogen cars per example.

Finally, due to the different sources and forms of renewable energy, and due to the different energy needs, a higher level of hybridation in a renewable energy system improves clearly the autonomy of the system, and this, for the same implantation of energy collectors. Creating crossovers between different energy forms allows a better useful of the collected energy.

In this study, a simple algorithm of energy management was implemented. The implantation of more sophisticated algorithm, including the weather forecasts, should allow with the same material configuration to improve the autonomy. Weather forecasts are in the context of renewable energy based on solar radiations and wind energy a way to estimate the energetic potential of the next days. Included in the algorithm, this can only improve the management of the energy.

Finally, one configuration was proposed for each site of this study, but a work has to be done to find the best configuration for each one. A methodology to find that specific configuration has to be developed too.

Ademe, 2008, *Chiffres clés 2007*. Available from: http://www.ademe.fr [accessed 12 December 2008]

Ahmed-Shata, A., Hanitsch, R., 2006, Evaluation of wind energy potential and electricity generation on the coast of Mediterranean sea in Egypt, *Renewable Energy* 31: 1183–1202

Al-Mohamad, A., 2004, Global, direct and diffuse solar-radiation in Syria, *Applied Energy* 79 : 191-200

Al-Nassar, W., Al-Hajraf, S., Al-Enizi, A., Al-Awadhi, L., 2007,Potential wind power generation in the state of Kuwait, *Renewable Energy* 30: 2149-2161.

Auzenet, E., Clerc-Renaud, M., 2004, Pompes à chaleur : systèmes à compression de vapeur, *Techniques de l'Ingénieur* BE9 620 : 1-20.

Bagiorgas, H., Assimakopoulos, M., Theoharopoulos, D., Matthopoulos, D., Mihalakakou, G., 2007, Electricity generation using wind energy conversion systems in the area of western Greece, *Energy Conversion Management* 48: 1640–1655.

Burton, T., Sharpe, D., 2005, *Wind Energy Handbook*. Chichester: Wiley.

Ciat Industrie, 2009, *technical documentation of air/water reversible single unit heat pump 33H with DC inverter technology for individual*

homes or small businesses. Available from: http://www.ciat.com [accessed 15 June 2009]

Elamouri, M., Ben-Amar, F., 2008, Wind energy potential in tunisia, *Renewable Energy* : 758-768

Flach-Malaspina, N., 2004, Conception globale d'une pompe à chaleur air-eau inversable à puissance variable pour le secteur résidentiel., Ph.D. thesis, Ecole des Mines de Paris.

Haillot, D., Pya, X., Goetza, V., Benabdelkrim, M., 2008, Storage composites for the optimisation of solar water heating systems., *Chemical Engineering Research and Design* 86: 612-617.

Joffre, A., 2009, Energie solaire thermique dans le bâtiment. chauffe-eau solaires, *Techniques de l'ingénieur* BE9 164 : 1-18.

Kyocera, 2010, *technical documentation of KD135 GH2-PU high efficiency multi-crystal photovoltaic module*. Available from: http://www.kyocerasolar.eu [accessed 18 February 2010]

Lemofouet-Gatsi, S., 2006. *Investigation and optimisation of hybrid electricity storage systems based on compressed air and supercapacitors*. Thesis (PhD). Ecole Polytechnique Fédérale de Lausanne.

Lucque, A., Hegedus, S., Jenkins, N., Bossanyi, E., 2001, *Wind Energy Handbook*. Chichester: Wiley.

Marciukaitis, M., Katinas, V., 2008, Wind power usage and prediction prospects in Lithuania, *Renewable and Sustainable Energy Reviews* 12: 265–277.

Moubayed, N., El-Ali, A., Outbib, R., 2009, *Renewable Energy in Lebanon*. In Hammons, T.J., eds. *Renewable Energy*. Vukovar: In-Teh.

Multon, B., Ben Ahmed, H., 2007, Le stockage stationnaire d'énergie électrique: pourquoi et comment?, *3EI* 48 : 18-29.

Ngala, G., Alkali, B., Aji, M., 2007, Viability of wind energy as a power generation source in Maiduguri, Borno state, Nigeria, *Renewable Energy* 32: 2242-2246.

Onar, O., 2008, Modeling control and simulation of an autonomous wind turbine/photovoltaic/fuel cell/ultra-capacitor hybrid power system, *Journal of Power Sources* 185: 1273-1283.

Ordonez, J., Jadraque, E., in press, Analysis of the photovoltaic solar energy capacity of residential rooftops in Andalusia (Spain), *Renewable and Sustainable Energy Reviews*s.

Radics, K., Bartholy, J., 2008, Estimating and modeling the wind resource of Hungary, *Renewable and Sustainable Energy Reviews* 12: 874–882.

Rahhal, C., 2006. *Conception d'une pompe à chaleur air/eau a haute efficacité énergétique pour la réhabilitation d'installations de chauffage existantes*. Thesis (PhD). Ecole des Mines de Paris.

Rehman, S., Al-Abbadi, N.M., 2007, Wind shear coefficient, turbulence intensity and wind power potential assessment for Dhulom Saudi Arabia, *Renewable Energy* 32 : 738-749.

Remund, J., Kunz, S., Schilter, C., Müller, S., 2009, *METEONORM version 6.1 Handbook*. Available from: http://www.meteotest.com [accessed 03 March 2009]

Santarelli, M., Cali, M., Macagno, S., 2004, Design and analysis of stand-alone hydrogen energy systems with different renewable sources, *International Journal of Hydrogen Energy* 29: 1571-1586.

Schenk, N., Moll, H., Potting, J., Benders, R., 2007, Wind energy, electricity, and hydrogen in the Netherlands, *Renewable Energy* 32: 1960–1971.

Tarkowski, R., Uliasz-Misiak, B., 2003, Renewable energy sources in Guadeloup, *Applied Energy* 74: 221-228.

Tchindaa, R., Kendjioa, J., Kaptouoma, E., Njomob, D., 2000, Estimation of mean wind energy available in far north Cameroon, *Energy Conversion Management* 41: 1917–1929.

Teknoenergy, 2008, S*ummary of EN 12975 test results, annex to solar keymark certificate, registration 002bn/o*. Available from http://www.estif.org/solarkeymark/ [accessed 20 June 2009].

Ucar, A.., Figen, B., 2009, Evaluation of wind energy potential and electricity generation at six locations in Turkey, *Applied Energy* 87: 1864-1872

Vosen, S.R., Keller, J.O., 1999, Hybrid energy storage systems for stand-alone electric power systems: optimization of system performance and cost through control strategies, *International Journal of Hydrogen Energy* 24: 1139-1156.

World Energy Council, 2007, *2007 survey of energy resources*. Available from: http://www.**worldenergy**.org [accessed 10 April 2009]

PSEUDO-DYNAMIC MODEL OF A BIO-ETHANOL PROCESSOR FOR A FUEL CELL HYBRID VEHICLE

Lucas Nieto Degliuomini[(a)], David Zumoffen[(a)], Diego Feroldi[(a)], Marta Basualdo[(a)], Rachid Outbib[(b)]

[(a)] CIFASIS-CONICET, Bv 27 de Febrero 210 bis, Rosario, Argentina.
[(b)] LSIS, Université Paul Cézanne Aix-Marseille, France.

[(a)] nieto,zumoffen,feroldi,basualdo@cifasis-conicet.gov.ar, [(b)] rachid.outbib@lsis.org

ABSTRACT

The transient behavior of a Fuel Processor System to produce Hydrogen from bio-ethanol with high performance, coupled with a Proton Exchange Membrane Fuel Cell is modeled. The Ethanol Processor is based on a previous steady state design, optimized to work with maximum efficiency around 10 kW of rated power. The Fuel Cell System is then hybridized with supercapacitors as auxiliary power source, to lower the overall consumption of hydrogen, hence of bio-ethanol too. The entire vehicle is tested using standard driving cycles, widely utilized in related literature and to measure pollutant emissions. The overall behavior reaches the expectations and is capable of fulfilling the requirements of urban and highway scenarios, and also suggests the possibility of resizing the components to improve fuel economy.

Keywords: Fuel Cell Hybrid Vehicles, Energy Management Strategies, Bio-ethanol Fuel Processor

1. INTRODUCTION

Fuel Cell Hybrid Vehicles (FCHV) is a promising application of fuel cell technology that has taken more and more importance in the last years and is considered the most attractive long-term option for passenger cars. Hybridization in FCHV consists in adding a supplementary energy storage element (e.g., a battery or an supercapacitor (SC) bank) to the primary power source, i.e. Proton Exchange Membrane Fuel Cell (PEMFC), in order to adequate optimally the energy generation to the consumption with almost zero emission. PEMFC are devices that convert chemical energy in the form of hydrogen into electricity with high efficiency, without passing through a combustion stage. Hybridization has important advantages, allowing a greater reduction of the hydrogen consumption, and its economical importance has been recently remarked in (Offer et al. 2010).

Validated mathematical models provide a powerful tool for the development and improvement of the fuel cell technology. Mathematical models can be used to describe the fundamental phenomena that take place in the system to predict the behavior under different operating conditions and to design and optimize the control of such complex systems. In this work, a complete model of a FCHV powered by a hybrid system composed by a PEM fuel cell and a supercapacitor bank is done. Besides, the PEM fuel cell is fed with hydrogen from a bio-ethanol processor, which is also modeled. Finally, the complete model is integrated with an Energy Management Strategy, which is in charge of properly managing the PEM fuel cell to supply the power requirements of the vehicle to fulfill the testing profiles. Some works have appeared regarding to the power management of hybrid vehicles with multiple energy sources, such as fuel cell, battery and supercapacitor (Thounthong et al. 2009, Li et al. 2009). The management strategy used in this work, developed by (Feroldi et al. 2009), is described in Section 3.

A preliminary plant-wide control structure for the process of producing hydrogen from bio-ethanol to be used in a PEM fuel cell has been presented in (Biset et al. 2009). This control structure accounts only steady-state information. In this work, the operational conditions for the PEMFC were adopted from recommendations given by (Pukrushpan et al. 2004). In this last work, a deep study about control of fuel cell systems, with focus on air-flow control was presented. Hence, believing on the high quality of that work, in this paper is used the same control oriented model of the PEMFC which is considered as a benchmark. In (Pukrushpan et al. 2004), several control strategies are proposed accounting abrupt current demand from the vehicle. They concluded that the air supply must be promptly increased to replenish the cathode with oxygen.

There are few publications regarding fuel processors dynamic behavior, some using methanol as raw material, such as (Chuang et al. 2008), and very recently some publications on using ethanol to produce hydrogen. Some of these are (Aicher et al. 2009, Garcia et al. 2009). Even though they present

dynamic models, or experimental results, and use them to synthesize control structures, they do not contemplate the energy integration, and the combination of the Fuel Cell System with energy storage devices, which makes this technology economically feasible and highly interacted. The research works previously mentioned highlighted the main difficulties and objectives to account in the operation of fuel processors and fuel cell systems, which are vital to assure the catalysts working life and to avoid damage to the components. This is the first work that deals with the entire hybrid vehicle integrated, meaning Fuel Processor Plant, Fuel Cell System, Energy Storage System, Energy Management Strategy and Powertrain models, and it is rigourously tested using standardized driving cycles.

The structure of the paper is as follows: in Section 2, the complete model of the system is described, while in Section 3 the model is integrated with an Energy Management Strategy. In Section 4, the model is validated through simulation using Standard Driving Cycles widely used in the literature. Finally, application results and conclusions are provided in Section 5 and 6, respectively.

2. DESCRIPTION OF THE MODEL

The model presented en this work consists of the following submodels: Fuel Processor model, PEM Fuel Cell model, Energy Storage System model and vehicle model.

2.1 Fuel Processor model

The Fuel Processor System (FPS) (illustrated in Fig. 1) consists of a Bio-Ethanol Steam Reforming (ESR) plug flow reactor, where most of the conversion of bio-ethanol to H_2 is made. Since carbon monoxide (CO), which poisons the fuel cell catalyst, is produced in the ESR, additional processing is needed to remove this substance. There are three reactors that configure the cleaning system. These are two Water Gas Shift (WGS), one of high temperature (fast) and the other of low temperature, that favors the equilibrium of the reaction to higher conversion rates of CO. The third is a Preferential Oxidation of Carbon monoxide (CO-PrOx) reactor, where oxidation of CO into CO_2 is made. Also, the undesired oxidation of H_2 occurs. Therefore, the catalyst is selected to improve the conversion of CO.

Ethanol and vaporized water are mixed and then supplied to the ESR reactor, to produce ethanol decomposition:

$$\text{(ESR)} \quad CH_3CH_2OH + 3H_2O \leftrightarrow 6H_2 + 2CO_2 \quad (1)$$

The overall reaction is endothermic, and heat requirement is supplied by a burner, which is fed with ethanol and compressed air. The transfer of heat is achieved passing the hot gases through the jacket of the reformer. The produced reaction inside the WGS is:

$$\text{(WGS)} \quad CO + H_2O \leftrightarrow CO_2 + H_2 \quad (2)$$

This reaction produces heat and creates more hydrogen. Levels of CO are still high even after the two WGS reactors. Therefore the final elimination is made in the CO-PrOx reactor, which produces the oxidation of CO. The WGS reaction takes place in this reactor too. Oxygen is injected into the CO-PrOx, the amount needed is about twice the stoichiometric relation to have a good selectivity and satisfy the requirements of the FC.

The plug flow reactors are modeled as 20 lined-up Continuous Stirred Tank Reactors (CSTR). The molar flow between two volumes is given by the orifice flow equation as a function of upstream pressure, and downstream pressure. Further details on the dynamic modeling, process constraints and normal behavior can be seen in (Nieto et al. 2009).

2.2 Proton Exchange Membrane Fuel Cell

Fuel cells convert chemical energy directly into electrical energy. They are constituted by an anode, where H_2 is injected, and a cathode, where the oxidant, normally air is injected. The electrodes are separated by a membrane that allows the proton exchange and contribute to the oxidation reaction to produce electrical power. The cell generates an open-circuit voltage which is affected by a number of losses (activation, concentration and ohmic) that leads to a useful actual voltage. (Pukrushpan et al. 2004) presents a rigorous dynamic model of a PEMFC which is used in this work. In this work, the model has been adapted to represent a PEM fuel cell model with a maximum power of 10 kilowatts. Transient behavior of manifold filling, membrane hydration, the air compressor and the heat management are included in the model. Interaction between processes are also included.

2.3 Energy Storage System model

The energy storage system, either if it is based on batteries or supercapacitors, can be modelled with two subsystems. One subsystem takes into account the system efficiency, both during charging and discharging, and the other subsystem computes the actual energy level. The energy stored in the storage system, $E_{ess}(t)$, results integrating $P_{ess}(t)$:

$$E_{ess}(t) = E_{ess}(0) + \int_0^{t_c} P_{ess}(t)dt. \quad (3)$$

It is useful to define a parameter that indicates the relative amount of energy in the *ESS*. The *State of Energy*, *SoE(t)*, is defined as

$$SoE(t) = \frac{E_{ess}(t)}{E_{cap}} \times 100 \qquad [\%], \quad (4)$$

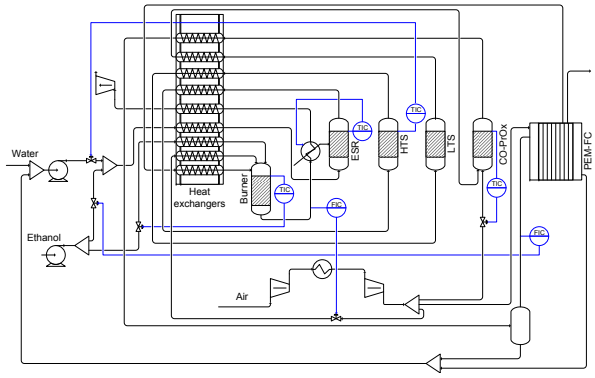

Figure 1: Complete prototype with control structure

where E_{cap} is the maximum energy that the storage system is capable to store.

The *ESS* efficiency, in this case a supercapacitor bank, is related with the equivalent series resistance (*ESR*). For a pure capacitor, having zero *ESR*, the efficiency of charge or discharge would be 100%. However, in a real capacitor, having nonzero *ESR*, the irreversible dissipation of power is $ESR \cdot I_{sc}^2$, giving efficiencies lower than 100%. The equivalent parallel resistance (*EPR*) represents the self-discharge losses and only impacts long-term energy storage performance of the *SC* and is extremely high (Uzunoglu et al. 2007). Thus, the time constant of the period of charge/discharge can be expressed by $ESR \cdot C$. Since *ESR* is as low as 0.019Ω and C is 58 F, it is possible to charge and discharge the *SC* in a very short time. The energy stored in the *SC* is directly proportional to the capacitance and the squared voltage.

2.4 Vehicle model

In order to integrate the Fuel Processor model and the Fuel Cell System model with an entire vehicle and the energy management strategy, a detailed vehicle model has been developed in ADVISOR, a MATLAB toolbox developed by the National Renewable Energy Laboratory with the aim of analyzing the performance and fuel economy of conventional, electric, and hybrid vehicles (Markel et al. 2002). The fuel cell model, the fuel processor model, the energy storage model, and the energy management strategy discussed in section 3 are integrated to form a complete model representing the FCHV with on-board bio-ethanol reforming. The integrated power train along with the energy flows is shown in Fig. 2.

In this work, we consider the performance of a FCHV based on a small car and the entire system being modelled in *ADVISOR* according with the principal parameters listed in Table 1.

Table 1: Vehicle specifications in the case of study.

Specification	Symbol	Value	Unit
Vehicle total mass	m_T	1380	kg
Vehicle mass[a]	m_{veh}	882	kg
Frontal area	A_f	2	m^2
Drag coefficient	C_d	0.335	-
Coefficient of rolling friction	f_r	0.009	-
Air density	ρ_a	1.2	$kg\,m^{-3}$
Gravity	g	9.8	$m\,s^{-2}$

[a] Vehicle mass without taking into account the *FCS* mass and the *ESS* mass.

2.5 Computational Model Implementation

The pressure requirements are satisfied in stationary state with compressors and turbines modeled in HYSYS (Aspen 2006). It supports the important data bank information for the different components. In addition, the LNG tool in HYSYS, that solves material and heat balances for multi-stream exchangers and heat exchangers networks. On the other hand, the dynamic model of the reactors is developed in MATLAB, which integrates the differential equations. The communication interface is performed by the use of the spreadsheets in HYSYS and a specific library for doing the corresponding data transference and updating at scheduled sampling time between both programs. Since the components in HYSYS are considered in steady state, and the reactors set in MATLAB are modeled dynamically, the communication protocol is required to coordinate the calculations. The dynamic behavior of the FPS is considerably slower than the auxiliary components, so this last one is neglected, considered in a pseudo-dynamic way. The frequency of update is fixed in 0.05 seconds of simulation time, in order to capture the fastest dynamics of the chemical reactions taking place

2.5.1 Heat Integration

The heat integration in the model is performed by the LNG tool working in a pseudo-dynamic mode. It is called by MATLAB for determining the instantaneous temperature values of the different cold and hot streams of the process. Therefore, it is assumed that the dynamic effect of the heat exchangers network is neglected. The minimum heat requirement of the system and the minimum heat to be evacuated can be computed for each operating point or with the system under different disturbances.

3. INTEGRATION OF THE MODEL WITH THE ENERGY MANAGEMENT STRATEGY

The management strategy used in this work is based on the fuel cell efficiency map and it operates the fuel cell preferably in its point of maximum effi-

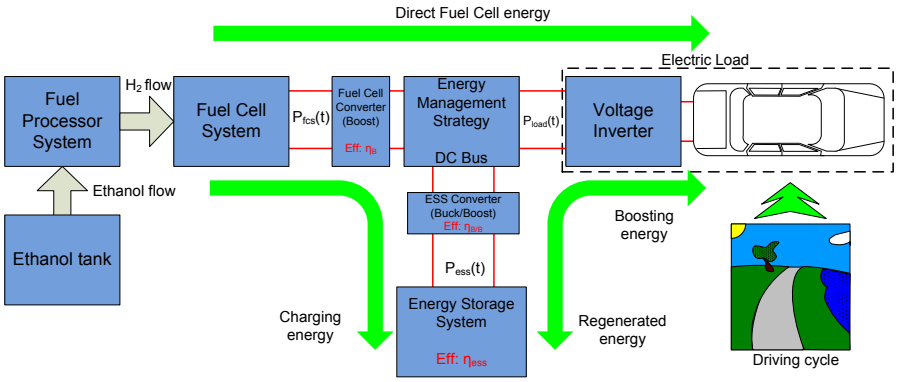

Figure 2: Configuration of the FCHV model with on-board bio-ethanol reforming

ciency in order to improve the hydrogen economy, although the final operating point of the fuel cell is determined based on the actual power demand and the state of energy (SoE) of the Energy Storage System (ESS) (Feroldi 2009).

The fuel cell power command is determined according to the following rules (the nomenclature is explained in Table 2). If the load power is

$$P_{fcs,lo} \cdot \eta_B \leq P_{load}(k) \leq P_{fcs,hi} \cdot \eta_B \tag{5}$$

and, the SoE is

$$SoE_{lo} \leq SoE(k) \leq SoE_{hi} \tag{6}$$

where $P_{fcs,hi}$ is

$$P_{fcs,hi} = P_{fcs,max} \cdot \eta_B \cdot X_{fcs,hi} \tag{7}$$

and $X_{fcs,hi}$ is a fraction of the maximum FCS power; then, the FCS is operated in its point of maximum efficiency (Zone 2 in Fig. 3)

$$P_{fcs}(k) = P_{fcs,maxeff} \tag{8}$$

The remaining power to achieve the load demand flows from or to the ESS according to

$$P_{ess}(k) = \min \left\{ \begin{array}{c} \frac{(P_{load}(k) - P_{fcs}(k) \cdot \eta_B)}{\eta_{B/B} \cdot \eta_{ess}} \\ (SoE(k) - SoE_{min})\, k_{ess} \end{array} \right\} \tag{9}$$

if $P_{load}(k) > P_{fcs,maxeff}$ (discharging mode), or

$$P_{ess}(k) = -\min \left\{ \begin{array}{c} \mid P_{load}(k) - P_{fcs}(k)\, \eta_B \mid \eta_{ess} \eta_{B/B} \\ \mid SoE(k) - SoE_{max} \mid k_{ess} \end{array} \right\} \tag{10}$$

if $P_{load}(k) < P_{fcs,maxeff}$ (charging mode).

If the load power is

$$P_{fcs,hi} \cdot \eta_B \leq P_{load}(k) \leq P_{fcs,max} \cdot \eta_B \tag{11}$$

and, the SoE is

$$SoE_{lo} \leq SoE(k) \leq SoE_{hi} \tag{12}$$

Table 2: Nomenclature utilized

Symbol	Description	Value
k	Current time	Seconds
$P_{fcs,lo}$	Lower net power	4000 W
$P_{fcs,hi}$	Higher net power	8000 W
P_{load}	Demanded Power	W
P_{fcs}	FC net power	W
P_{ess}	ESS output power	W
$P_{fcs,max}$	Maximum net power	10000 W
$P_{fcs,maxeff}$	Maximum efficiency net power	8000 W
η_B	FC converter efficiency	0.95
$\eta_{B/B}$	ESS converter efficiency	0.95
η_{ess}	ESS efficiency	0.95
SoE_{lo}	Lower SoE	0.4
SoE_{hi}	Higher SoE	0.8
SoE_{min}	Mimimum SoE	0.3
SoE_{max}	Maximum SoE	0.9
T_{off}	Time to turn off FC	60 sec

then, the FCS is operated in load following mode (Zone 3 in Fig. 3)

$$P_{fcs}(k) = \frac{P_{load}(k)}{\eta_B} \tag{13}$$

and $P_{ess}(k)$ is as indicated in (10) or (9).

On the other hand, if

$$P_{load}(k) \geq P_{fcs,max} \cdot \eta_B \text{ and } SoE(k) \leq SoE_{hi} \tag{14}$$

or

$$SoE(k) \leq SoE_{lo} \tag{15}$$

then, the FCS is operated at its maximum power (Zone 4 in Fig. 3)

$$P_{fcs}(k) = P_{fcs,max} \tag{16}$$

and $P_{ess}(k)$ is as indicated in (9). If, on the contrary

$$P_{load}(k) \leq P_{fcs,lo} \cdot \eta_B \text{ and } SoE(k) \geq SoE_{lo} \tag{17}$$

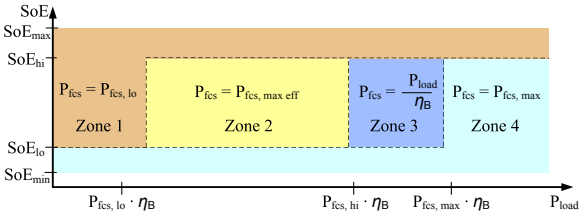

Figure 3: FCS operating point as a function of the SoE and the load power for the strategy based on efficiency map.

or $SoE\,(k) \geq SoE_{hi}$, then, the FCS is working at its lower operating point (Zone 1 in Fig. 3)

$$P_{fcs}\,(k) = P_{fcs,lo} \tag{18}$$

and $P_{ess}\,(k)$ is as in (10). Additionally, if $P_{load}\,(k) = 0\ \forall t \in [k1, k2]$ with $(k2 - k1) > T_{off}$, and, $SoE\,(k) > SoE_{hi}$ with $k > k2$, then, the FCS is turned off to avoid unnecessary hydrogen consumption because the parasitic losses in the FCS. Fig. 3 indicates the FCS operating point as a function of the $SoE\,(k)$ and the load power $P_{load}\,(k)$. The transition between operating points is performed according to the constraints concerning the maximum fall power rate and the maximum power rate.

4. VALIDATION OF THE MODEL

In order to evaluate the performance of a given hybrid vehicle, standard driving cycles are widely utilized in the literature. They represent urban and highway scenarios and were originally stated for measuring pollutant emissions and fuel economy of engines (DieselNet 2010).

In the driving cycles high power requirements take place during a relatively short fraction of time. If there is no energy storage, the FCS must meet the highest peak power and, therefore, the FCS is oversized most of the time. In addition, the efficiency of a FCS is strongly degraded at low powers. Thus, if no hybridization is present, the FCS has to work in large periods of time at a low efficiency zone.

On the contrary, with an additional power source and a suitable energy management strategy it is possible to avoid these unfavorable operating zones. In a fuel cell hybrid system it is possible to boost the FCS supplying energy to the load from the energy storage system. This energy was previously charged from the FCS or regenerated from the load, e.g., from regenerative braking in automotive applications.

5. APPLICATION RESULTS

The FCHV with on-board bio-ethanol reforming is tested using four standardized driving cycles: the New European Driving Cycle (NEDC), the Urban Dynamometer Driving Schedule (UDDS), the Federal Test Procedure (FTP), and the Highway Fuel Economy Cycle (HWFET). The results corresponding to the NEDC and the UDDS are shown in Figs. 4 and 5, respectively. For each group of figures, the speed requirements; power split between the FC and storage system; O_2 excess ratio in the cathode; working zone, and H_2 production are plotted. It can be seen that both the management strategy and the FCS are capable of working properly against the wide range of power demands proposed by the driving cycles.

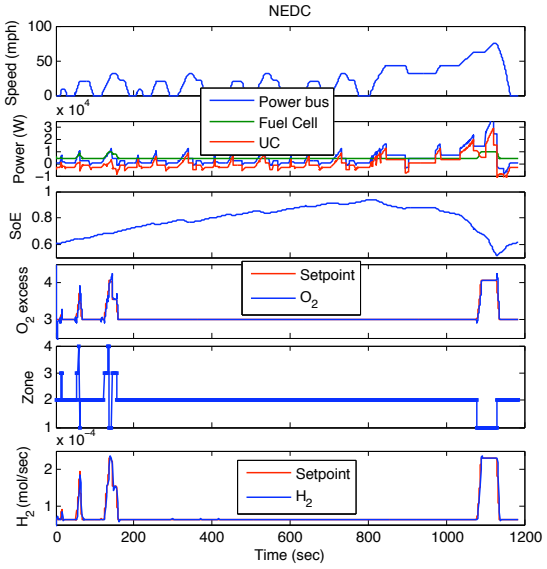

Figure 4: Simulation results for NEDC.

In Fig. 6, an evaluation of the bio-ethanol consumption is done, for the four cycles in study. The evaluation is done through a comparative between the bio-ethanol consumption of the FCHV, the ideal case and the pure fuel cell case without supercacitors (FC). The ideal case is a reference scenario where the fuel cell always operates in the point of maximum efficiency. The negative percentages in the graph represent the savings of bio-ethanol compared to the pure fuel cell case.

It is remarkable that for the pure fuel cell case, the peak load power required can not be supplied by the fuel cell in the FCHV case. Thus, in the pure fuel cell case is necessary a large fuel cell, thus increasing the cost and consumption. On the other hand, in all driving cycles, hybridization represents an important fuel economy, consuming significantly less than the pure fuel cell case. In fact, in some of them, the hybrid vehicle consumption is very close to the ideal case.

6. CONCLUSIONS

From the simulated results it is concluded that the proposed FCHV pseudo-dynamic model, that includes the entire power train, from the raw material, bio-ethanol, up to the drive train of the vehi-

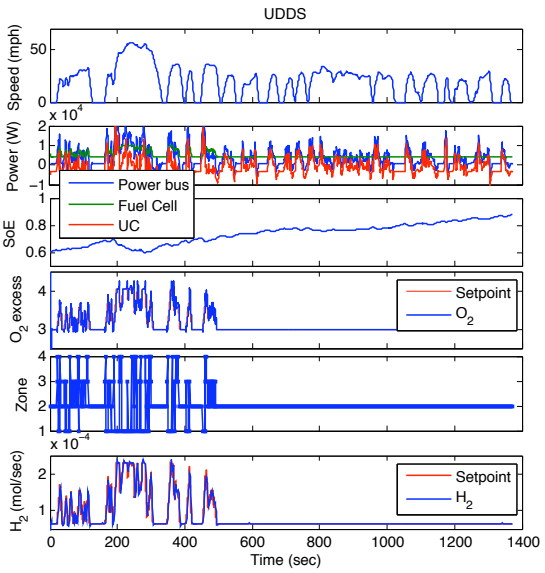

Figure 5: Simulation results for UDDS.

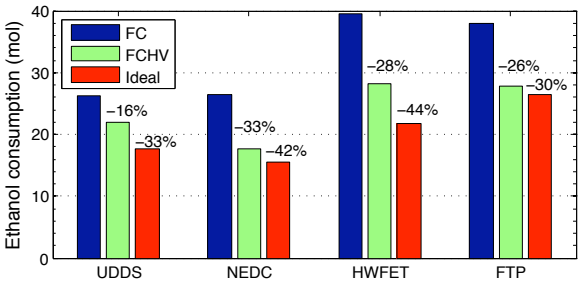

Figure 6: Evaluation of the bio-ethanol consumption for the four driving cycles

cle, is able to support several tests for urban and highway scenarios. Hence, the model helps for developing the conceptual design of a proper energy management strategy. It can be done thanks to the good connection of three different softwares, each of them characterize specific part of the complex real system.

The adequate energy management design, is capable to handle well the required power working inside the good efficiency zones. In addition, the study for two standard driving cycles show that hybridization consumes less bio-ethanol than the FC working alone. The model is used too for plant-wide control structure design.

References

Aicher, T., Full, J. and Schaadt, A., 2009. A portable fuel processor for hydrogen production from ethanol in a 250Wel fuel cell system. International journal of hydrogen energy, 34, 8006-8015.

Aspen Technology Inc. 2006. HYSYS User Manual. Available from: http://www.aspentech.com/hysys/ [Last accessed 2 Jule 2010].

Biset, S., Nieto Degliuomini, L., Basualdo, M., Garcia, V. M., and Serra, M., 2009. Analysis of the Control Structures for an Integrated Ethanol Processor for Proton Exchange Membrane Fuel Cell Systems. *Journal of Power Sources*, 192(1), 107-113.

Chuang, C. C., Chen, Y. H., Ward, J. D., Yu, C. C., Liu, Y. C. and Lee, C. H., 2008. Optimal design of an experimental methanol fuel reformer. *International journal of hydrogen energy*, 33, 7062-7073.

DieselNet, 2010. *Emission Test Cycles*. Available from: http:// www.dieselnet.com / standards / cycles/ [Accessed 29 June 2010].

Feroldi, D., 2009. *Control and design of PEM fuel cell-based systems*. Thesis (PhD).Universitat Politècnica de Catalunya.

Feroldi, D., M. Serra and J. Riera, 2009. Design and analysis of fuel cell hybrid systems oriented to automotive applications, *IEEE Transactions on Vehicular Technology*, 58, 4720-4729.

García, V. M., López, E., Serra, M., Llorca, J., and Riera, J., 2009. Dynamic modeling and controllability analysis of an ethanol reformer for fuel cell application. I*nternational journal of hydrogen energy*, in press, DOI: 10.1016/j.ijhydene.2009.09.064.

Li, X., Xu, L., Hua, J., Lin, X., Li, J. and Ouyang, M., 2009. Power management strategy for vehicular-applied hybrid fuel cell/battery power system. *Journal of Power Sources*, 191(2), 542-549.

Markel, T., Brooker, A., Hendricks, T., Johnson, V., Kelly, K., Kramer, B., O'Keefe, M., Sprik, S., and Wipke, K., 2002. Advisor: a system analysis tool for advanced vehicle modeling. Journal of Power Sources, 110, 255-266.

Nieto Degliuomini, L., Biset, S., Domínguez, J.M. and Basualdo M.S., 2009. Control Oriented Dynamic Rigorous Model of a Fuel Processor System and Fuel Cell Stack. *Computer Aided Chemical Engineering*, 27, 609-614.

Offer, G. J., Howey, D., Contestabile, M., Clague, R. and Brandon, N. P., 2010. Comparative analysis of battery electric, hydrogen fuel cell and hybrid vehicles in a future sustainable road transport system. Energy Policy, 38(1), 24-29.

Pukrushpan, J. T., Stefanopoulou, A. G. and Peng, H., 2004. *Control of Fuel Cell Power Systems: Principles, Modeling, Analysis and Feedback Design*. London: Springer-Verlag.

Thounthong, P., Rael, S., and Davat, B., 2009. Eergy management of fuel cell/battery/supercapacitor hybrid power source for vehicle applications. *Journal of Power Sources*, 193(1), 376-385.

Uzunoglu, M. and Onar, O. and Alam, M., 2007. Dynamic behavior of PEM FCPPs under various load conditions and voltage stability analysis for standalone residential applications. *J. Power Sources*, 168(1), 240-250.

DEPENDABILITY EVALUATION OF SAFETY INSTRUMENTED SYSTEMS INCORPORATING INTELLIGENT INSTRUMENTS

A. Mkhida[(a)], B. Bououlid[(b)], J.M. Thiriet[(c)]

[(a) (b)] ENSAM (Ecole Nationale Supérieure d'Arts et Métiers), Meknes BP 4024, Marjane II, Morocco
Moulay Ismaïl University. MTICS (Modeling, Information Processing and Control Systems).
[(c)]Grenoble University, GIPSA-Lab (Grenoble Images Parole Signal Automatique UMR 5216 CNRS-INPG-UJF), BP 46, 38402 Saint Martin d'Hères France

[(a)] Abdelhak.Mkhida@esstin.uhp-nancy.fr, [(b)] bbououlid@yahoo.fr, [(c)] jean-marc.thiriet@ ujf-grenoble.fr

ABSTRACT
In this paper, the modelling and thus the performance evaluation relating to the dependability are studied for structures which have intelligence in the instruments constituting the Safety Instrumented Systems (SIS) in order to determine the contribution of the intelligent instruments in the safety applications. Dynamic approach using Stochastic Petri Nets (SPN) is proposed and the metrics used for the evaluation of the dependability of the Intelligent Distributed Safety Instrumented Systems (IDSIS) refer to two modes of failures mentioned by the safety standards: mode of dangerous failure and mode of safe failure.

Keywords: Communication Network, Safety Instrumented Systems, Mode of dangerous failure, Mode of safe failure, Stochastic Petri Nets, Sampling Period.

1. INTRODUCTION

Safety Instrumented Systems (SIS) has been used for many years to perform safety instrumented functions in the process industries (IEC61511 2003). The SIS are defined as the collection of all safety related sensing elements to determine an emergency situation, all safety related logic solvers to determine what action to take and all safety related final elements to implement the action (Knegtering 2002).
Adding a network communication and intelligent instruments such as intelligent sensors and actuators to the SIS makes this system intelligent. These instruments with a network communication provide several advantages such as integration of diagnosis, cabling reduction, increasing of reconfigurability etc (Lian, Moyne, and Tilbury 2002).
The problem is to quantify the contribution of the use of the intelligent instruments in the safety loops in compliance with related standards. In safety systems many studies were developed for dependability evaluation. These approaches ignore the use of intelligent instruments.
The dependability evaluation of such systems is a difficult task and can concern two approaches: a static approach which deals with the analysis of functioning and malfunctioning states of a given architecture, and a dynamic approach which takes into account the progressive evolution of system states and functioning modes (Mkhida, Thiriet, and Aubry 2008). The potential application of such systems is very widespread from electronic trippers to some critical real-time systems such as X-by wired cars, drones (Berbra, Lesecq, Gentil, and Thiriet 2007) or aeronautics…
The use of the intelligent instruments in safety applications leads to the concept of the intelligent safety where advanced safety systems are developed for collecting and analysing data on the detection of dangerous conditions. This should provide a basis for creating new intelligent safety systems. The intelligent safety loops (or intelligent distributed safety instrumented systems) enable us to implement safer plants by using the intelligent devices for safety application in compliance with the new IEC 61511 standard.
The methodology used for the dependability evaluation for these systems consists on the structuring and the modelling of these systems; the purpose is to make the verification and analysis by mean of stochastic Petri nets in order to exploit the models.
Modelling is achieved by a stochastic approach using the Stochastic Activity Network (SAN). The SAN is a powerful formalism of the stochastic Petri nets (Moghavar and Meyer 1984) .
The following sections describe the intelligent distributed safety instrumented systems, how they are modelled and the procedures proposed for their evaluation. The two metrics related to safety performance (PFD & PFS) are calculated. The results are compared, presented and conclusions are drawn.

2. INTELLIGENT INSTRUMENT

2.1. Intelligent Distributed Control Systems (IDCS)

Intelligent or smart instruments have been known for more than two decades. These instruments are more sophisticated than traditional instruments (Mekid 2006).

An intelligent instrument is a component part of Intelligent Distributed Control Systems. These systems are thus composed of smart sensors and actuators with calculations capabilities and communication interfaces. Traditional control systems are connected by analogue current (4-20 mA) and voltage loops whereas IDCSs are connected by a communication network (generally a fieldbus).
The particularity of a distributed system relates to data exchange between the devices via a communication medium supposed to be a network or a fieldbus. Thereby, the intelligent distributed control system becomes more and more complex and sophisticated, and consequently, makes the design step more difficult.

2.2. Structure and functions of an intelligent instrument

The intelligent instruments offer the possibility of a local processing of the information which is distributed on the various entities thus allowing a distribution of the execution of the tasks and appearing a distributed control.
The intelligent instruments are basic instruments that contain microprocessors (Nobes 2004), these instruments meet the following criteria:
- the main purpose of the instrument is to measure or directly control a single process variable,
- these instruments include some flexibility in their use due to parameters that are set by the manufacturer or operator,
- intelligent instruments are not restricted to measurements but also include actuators (valves, motors) and other control equipment.

Intelligent instruments offer considerable lifetime cost reductions. These cover the whole life cycle, including specification, installation, operation, maintenance, decommissioning…
Various functionalities have been suggested for intelligent sensors. (Robert, Riviere, Noizette, and Hermann 1993) proposed that the intelligent sensors should contain configuration, communication, measurement and validation functionalities. (Meijer 1994) includes three functionalities: compensation, computing and communication. (Tian, Zhao, and Baines 2000) suggested the functions of compensation, validation, data-fusion, and communication. While (Mekid 2006) propose that what is called an intelligent sensor should have the functions of compensation, processing, communication, validation, integration and data-fusion.

We propose for the generic intelligent instrument (Mkhida, Thiriet, and Aubry 2008) the functions of measurement, configuration, test, validation, control and communication. Figure 1 illustrates these functionalities.

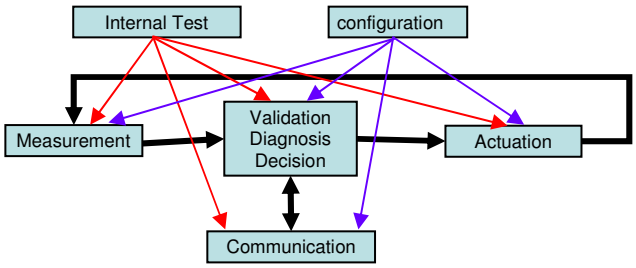

Figure 1: Functional architecture of an intelligent instrument

3. SAFETY INSTRUMENTED SYSTEMS

Safety instrumented systems are used in many industrial processes to reduce the consequences of process demands on humans, the environment and material assets.
Different standards can be used to design safety instrumented systems for process industry like IEC 61508 and IEC 61511 (IEC61508 2000, IEC61511 2003, ISA84 1996). These standards have been developed to ensure that the SIS is designed, implemented and operated according to the specified needs.

3.1. Objectives of a safety instrumented system

The IEC 61511 defines a safety function as: “function to be instrumented by a SIS, other technology safety-related system or external risk, which is intended to achieve or maintain a safe state for the process, with respect to a specific hazardous event”. The Safety Instrumented Function (SIF) is used to describe the safety functions implemented by instrumented technology. The SIS is the physical system implementing one or more SIFs.
The objectives of SIS is to reduce the frequency at which hazard may occur to an acceptable level (Wiegerinck 2002). The safety function only reduces the risk (multiplication: probability x consequences) and never completely eliminates the risk. Some safety functions do not reduce the probability of the consequences.

3.2. Safety Integrity levels (SIL)

Once the required level of risk reduction to be achieved by the SIS is established, expressed as risk reduction factor (RRF), this level can be translated into the required Safety Integrity Level (SIL) (Knegtering 2002).
IEC 61508 and IEC 61511 split the safety integrity into hardware safety integrity and systematic safety integrity. The safety integrity is split into four discrete safety integrity levels (SILs), SIL1 to SIL4. Each SIL represents a maximum allowed probability of failure on demand of the SIS. SIL4 is the level with the most stringent requirements. To fulfil a specific SIL, the SIL requirements related to hardware safety integrity as well as systematic safety integrity must be met (Lundteigen and Rausand 2006).
To calculate the SIL of a safety function it is required that the complete safety loop from sensor to actuator is

considered. Therefore, it is not sufficient to only analyze one subsystem of the safety process, such as the logic solver, and determine the realized SIL.

4. INTELLIGENT SAFETY CONCEPT

The intelligent safety loops (or intelligent distributed safety instrumented systems) enable us to implement safer plants by using the intelligent devices for safety application in compliance with the new IEC 61511 standard.

We introduce the concept of intelligent safety to show the inherence in the use of intelligence within safety instrumented systems. Several manufacturers claim the certification of intelligent products in the applications of safety while launching "smart SIS" but without real justification to the level of the reliability performances. The use of intelligent instruments in the process industry was facilitated by the increasing of microprocessor performances; microprocessors are used in particular in instrumentation. The justification of the use of these instruments in safety applications is not completely proven; even if these instruments have important benefits which are useful for this type of applications (Nobes 2004).

There is a trend toward the use of intelligent instruments in safety applications. The inherent ability to diagnose failure is the primary reason. The ability of intelligent instruments to reliably measure complex parameters is another reason.

Intelligent instruments offer a means of incorporating higher levels of intelligence into safety instrumented systems to make them more efficient.

5. MODELLING AND TOOLS

5.1. Stochastic Activity Network

Stochastic activity networks (SANs) (Movaghar and Meyer, 1984) are a stochastic generalization of Petri nets. SANs are a powerful modelling formalism which extends GPSN (generalized stochastic Petri nets) in many ways. These models allow the representation of concurrency timeliness, fault-tolerance and degradable performance in a single model. SANs are more flexible than most other stochastic extensions of Petri nets (Abdollahi and Movaghar, 2005).

The most relevant high-level modelling constructs offered are the input and output gates, which allow specifying controls on the net execution and define the marking changes that will occur when an activity completes. SANs also consist structurally of activities and places. Activities which are similar to transition in normal Petri nets are of two types: timed and instantaneous. Timed activities represent activities of the modelled system whose duration impact the performance. Instantaneous activities represent system activities which occur immediately.

SAN models have been used to evaluate a wide range of systems and are supported by several modelling tools such as UltraSAN (Sanders, Obal, Qureshi and Widjanarko 1995) and Möbius (Deavours, Clark, Courtney, Dalys, Derisavi, Doyle, Sanders, and Webster 2002). The models are developed using this SAN-based tool. Möbius tool consists in the description of the net structure and of the desired performance variables and solutions methods to be used in the evaluation.

SAN is defined with the express purpose of facilitating the performance in the dependability evaluation by defining a set of measures in the model. In the context of Stochastic Petri Nets, these measures are derived from the concept of reward (Malhotra and Trivedi, 1995).

5.2. Modelling approach

The modelling problem consists in achieving the evaluation of dynamic systems which evolve as a function of the time. SPNs give the possibility to model a system in which cooperate discrete-time variables and discrete events, which can occur on a stochastic basis. The formalism used for the behavioural modelling will naturally be able to represent these characteristics. The use of this formalism will allow the representation of a component failure in interaction with the functional behaviour.

Petri nets, as tools for discrete event simulation are of large use in dependability evaluation. Dynamic changes in the PNs are induced by transition firing. Firing of one or of several transitions changes the net marking. In other terms, it induces a discrete change of states. Thus, dynamic properties of PNs such as parallel firing, successive firing or firing of concurrent transitions may be used to simulate complex events sequences (Vernez, et al., 2003).

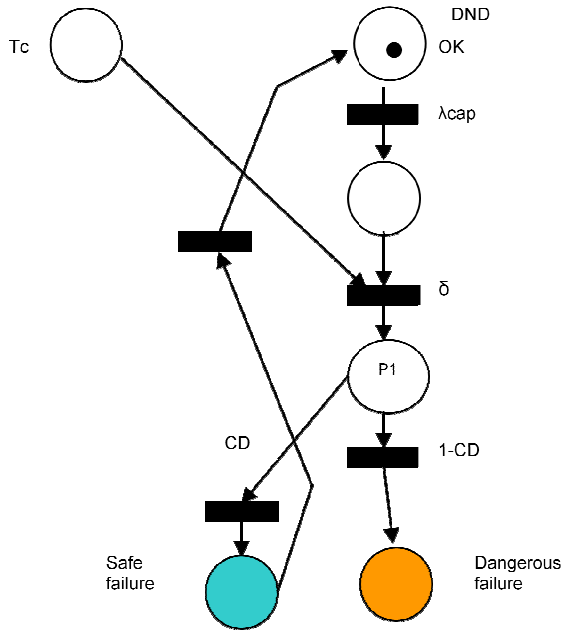

Figure 2 : Example of sensor modelling and its failures

The modelling problem consists in achieving the evaluation of dynamic systems which evolve as a function of the time. SPN give the possibility to model a system in which cooperate discrete-time variables and discrete events, which can occur on stochastic basis. The formalism used for the behavioural modelling will naturally be able to represent these characteristics. The use of this formalism will allow the possibility to represent component failure in interaction with the functional behaviour. Other techniques like Markov graphs present some limits when used to resolve a reliability computation problem (Schoenig, et al,. 2006). Logic based quantitative methods (as fault trees) do not easily handle strongly time-dependant behaviours, because they do not consider the order of failure occurrences. Statistical data regarding the system dynamics are missing. A Monte-Carlo simulation of the whole model (both discrete and continuous parts) reproduces the real operation of the process (featured by its own dynamic), and the control subsystem behaviour according to both process state and current failure. The marking of the place Dangerous Failure on Figure 1 means that a feared event arises. A quantitative study allows assessing the occurrence probability by simulation.

In the present approach, it is assumed that the failure distributions of individual components of a system are given, and the dependability measures of the stochastic system are sought. Furthermore, the system is assumed to be dynamic (its properties change with time).

For all the models, they are made in the stochastic Petri nets (SPN) and they are transformed in the stochastic activity network (SAN).

5.3. System modelling

In the modelling of the system, the functional and dysfunctional aspects coexist and the dynamic approach using the Stochastic Activity Network (SAN) is proposed to overcome the difficulties mentioned above. Monte-Carlo method is used to assess the dependability parameters in compliance with safety standards related to SIS (IEC 61508 & IEC 61511). The proposed method and associated tools allow this evaluation by simulation and thus provide assistance in designing SIS integrating intelligence.

A dangerous failure results in an absence of reaction of the safety function. A safe failure results by the setting in a safe position of the system or in an unexpected execution of the safety function. The detection of a safe or dangerous failure, results in a setting into safe position of the system or a forced execution of the safety function.

At the beginning, we present SIS without incorporation of intelligent instruments nor communication network. The model of the logic solver is shown in figure 3.

The model of the logic solver presented figure 2 shows a disposition of two parts, one functional and the other dysfunctional. In the functional part (on the left), the cycles of the logic solver are carried out by a periodic clock (*periode*). The self-tests of the various devices are managed locally according to a policy allocating the same duration of test for the various devices and starting with the test of the sensor (*Tc*), then the actuator (*Tv*) and finally the logic solver (*Ta*). This policy is not the only possible and other policies can be possibly established. For the dysfunctional part, it should be made sure that the token is carried of functional part when the system fails safe or dangerous. The logic solver can be also restored in the event of safe failure and it also has a coverage rate of diagnosis which is inherent to him.

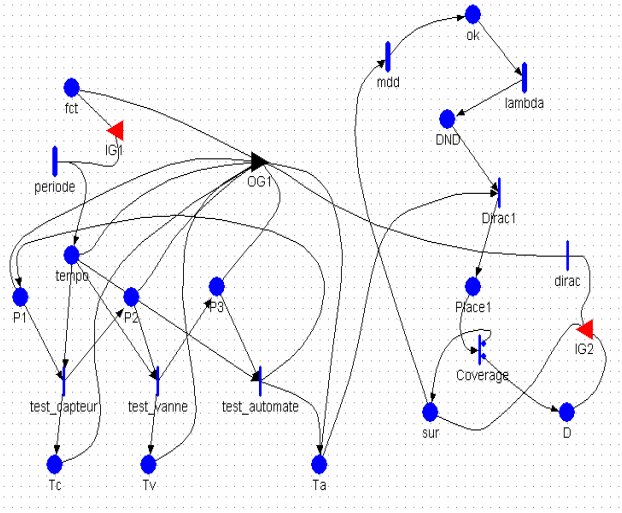

Figure 3: Structure of Logic solver

Now, we will be interested in a model of the system with a communication network (*CAN*: *Control Area Network*) and then we will also introduce intelligent instruments instead of traditional instruments. Indeed, CAN protocol is used as a communication architecture for safety critical applications (Carvalho, Freitas, Pereira, and Ataide 2006). In this article, we focus on CAN while in this study can be extended to other types of communication network. The Network model is shown in figure 4.

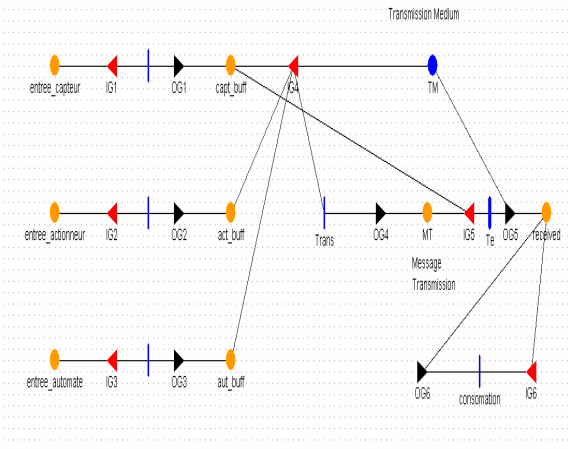

Figure 4 : Network model

This submodel represents the behaviour of the CAN network (Mkhida, Thiriet, and Aubry 2008). The

network is made up in this example of three transmitting stations which will be able to send messages on a shared medium (transmission channel). The messages sent are placed in buffer places which are extended places, messages then await the release of the channel to be transmitted towards their destination. The channel access is based on messages priorities. This means that each subscriber will be affected by a priority allowing him or not to send these characteristics via the channel, to avoid the collisions on the channel. The medium (channel) is affected of a delay representing the time of transmission of the messages. The output message of the channel is ready to be sent and it is available in the place *" received "*.

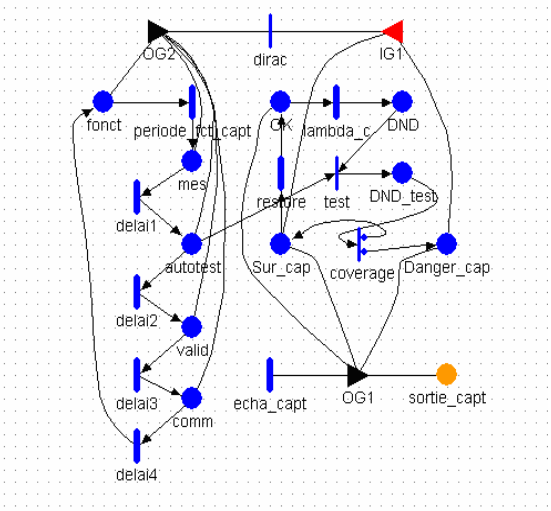

Figure 5: intelligent sensor model

In the intelligent sensor model (see figure 5), the order of test is not transmitted any more via communication network by the logic solver and the functionality relating to the test as well as the other functionalities of the intelligent sensor is treated locally. The modules of test can be requested either when it is necessary, or in a cyclic way, or permanently according to an active monitoring principle (the intelligent sensor has at one's disposal a self-tests). In our model, the intelligent sensor has self-tests in a cyclic way according to the instants of period. The other functionalities are also synchronized by this period.

The model of the actuator does not differ much from that of the intelligent sensor and the dysfunctional parts are similar. It should be noted that the model of the sensor, the actuator and the logic solver are sampled models and information is sent to the communication network periodically.

6. RESULTS OF SIMULATION

When analytical methods fail to provide results, the traditional way is to use Monte Carlo simulations (Signoret, et al., 2007). For doing that, a model simulates properly the behaviour of the system upon failure. With the Möbius models, parameters to evaluate like probability or sojourn of time I any place is defined via reward functions (Malhorta and Trivedi, 1995). The procedure used for the calculus of probability of dangerous failures (PFD) and the probability of safe failures (PFS) consists in the presence of tokens in the places which describe the safe failures and the dangerous failures for the whole system.

Reference diagnostics are performed by a single instrument. The notation coverage is used to designate the dangerous diagnostic coverage factor due to single unit reference diagnostics. The coverage factor of diagnostics will vary widely with results ranging from 0 to 99%. The coverage rate of diagnosis is taken in this example equal to 60% for all the devices. It was chosen in compliance with the IEC 61511 standard. The activity "restore" is the time required to restart the component after a shutdown. The failures rates are obtained from industry databases (Goble and Cheddie, 2005). These data used in safety components to evaluate their dependability parameters are approximate. Also, due to the lower solicitation of safety systems in process, safety components have not been operating long enough to provide statistical valid failure data. Furthermore, measuring and collecting failure data have uncertainty associated with them, and borrowing data from laboratory and generic data sources involve uncertainty as well.

The procedure used for the calculus of probability of dangerous failures PFD and the probability of safe failures PFS consists of the presence of tokens in the places which describe the safe failures and the dangerous failures for the whole system.

Figure 6 shows the evolution of PFD and PFS for a 10000 hours duration which is a little higher than one year (8760 hours).

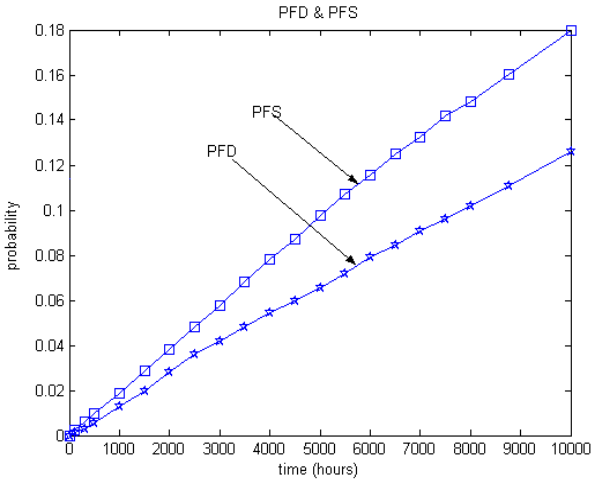

Figure 6: Evolution of PFD and PFS according to time

The coverage rate of diagnosis is taken in this example equal to 60% for the whole of the devices. The period of the self-tests operated by the logic solver is selected equal to one hour. I.e., that in compliance with the policy of test chosen, the duration of cycle of the logic

solver is 3 hours Also let us note that this duration affects the PFD and PFS when it is changed. For example, for a value of period of test of 1 hour such as it is presented in figure 7, the PFD is 0.1113 and the PFS is 0.1604 for a time of 8760 hours mission. While these values apply to one duration of test of the logic solver equal to 2 hours, the PFD passes to 0.107 and the PFS becomes equal to 0.165. It is to show the influence of the frequency of the period of the test of the logic solver on the total performances in safety of the system.

Now, we will be interested in the performance evaluation in safety after the introduction of the intelligent instruments. The results are given for duration of simulation equal to 8760 hours.

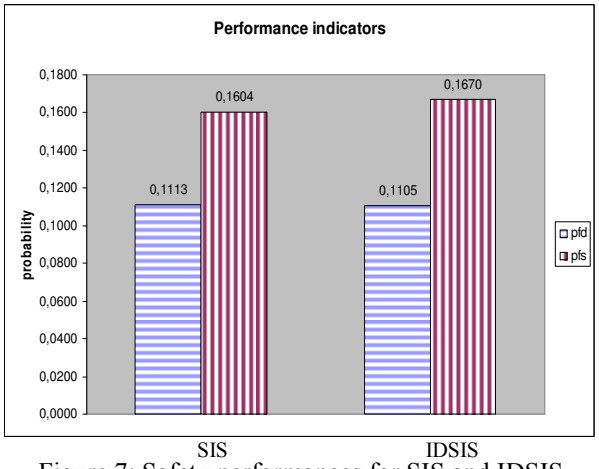

Figure 7: Safety performances for SIS and IDSIS

The evolution of the two metrics (see figure 6) which describe the performances in safety of the studied system show a clear improvement of the probability of dangerous failure according to the addition of intelligence and a weak degradation of the probability of safe failures. Indeed, more there are high rates of detection by the integrated means of self-tests, more the failure rate weakens and the safe failure rate increases by the means of the dangerous failures which were transformed into some kind of safe failures.

The addition of the validation functionality (intelligence) has contributed to improve safety performance slightly. Indeed, the probability of dangerous failures will have to improve further with the introduction of intelligence in the actuators.
The difference between the performance of conventional systems and systems with intelligence is not significant. But in a context of functional safety, differences between the safety integrity levels (SIL) are very small and any variation remains important.

The parameters used for the system without network are listed with the same values as before. Other parameters are introduced; they are suitable for use in the communication network such as the delay in the transmission, the sampling periods of different devices (sensor, controller and actuator).

The communications network ensures timely transmission below the sampling period. It is the only component in the system that works in a manner of events. The delay is constant. It should be noted that the emphasis is not on the influence of the delay or loss or alteration of frames.
The introduction of the network has resulted in some changes in the basic models of the components of the safety circuit to take account of the mechanisms of transmission of data over the network
We proceeded to check the values of the sampling period other than Te = 0.5 s and we obtained the following results:

Table 1: Performance safety based on the sampling period

Te	0,5	1	5	8
PFD	$7{,}7.10^{-2}$	$7{,}33.10^{-2}$	$7{,}08.10^{-2}$	$7{,}03.10^{-2}$
PFS	$2{,}1.10^{-1}$	$2{,}078.10^{-1}$	$2{,}05.10^{-1}$	$1{,}995.10^{-1}$

In the Table 1, the evolution of the two metrics which describe the performances in safety of the studied system show an improvement of the probability of dangerous failure and the probability of safe failures according to the change of the sampling period.

7. CONCLUSION

This paper deals with the assessment of Safety Instrumented Systems using intelligence in the field devices. The integration of intelligent instruments within safety oriented applications presents a challenge. The justification for using these instruments in safety applications is not fully proven and the dependability evaluation of such systems is not trivial.

The performance of these systems is evaluated and compared to the systems without intelligence. The results express the safety performance of these systems, using the particular modelling assumptions made, and the reliability data chosen. Some parameters have a significant impact on the PFD and PFS values, but the accent was put on the contribution of intelligence on the SIS. The setting of the intelligence in SIS improves the PFD but not in a significant way and degrades the PFS slightly.

Special focus was given to the intelligent instruments introduced in the SIS with their failures without counting the failure of network that can influence the performance of safety. In general, the probability of dangerous failures decreased and the probability of failure safe. This is due to the fact that information concerning the failures is only sent during discrete moments and not continuous. The performances are indeed very sensitive to sampling periods of different devices. And thus the moments of revelations depend

largely on the sampling periods, thus causing the change of values of these two metrics.

REFERENCES

Abdollahi Azgomi and A. Movaghar (2005), Hierarchical Stochastic Activity Networks: Formal Definitions and Behaviour, International Journal of Simulation, Systems Science and Technology, Vol. 6, N°. 1-2, pp. 56-66.

Berbra C., S. Lesecq, S. Gentil, J-M. Thiriet (2007), Diagnosis of a safe networked quadrotor, *ACD'07 workshop on Advanced Control and Diagnosis*, Grenoble, 15-16 novembre 2007.

Carvalho F.C., E.P. Freitas, C.E. Pereira and F.H. Ataide (2006). A time-triggered controller area network platform with essentially distributed clock synchronisation. A *Proceedings Volume from the 12th IFAC Conference*. Saint-Etienne, France. pp, 93-98.

Deavours D.D., G. Clark, T. Courtney, D. Dalys, S. Derisavi, J.M. Doyle, W.H. Sanders, and P.G. Webster (2002). The Möbius framework and its implementation. IEEE Trans. On Soft. Eng, Vol. 28, no 10. pp 956-969.

Goble W. M. and H. Cheddie (2005). Safety Instrumented Systems Verification, Practical Probabilistic Calculations. ISA (The instrumentation, Systems, and Automation Society).

IEC61508 (2000). Functional safety of electrical / electronic / programmable electronic safety related systems. IEC, International Electrotechnical Commission.

IEC61511 (2003). Functional safety – Safety instrumented Systems for the process industry sector. IEC, International Electrotechnical Commission.

ISA84 (1996). Application of Safety instrumented Systems for the process industries. ANSI/ISA-S84.01.

Knegtering B., (2002). Safety lifecycle management in the process industries: the development of a qualitative safety-related information analysis technique. *Phd thesis.* Technische Universiteit Eindhoven.

Lian, F., J.R. Moyne and D.M. Tilbury (2002). Network design consideration for distributed control systems. *IEEE Transactions on Control Systems Technology*. **Vol 10(2)**. pp 297-307.

Lundteigen, M.A. and M. Rausand. (2006). Assessment of hardware safety. *Proceedings of the 30th EDReDA Seminar*. Trondheim, Norway.

Malhotra, M. and K. Trivedi (1995). Dependability Modelling using Petri Nets, IEEE Transaction on reliability, Vol. 44, N°. 3, pp. 428-440.

Meijer G.C.M., (1994). Concepts and focus point for intelligent sensor systems. *Sensors and Actuators A*, **Vol. 41-42**, pp. 183-191.

Mekid S. (2006). Further structural intelligence for sensors cluster technology in manufacturing. *Sensors*, **Vol 6**, pp. 557-577.

Mkhida A, J.M. Thiriet and J.F. Aubry (2008). Toward an Intelligent Distributed Safety Instrumented Systems: Dependability Evaluation. 17th IFAC World Congress, July 6-11, 2008, Seoul, Korea.

Movaghar A, and J.F. Meyer (1984). Performability modelling with stochastic activity networks. *Proceddings of the 1984 Real Time Systems*, Symposium, Austin, TX. pp 215-224.

Nobes, T (2004). , Smart instruments in protective measures, Is your product safe? *–IEE Seminar*. pp 67-74.

Robert M., J. M. Riviere, J. L. Noizette, and F. Hermann (1993). Smart sensors in flexible manufacturing systems. *Sensors and Actuators A,* **Vol. 37-38,** pp.239-246.

Sanders, W.H., W.D. Obal, M.A. Qureshi and F.K. Widjanarko (1995). The UltraSAN modelling environment. Performance Evaluation, Vol. 24, N°. 1-2, pp 89-115.

Signoret J. P., Y. Dutuit, A. Rauzy 2007. High Integrity Protection Systems (HIPS) : Methods and tools efficient Safety Integrity Levels (SIL) analysis and calculations. Risk, Reliability and Societal Safety, Taylor & Francis Group, pp. 663-669.

Schoenig R., J.F. Aubry, T. Cambois and T. Hutinet 2006. An aggregation method of Markov graphs for the reliability analysis of hybrid systems. *Reliability Engineering and System Safety*. **Vol 91**, **no 2**, pp, 137-148.

Tian G. Y., Z. X. Zhao and R. W. Baines (2000). A fieldbus-based intelligent sensor. *Mechatronics*, **Vol. 10**, pp. 835-849.

Weiegerinck Jan A.M., (2002). Introduction to the risk based design of safety instrumented systems for the process industry. *Seventh International Conference on Control, Automation, Robotics And Vision (ICARV'02)*. Singapore.S.E.

DEVELOPING INTEGRATED PERFORMANCE MEASUREMENT SYSTEM - USING MDA APPROACH

Souhail Sekkat[(a), (b), (c)] , Jean Luc Paris[(a)], Khalid Kouiss[(a)], Janah Saadi[(c)] , Laurant. Deshayes[(d)]

[(a)] LIMOS – IFMA Campus de Clermont-Ferrand/Les Cézeaux - BP 265 - 63175 Aubière Cedex, France.
[(b)] ERCSSP- ENSAM Marjane II Beni M'hammed, BP 4024, Meknes Alismailia, Meknes, Maroc.
[(c)] LAP - ENSEM Casablanca B.P. 8118, OASIS. Route d' EL JADIDA, Casablanca.
[(d)] MANBET TECHNOLOGY : 5 Avenue Abou Taeib Al Moutanabi Residence Walili Apt 13, Fes.

[(a)]paris@ifma.fr, kouiss@ifma.frail, [(b)]s_souhail@hotmail.com [(c)]janah1@menara.ma [(d)]laurent.deshayes@gmail.com

ABSTRACT
In an industrial context defined by more acute competition, performance measurement becomes a control tool. The Manufacturing Execution System (MES) software achieves control and execution of production functions, as Performances analysis. However, to choose the adequate performance indicators and to implement them is a difficult problem. Indeed, the enterprises need methods to specify and to install their Performance Measurement System (PMS). In this paper, we propose a methodology of performance indicators implementation. We use the Component Oriented Programming with a Model-Driven Architecture (MDA), to generate applications' final code. This method facilitates the design of Performances Measurement System and its implementation.

Keywords: Manufacturing Execution Systems MES, Performances Measurement Systems PMS, Component Oriented Programming COP, Model-Driven Architecture MDA.

1. INTRODUCTION

Nowadays, the level of integration determines the effectiveness of modern technical systems. Application of the system engineering results in that systems become distributed, and consist of a number of physically or logically distributed components that constitute the system to reach the common goal. Communication between such components is a crucial issue.

The performances analysis is among the important components of computer control system. The development and the implementation of a Performances Measurement System (PMS) is a difficult problem. Indeed, to design and implement a Performances Measurement System (PMS), we must properly model identities, attributes and operations of individual objects as well as the sequence of operations and data flow in a shop floor control system. What will allow, thereafter, the time follow-up of the key performance indicator (KPI).

Therefore, in this paper, we present a shop floor control model and its implementation using Object and Component Oriented Approach.

Several researchers have applied Object-oriented and Component-oriented concepts in implementing manufacturing execution systems MES. For instance, (Yang and al 2000) applied object-oriented programming (OOP) to develop a CIM system. In addition, a distributed automation and control system has been implemented in (Krassi 2002). For system integration a middleware CORBA were used. Another work was addressed on applying COP methodology to develop a controller, in robotic palletization area (Chiron 2009).

Although various works related to the modeling and implementation of shop floor controllers were presented, the implementation of PMS was not addressed by those researchers. MDA approach can be used to support this issue. Basically, it focuses on:

1. Identifying objects and their related properties,
2. Building the relationships among objects,
3. Describing the data transformation within the system.

The main body of this article is organised as follows. In the next section, the methods of PMS software design are presented and discussed. Then, proven industrial technology used in the process of application tool integration is presented. After then, proposed approach for specification and implementation of PMS is outlined. The article closes with a practical example and drawing a conclusion.

2. THE DESIGN OF PERFORMANCE MEASUREMENT SYSTEM (PMS)

The rapid progress of computer technologies brings shop floor control functions into a new area. Many advanced functions have been introduced as the results of improving computing power. These functions include

real time scheduling, networking, cell coordination and Performance analysis (Halang and al 2006).

In this section, we will present the PMS software and the different methods used for its design. First, we are going to describe the Computer Integrated Manufacturing (CIM) pyramid and to position the PMS in this pyramid. Then we will define the Overall Equipment Effectiveness (OEE). It is the PMS we will implement. Finally we are going to describe the methods used to develop shop floor control system.

2.1. CIM Pyramid

Since the functions of shop floor control have become more complex than before, several control architecture and models were proposed. One of the most famous models is NIST AMRF (National Institute of Standard and Technology / Advanced Manufacturing Research Facility) Proposed by National Bureau of Standards.

The AMRF model is applying hierarchical control architecture; it is composed of five-level hierarchy: facility, shop, cell, workstation and Actuator/Sensor. Each level has its specific functions.

The business functions such as; cost accounting, aggregate planning are executed in the facility level. It is done generally by ERP software. Shop level is responsible for coordinating production tasks including resource allocation and task assignment. The tool used at this level is The Manufacturing Execution Systems MES. Cell level is subject to sequence similar parts in batch jobs and supervises supporting tasks such as material handling and transportation. The supervision is achieved, generally by SCADA software A workstation level is responsible for monitoring the execution of production tasks. It consists of a robot, a fabrication station or a material storage buffer.

The Manufacturing Execution Systems MES provide a module for performances Analysis. Within the functions of this module, there is computation of performance indicators and display of scorecards functions (MESA, 2000). The PMS is based on the computer controller systems for:

1. The data collection (starting time, break times, completion time, products quality…),
2. The computation of performance indicators and
3. The display of scorecards.

2.2. OEE Overall equipment effectiveness

The more utilized PMS, is the OEE Overall equipment effectiveness measures, there are three underlying metrics that provide understanding as to why and where the OEE gaps exist.

These measurements are described below:

- Availability: The portion of the OEE Metric represents the percentage of scheduled time that the operation is available to operate. Often referred to as Uptime.
- Performance: The portion of the OEE Metric represents the speed at which the Work Center runs as a percentage of its designed speed.
- Quality: The portion of the OEE Metric represents the Good Units produced as a percentage of the Total Units Started. Commonly referred to as First Pass Yield.

OEE is computed as follows:

$$OEE = Availability \times Performance \times Quality \quad (1)$$

To implement the PMS, we must integrate it within the control system. Indeed, it should collect the data, from the shop floor control and send the performance indicators to the business information system.

2.3. The design of Integrated Production System

A design of an integrated production system is a big project that includes several jobs; programmers, automation engineer, mechanics… A design of shop floor controller is achieved through several steps:

- Definition of needs
- Product and process Analysis
- System Specification
- Equipments installation
- Controller Implementation
- Operation and maintenance

The main process steps are the specification and the implementation.

During the Specification, it is necessary to describe functionalities of equipments (production system) and the controller (information system). Thus, modeling methods are used. Business process modeling is the activity of representing a company processus, so that the current process may be analyzed and improved. BPM is typically performed by managers who are seeking to improve process efficiency and quality. It allows the construction of models of a determined part of an enterprise.

The evolution of the complexity of information systems, the worry of optimization of software applications design drove the scientists to develop some modeling methods. The classic modeling methods are ones that describe the Information system and proceed to separate treatment of data and processes. The object-oriented methods are new approaches of development. It considers a system like a set of objects in interactions (every object achieves or undergoes some operations), examples of these methods (UML, OMT) (Kettani and al 1999). The methods dedicated to distribute systems are those allowing the development of multi agents systems (with distributed execution objects).

Implementation: It is a setting step, which consists in the choice of the machines, control software's, the programming of supervisory control interfaces and tests.

Shop floor control must be integrated system. Interoperability requirement is difficult to achieve. Indeed, many companies selling industrial software tools and hardware, such as distributed control systems, SCADA (Supervisory Control And Data Acquisition) packages, programmable controllers, etc., provided external interfaces for interoperability but employed proprietary protocols requiring custom software development. Integration of applications meant substantial development effort to provide adapter layers so that applications could operate collaboratively and share data.

3. APPLICATION TOOL INTEGRATION

To harmonize different vendors' solutions (non-proprietary) for distinct information domains accomplishing the engineering requirements, it is common sense that the enterprise automation system might rely upon a common architecture to enable open standards interoperability.

The evolution of the Internet has played a major role in the area of application interoperability by providing an infrastructure that links applications, businesses, and users. It has promoted the adoption of standards, such as XML for data representation, and the use of common software protocols, such as TCP/IP and SOAP (Simple Object Access Protocol). These advances combined with the adoption of industry standards, such as OPC, by major equipment and system vendors has given end-users the means to greatly simplify the sharing of data at all levels of an enterprise, from the production level up to the executive level. Indeed, international non-profit organizations, like OPC Foundation (OPC – OLE for Process Control) and OMG (Object Management Group) cooperate among themselves to enable the development of open and consistent automation system architectures. Examples of such efforts are OPC UA (Unified Architecture) and CORBA (Common Object Request Broker Architecture).

In this section we will present the two more used standards for interoperability of industrial systems: the OPC standard and the CORBA bus.

3.1. The OPC standard

The rising of OPC technology made the HMI software manufacturers have to develop only a driver for communication with devices, differently of the way before, which each manufacturer had to develop proprietary drivers for supporting its devices. In industrial automation, companies like Rockwell Automation, Simens … wrote their own HMI software and a proprietary driver for each industrial device including every PLC (Programmable Logic Controller) brand in order to retrieve process data. The standardization of these drivers was developed by a group of manufactures that have improved the OPC model due to them additions based on past experiences. It is mentioned for example the navigation system of the OPC tags through tree structure and its division by sectors.

The OPC standards are based on *Microsoft* Object Linking and Embedding (OLE), Component Object Model (COM) and Distributed Component Object Model (/DCOM) technologies and provide the foundation for developing OPC compliant software. In order to address the specific needs of the process industry, the original OPC standards for process data acquisition has been extended through the following sets of specifications: OPC-DA (data access for real-time data), OPC-HDA (historical data access), OPC-AE (alarms and events), OPCXML, and OPC Batch (OPC Task Force 1998).

Since 2003, OPC Foundation and a group of IHM and device manufactures have been working in a joint venture to define and implement a new OPC Specification. This new Specification is the OPC UA. The purpose of OPC UA is to provide enhancements for existing and next generation OPC products in the areas of security, reliability, and interoperability. OPC UA is designed to unify existing OPC specifications into an environment that will leverage Web-based technologies and standards such as Web Services, WSDL (Web Services Description Language), XML and SOAP (Simple Object Access Protocol).

The OPC UA is based on SOA (Service Oriented Architecture) through Web Service that transports XML data, which provides the communication among different software of different platforms, providing interoperability. XML lets interoperability of different software of different platforms to transfer information using a common language. Since XML is a meta-language, it is possible to create new languages to make a standard talk. Thus, OPC UA is the key to improve the transformation of simple data in knowledge, due to the open high-level mechanism, open the doors to store the information by an easier way for MES (Manufacturing Execution System) and ERP (Enterprise Resource Planning) applications.

3.2. CORBA-BASED AUTOMATION SYSTEMS

The Common Object Request Broker Architecture (CORBA) is a widely recognized by the control community object-oriented open-standard-based middleware for distributed systems integration. CORBA supports interoperability, portability and reusability of systems' components. There is a number of CORBA implementations and mappings to various programming languages that are available from different vendors. Also, its real-time and fault-tolerant specifications have been developed recently (Curtis, Stone and Bradley 2009).

A CORBA system is based on client/server and oriented object model. The different components of this model are:

- **The client application** it is a program that invokes the methods of the objects through the CORBA bus.

- **The object interface** (Stub) allows clients to use objects without compile-time knowledge of their interfaces. It is generated by the IDL compiler to provide a "proxy" to an object to make it appear local to the client.
- **ORB (Object Request Broker)** is the communications system which passes requests to objects, and results back to clients.
- **Object Adapter**: provides services to implementations (e.g. registration, management of object's lifetime).
- **The object implantation** is generated by the IDL compiler to invoke the implementation using a set of conventions. It is special ORB functionality which allows invocation of implementations without compile-time knowledge of their interfaces.
- Implementation: code to implement the object.

These abstract notions result in technological components provided by the CORBA norm.

CORBA component's interface is described in a neutral Interface Definition Language (IDL). CORBA IDL is a declarative non-programming language; it does not provide any implementation details. The methods that are specified in IDL can be implemented with any programming language such as C++ and Java using rules defined by OMG. The Object Request Broker (ORB) is an object bus that provides a transparent communication, means for objects to send message to and receive message from other objects.

The General Inter-ORB Protocol (GIOP) provides interoperability (a set of message formats) between ORB implementations from different vendors. The GIOP can be mapped onto different telecommunication protocols for transport protocol independence. Thus, the Internet Inter-ORB Protocol (IIOP) is a mapping of GIOP onto the TCP/IP protocol stack.

From the automation systems viewpoint, CORBA is a layer for abstracting communications among components of the system, and a means for systems integration. Various components, which have different functionality, hardware and software, but compatible CORBA-interface, are plugged into the ORB but for higher level of interoperability and integration.

Finally we conclude that the requirement for data to be available across all levels within an enterprise is increasing. The business information technology markets have been addressing the challenges of interoperability and application integration for many years through Enterprise Application Integration (EAI). The trend is towards distributed architectures with increased interoperability among applications from multiple vendors.

4. THE PROPOSED APPROACH

The proposed approach can be used to develop a manufacturing execution system (MES). It is an iterative approach; the technical details are differed until the implementation step.

As a first step, we propose to model the system by using UML language (Kettani and al 1999). We adopt the use cases diagram to elaborate the functional model of the system. The use cases identified are the different activities proposed by the ISA S95 standard (ISA 2000):

- The product definitions and production resources management
- The detailed production scheduling, production dispatching and execution.
- The production data collection, production tracking and production performance analysis.

As far as we are considered, we deal with big interest with production data collection and performances analysis activities.

The products, processes, workforce, and other elements in manufacturing are modeled, in UML as "objects" in computer based graphical diagrams. In the static model, we use class diagram, which describes, the major structure of objects in a system including the identities, attributes and operations of individual object.

The staffs that exploit the production cell (operators) as well as the facilities (machines) are modeled by a class RESSOURCE "figure 1". The factory is subdivided in REGION that regroups the facilities treating a products family. The raw materials, Work in Progress and finished products are described by a class MATIÈRE. The process is described by a class OPERATION. The methods used to execute these operations are described by the class GAMME. The performance information of the different operations is stocked in the data base RAPPORT.

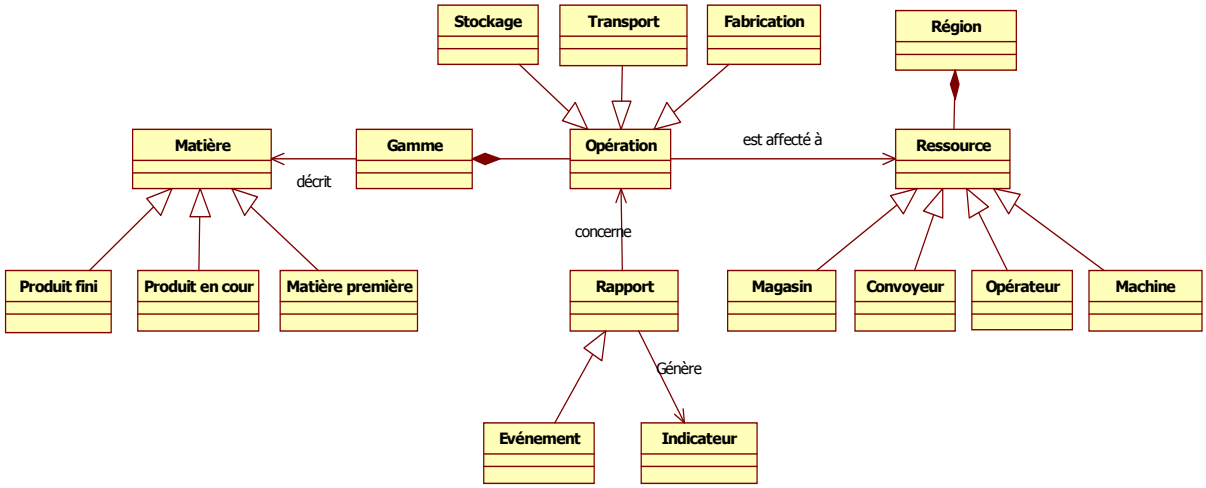

Figure 1: Class Diagram of the ENSAM Cell PMS.

The dynamic model describes the functions of the objects and their interfaces that they share with the other objects. Thus, we propose the use of sequence diagrams and state machine diagrams, which show the sequence of events both from a product perspective and from an information transaction viewpoint.

The script achieved by the SIP module of an MES software is as follow:

1. The class **Operation s**ends data collection demand to the class **Resource**.
2. The class **Resource** collects the data and sends back them in the **RAPPORT** class, the collected data are the starting time and the completion time of each operation as well as the mistake messages of the machine.
3. If there is an abnormal situation, the collected data will be sent back to the class **Operation**.
4. To analyze the performances, the **RAPPORT** class will collect the following shop floor data. The collected data will permit to analyze the performances and to compute the performance indicators.
5. The report of production will be produced and will be sent to management system.

As a second step, we propose to adopt a Component-oriented approach and use the MDA for the mapping of the UML models to the information system. Indeed, the proposed UML models are platform independent (PIM). It is necessary, therefore, to select a middleware platform that allow an interoperability of the distributed system, and refine the engineering models of the system in technical models, on describing how the platform is used to accomplish the interoperability requirements. In the context of MDA, the technical models are also called Platform Specific Models (PSM).

We propose to use Enterprise Application Integration (EAI) architecture, to allow interoperability, application integration and PMS implementation. (EAI) is an integration framework composed of a collection of technologies and services which form a middleware to enable integration of systems and applications across the enterprise. The middleware connects to applications through a set of adapters, also referred to as connectors. These are programs that know how to interact with an underlying business application, using different communication protocols. It acts as a workflow between the applications. We propose an integrating infrastructure based on computer standards, such as XML (data representation technologies) that allows the different heterogeneous applications to communicate by sending and receiving messages.

The Integration Platform, is therefore centered on a message server, it regroups the components that support the interoperability of tools. It essentially provides both data centralization and communication services that allow tools to share data and communicate between themselves. In addition to communication services, the integration platform contains a user interface module for indicators display. It hides all aspects of transport protocols from the component that it interfaces.

As an implementation step, we propose to elaborate, deployment diagram and component diagram. Deployment diagram serves to model the hardware used in system implementations, and the execution environments and artifacts deployed on the hardware. Component diagram depicts how a software system is split up into components and shows the dependencies among these components.

We must identify system components and affect them with responsibilities. For this, we will firstly make an external view representation, named black box view, and we will then, retail the component internal behavior by white box representation (Kouiss and al 2006).

The responsibilities of the KPI component are; data collection (machines status, product quality, execution time …), data verification, reaction when anomalies occur. In addition, KPI such as equipment utilization rate will be computed and displayed in business information system window.

5. PRACTICAL EXAMPLE

The proposed method is applied to the flexible machining cell in ENSAM. We will develop a PMS for its control. The system is organized around a belt trolley which allows a routing of the part toward a CNC milling machine "figure 2". A jointed-arm robot is used to load and unload parts for CNC machine.

- A 3 axes milling machine CNC MILL 55 with FANUC 21 controller is used to produce parts.
- A 5 axes industrial Robot RV-2AJ with an air gripper is used to load and unload of the CNC machine. The robot controller is a RISC processor, 64 bits, multitask and real time operating system. Robots programming is done by (Cosirop) software.
- A buffer with belt trolley, sensors and air stoppers, takes charge of storing and routing raw materials and finished parts. The belt allows a routing of the part. It is moved by electric motor. The storage system is controlled by the robot controller.

Figure 2: the ENSAM machining Cell.

In the control architecture of the system, a SCADA software (COSIMIR Contrôle) is installed in the top-level computer. An Ethernet network is connecting several machine controllers. The CNC machine is equipped with a DNC link based on RS-232 and the robot with Ethernet extension "figure 3".

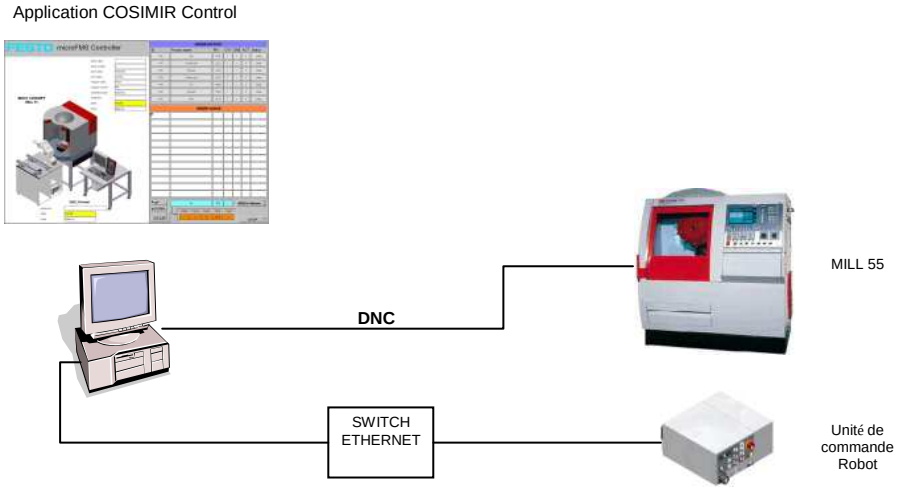

Figure 3 : Cellule flexible (partie commande).

The PMS must communicate with the SCADA software COSIMIR, it must also communicate with a MRP software.

Let us consider a work order sent by the MRP Software to the cell controller COSIMIR. The cell controller will select the production routine of the considered part from the Routine File database. It will check about the resources status. If all necessary resources are available, it will determine adequate material and start the tasks.

The strategy of integration was to provide a common software infrastructure (Integration Platform) that would allow a wide variety of application tools to communicate and share data, while minimizing the specific development for each tool. The heart of the Integration platform is SCADA software **COSIMIR Control**. It is a real-time, object-oriented development environment.

It is necessary to ask the COSIMIR software to collect the status machine during each process step. Thus, we elaborate an UML component diagram. We intend to implement the components in Visual C++. The data files required by the system like work orders, the routing, the workstation files, are stored in Access database.

Each UML class diagram proposed at the modelling step will be transformed in C++ code during the implementation step. Each class attribute will be declared like a variable. In addition, each class operation will be described like a method that executes the considered task.

6. CONCLUSION

The use of Object and Component approach, proven industrial technology coupled with message oriented middleware considerably eased the process of application tool integration. it allowed a better flexibility of the PMS.

Although the proposed model is focused on a CIM system in the educational environment, several concepts developed from this model still can be applied in the shop floor controller utilized in other environment.

Applying the techniques of business application interoperability to process applications implies that many other issues must be addressed when considering interoperability especially those related to safety and performance.

GLOSSARY

CIM Computer Integrated Manufacturing
COP Component Oriented Programming
CORBA Common Object Request Broker Architecture
EAI Enterprise Application Integration
ERP Enterprise Resource Planning
HMI Human Machine Interface
KPI Key Performance Indicator
MDA Model-Driven Architecture
MES Manufacturing Execution System
OEE Overall equipment effectiveness
OOP Object Oriented Programming
OPC OLE for Process Control
PLC Programmable Logic Controller
PMS Performances Measurement Systems
SCADA Supervisory Control And Data Acquisition
SOAP Simple Object Access Protocol
UML Unified Modeling Language
XML eXtensible Markup Language

REFERENCES

Chiron, F., 2009. Contribution à la flexibilité et à la rapidité de conception des systèmes automatisées avec l'utilisation d'UML. Thèse de Doctorat en Informatique ; université Blaise Pascal – Clermont

Curtis, D., Stone, C., Bradley, M., 2009. IIOP: OMG's Internet Inter-ORB Protocol A Brief Description. Object Management Group (OMG). Available from: http://www.omg.org. [accessed 10 May 2010]

Halang, W. A., Sanz, R., Babuska, R., Roth, H., 2006. Information and communication technology embraces control. Status report prepared by the IFAC: Coordinating Committee on Computers, Cognition and Communication. Annual Reviews in Control 30 31–400

ISA. 2000. ANSI/ISA 95.00 03-2000. Enterprise/Control System Integration - Part 3: Activity Models of Manufacturing Operations Management. The Instrumentation, Systems, and Automation Society.

Kettani. N., D. Mignet, P. Paré, C. Rosenthal-Sabroux, 1999. De Merise à UML. Editions Eyrolles.

Kouiss, K., Chiron, F., David, S., Thomas, M., 2006. A Component based development of user manufacturing systems. IDMME 2006. Grenoble France.

Krassi. B. A., 2002. Distributed computing and automation: Industrial applications. URL : http://www.automationit.hut.fi/julkaisut/documents/seminars/sem_s02/Krassi_paper.pdf.

MESA International. 2000. "Control definition and MES to control data flow possibilities". White paper. N :3 pp :1-7. http://www.mesa.org.

OPC Task Force., 1998. OPC Overview. Version 1.0. OPC Foundation. Available from: www.opc.org. [accessed 10 May 2010]

Yang. C. O., Guan, T. Y., Lin, J. S., 2000. Developing a computer shop floor control model for CIM systems – using object modelling technique, Computers in Industry 41. pp: 213-238.

TRAFIC CONTROL AND QUEUES MANAGEMENT FOR A SINGLE INTERSECTION

Fadi Motawej, Rachid Bouyekhf, Abdellah EL Moudni

Laboratoire Systèmes et Transports UTBM,
Site de Belfort, Belfort Technopôle,
90010 Belfort Cedex, France.

fadi.motawej@utbm.fr, rachid.bouyekhf@utbm.fr, abdellah.el-moudni@utbm.fr

ABSTRACT
It is by now well known that, the traffic signal control is the most effective measure for reducing traffic congestion in an intersection. Traffic congestion arises when arrival rate exceeds capacity in the intersection. The most undesirable symptom of this kind of instability is an unbounded accumulation of vehicles in the system. Our contribution in this paper is to show that, for a single intersection, congestion can be prevented by using a state feedback controller having an appropriate positive structure. It is shown that two main objectives are achieved with the proposed controller: firstly, when traffic flow is not in excess, the queuing of automobiles cannot exceed intersection capacity. Secondly, in order to fit physically reasonable signalization, the controller respects the boundary conditions. Example is worked out to illustrate the results.

Keywords: Traffic lights control, Single intersection, State feedback control.

1. INTRODUCTION

As the number of vehicles and the need for transportation grow, cities around the world face serious road traffic congestion problems. In general there exist different methods to tackle the traffic congestion problem. The most effective measures in the battle against traffic congestion seem to be a better control of traffic through traffic management. Traffic light control can be used to manage the traffic flow in urban environments by providing a smooth circulation of the traffic. The purpose of traffic lights is to provide safe and efficient interaction of vehicles within the intersection.

In the past 40 years, great effort has been made in the area of signal timing optimization techniques (Gazis 1974, Green 1968, Kaltenbach and Koivo 1974, Dans and Gazis 1976, Michalopoulos and Stephanopolos 1978, Wey 2000, Barisone, Giglio, Minciardi and Poggi 2002, Abu-Lebdeh and Benekohal 2000, Girianna and Benekohal 2000). Most of these control strategies are based on a preprogrammed periodic cyclic rhythm. These approaches are easy to implement but may be not efficient and flexible because they do not take into account traffic changes.

Michalopoulos and Stephanopolos (Michalopoulos and Stephanopolos 1978) were probably the first to propose a two-stage timing method. The method attempts to find an optimal switch-over point during the over-saturated period to interchange the timing of the approaches. Their model is a continuous type and does not address the problem of cycle length optimizing. Recently, Tang-Hsien and Lin (Tang-Hsien and Lin 2000), have studied a discrete delay type model, involving *bang-bang* like control, to improve Michalopoulos and Stephanopolos model. The *bang-bang* control operates alternatively and sequentially with a given only minimal and maximal green time boundaries. However, there is a limited evolution of this control strategy because the *bang-bang* control does not consider the deviation of a system from its nominal behavior caused by deviation of system components and parameters from their nominal performance characteristics. Another notable work in this area is the one presented by Schutter and Moor (Schutter and Moor 1998) in which the authors have shown how an optimal traffic light switching scheme for an over-saturated intersection of two streets can be determined. In general, this leads to a minimization problem over solutions set of an extended linear complementarity problem. However, it is well-known that the linear complementarity problem is NP-hard. Hence, as claimed by authors, this approach is not feasible if the number of switching cycles is large.

In conclusion, all these works are based mainly on an open loop and rolling horizon techniques. However, due to the substantial changes in the traffic characteristics at different times of the day, control strategies should be such that the signal takes into account the effects of the abrupt change in any period. In fact, the feedback control method may be the best means to achieve this aim. This is the objective of the paper.

Our contribution in this paper is to show that congestion can be prevented by using a state feedback controller having an appropriate positive structure. More precisely, we propose a state feedback control scheme able to achieve the objective of congestion avoidance and to satisfy a queue length of vehicles that does not exceed the intersection capacity.

2. SYSTEM DESCRIPTION AND MODELING

We consider here an isolated two-phase intersection with controllable traffic lights on each corner (Figure 1). It is supposed that there are two traffic flows of vehicles to be served (movements 1 and 2). To be able to present the model, a certain number of definitions are necessary.

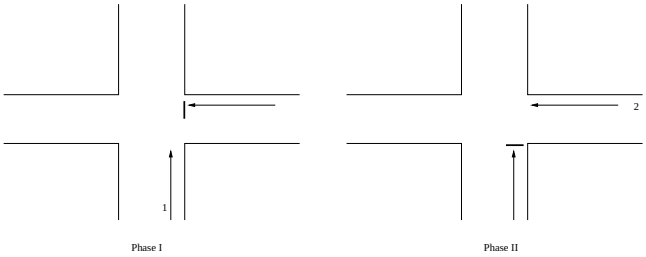

Fig. 1. Four-leg intersection with two-phase signal control.

Lost time L: time when an intersection is not effectively used by any approach. Lost time occurs during a part of the change interval and at the beginning of each green due to start-up delay. It is defined by $L = l_1 + l_2$, where l_1 represents the startup lost time and l_2 the clearance lost time.

Effective green time g_e: time actually available for movement. It excludes start-up delay that occurs at the beginning of the phase as well as any lost time that might occur near the end of the phase. It is defined by

$$g_e = g + y - L,$$

where g is the green time interval, y represents the amber interval. The effective green time g_{e_2} on phase II is determined from the effective green times g_{e_1} on phase I by the relation

$$g_{e_1} + g_{e_2} = c. \tag{1}$$

where c is the cycle length. Notice that it makes no sense to speak of negative g_{e_i}. Therefore, equation (1) leads to constraints on the pair of control variables (g_{e_i}, c), that is

$$0 \leq g_{e_i} \leq c; \quad c > 0.$$

In other words, the effective green time can be at most equal to the length of the cycle. However, certain boundary points may not fit physically reasonable signalization settings. In particular, $g_{e_1} = 0$ corresponds to no effective green time for phase I, $g_{e_1} = c$ corresponds to no effective green time for phase II. Therefore, it is important to select tow boundary values g_{min} and g_{max} so that

$$g_{min} \leq g_{e_i} \leq g_{max} \tag{2}$$

The values of g_{min} and g_{max} must be well selected. For instance, too short effective green lights are impractical and too long effective green lights are unacceptable to the stopped drivers of the other approach. Hence, any g_{e_i} satisfying this constraint leads to a viable signalization control strategy.

Saturation flow rate s: the discharge process of the vehicles in the queue is controlled by reaction times and desired acceleration rates of drivers as well as acceleration rates of vehicles ahead. At the beginning of the green interval, the discharge rate at stop lane starts to increase. As the queuing vehicles have reached a constant speed at stop line, the discharge rate has reached its maximum, called the saturation flow rate. More precisely, the saturation flow rate is defined as the maximum number of vehicles being able to use the corridor without interruption during the effective green time g_e. The saturation flow rate may vary from cycle to cycle, but an average value can be used for given conditions.

Let us now write down a discrete model that describes the evolution of the queue lengths. This will then yield the equations that give the relation of the queue lengths between cycle k and $k+1$. Let us denote $I = \{1, 2\}$ and define

x_i : queue length of movement $i \in I$,
q_i : input flow rate of movement $i \in I$,
s_i : saturated flow rate of movement $i \in I$,
g_{e_i} : effective green time of phase $i \in I$

where in general $q_i < s_i$. The fundamental idea of the described traffic model design technique is based on the traffic flow conservation principle. It means that the queue at time $k+1$ is equal to the sum of the previous queue at time k and the number of arrivals $E_i(k)$ minus the number of departures $D_i(k)$ from the lane i.

The number of arrivals $E_i(k)$ is given by the input flow rate q_i of movement i and the cycle length c. The quantity $E_i(k)$ can be written as $E_i(k) = q_i\, c(k)$. The maximal number of passing vehicles $D_i(k)$ is given by the saturation flow s_i and the effective green time g_{e_i}. The quantity $D_i(k)$ can be written as $D_i(k) = s_i\, g_{e_i}(k)$.

Now, let $x_i(k+1)$ be a queue length of approach i when the cycle k is terminated, then the relation of the queue lengths between cycle k and $k+1$ can be represented by the following equation:

$$x_i(k+1) = x_i(k) + E_i(k) - D_i(k) \tag{3}$$

Hence, equation (3) becomes:

$$x_1(k+1) = x_1(k) + q_1 c - s_1 g_{e_1}(k)$$
$$x_2(k+1) = x_2(k) + q_2 c - s_2 g_{e_2}(k)$$

Since $g_{e_1} + g_{e_2} = c$, it follows

$$x_1(k+1) = x_1(k) + (q_1 - s_1)c + s_1 g_{e_2}(k)$$
$$x_2(k+1) = x_2(k) + q_2 c - s_2 g_{e_2}(k)$$

The above equations can be equivalently restated as a state space expression

$$x(k+1) = x(k) + Bu(k) + L \tag{4}$$

where $x(k)$ is the state vector, $u(k) = g_{e_2}(k)$ is the control variable, and

$$B = \begin{pmatrix} s_1 \\ -s_2 \end{pmatrix} = \begin{pmatrix} b_1 > 0 \\ b_2 < 0 \end{pmatrix};\ L = \begin{pmatrix} (q_1 - s_1)c \\ q_2 c \end{pmatrix} = \begin{pmatrix} \ell_1 < 0 \\ \ell_2 > 0 \end{pmatrix}$$

Notice that, it makes no sense to speak of negative queue. Hence, if x_0 describes queue at time $k = 0$ then $x(k) \geq 0$ for all $k \in \mathbb{N}$. Therefore, the system (4) has physical meaning only if x belongs to the region of admissible states $\Omega_x = \{x \in \mathbb{R}^n / x \geq 0\}$.

3. CONTROL PROBLEM FORMULATION

The control problem is formulated as follows. We consider

the system (4) with a maximal capacity of each lane x_1^* and x_2^*. Then, congestion may occur in the system if the queue length of each lane exceeds its capacity. The most undesirable symptom of this kind of instability is an unbounded accumulation of vehicles in the system.

The control objective is then to find a state feedback controller that respects the constraint (2) and is able to satisfy

$$0 \leq x(k) \leq x^*, \quad \forall k \geq 0, \quad \forall\, 0 \leq x_0 \leq x^* \tag{5}$$

Motivated by (Rami, Tadeo, and Benzaouia 2007), the following proposition gives an answer to this problem.

Proposition 1: Consider system (4) *with parameters* $x^* > 0$, $g_{\min} > 0$ *and* $g_{\max} > 0$. *Suppose that* $1 + \frac{b_1 b_2}{x_i^*} \geq 0$. *Then, if there exists a positive scalar* α *with* $\alpha \geq \max(\frac{-\ell_1}{b_1}; \frac{-\ell_2}{b_2})$ *such that*

$$B(b_1 + b_2 + \alpha) + L \leq 0 \tag{6}$$

$$b_1 + \alpha \leq g_{\max} \tag{7}$$

$$b_2 + \alpha \geq g_{\min} \tag{8}$$

then there exists a positive control $u(k) = Q^T x(k) + \alpha$ *such that* $0 \leq x(k) \leq x^*$ *for all* $0 \leq x_0 \leq x^*$ *and* $g_{\min} \leq u(k) \leq g_{\max}$.

Proof: Define the vector $Q^T = [\frac{b_2}{x_1^*}, \frac{b_1}{x_2^*}]$ and observe that since $1 + \frac{b_1 b_2}{x_i^*} \geq 0$, it follows $I + BQ^T \geq 0$. Furthermore, $\alpha \geq \max(\frac{-\ell_1}{b_1}; \frac{-\ell_2}{b_2})$ implies $B\alpha + L \geq 0$. Now, under the state feedback control $u = Q^T x + \alpha$ the closed-loop system becomes

$$x(k+1) = (I + BQ^T)x(k) + B\alpha + L \tag{9}$$

Since $I + BQ^T \geq 0$ and $B\alpha + L \geq 0$, it is easy to show that $x(k) \geq 0$ for all $x_0 \geq 0$. With this in mind, observe that $b_1 + b_2 = Q^T x^*$, hence (6) implies

$$B(b_1 + b_2 + \alpha) + L = BQ^T x^* + B\alpha + L < 0. \tag{10}$$

This and the fact that $I + BQ^T \geq 0$ and $x_0 \leq x^*$ imply

$$\begin{aligned} x(1) &= (I + BQ^T)x_0 + B\alpha + L \\ &\leq (I + BQ^T)x^* + B\alpha + L \\ &= x^* + BQ^T x^* + B\alpha + L \leq x^* \end{aligned}$$

it follows

$$\begin{aligned} x(2) &= (I + BQ^T)x(1) + B\alpha + L \\ &\leq (I + BQ^T)x^* + B\alpha + L \\ &= x^* + BQ^T x^* + B\alpha + L \leq x^* \end{aligned}$$

By induction it can be shown that

$$\begin{aligned} x(k) &= (I + BQ^T)x(k-1) + B\alpha + L \\ &\leq (I + BQ^T)x^* + B\alpha + L \\ &= x^* + BQ^T x^* + B\alpha + L \leq x^* \end{aligned}$$

Hence, the first objective (5) of the control is achieved with the proposed controller. Now, observe that

$$u(k) = Q^T x(k) + \alpha = \frac{b_2}{x_1^*} x_1 + \frac{b_1}{x_2^*} x_2 + \alpha$$

Since $0 \leq x_1 \leq x_1^*$, $0 \leq x_2 \leq x_2^*$, $b_1 > 0$ and $b_2 < 0$ then

$$b_2 + \alpha \leq u(k) \leq b_1 + \alpha$$

Hence, (7) and (8) imply

$$g_{\min} \leq u(k) \leq g_{\max}$$

which completes the proof. ■

It follows immediately from Proposition 1 that, for an arbitrarily selected positive $\alpha > \max(\frac{-\ell_1}{b_1}; \frac{-\ell_2}{b_2})$ that satisfies constraints (6), (7) and (8), the feedback controls defined by $u(k) = Q^T x(k) + \alpha$ exhaust the class of control laws u which maintain the queue length of each lane less than its capacity. Hence, Proposition 1 gives explicit and non-unique solution of the congestion control.

Remark 1: As we can see, the control law $u(k) = Q^T x(k) + \alpha$ is positive and its input data are the estimated values of the queues level during each cycle k. Hence, the control policy evaluates the green light for each traffic cycle following the calculation process of vehicles stored in the intersection. The real-time availability of $x(k)$ can be measured by a traffic detector installed at the corresponding lanes. This situation allows us to use effectively the available information on the system to perform closed loop control of the traffic signals in real time.

The performance of the proposed control law is illustrated in the simulation studies of two-phase intersection. Figure 2 represents the evolution of the queue lengths x_1 and x_2 stored in the system within 6000 cycles. One can immediately observe that the application of feedback control $u(k) = Q^T x(k) + \alpha$ prevents the queue lengths reaching the lanes capacities and hence avoids the congestion. This simulation is carried out by holding account the following data: $s_1 = 0.2veh/s; s_2 = 0.2veh/s; q_1 = 0.1veh/s; q_2 = 0.1veh/s; c = 160s; u_{max} = 120s; u_{min} = 30s; x_1^* = 50veh; x_2^* = 45veh$. According to these parameters, we have $1 + \frac{b_1 b_2}{x_1^*} = 0.9992 \geq 0$, $1 + \frac{b_1 b_2}{x_1^*} = 0.9991 \geq 0$, $Q^T = (-0.0041, 0.0044)$ and the scalar α is found to be 80.

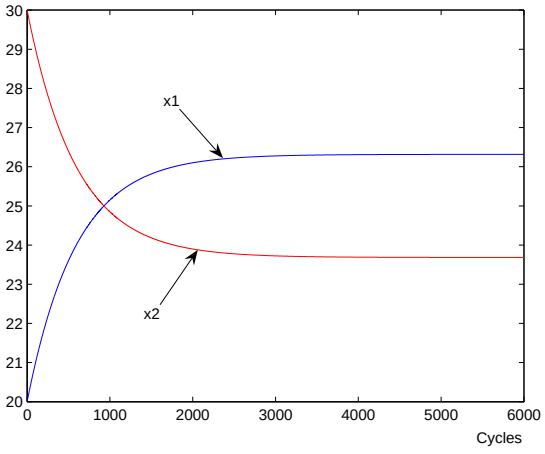

Fig. 2. Queue lengths evolution system

In the following section, we address the case where the cycle length is time varying and it is considered as a second control variable. The importance of this comes from the fact that it gives us a degree of freedom and a flexibility for the control strategy, because its variation will take into account the effects of the abrupt change in real traffic situation.

4. CASE WHERE THE CYCLE LENGTH IS TIME VARYING

In this case equation (3) becomes:

$$x_1(k+1) = x_1(k)+(q_1 - s_1)c(k)+ s_1 g_{e_2}(k)$$
$$x_2(k+1) = x_2(k) + q_2 c(k) - s_2 g_{e_2}(k)$$

The above equations can be equivalently restated as a state space expression

$$x(k+1) = x(k) + Bu(k) \tag{11}$$

where $x(k)$ is the state vector, $u(k) = (c(k), g_{e_2}(k))^T$ is the control variable, and

$$B = \begin{pmatrix} q_1 - s_1 & s_1 \\ q_2 & -s_2 \end{pmatrix}$$

Furthermore, the system is to be analyzed under the following constraint

$$\begin{pmatrix} c_{\min} \\ g_{\min} \end{pmatrix} \leq \begin{pmatrix} c(k) \\ g_{e_2}(k) \end{pmatrix} \leq \begin{pmatrix} c_{\max} \\ g_{\max} \end{pmatrix}$$

which is equivalent to

$$0 < u_{\min} \leq u \leq u_{\max}. \tag{12}$$

As in the preceding section, the control objective is then to find a state feedback controller that respects the constraint (12) and is able to satisfy

$$0 \leq x(k) \leq x^*, \quad \forall k \geq 0, \quad \forall\, 0 \leq x_0 \leq x^*$$

This control problem is the same as the one described in section II except that the control variable in this case is depending on effective green time $g_{e_2}(k)$ and the cycle length $c(k)$. This situation leads us towards a square matrix B. Thus, the feedback control law derived in section II does not work in this context because the control is not a scalar. To overcome this inherent difficulty the following lemma will be useful.

Lemma 1: Consider a linear system of the form:

$$x(k+1) = x(k) + Bv(k) + L \tag{13}$$

with $x^* > 0$ and $v^* > 0$, if there exist three positive vectors $y^1, y^2, \alpha \in \mathbb{R}^2$ such that

$$B(y_i^1 + y_i^2 + \alpha) + L \leq 0 \tag{14}$$
$$B\alpha + L \geq 0 \tag{15}$$
$$y^1 + y^2 + \alpha \leq v^* \tag{16}$$
$$1 + b_i \frac{y^i}{x_i^*} \geq 0 \tag{17}$$
$$b_i \frac{y^j}{x_j^*} \geq 0, \text{for } i \neq j \tag{18}$$

where b_i is the i row of the matrix B, then there exists a positive control $v(k) = Qx(k)+\alpha$ such that $0 \leq x(k) \leq x^*$ and $0 \leq v(k) \leq v^*$ for all $0 \leq x_0 \leq x^*$.

Proof: Define the matrix $Q = [\frac{1}{x_1^*} y^1, \frac{1}{x_2^*} y^2]$ and observe that (17) and (18) imply $I + BQ \geq 0$. Now, under the state feedback control $v = Qx + \alpha$ the closed-loop system becomes

$$x(k+1) = (I + BQ)x(k) + B\alpha + L \tag{19}$$

Since $I + BQ \geq 0$ and $B\alpha + L \geq 0$ in view of (15), it is easy to show that $x_k \geq 0$ for all $x_0 \geq 0$. With this in mind, observe that $y^1 + y^2 = Qx^*$, hence (14) and (19) imply

$$B(y_1 + y_2 + \alpha) + L = BQx^* + B\alpha + L \leq 0. \tag{20}$$

This and the fact that $I + BQ \geq 0$ and $x_0 \leq x^*$ imply

$$\begin{aligned} x(1) &= (I + BQ)x_0 + B\alpha + L \\ &\leq (I + BQ)x^* + B\alpha + L \\ &= x^* + BQx^* + B\alpha + L \\ &\leq x^* \end{aligned}$$

it follows

$$\begin{aligned} x(2) &= (I + BQ)x(1) + B\alpha + L \\ &\leq (I + BQ)x^* + B\alpha + L \\ &= x^* + BQx^* + B\alpha + L \\ &\leq x^* \end{aligned}$$

By induction it can be shown that

$$\begin{aligned} x(k) &= (I+BQ)x(k-1)+B\alpha+L \\ &\leq (I+BQ)x^*+B\alpha+L \\ &= x^*+BQx^*+B\alpha+L \\ &\leq x^* \end{aligned}$$

Hence, the first objective of the control is achieved with the proposed controller. Now, since $0 \leq x(k) \leq x^*$ and $Q > 0$, then $0 \leq u(k) = Qx(k)+\alpha \leq Qx^*+\alpha = y^1+y^2+\alpha \leq v^*$ in view of (16), which completes the proof. ■

Now, the congestion control problem of system (11) can be solved by putting $u = v + u_{\min}$. In this case the constraints (12) yield $0 \leq v \leq u_{\max} - u_{\min} = v^*$ and system (11) becomes

$$x(k+1) = x(k) + Bv(k) + L \tag{21}$$

where $L = Bu_{\min}$, which is the same as equation (13). Hence, if all conditions of Lemma 1 are verified then the control $u = v + u_{\min} = Qx + \alpha + u_{\min}$ respects the constraint (12) and achieves the following objective:

$$0 \leq x(k) \leq x^*, \quad \forall k \geq 0, \quad \forall\, 0 \leq x_0 \leq x^*.$$

The performance of the proposed control law is illustrated in the simulation studies of two-phase intersection. Figure 3 is obtained with the following data: $s_1 = 0.6veh/s; s_2 = 0.4veh/s; q_1 = 0.3veh/s; q_2 = 0.2veh/s; c_{max} = 160s; c_{min} = 120s; g_{max} = 96s; g_{min} = 30s; x_1^* = 80veh; x_2^* = 70veh$. According to these parameters,

we have found $y^1 = (18.2789, 5.0991)^T$, $y^2 = (7.6539, 7.8673)^T$, $\alpha = (6.5315, 33.2657)^T$.

As in the preceding section, one can conclude that the application of feedback control $u(k) = Q^T x(k) + \alpha + u_{\min}$ prevents the queue lengths reaching the lanes capacities and hence avoids the congestion.

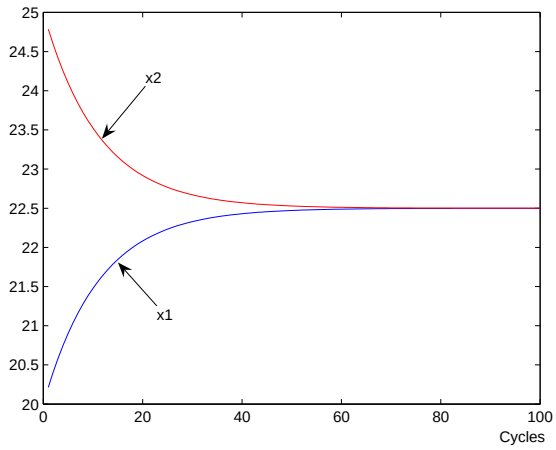

Fig. 3. Queue lengths evolution system

5. CONCLUSION

In this paper, it was shown that congestion in a single intersection can be prevented by using a state feedback controller having an appropriate positive structure. We have shown that two main objectives are achieved with the proposed controller: firstly, when traffic flow is not in excess, the queuing of automobiles cannot exceed intersection capacity. Secondly, in order to fit physically reasonable signalization, the controller respects the boundary conditions.

Upon application of the control strategy described in this paper, the process model is used on-line. Great computational effort is therefore desirable in this context. However, the rapid development of the numerical performance of computer hardware makes computationally extensive control concepts, such as on-line application, more and more feasible and also reasonable in terms of cost.

REFERENCES

Abu-Lebdeh. G and Benekohal. R., 2000. Genetic algorithms for traffic signal control and queue management of oversaturated two-way arterials. Transportation Research Record, 1727, 61–67.

Barisone. A, Giglio. D, Minciardi. R and Poggi. A., 2002. A macroscopic traffic model for real-time optimization of signalized urban areas. it Proceedings of IEEE conference on decision and control, 900–903.

Chang. T and Lin. J., 2000. Optimal signal timing for an oversaturated intersection. Transportation Research, 34, 471–491.

Dans. G and Gazis. D., 1976. Optimal control of oversaturated store-and-forward transportation networks.Transportation Science, 10 (1), 1–19.

Gazis. D., 1974. Modeling and optimal control of congested transportation systems. Network, 4, 113–124.

Green. D.,1968. Control of oversaturated intersections. Operational Research Quarterly, 18 (2), 161–173.

Grianna. M and Benekohal. R., 2000. Dynamic signal coordination for networks with oversaturated intersections. Transportation Research Record, 1811, 122–130.

Kaltenbach. M and Koivo. H., 1974. Modelling and control of urban traffic flow. *Proceedings of the Joint Automatic Control Conference*, pp. 147–154, Houston USA.

Mchalopoulos. P and Stephanopolos. G., 1978. Optimal control of oversaturated intersections theoretical and practical consideration. Traffic Engineering and Control, 216–221.

Rami. F. T. M. A and Benzaouia. A., 2007. Control of constrained positive discrete systems. *Proceedings of the 2007 American Control Conference*, pp. 5851–5856.

Shutter. B and B. Moor. B., 1998. Optimal traffic light for a single intersection. European Journal of Control, 4 (3), 260–276.

Wey. W., 2000. Model formulation and solution algorithm of traffic signal control in an urban network. Computers, Environment and Urban Systems, 24 (4), 355–377.

AUTHORS BIOGRAPHY

Motawej Fadi was born in Lattakia, Syria, in 1981. He received the Dipl.-Eng. degree in electrical engineering from the Tishrine University, Syria, in 2004, the Master 2 degree from the University of technology of Belfort-Montbliard, France, in 2008. He is currently working toward the PH.D. degree in the System and transports Laboratory(SET) of the University of technology of Belfort-Montbliard .

Rachid Bouyekhf received the Ph.D degree in automatic control in 1998 from Franche-Comté University, Besançon, France. He is currently an Associate Professor at University of Technology of Belfort-Montbéliard (UTBM), where he is in charge of courses in automatic control and information theory. His research interests include hybrid systems, H_∞ control, transportation systems, discrete event systems.

Abdellah El Moudni received the Ph.D degree in automatic control in 1985 from Lille University, Lille, France. He is currently a Professor at University of Technology of Belfort-Montbéliard (UTBM), where he is in charge of courses in automatic control. He is the Director of the Transportation systems laboratory at UTBM. His research interests include transportation systems, nonlinear control theory, dynamic systems, control of discrete event systems and singular perturbation methods in discrete time .

AN ALTERNATIVE WAY TO THE PWM CONTROL OF SWITCHED RELUCTANCE MOTOR DRIVES

Hedi YAHIA[(a)], Mohamed Faouzi MIMOUNI[(b)], Rachid DHIFAOUI

[(a)]Engineering School of Monastir 5019 Tunisia
[(b)]Engineering School of Monastir 5019 Monastir Tunisia
[(c)]Institute of Applied Science 3012 Tunis Tunisia

[(a)]Hedi.Yahia@enim.rnu.tn, [(b)]MFaouzi.Mimouni@enim.rnu.tn, [(c)]Rachid.Dhifaoui@insat.rnu.tn

ABSTRACT
The paper presents one alternative method to the conventional PWM control that provides high performance at low speed. The new developed control concept can significantly accomplish the performance of the SRM in terms of efficiency, torque ripple and power quality when compared to standard PWM current control. This control consists of feeding each phase with a constant volt per hertz (V/f) law for low speed range. The suggested V/f method is simple and is easy for practical implementation. Principle of this mode of control and analytical expressions for current calculation are provided and discussed. Obtained simulation results demonstrate the effectiveness of the proposed control strategy.

Keywords: PWM current control, single pulse, switched reluctance machine, V/f.

1. INTRODUCTION

By construction, the SRM is the simplest of all electrical machines. Only the stator has windings. The rotor contains no conductors or permanent magnets. It consists simply of steel laminations stacked onto a shaft. Motion is produced by the variation of the reluctance in the air gap between the rotor and the stator. The simple mechanical construction is one of the main attractive features which have motivated a large amount of research on SRM (Pillay et al 1997). One of the drawbacks of the SRM is the relatively large torque ripple when controlled by basic control strategies as compared to other types of electric machines (Mademlis and Kioskeridis 2003). This large torque ripple produces intensive and undesirable vibration and acoustic noise and limits the application areas of SRM (Venkatesha and Ramanarayanan 1998).

To reduce these disadvantages, most of the published papers are supported by exhaustive measurements of SRM magnetic characteristics. Sophisticated nonlinear adaptive control schemes of SRM have also been proposed (Henriques et al 2002, Zhang et al 2009). The disadvantages of these methods are that they are complex and computationally expensive which makes real-time implementation difficult (Russa et al 1997). To maintain SRM drives at low cost, there is a need for an easy to implement and cost-effective control method that provides acceptable performance over a wide speed range (David and Fukuda 2002).

There are several parameters for controlling SRM, such as turn-on angle, turn-off angle, and exciting voltage and controlling mode. In this paper, a novel control method that applies V/f law is developed. The optimal turn-on angle is fine-tuned referring to conventional control method. The optimal turn-off angle is defined at the critical rotor position where the current of next winding phase reaches its desired value (Kioskeridis and Mademlis 2007).

The purpose of this paper is to propose a novel strategy of control for SRM drives, which entirely operates on single-pulse mode. Variable DC voltage and full DC voltage are available for magnetization and demagnetization purposes respectively. The model and the basic equations of the SRM are first explained. This is followed by the presentation of the control parameters. The effectiveness of the proposed strategy is assessed by comparing the simulation results of the novel strategy with the PWM control. Finally, conclusions are given.

2. MATHEMATICAL MODEL OF SRM AND CURRENT ANALYSIS

2.1. Linear Math Model

The SRM used in this study is an 8/6 SRM Oulton with split dc supply converter. We model SRM in the linear region and we neglect effect of mutual inductances. The idealized obtained inductance profile for one phase is shown by Figure 1. The significant inductance profile changes are determined in terms of the stator and rotor pole-arcs and number of rotor poles (Krishnan 1994). The various angles are derived as follows. In this set of equations, β_s and β_r are stator and rotor pole-arcs, respectively. N_r is the number of rotor poles.

$$\begin{cases} \theta_1 = \dfrac{1}{2}\left[\dfrac{2\pi}{N_r} - (\beta_s + \beta_r)\right] \\ \theta_2 = \theta_1 + \beta_s \\ \theta_3 = \theta_2 + (\beta_s + \beta_r) \\ \theta_4 = \theta_3 + \beta_s \\ \theta_5 = \theta_2 + \theta_1 = \dfrac{2\pi}{N_r} \end{cases} \quad (1)$$

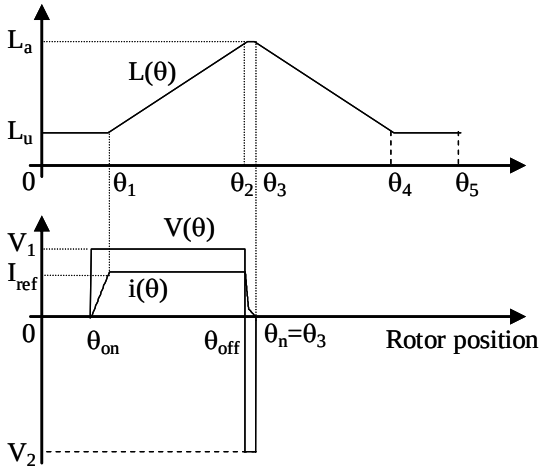

Figure 1: Idealized inductance profile vs. rotor position of a SRM

During rotor running, inductance changes from the minimum L_u to the maximum L_a periodically. L_u occurs when the axis of the rotor pole is aligned with axis passing by the center of the stator pole. On the other hand, maximum inductance La corresponds to the situation where the axes of rotor pole and stator pole are in the same position. The relationship between inductance L(θ) and the position θ of the rotor can be shown through the following function (Zai-ping and Hu 2004).

$$L(\theta) = \begin{cases} L_u & 0 \le \theta \le \theta_1 \\ L_u + L_s(\theta - \theta_1) & \theta_1 \le \theta \le \theta_2 \\ L_a & \theta_2 \le \theta < \theta_3 \\ L_a - L_s(\theta - \theta_3) & \theta_3 \le \theta \le \theta_4 \\ L_u & \theta_4 \le \theta < \theta_5 \end{cases} \quad (2)$$

Among the functions, $L_s = \dfrac{L_a - L_u}{\theta_2 - \theta_1}$ is the slope increasing inductance.

2.2. Converter Configuration

SRM converter configuration is a split dc converter as shown in Figure 2. The phase A is energized by turning on transistor T_1. In this step, the current flows through transistor T_1, phase winding A and the capacitor C1. When T_1 is turned off, the current will continue to flow (decreasing phase) through phase winding A, diode D_1, and capacitor C_2. Similar operations follow for phases B, C, and D. During increasing interval when T_1 is on, the winding phase voltage is V_1 whose amplitude is proportional to the reference speed. During decreasing interval when T_1 is off, the winding phase voltage is V_2 whose amplitude is kept constant to the rated value. When the speed becomes higher than the rated value, the voltage magnitude of V_1 is also kept to the rated value. More care has to be exercised in balancing the charges of C_1 and C_2 by adequate design measures (Ertl and Kolar 2008, Lee et al 2006). Here, to satisfy the functional requirements of C_1 and C_2 neutral point and variable voltage of V1, a three phase, four wire semi-controlled rectifier topology is proposed in Figure 3.

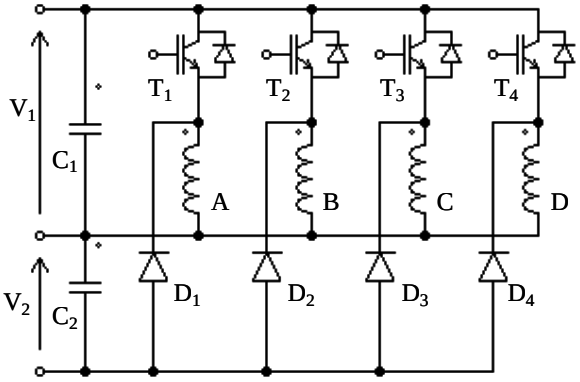

Figure 2: Split dc converter topology of a four-phase SRM

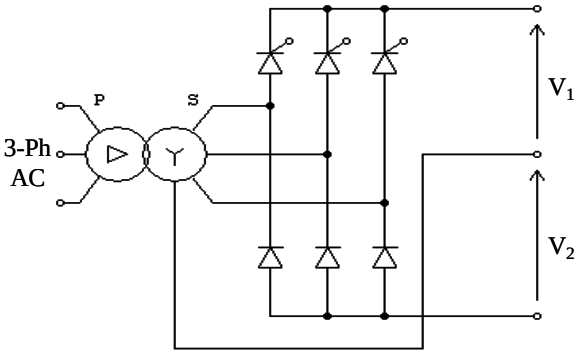

Figure 3: Three phase, four wire semi-controlled rectifier

2.3. Current Analysis

Figure 1 indicates that $dL/d\theta$ is negative for $\theta \rangle \theta_3$. To avoid any negative torque production, equation 5 indicates that the phase current should be regulated to zero before reaching θ_3. On the other hand, to ensure instantaneous torque production, it is essential that the

phase current is expected to reach a high value when inductance begins to increase. This means that the stator phase winding should be excited between 0 and θ_1.

Analysis of current shape considered in Fig. 1 is based on the following electrical equation where θ is the electrical angle, ω is the angular speed, R is the phase resistance, and V is the phase voltage. The mutual flux between the phases is assumed to be zero.

$$V = iR + \frac{d\Phi(\theta,i)}{dt} = iR + \frac{d\Phi(\theta,i)}{d\theta}\omega + \frac{d\Phi(\theta,i)}{di}\frac{di}{dt} \tag{3}$$

For the linear phase inductance model adopted in this study, (3) can be rewritten as follows where L(θ) is given in Fig. 1.

$$V = iR + \frac{d}{dt}\left[iL(\theta)\right] = iR + i\omega\frac{dL(\theta)}{d\theta} + L(\theta)\frac{di}{dt} \tag{4}$$

The developed torque in the n^{th} phase is given by (5). The total torque is then equal to the sum of the contributions from the 4 phases, (6).

$$T_{en} = \frac{1}{2}i_n^2\frac{dL_n(\theta)}{d\theta} \tag{5}$$

$$T_e = \sum_1^4 T_{en} \tag{6}$$

According to the above, the change of phase current can be divided in four stages assuming constant speed and zero current initial condition $i(\theta_{on})=0$. Solving (4) analytically, current's change can be expressed by the following functions

- Starting phase $\theta_{on} \le \theta \le \theta_1$;

$$i(\theta) = \frac{V_1}{R}\left[1 - \exp(\frac{R(\theta_{on}-\theta)}{\omega L_u})\right] \tag{7}$$

- Holding phase $\theta_1 \le \theta \le \theta_{off}$;

$$i(\theta) = \frac{V_1}{R+\omega L_s} + \left[I(\theta_1) - \frac{V_1}{R+\omega L_s}\right]\left[\frac{L_u}{L_u + L_s(\theta-\theta_1)}\right]^{(1+\frac{R}{\omega L_s})} \tag{8}$$

- Decreasing phase on positive slope of inductance $\theta_{off} \le \theta \le \theta_2$;

$$i(\theta) = \frac{V_2}{R+\omega L_s} + \left[I(\theta_{off}) - \frac{V_2}{R+\omega L_s}\right]\left[\frac{L_u}{L_u + L_s(\theta-\theta_{off})}\right]^{(1+\frac{R}{\omega L_s})} \tag{9}$$

- Continued decreasing phase in aligned position $\theta_2 \le \theta \le \theta_3$.

$$i(\theta) = \frac{V_2}{R} + \left[I(\theta_2) - \frac{V_2}{R}\right]\left[\exp(\frac{R(\theta_2-\theta)}{\omega L_a})\right] \tag{10}$$

3. DEFINING THE CONTROL PARAMETERS

The proposed control is operated in a single pulse mode over the whole speed range of the motor. The current amplitude is controlled by tuning the voltage level and commutation angle θ_{on} according to the desired motor speed. The commutation angles θ_{off} are adjusted to values causing an appropriate duration of the demagnetizing interval to occur at the aligned region (Kioskeridis and Mademlis 2006).

3.1. Selected Turn-on and Turn-off Angles

The analytical expression for determining the turn-on and turn-off angles is adopted in this paper.

We select the turn-on angle so that the phase current reaches its reference value I_{ref} at the angle θ_1. Thus, we establish on the basis of (3)

$$\theta_{on} = \theta_1 + \frac{\omega L_s}{R} Log\left(1 - I_{ref}\frac{R}{V_1}\right) \tag{11}$$

Turn-off angle value is usually variable and depends on the motor speed and electromagnetic torque. Here, we consider variable turn-off angle. To inhibit the uprising of a negative torque in the zone of decreasing inductance, θ_{off} is limited to θ_2 in low speed range. Otherwise, θ_{off} limit must be decreased to fulfill the constraint $\theta_e = \theta_3$ which ensures the extinction of the phase current.

During the aligned zone θ_2–θ_3, phase current is expressed by (4) which depend upon the current acquired at angle θ_2. Solving (4) for initial condition $I(\theta_2)$ yields the equation,

$$I(\theta_2) = \frac{V_2}{R}\left(1 - \exp(\frac{-R(\theta_2-\theta_3)}{\omega L_a}\right) \tag{12}$$

In demagnetization period $\theta_{off} - \theta_2$, since full negative voltage V_2 is supplied to motor winding, phase current is fast decreased and is given by (3). On intersection angle θ_2, the current values obtained by (3) and (4) are equal, thus

$$\frac{V_2}{R}\left[1 - \exp(\frac{-R(\theta_2-\theta_3)}{\omega L_a}\right] = \frac{V_2}{R+\omega L_s} + \left[I(\theta_{off}) - \frac{V_2}{R+\omega L_s}\right]\left[\frac{L_u}{L_u + L_s(\theta_2-\theta_{off})}\right]^{(1+\frac{R}{\omega L_s})} \tag{13}$$

The turn-off angle is obtained by solving (13), yielding,

$$\theta_{off} = \theta_2 + \left\{1 - \left[\frac{I(\theta_{off}) - \frac{V_2}{R+\omega L_s}}{I(\theta_2) - \frac{V_2}{R+\omega L_s}}\right]^{\frac{\omega L_s}{R+\omega L_s}}\right\}\frac{L_u}{L_s} \qquad (14)$$

where $I(\theta_{off})$ is equal to I_{ref}.

The above conditions are applied for SRM single-pulse operation. The effect of adopted turn-off angle on the total torque produced is observed in Figure 4. It can be seen that the torque ripple is very significantly increased. To keep the torque ripple level low, it appears preferable to commutate around another rotor position, where next winding phase reaches its respective reference value I_{ref} at the angle $\theta_1+\pi/2$. The new extinguishing angle θ_e is given by (15) and typical torque waveforms for the same mechanical speed ω_r are sketched in Figure 5. We observe an effective amelioration.

$$\theta_e = \theta_{off} + \frac{L_u}{L_s}\left\{\left[\frac{V_2 - I_{Max}(R+\omega L_s)}{V_2}\right]^{\frac{\omega L_s}{R+\omega L_s}} - 1\right\} \qquad (15)$$

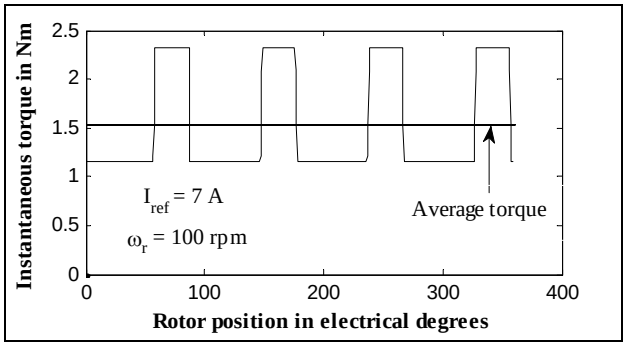

Figure 4: Developed torque with commutation angle θ_{off} calculated from (14)

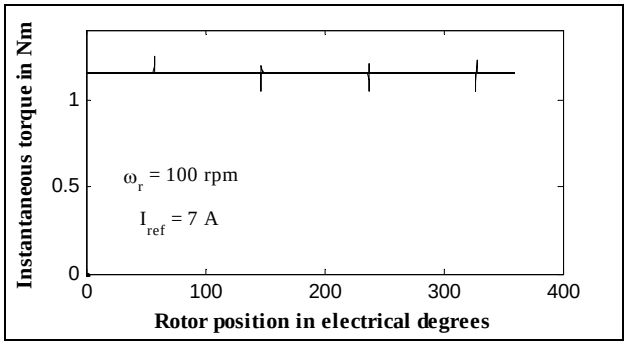

Fig.ure5: Developed torque with commutation angle $\theta_{off} = \theta_1+\pi/2$

3.2. Selected V/f Slope

Assume the speed of the machine is constant and neglect the voltage drop across the stator resistance. The rate of change of phase current can be derived from (4) as follow

$$\frac{di}{dt} = \frac{V - E}{L(\theta)} \qquad (16)$$

where $E = i\omega\frac{dL(\theta)}{dt}$ corresponds to the back-EMF. The behavior of the phase current depends on the relationship between the back-EMF and the source voltage V_1. An uncontrollable rise of the phase current is obtained when back-EMF and voltage V_1 are in balance. Recognizing that electrical speed $\omega = \frac{d\theta}{dt}$, the electrical frequency can be written as

$$f = \frac{\omega}{2\pi} \qquad (17)$$

The slope that defines the relation between the voltage magnitude and the voltage frequency is deduced from the condition that limits the rate of rise of current. Therefore, the condition to be satisfied is given by

$$V_1 = E = I_{ref}\,\omega L_s \qquad (18)$$

Substituting (17) in condition (18), the slope V/f, is derived as

$$\frac{V_1}{f} = 2\pi I_{ref} L_s \qquad (19)$$

However, when the running speed and hence also the voltage are very low, the voltage drop across the stator resistance cannot be neglected and must be compensated. The simplest stator resistance compensation method consists of boosting the stator voltage V_1 by the magnitude of the current– resistance (I_{ref}*R) drop (Muoz-Garcıa and Novotny 1998). The compensation influence is proved as shown by Figure 6.

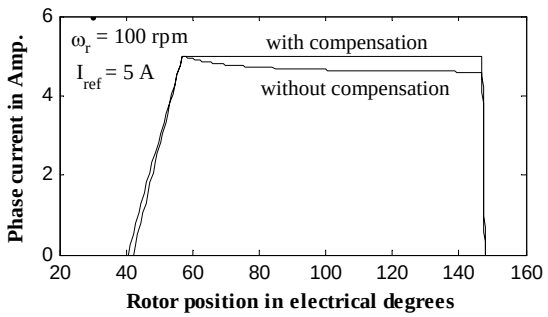

Figure 6: Current waveforms for 100 rpm without and with compensation

4. SIMULATION RESULTS

Simulation tests allowed initial testing of the new control concept. In addition, the objective of the simulation is to predict results that would match the experimental results such that lengthy experimental procedures can be eliminated during development stage. Simulation results are given based on comparison between V/f strategy and conventional PWM control. The motor used for simulation is a 4 kW, 8/6, four-phase SRM. The motor parameters are given in Table I.

V/f and PWM control results of the SRM drive are illustrated in Figures. 7 and 8, respectively. Specifically, the phase current profile and the developed torque for various speeds and limitation levels of desired current of Figures 7 (a), 7 (b), and 7 (c) are compared to Figures 8 (a), 8 (b), and 8 (c) respectively. It is concluded that the V/f control strategy enhances significantly the phase current and the generated torque shapes.

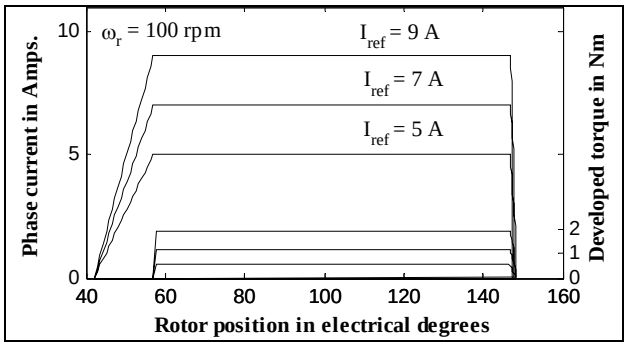

(a)

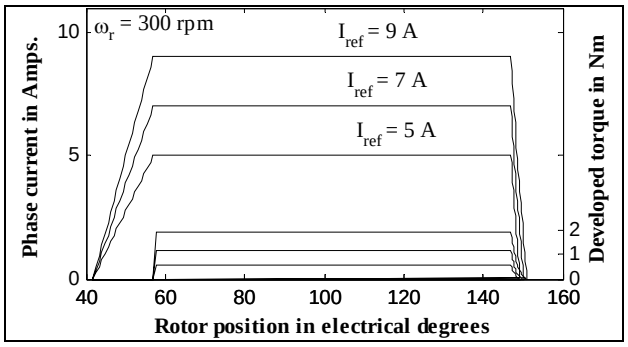

(b)

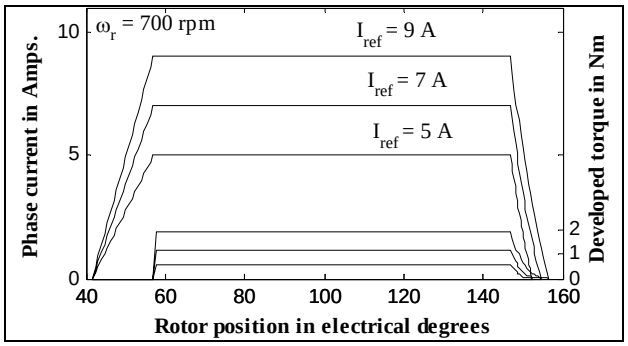

(c)

Fig. 7. The waveforms of current and torque for various current limitation values: (a) ω_r = 100 rpm, (b) ω_r = 300 rpm, and (c) ω_r = 700 rpm with V/f control

Table 1: Four Phase, 4 kW Oulton SRM Parameters

Ns/Nr = 8/6	Phase resistance = 0.3 Ω
La=117.8 mH	Inertia = 0.008 Kgm^2
Lu=12.8 mH	Base speed = 1500 rpm
βs=20°	Rated voltage = 300 V
βr=21°	RMS current = 9 A

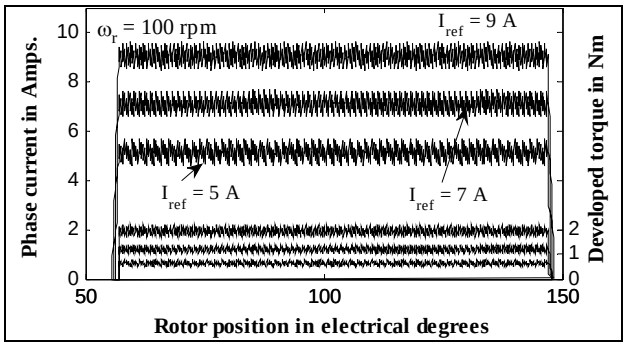

(a)

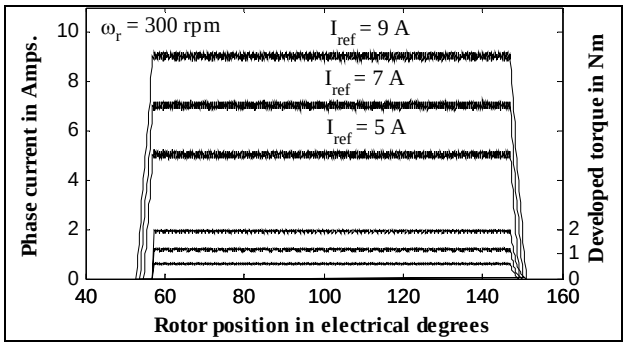

(b)

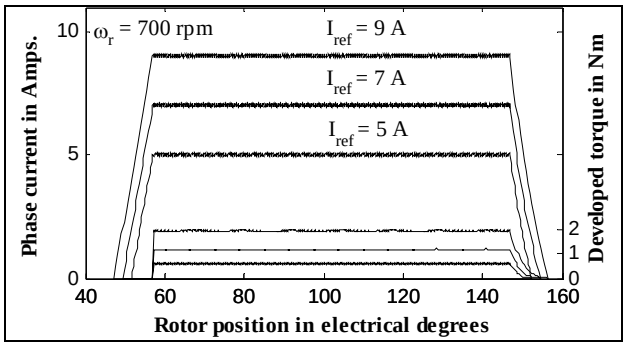

(c)

Figure 8: The waveforms of current and torque for various current limitation values: (a) ω_r = 100 rpm, (b) ω_r = 300 rpm, and (c) ω_r = 700 rpm with PWM control

Simulation results for phase torque and total motor torque waveforms are presented in Figure 9 for a conventional PWM mode controller, while same results for a V/f mode are shown in Figure 10. It can also be seen that the total motor torque has a low torque ripple. The impulses associated with total torque are resulting from the simple model adopted in this paper, and may be eliminated by fine tuning of the commutation angles.

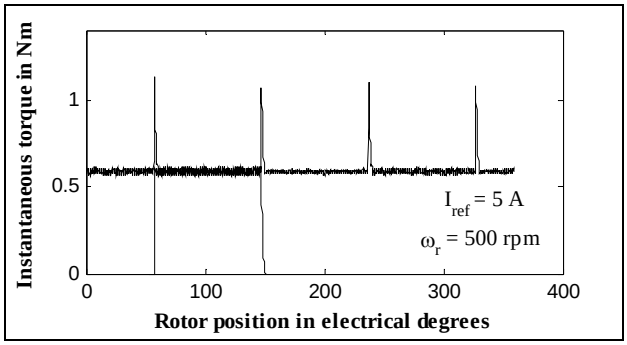

Figure 9. Phase torque and total motor torque waveforms for a PWM control

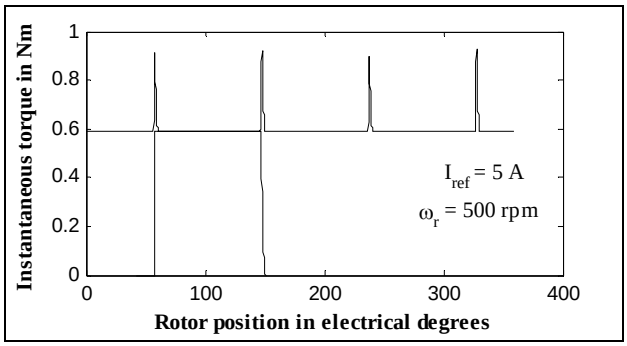

Figure 10: Phase torque and total motor torque waveforms for a V/f control

The torque-speed and the torque ripple-speed capabilities of the PWM control are illustrated by Figure 11. In order to examine the performance of the SRM with the proposed control strategy, Figure 12 displays the informative results for comparison purpose. However, the V/f produces less torque ripple in SRM developed characteristics.

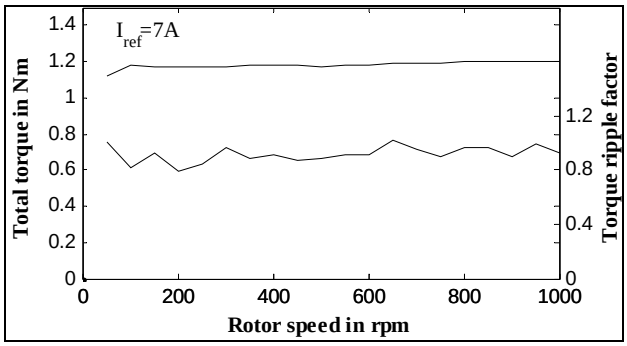

Figure 11: Variation of torque and torque ripple factor versus rotor speed for a PWM control

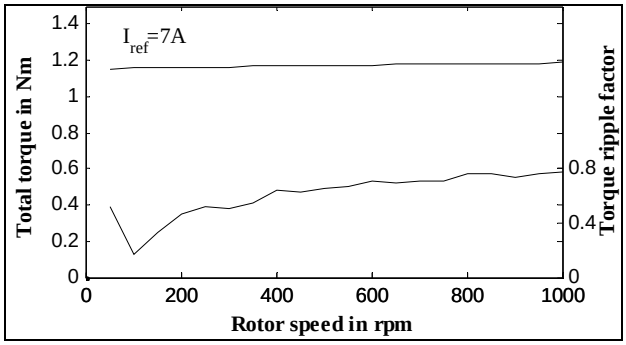

Figure 12: Variation of torque and torque ripple factor versus rotor speed for a V/f control

5. CONCLUSIONS

This paper has described V/f method capabilities for achieving a simplest and optimum control strategy for an SRM drives. Firstly, analytical solutions for winding phase current changes were determined. Then, control parameters of V/f law were selected. Simulation results are presented for SRM drive model generated with complete M-file scripts. Some important finding characteristics and current waveforms were obtained in this study, which provides theoretical basis for further development and experimental set-up. We are currently working on verifying the simulation results with the real hardware system.

REFERENCES

Cheok, A.D., and Y. Fukuda, Y., 2002, A New torque and Flux control method for Switched reluctance motor drives, *IEEE Trans. On Power Electronics,* Vol. 17, no. 4, pp. 543-556.

Christos, M., Iordanis, K., 2003, Performance optimization in switched reluctance motor drives with online commutation angle control, *IEEE Trans. On Energy Conversion, Vol.18, no. 3,* pp. 448-457.

Ertl, H., Wiesinger, T., Kolar, J.W., 2008, Active voltage balancing of DC-link electrolytic capacitors, *IET Power Electronics,* Vol. 4, pp. 488-496.

Henriques, L.O.P., et al., 2002, Review of the ripple reduction strategies in SRM, *XIV-congresso brasileiro de automatica,* pp. 1164-1169.

Kioskeridis, I., Mademlis, C., 2006, Optimal Efficiency Control of Switched Reluctance Generators, *IEEE Trans .on Power Electronics,* Vol. 4, pp. 1062-1072.

Krishnan, R., 2001, Switched Reluctance Motor Drives*, CRC Press, pp. 1-62, Cambridge, UK.*

Lee, T., et al., 2006, Control of c-dump converters fed switched reluctance motor on an automotive application, *Electric Power Systems Research 77,* pp. 804-812.

Mademlis C., Kioskeridis, I., 2007, Smooth Transition between Optimal Control Modes in Switched Reluctance Motoring and Generating Operation, *International Conference on Power Systems Transients,* pp. 1-7.

Muñoz-Garcıa, A., Lipo, T.A., Novotny, D.W., 1998, A new induction motor *V/f* Control method capable of high-performance regulation at low speeds, *IEEE Trans. On Industry App.,* Vol. 34, no. 4, pp. 813-821.

Pillay, P., Liu, Y., Cai, W., Sebastian, T., 1997, Multiphase operation of switched reluctance motor drives, *IEEE Industry Applications Conference (*New Orleans, USA*)*, Vol. 1, no. 1, pp. 310-317.

Russa, K., Husain, I., Elbuluk, M., 1997, Torque ripple minimization in switched reluctance machines over a wide speed range, *IEEE –IAS Annual Meeting,* pp. 668-675.

Venkatesha, L., Ramanarayanan, V., 1998, Torque ripple minimization in switched reluctance motor with optimal control of phase currents, *International Conference on Power Electronic Drives and Energy Systems for Industrial Growth,* Vol. 2, pp. 529-534.

Zai-ping, P., Ying, J., Hui, Z., 2004, Study on switched reluctance generator, *Journal of Zhejiang University Science,* Vol. 5, pp. 594-602.

Zhang, H., Zhang, J., Gao, R., 2009, A novel method of phase current compensation for switched reluctance motor system based on finite element, *Journal of Computers,* Vol. 4, no. 10, pp. 1064-1071.

EXPERIMENTAL ASSESSMENT OF TRAPEZOIDAL COMMUTATION AND FOC PERFORMANCES OF 3-PHASE PERMANENT MAGNET BRUSHLESS MOTOR

R. Askour[(a)], B. Bououlid [(b)]

[(a)] [(b)] Equipe Modélisation, Traitement de l'Information et Commande des Systèmes (MTICS)
Ecole Nationale Supérieure d'Arts et Métiers (ENSAM-Meknès)
Université Moulay Ismaïl, Morocco

[(a)] rachid.askour@yahoo.fr, [(b)] bbououlid@yahoo.fr

ABSTRACT
In this paper, we present experimental results of 3-phase permanent magnet brushless motor speed control using trapezoidal commutation (BLDC mode) and Field Oriented control (BLAC mode). Two control applications have been developed in C language and implemnted using the Texas Instruments TMS320LF2812 digital signal processor (DSP). This new processor enables intelligent control for motors. We used to test the drive a professional development kit available from Technosoft company. This paper discusses the DSP real implementation of speed control (*Current sensing and scaling*, software organization, etc.). Dynamic performances are compared for the two modes in the case of speed reversal test at no-load conditions. We also present the real-time armature current logged at load conditions in both BLAC and BLDC modes. An evaluation of the results is presented and digital implementation aspects are discussed.

Keywords: PM Brushless motor, Digital speed control, BLDC and BLAC controls, DSP implementation.

1. INTRODUCTION

Because of their higher efficiency and power density, permanent magnet (PM) motors have been widely used in a variety of applications in industrial automation and consumer electric appliances (Murugan, Nandakumar and Mohiyadeen 2008).
A brushless Permanent Magnet Synchronous motor has a wound stator, a permanent magnet rotor assembly and internal or external devices to sense rotor position. The sensing devices provide logic signals for electronically switching the stator windings in the proper sequence to maintain rotation of the magnet assembly. The combination of an inner permanent magnet rotor and outer windings offers the advantages of low rotor inertia, efficient heat dissipation, and reduction of the motor size. Moreover, the elimination of brushes reduces noise, EMI generation and suppresses the need of brushes maintenance.
Two configurations of permanent magnet brushless motor are usually considered: The trapezoidal type and the sinusoidal type. Depending on how the stator is wounded, the back-electromagnetic force (BEMF) will have a different shape. To obtain the maximum performance from each type of PM motor, an appropriate control strategy has to be implemented. The trapezoidal BEMF motor uses a "two phases on" strategy, whereas the sinusoidal BEMF motor offers its best performances when driven by sinusoidal currents (three phases on strategy). This paper presents the DSP implementation of a speed control for the two strategies. In BLAC mode, the sinusoidal voltage waveform applied to this motor is created using sinusoidal PWM technique. This method will enable real-time control of torque and rotation speed and is accurate in every mode of operation (steady state and transient). The transient currents are constantly controlled in amplitude. However, such a control requires precise motor position sensor like encoder. In BLDC mode (MadhusudhanaRao, SankerRam, Smapath Kumar and Vijay Kumar, 2010; Dixon and Leal, 2002), a special commutation scheme is used to generate the PWM commands to motor phases. Based on the Hall sensor information, only two of the motor phases are supplied, while the third phase is not powered, for each Hall signals combination. After each change of 60 electrical degrees of motor position, a new combination of motor phases is supplied. Two phase's currents and motor position are measured. The measured phase currents are used to compute the equivalent DC current in the motor, based on Hall sensors position information. The speed controller generates the reference of the equivalent DC current.
In this work, we compare real-time results in the case of a speed reversal test. Figures show the good dynamic behavior of the FOC method.

2. THEORETICAL BACKGROUND

2.1. PM motor model

The operation of a brushless PM motor relies on the conversion of electrical energy to magnetic energy and then from magnetic energy to mechanical energy. It is possible to generate a magnetic rotating field by applying sinusoidal voltages to the three stator phases of a three phase motor. A resulting sinusoidal current

flows in the coils and generates the rotating stator flux. The rotation of the rotor shaft is then created by attraction of the permanent rotor flux with the stator flux.
To create the rotating stator flux, the commonly applied phase voltages present a phase shift of 120 electrical degrees from one to another and are given by:

$$\begin{aligned} v_a &= V\cos(\omega_e t) \\ v_b &= V\cos(\omega_e t - 2\pi/3) \\ v_c &= V\cos(\omega_e t - 4\pi/3) \end{aligned} \quad (1)$$

where ω_e corresponds to the electrical speed. A one phase electrical equation can be written like:

$$v = Ri + L\frac{di}{dt} + E(\theta) \quad (2)$$

Where $E(\theta)$ corresponds to the back-emf (induced voltage) and can also be written like:

$$E(\theta) = \frac{d\,\psi_m(\theta)}{d\,t} = \frac{d\,\psi_m(\theta)}{d\,\theta} * \omega_e \quad (3)$$

where $\psi_m(\theta)$ corresponds to the amplitude of the natural magnetic flux of the permanent magnets.
Electrical speed ω_e is related to mechanical speed ω_m by the following equation :

$$\omega_e = p * \omega_m \quad (4)$$

where p is the number of pole pairs.
From the electrical power delivered to the motor, a part of it ($R\,i^2$) is transformed in Joule losses, another part ($L.i.di/dt$) is going to the energy stored in the magnetic field and the last part ($i.d\psi_m(\theta)/dt$) is transformed in mechanical energy (torque production).
Electromagnetic torque can be expressed by :

$$T_e = p\,(E_a i_a + E_a i_a + E_a i_a)/\omega_e \quad (5)$$

Supposing that the machine is sinusoidal, the induced voltage has the following form:

$$\begin{aligned} E_a(\theta) &= -\omega_e \psi_{max} \sin(\theta_e) \\ E_b(\theta) &= -\omega_e \psi_{max} \sin(\theta_e - 2\pi/3) \\ E_c(\theta) &= -\omega_e \psi_{max} \sin(\theta_e - 4\pi/3) \end{aligned} \quad (6)$$

where ψ_{max} is the flux amplitude and θ_e is the electrical position of the rotor.
It can be proven that the best solution to produce a constant torque is to drive a sinusoidal motor by sinusoidal currents. In the case of a phase shift of β between currents i_a, i_b et i_c and back-emfs E_a, E_b et E_c, the torque expression becomes :

$$T_e = \frac{3}{2}\, p\, \psi_{max}\, I_{max}\, \cos\beta \quad (7)$$

where I_{max} is the current amplitude. It is easy to see that maximum torque is obtained when phase shift β is zero. This objective can be achieved by electronically switching the PM motor windings in concordance with rotor electric position. This enables a real time control of the torque demand without ripples.
The torque created by the energy conversion process is then used to drive mechanical loads. Its expression is related to mechanical parameters via the fundamental law of the dynamics as follows:

$$J\frac{d\omega_m}{dt} + B\,\omega_m + T_L = T_E \quad (8)$$

where J is rotor inertia, B is viscosity coefficient, T_L is load torque and Te is electromagnetic torque.

2.2. Field oriented control (BLAC mode)

The goal of the Field Oriented Control is to perform real-time control of torque variations demand, to control the rotor mechanical speed and to regulate phase currents in order to avoid current spikes during transient phases (Texas Instrument SPRA588 1999). To perform these controls, the electrical equations are projected from a three phase nonrotating frame into a two co-ordinate rotating frame. This mathematical projection (Clarke & Park) greatly simplifies the expression of the electrical equations and removes their time and position dependencies. A block diagram for a Field Oriented Controller can be seen in figure 1. This decouples the torque and flux producing components of the stator currents allowing the PM motor to be controlled in such the same way as a separately excited DC machine.
In this new system, the expression of the electrical equations is greatly simplified:

$$\begin{aligned} v_{sd} &= R\, i_d + \frac{d\psi_{rd}}{d\,t} - \omega_e\, \varphi_{rq} \\ v_{sq} &= R\, i_q + \frac{d\psi_{rq}}{d\,t} + \omega_e\, \varphi_{rd} \end{aligned} \quad (9)$$

and for a multiple pole synchronous motor, the expression of the torque in (d,q) is:

$$T_e = \frac{3}{2}\, p\, (\psi_{rd}\, i_{sq} - i_{sd}\, \psi_{rq}) \quad (10)$$

In the specific case of a permanent magnet synchronous motor without salient poles, most of the natural magnetic flux is on the d axis. In order to optimize the torque production for a given stator current i_s value, the appropriate strategy is to set reference direct current i*sdref* to zero.
The action of the current regulators is then to shift the current vector Is onto the q axis. The torque is now given by:

$$T_e = k\,\psi_{rd}\, i_{sq} \quad (11)$$

which is similar to DC machine torque expression. The relationship between mechanical speed and torque is given by the mechanical differential equation.

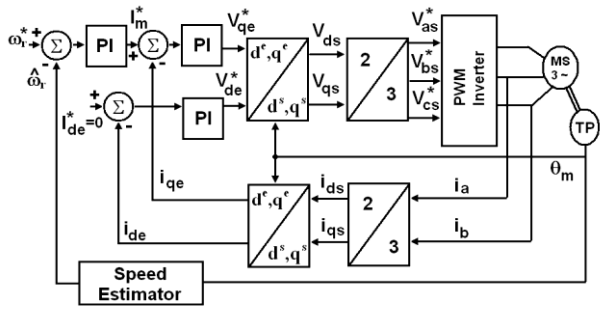

Figure 1 : FOC Bloc Diagram (BLAC mode)

2.3. BLDC control Structure

The BLDC application control scheme is presented in the figure 2 (Singh, B., Singh, B.P. and Jain 2003). As one can see, the scheme is based on the measure of two phase's currents and of the motor position. The speed estimator block is a simple encoder position difference block over one sampling period of the speed control loop. The measured phase currents, ia and ib, are used to compute the equivalent DC current in the motor, based on the Hall sensors position information (see Table 1).

Table 1: DC current I_q generation

Rotor Position Signal θ_r	Equivalent DC current
0° - 60°	i_a
60° - 120°	i_b
120° - 180°	i_a
180° - 240°	$- i_a$
240° - 300°	$- i_b$
300° - 360°	$- i_a$

The Hall sensors give a 60 electrical degrees position information. The speed and current controllers are PI discrete controllers.

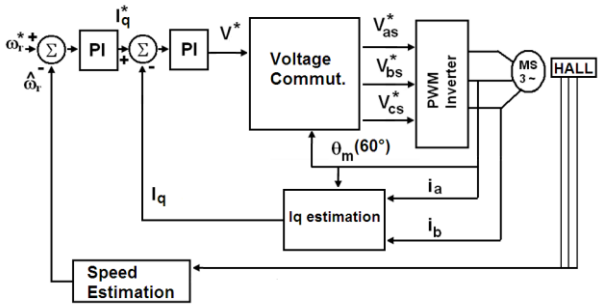

Figure 2 : Trapezoidal comutation Control Scheme (BLAC mode)

Only one current controller is needed in this case, similar to a DC motor case. The voltage commutation block implements (by software) the computation of the phase voltages references, V^*_{as}, V^*_{bs} and V^*_{cs}, applied to the inverter. Practically, the six full compare PWM outputs of the DSP controller are directly driven by the program, based on these reference voltages. In this case, only four of the inverter transistors are controlled for a given position of the motor.

The scheme will commute to a specific command configuration, for each of the 60 degrees position sectors, based on the information read from the Hall sensors.

3. DSP REAL IMPLEMENTATION

This chapter covers each components modules used to implement the solution of the PM motor drive.

3.1. The PM motor

The PM motor used for the application is a trapezoidal Back EMF 4-poles three phases motor equiped with 500 lines encoder. The characteristics of this motor are given in table 2.

Table 2: Motor Characteristics

Motor parameter	Value
Rated Voltage (V) (Y-connexion)	19,10
Nominal torque (mN)	0,029
Maximum current (A)	3,64
Stator Inductance (mH)	0,46
Stator resistance (Ω)	5,25
Rotor Time constant (ms)	7,92
Electrical constant (ms)	0,09
Rotor inertia (kgm²)	$0,9\ 10^{-6}$

3.2. *DSP* development kit

A professional development kit (MCK2812) available from Technosoft compagny has been used for the application. The kit includes :

- A 3-phases AC power module PM50 : it consists of a 50 W six IGBT inverter with integrated phases current sensors and protection hardware.
- The TMS320LF2812 DSP based development board with on-board peripherals : DACs, RS232 connector, etc. The PLL unit is set for 150 MHz CPU clock speed (Texas Instrument SPRU430B 2002).
- A Digital motion control development software called DMCD-Pro enabling data logging, real-time debugging and other useful features.

3.3. Software organization

The code is developed mainly in C/C++ language (both the main structure of the application and the time-critical parts as controllers, coordinates transformation, etc.). Using DMCD-Pro, the motion reference can be defined at high-level from the windows environment. The data logger feature allows the user to visualize any of the global variables of the program such those presented in this paper (speed and quadrature current). The program is based on two modules : initialization and magnetic stall module and the interrupt module (see

figure 3). The interrupt module handles the whole control algorithm. It's periodically computed according to a fixed PWM period value.
The two applications use a specific real-time environment, structured on two levels :

- a high priporiy interrupt function triggered every 100 μs, mainly for current control implementation
- a lower priority interrupt function triggered every 1 ms, for speed reference and speed control implementation.

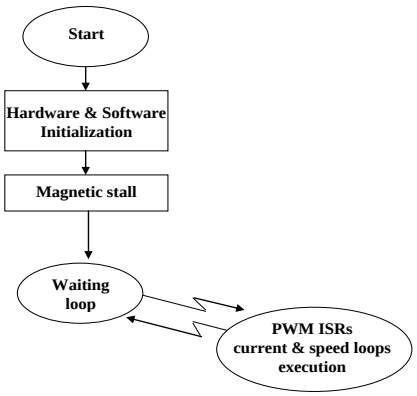

Figure 3: General Software Flowchart

The choice of the PWM frequency depends on the motor electrical constant. In this application, the PWM frequency has been set to 20 kHz. After the initialization module has completed, a magnetic stall is performed by applying a constant voltage vector to the stator phase : the constant phase currents flowing in the coils create a fixed stator flux. As a consequence, the rotor flux aligns itself naturally onto this stator flux (the rotor is stalled in this position).
Then, a waiting loop starts, and corresponds to an interruptible communication between the DSP monitor and the graphical user interface. If the user sends the start command, the control algorithm start executing. The data-logging allows real-time debugging of the application.

3.4. Current sensing and scaling

The control structures require two phase currents as input. PM-50 current measurement scheme is based on shunts mounted on each lower leg of the inverter. The voltage drop on a shunt is amplified and sent to TMS320LF2812 A/D channels. The complete process of acquiring the current is depicted in figure 4. Note that Imax (6,33A) represents the maximum measurable current, which is not necessarily equal to the maximum phase current. This information is useful at the point where current scaling becomes necessary. The ADC input voltage is now converted into a twelve bits digital value.
Note that reading the 12 bits value in the TMS320F2812 DSP is done with a shift of 4 bits to left, i.e. the 12 bits of the measured value are stored in the 12 most significant bits of a 16-bit value.

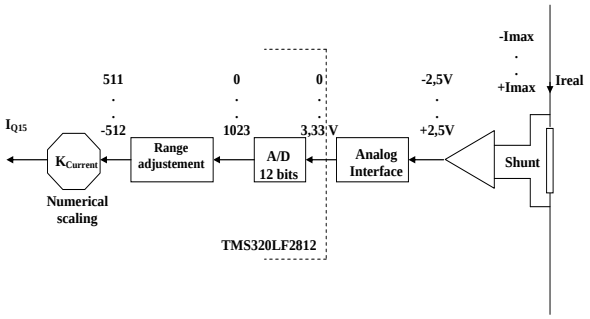

Figure. 4: Current Sensing and Scaling Block Diagram

3.5. The PI regulators

The PI regulators design has been done in continuous domain. We used poles cancellation method for PI regulator parameters calculation. The continuous PI regulators are then converted to their equivalent digital forms using time discretization. The PI regulators are implemented with output saturation. Electrical (current loop) and mechanical (speed loop) open loop transfer functions are considered as first order systems in both BLAC and BLDC modes.
Though the theory and simulation assist in calculating the controller parameters for a pratical implementation of the drive, further tuning of the PI regulator coefficients still be necessary.
We found that current loop PI controller parameters are the same for the two modes. It is not the case for speed loop because the two strategies have different real-time torque controls.

3.6. PWM outputs generation

The sinusoidal voltage waveforms are generated using the full compare PWM unit of the DSP controller. The PWM outputs are applied to the six transistors of the power inverter, based on sinusoidal reference values for the motor phase voltages. These are computed at the output of the current controller routine. The voltage references are used to compute the value of the compare registers corresponding to the three phases of the motor.

3.7. Clarke and Park transformations

Clarke and Park transformations have been developed as C/C++ functions which takes as input the sinus and cosines values of electrical angle as input parameters. To obtain cosines and sinus values from the electrical angle, a built-in sinus look-up table has been used.

4. REAL-TIME RESULTS

Experimental tests have been carried on the MCK2812 kit, which is a professional DSP development kit available from Technosoft compagny. The real-time logged data are speed and stator current quadrature component. In BLDC mode, Iq corresponds the equivalent DC current in the motor based on hall sensors position information. Experimental results are compared for the two modes in the case of speed reversal test at no-load conditions (figures 6 and 7). The speed reference is a 1,25 Hz - ± 50 rad/s square

function.

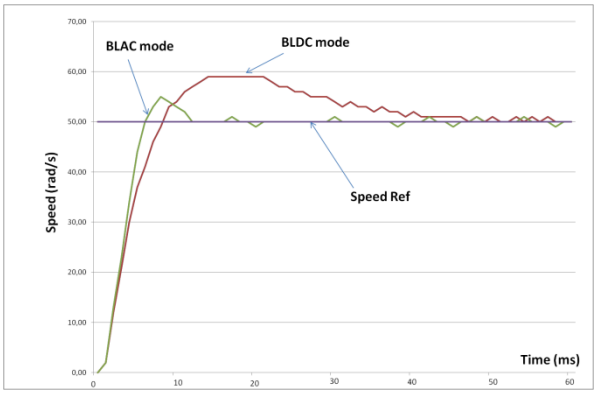

Figure 5 : Real-Time Variation of Speed

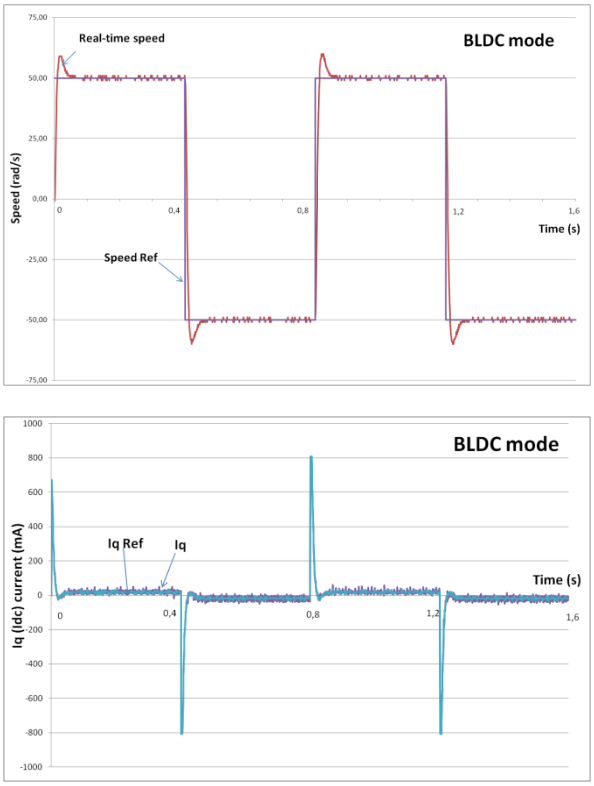

Figure 6 : Time variation of speed and Iq current at no load conditions (BLDC Mode)

The results show that good dynamic behaviour has been achieved by the implemented control. Indeed, during speed reversal phases, torque demand causes large q-current spikes and when speed tends to be equal to ± 50 rad/s, q-current decreases to a non zero steady state value due to viscous damping. The plots show clearly the effectiveness of speed PI regulator. Notice also that stator current torque component follows the output reference value calculated by speed PI regulator. As expected, zooming in the real-time speed plot (see figure 5) shows that BLAC control presents better dynamic performance (good response time) than BLDC control.

Figures 8 and 9 shows a current (armature and Iq current) comparaison between two modes at load conditions. The load torque is constant and speed is 157 rad/s. As expected, the PM motor is driven by sinusoidal current in BLAC mode whereas quasisquare current waveform are obtained in BLDC mode.

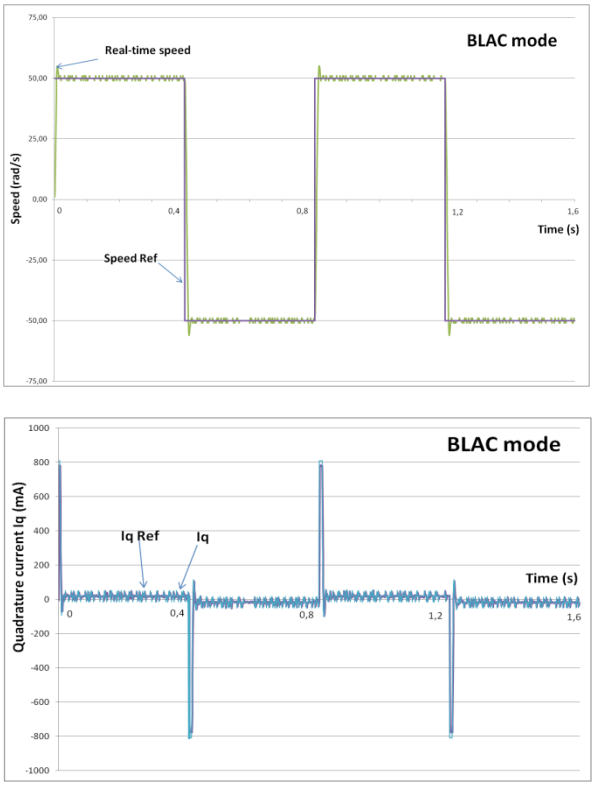

Figure 7 : Time Variation of Speed and Iq Current at No Load Conditions (BLAC Mode)

5. CONCLUSION

In this paper, an analysis of the performances of the BLDC motor using two control strategies : FOC and trapezoidal commutation, is presented. Experimental results were satisfactory and show differences in term of transient responses. Trapezoidal commutation control is found to be interesting as a low cost solution where high efficiencies and dynamics are not required. Indeed, this control structure has several advantages :

- very simple control scheme;
- only one current at a time needs to be controlled.

On the other hand, a great part of the software was written in C/C++ langage. The use of a higher level language (especially, the use of C++ classes) eases greatly programming and is well suited to managing variables and controlling program flow. This application implements some common real-time motion control features (real-time kernel, inverter control, current and speed measuring, regulators, etc.) which can be used in further control implementations such as sensorless or adaptive control.

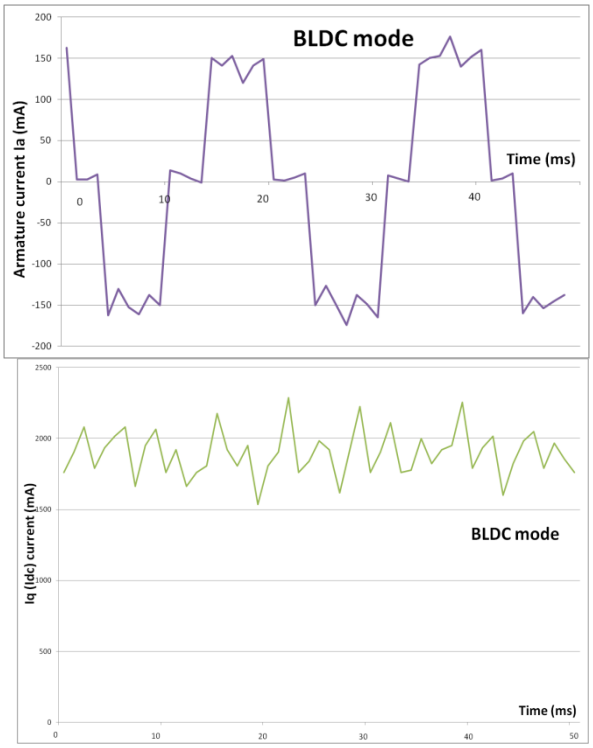

Figure 8 : Time Variation of Armature Current and Iq Current at Load Conditions (BLDC Mode)

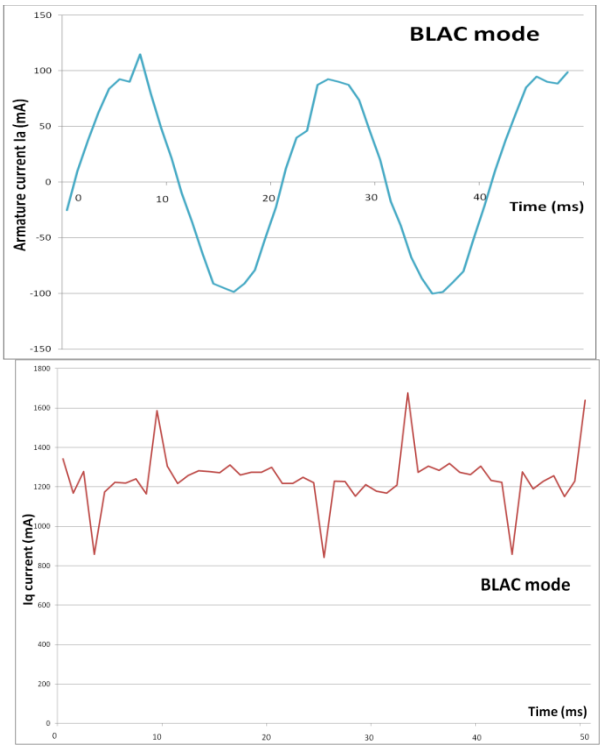

Figure 9 : Time Variation of Armature Current and Iq Current at Load Conditions (BLAC Mode)

REFERENCES

Dixon, J.W. and Leal, I.A., 2002. Current Control Strategy for Brushless DC Motors Based on a Common DC Signal, *IEEE Transactions on Power Electronics*, Volume 17, 232-240.

MadhusudhanaRao, G., SankerRam, B.V., Smapath Kumar, B., Vijay Kumar, K., 2010. Speed Control of BLDC Motor Using DSP. *International Journal of Engineering Science and Technology*. Volume 2(3), 143-147.

Murugan, R., Nandakumar, S., Mohiyadeen M.S., 2008. DSP-based electric power assisted steering using BLDC motor. *SADHANA - Academy Proceedings in Engineering Sciences*. Volume 33, Part 5, 581-590.

Singh, B., Singh, B.P., Jain, K., 2003. Implementation of DSP Based Digital Speed Controller for Permanent Magnet Brushless DC Motor. *IE(I) Journal-EL***.** Volume 84, 16-21.

Texas Instrument SPRU430B, 2002. *TMS320C28x DSP CPU and Instruction Set Reference Guide*.

Texas Instrument SPRA588, 1999. *Implementation of a Speed Field Oriented Control of 3-phase PMSM Motor using TMS320F240*.

AUTHORS BIOGRAPHY

Askour Rachid was born in Casablanca, Morocco. He received the engineer's degree from Ecole Nationale de l'Industrie Minérale, Rabat, Morocco, in 1996 and the Master degree (Diplôme des Etudes Approfondies) from Université des Sciences et Technologies de Lille, Lille, France, in 2002. Since 1997, he has been working at Ecole Nationale Supérieure d'Arts et Métiers (ENSAM-Meknès), Moulay Ismaïl University, Meknès, Morocco, where he is an engineer in the Department of Electromechanical Engineering, in the areas of power electronics and electrical machines.

Bououlid Idrissi Badr was born in Marrakech, Morocco. He received the Ph.D. degree from Faculté Polytechnique de Mons, Mons, Belgium, in 1997 and the engineer's degree from Ecole Nationale de l'Industrie Minérale, Rabat, Morocco, in 1992. Since 1999, he has been working at Ecole Nationale Supérieure d'Arts et Métiers (ENSAM-Meknès), Moulay Ismaïl University, Meknès, Morocco, where he is a Professor in the Department of Electromechanical Engineering, in the areas of power electronics and electrical machines.

IMPLEMENTATION OF IDENTIFICATION ALGORITHM USING RECURRENT RBF NEURAL NETWORKS FOR THE INSIDE TEMPERATURE IN A GREENHOUSE

L. Ezzine[(a)], M. Guerbaoui[(a)] ,Y. El Afou[(a)], A. Ed-dahhak[(a)], A. Lachhab[(a)], L. Belkoura[(b)], B. Bouchikhi[(a)],

[(a)]Sensor, Electronic and Instrumentation Team, Faculty of Science
BP: 11201, Zitoune, Meknes, Morocco
[(b)]LAGIS UMR CNRS, 8146 USTL – Bâtiment P2
59655, Villeneuve d'ascq Cedex, France

[(a)]latifae@yahoo.com, [(a)]guerbaoui@gmail.com, [(a)]elafou.youssef@gmail.com,
[(a)]a.eddahhak@yahoo.fr,[(a)]abd_lachhab@yahoo.fr, [(b)]lotfi.belkoura@univ-lille1.fr, [(a)] benachir.bouchikhi@gmail.com,

ABSTRACT
The goal of this paper is to carry out a statistical study whose objective is the identification of time series of the greenhouse climatic parameters, in order to optimize the expenditure in cost and time of the culture under greenhouse. In this study, we showed that the inside temperature is the most influential parameters on the greenhouse. However, the automatic climate control requires the development of appropriate control laws that are based on models representing linear and nonlinear system. We are therefore forced to make a study of the system to generate a model that faithfully reproduces the operating parameters of greenhouse climate. In order to achieve the maximum benefit it is important to exploit the available data and an obvious choice here are the machine learning methods such as artificial neural networks. The use of recurrent Radial Basis Function (RBF) models is justified by employing a nonlinear greenhouse system, and hence to give the possibility to identify and to control in the real time the inside temperature in the greenhouse, taking into accounts other climatic parameters within and outside the greenhouse. A comparison of the measured and simulated data proved that the found model can envisage correctly the inside greenhouse temperature.

Keywords: RBF networks, Recurrent RBF Networks, Nonlinear systems, Climatic Parameters, Greenhouse.

1. INTRODUCTION

The main aim of this paper is to provide a methodology of implementation of Radial Basis Function Networks (RBF) for identification of the inside temperature model in a greenhouse. The conventional techniques for this identification are based upon polynomial regression or auto-correlation-based statistical methods such as ARIMA (Ezzine, Lachhab, Eddahhak, and Bouchikhi 2007; Ezzine, Lachhab, Eddahhak, and Bouchikhi 2008; Lachhab, Ezzine, Eddahhak, Didi, Salinas Vazquez, García Lagos, Atencia, Joya, and Bouchikhi 2008). However, the functional relationship between the different climatic parameters is complex and cannot always be captured by these traditional modelling techniques. Often this limits the practical usefulness as it is the case, the use of simplified traditional techniques based on conceptual models, such as regression techniques, may hardly be justified. In order to achieve the maximum benefit, it is important to exploit the available data and an obvious choice here are the machine learning methods such as artificial neural networks.

In the present work, a special type of neural networks that employs RBF network in the hidden layer has been utilized (Dreyfus, Martinez, Samuelides, Gordon, Badran, Thiria, and Herault 2002; Haykin 1994). Recurrent Radial Basis Function (RBF) Networks architecture is used to learn temporal sequences. It is based on the advantages of Radial Basis Function Networks in terms of training process time (Catfolis 1993; Chen, Giles, Sun, Chen, Lee, and Goudreau 1993). The recurrent or dynamic aspect is obtained by cascading looped neurons in the first layer. This layer represents the dynamic memory of the recurrent RBF network that permits to learn temporal data. The proposed network combines the easy use of the RBF network with the dynamic performance of the Locally Recurrent Globally Feed forward network.

In the present model, the variables eventually used included the inside temperature, the outside temperature, the inside humidity, the outside humidity, the CO_2 and the solar radiation, which produced the smallest error in the validation data. At a first stage, all climatic parameters are used, but we noted that the concentration of CO_2 and the solar radiation have little influence compared to other variables (Ezzine, Lachhab, Eddahhak, and Bouchikhi 2008). Thus these two parameters are eliminated at the second stage.

The rest of the paper is organised in three sections: a brief survey of system is presented in the second section. The third section describes the Radial Basis Function (RBF) Networks, their training process algorithms and the architecture of recurrent RBF Networks for the time series prediction. Finally, the models and the results obtained for the temperature and the humidity under greenhouse are presented.

2. MATERIAL AND EXPERIMENTAL DEVICE

The greenhouse environment is automated with several actuators and sensors that are connected to an acquisition and control system based on a personal computer (Figure 1). Sensor devices are the basics of climate control because they provide necessary data for optimisation. Productivity, repeatability, output signal and usability by growers are the required characteristics of sensors (Bouchikhi, Eddahhak, El Harzli, and El Bari 2004). The developed system allows the acquisition of measurements of internal and external temperature and hygrometry, and global radiation.

It consists of a heating system, moistening ducts and a static ventilation to control the internal climate. In order to improve the climate and water conduct of a culture under greenhouse, a tool of supervision is associated to the actuator system. After the phase of installation and standardization of sensors inside and outside the greenhouse, a climatic data base of the greenhouse can be generated (Eddahhak, Lachhab, Ezzine, and Bouchikhi 2005; Eddahhak, Lachhab, Ezzine, and Bouchikhi 2007; Lachhab, Eddahhak, Ezzine, and Bouchikhi 2005; Lachhab, Eddahhak, Didi, Ezzine, Salinas, García-Lagos, Atencia, Joya, and Bouchikhi 2007).

The controller is designed to insure:

- The measurement, via some sensors, which monitor climate parameters, especially temperature (LM35), humidity (HIH 4000-001), carbon dioxide (FIGARO AM4 module), lighting (Photo Resistor) and water availability in a desired range;
- The processing of the data and storage of the results;
- The operating of the climatic control devices, usually installed at a modern greenhouse.

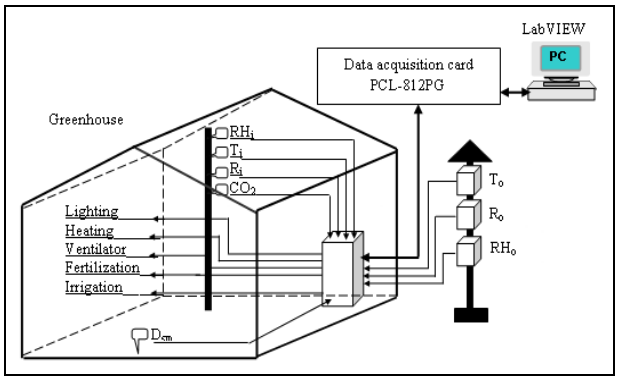

Figure 1: Synoptic diagram of the experimental device

A supervision tool optimises the commands sent to actuators, in order to optimize the climate under the greenhouse. We opted for a graphic program, carried out using LabVIEW (Figure 2), regrouping the following functionalities: acquirement of sensor data outputs, display and treatment of information in real time, commands to actuators, and, in short, creation of a historic based upon a picture database. The driving software permanently compares the magnitudes measured with the reference range in order to start or stop the appropriate actuators. The user has a possibility to fix the threshold of the inside temperature that start up the audible and visual alarms (Eddahhak, Lachhab, Ezzine, and Bouchikhi 2007).

Data were collected in a greenhouse located at the Faculty of Sciences, Meknes, Morocco, between 11 and 18 December 2007. The system is based around a Personal Computer (PC). Sensors and conditioning modules permit to measure the different climatic parameters inside and outside the greenhouse.

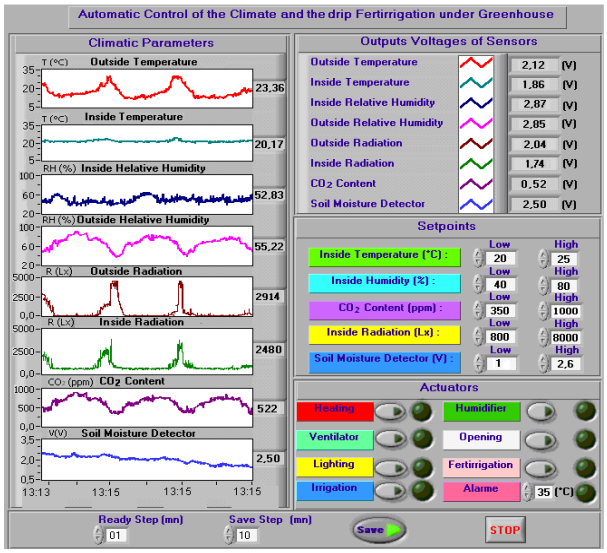

Figure 2: Graphical User Interface based on LabVIEW

3. METHODOLOGY

3.1. Model description

The typical structure of an RBFN consists of three layers, namely the input, hidden and output layers. Each layer consists of a number of neurons (nodes). The nodes in the input layer are used only to pass the input data to hidden layer. No calculations are performed in the input layer nodes, and the connections between the input and the output layer are not weighed (Dreyfus, Martinez, Samuelides, Gordon, Badran, Thiria, and Herault 2002; Haykin 1994).

The hidden layer contains k nodes, which apply a nonlinear transformation on the input variables. More specifically, each node j = 1, 2, …, k has a center value cj, where cj is a vector whose dimension is equal to the number of inputs to the node. For each new input vector x = [x1, x2, …, xN], the Euclidean norm of difference between the input vector and the node center is calculated as follows:

$$v_j = \|c_j - x\| = \sqrt{\sum_{i=1}^{N} (x_i - c_{j,i})^2} \qquad (1)$$

the output of the hidden layer nodes is determined by a nonlinear function, called the 'activation function' of

the network. A typical selection for the activation function is the Gaussian function:

$$f(v) = e^{\left(-\frac{v^2}{2\sigma^2}\right)} \quad (2)$$

where the width σ^2 is a variance. Thus, the output of the hidden layer node j is:

$$z_j = f(v_j) \quad (3)$$

A set of synaptic weights w_j, j = 1, 2, …, k is applied to the connections between the hidden and the output layer. The nodes in the output layer serve only as summation units, which produce the final output of the network. Considering a one-output network (Figure 3), the overall output will be:

$$\hat{y} = \sum_{j=1}^{k} w_j z_j \quad (4)$$

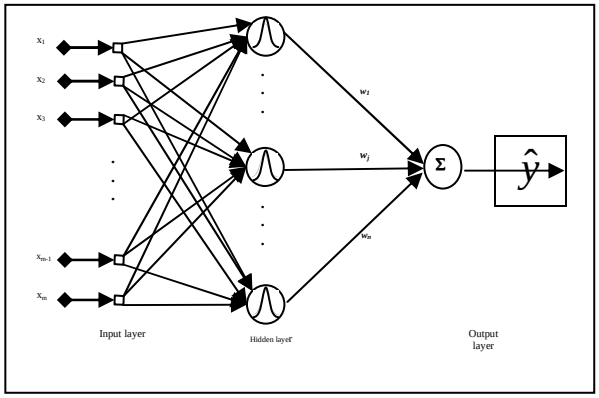

Figure 3: Typical structure of an RBF Networks

3.2. Model training and validation

3.2.1. Training of RBF networks

From a design point of view, the training of RBF Networks is to find the number of hidden layer neurons N and the appropriate parameter set {yk, σ, wk} to map a given input vector to a desired output scalar efficiently with good accuracy and generalization. Many different approaches have been proposed in the literature over recent years for selecting these free parameters and optimizing the complexity of RBF networks. Normally, after the network structure parameter N is determined, the RBF networks are trained by using a two-phase approach, where the centres and width are computed first, and the output weights are calculated in the second phase.

In the phase of selecting the locations of centres, three main strategies have been put forward. The first one is to randomly select a set of samples from training set and the positions of the centres are set according to these samples. This approach can only produce reasonable results when the training data are distributed in a representative manner. The second approach is to perform a pre-clustering on the training set, and the centres of the clusters are used as the centres of the RBF network. Since this clustering is performed without the knowledge of the weights of the output nodes, it is likely that the selection of the centres is sub-optimal with respect to the accuracy of the final result. The selection of the initial values of the centres is also a key problem. The third strategy is to use a gradient descent algorithm to determine the centres. Convergence to a global minimum cannot be guaranteed since the problem is nonlinear with respect to the centres. Therefore, all these approaches have various shortcomings in selecting appropriate centres. Since the practical signals are inevitably disturbed by stochastic noise, training data cannot always represent all samples even if they are acquired from a wide range of amplitude and frequency. Therefore, the pre-clustering is necessary either for the training data, or for the simplification of the networks (Dreyfus, Martinez, Samuelides, Gordon, Badran, Thiria and Herault 2002; Haykin 1994).

When the centres are selected, a uniform width can be heuristically determined by the equation in the following section $\sigma = d/\sqrt{M}$, where d : the maximum distance between the chosen centres and M: is number of centres.

Once the centres and width are fixed, the weights can be known very efficiently, since the computation is reduced to a linear or generalized linear model. There are also some approaches for output layer weights training. One approach, which is called generalized regression neural network (GRNN), assigns the target values as the output layer weights and the output of the network is divided by the sum of the output of a hidden layer neuron. GRNN is effective when a large amount of training data is used and no new training data is far from them. The other approach is to use an iterative training technique such as gradient descent algorithm. In fact, from Equation (4), when the centers and width are determined, weights can be trained by solving the system of linear equations directly. After the final step of calculating the output layer weights is finished, all parameters of the RBF network have been determined.

3.2.2. Evolving RBF networks

The algorithm of gradient descent have been used to train RBF networks, which are called evolving RBF networks. In fact, we specially present the algorithm of training RBF networks.

However, in the learning procedure of an RBF neural network, the determination of the hidden centres and the widths is of particular importance to the improvement of the performance of networks, and the proposed algorithm consists of Gradient descent (Du, Lam, and Zhang 2006; Fahlman and Lebiere 1991; Fahlman 1991; Lee and Sankar 2007, Venkateswarlu and Venkat 2005).

This algorithm is used for both simple models. As for recurring patterns using the same instructions that algorithm, except that it adds the recurrence for the variable in question (the temperature and humidity).

However, for the standardization of data, an uncertainty of 10% was adopted, but the results found were not interesting. In a second time we took incertitude 1%. Standardization of the equation is given as follows:

$$0,99\times\left(\frac{x_i-\min\limits_{1\le i\le N}(x_i)}{\max\limits_{1\le i\le N}(x_i)-\min\limits_{1\le i\le N}(x_i)}\right)+0,01 \qquad (5)$$

As there are no methods that provide a way to correct the centres used, it adopts an estimate with the arithmetic average for all variables, then the weighting coefficients with "random" is that minimize total error of the model. The width of the Gaussian is defined by the maximum distance between the centres divided by the square root of the number of centres. In step (6) for the algorithm, a gradient descent is used to correcting the weight of which to minimize the error.

The proposed Recurrent RBF neural network considers the time as an internal representation (Du, Lam, and Zhang 2006, Lee and Sankar 2007; Venkateswarlu and Venkat 2005). The dynamic aspect is obtained by the use of an additional self-connection on the input neurons. The recurrent RBF network can thus take into account a certain past of the input signal.

Algorithm

Step learning

1. Normalization of the database and Choice of centres
2. Set the width of the Gaussian
   The estimator adopted is:

$$\sigma=\frac{d}{\sqrt{M}}$$

With **M** is the number of centres

$$d=\max_{1\le i,j\le M}\left\|c_i-c_j\right\|$$

3. Initializing weight
4. Creating the matrix of distances.

$$\left[f(\|t_i-c_1\|)\ \ \ldots\ \ f(\|t_i-c_M\|)\right]\begin{bmatrix}w_1\\ \ldots\\ w_M\end{bmatrix}=output$$

5. Calculate error.

Calculate the error measure E during the learning

6. Correcting weight used the method of gradient descent

$$W_{i+1}=W_i-\alpha\times E_i\times\frac{d}{t_i}\left[f\left(\left\|t_i-c_1\right\|\right)\cdots f\left(\left\|t_i-c_M\right\|\right)\right]$$

With E_i is the error at time i

7. Return to step **(4)** until to finish learning data.

Step test

In this step, the same treatment for learning data is adopted and the calculation of the output used the following equation:

$$\left[f(\|t_i-c_1\|)\ \ \ldots\ \ f(\|t_i-c_M\|)\right]\begin{bmatrix}w_1\\ \ldots\\ w_M\end{bmatrix}=output\_test$$

Calculate the error measure for every example.

4. RESULTS AND DISCUSSIONS

Our work above shows that the inside temperature is the important parameter in the greenhouse and they influence most the culture under greenhouse (Ezzine, Lachhab, Eddahhak and Bouchikhi 2008). So we have chosen these parameters in order to identify the climatic evolution under greenhouse using the RBF networks. In this section we present the results obtained for a model of temperature.

It is important to avoid extrapolations, especially with non-linear, over-parameterized models such as neural networks. Reducing the number of inputs to the bare minimum is: therefore, advisable. This can be done by removing less-relevant and well-correlated inputs; in our case we have eliminated the lighting and CO_2 concentration. When the least important variables cannot be readily identified, statistical reduction (compression) methods, such as regression linear model or bottleneck neural networks may be used to reduce the effective system's dimension. These methods can be applied to the inputs as well as to the state variables.

The model uses a simple RBF neural network consists of four inputs and one output. And in the recurrent against the model consists of five inputs and one output.

From the whole database, we have reserved data from different, but not too far, days to be used as an independent verification set. This prevents over-training and may help to identify outlying records. This technique is superior to, e.g., splitting the weather-dependent data set into odd and even records (or groups of records), since then the two resulting sub-sets are likely to be statistically similar, although they do not share even a single record.

In this section, we will present model temperature. In a first step we use a simple model using the RBF network.

Figure 4 and 5 give the curves of adjustment of the inside temperature according to the found model in a step learning and test. We notice that the desired (measured temperature) and the simulated temperature's evolve in the same direction and the recorded error is understood about between -0,5 °C and 0,5 °C.

The search results are not satisfying the error estimate. To address this problem we introduced the dynamic factor using the RBF recurrent network. The graphic representation for the inside temperature is a single day. This is done in order to have a clearer view on the networks used.

The table 1, gives results of the minimal and maximal of the errors, the average errors and the standard deviations.

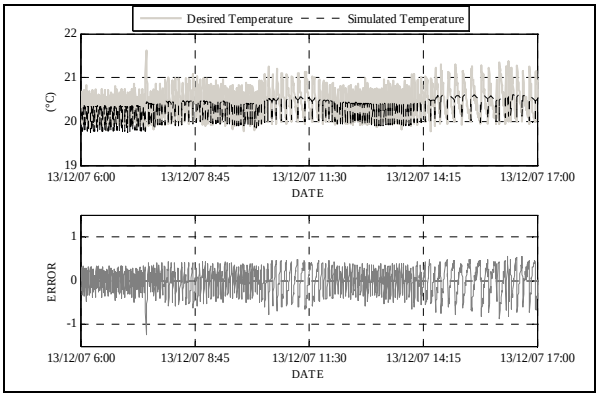

Figure 4: Learning of Simple Model of the temperature

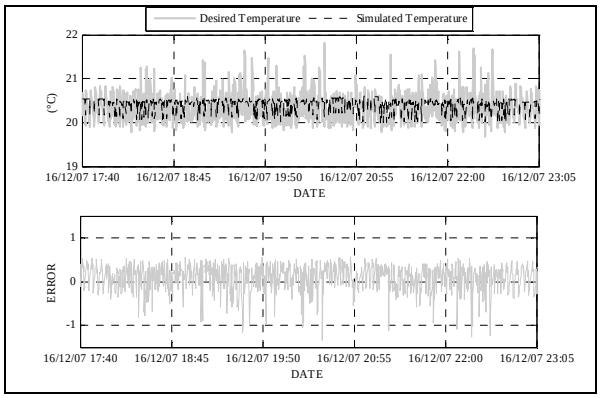

Figure 5: Test of Simple Model of the temperature.

In the test phase, error keeps almost the same pace as that found in the phase of training. Hence our model is validating. Despite this improvement in non-linear modelling of the inside temperature in greenhouse, relative to that linear; the error is always important in the sense dispersion (important variance) (table 1).

Table 1: Results of the RBF and recurrent RBF models for the temperature under greenhouse

		The Simple Model of the temperature (°C)	The Recurrent Model of the temperature (°C)
Learning	Mean error	0,23640	0,23644
	Max error	1,47651	0,56085
	Min error	0,00001	1,44364E-05
	Std error	0,29832	0,06403
	variance	0,08900	0,00410
Test	Mean error	0,28652	0,34538
	Max error	1,45759	0,40031
	Min error	0,00000	0,00015
	Std error	0,31937	0,05831
	variance	0,10200	0,00340

So in order to improve the prediction we can go from a simple model to the recurrent model. With the training and testing data established, an evolving recurrent RBF network is used to create a mapping model that simulated the evolution of the temperature and it show the relationship between the inside humidity, outside humidity, outside temperature and command.

Table 1 shows the results of the network training for the temperature under Greenhouse. The recurrent RBF Neuronal Networks gives better results than the simple model RBF with percentage 70,98 %.This model does not take account of the interaction between the inside temperature and its past which gives an error a bit important. So, to remedy this problem, the recurrent RBF networks model is used.

In Figure 6 and 7, the identification of the temperature, where the learning phase data are taken from a period of three days, whereas a one day period is extracted for the test phase. The results illustrated in the figure 6 show the evolution of the experimentally observed temperature inside the greenhouse and the one determined after training the network.

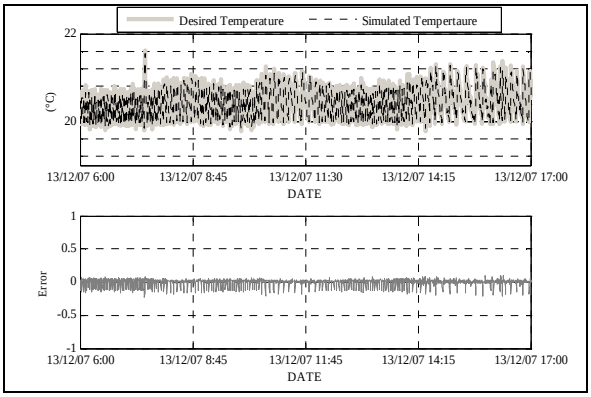

Figure 6: Learning of the Recurrent Model of the temperature.

The sequences are memorized by the Gaussian nodes and the temporal distances between the temperature at time t and their observation at time t-1 by the looped neurons. The recurrent RBF network has the advantage of the local generalization of the Gaussian node while the RBF networks are easier to use, but they have a significant error in comparison with that of recurrent RBF networks.

The test phase is to validate the model developed in phase learning using a new database. The results of this phase are shown in figure 7. A fully connected recurrent RBF network with one hidden layer is selected to be trained using the training data for the forward model. The model is determined to have four input neurons and one output neuron by trial and error. The four inputs to the model include current outside humidity Hot, outside temperature Tot, inside humidity Hit, the command and past inside temperature Tit-1, where t denotes the time variable. The output is the predicted inside temperature. This can be explained that to predict the inside temperature at time t, the inputs of the recurrent RBF network are taken t and the target temperature at time t-1. In order to compare the effectiveness of this

approach in training and testing the recurrent RBF network, the Standard Square Error (SSE) between the true outputs and the network predictions are calculated for this approach are shown in Table 1.

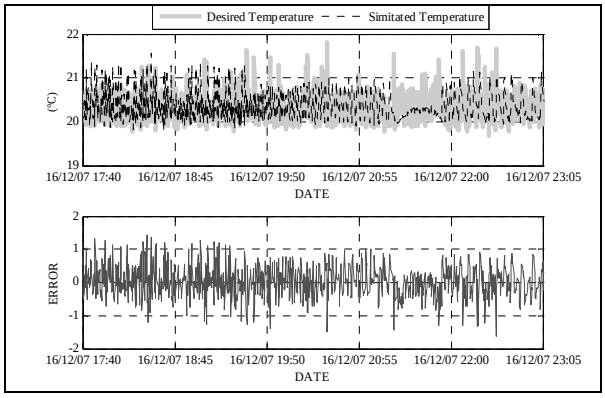

Figure 7: Test of the Recurrent Model of the temperature.

We can notice that the maximum error committed during the Learning is 0,4003 °C and the average error in the east of learning 0,23644 °C. The RRBF can so detect some degradation and gives some solutions to diagnose new failures.

Based on these results, the error is acceptable given the field of variation in temperature, and we can say that the error is like a white noise, namely its average tends to 0. Then we compare the results achieved by the simple model and the recurrent model, a clear improvement of the error is observed.

5. CONCLUSION

This short review covered a few potentially useful neural network applications for greenhouse environmental control. It should be emphasized that the neural network greenhouse modelling refers only to existing structures. These models cannot be used to design new greenhouses, since they lack explicit expressions for the various components and transfer coefficients. Changes in equipment will also require model modification. However, this model could later be fine-tuned to local conditions and requirements, based on data collected on location.

The neural network model can also be useful as controllers, since they may be taught various control rules. Two examples are the simulating of a model-based optimal (feed-forward) controller and a human optimizer (expert grower), who uses some feedback information from the state of the crop.

A comparison of the measured and simulated recursive model proves that the found model can envisage correctly well the inside temperature and humidity in the greenhouse.

ACKNOWLEDGEMENTS

This works was supported by “Volubilis Programm” N° MA/09/211.

REFERENCES

Bouchikhi, B., Eddahhak A., El Harzli M., and El Bari N., 2004. Les capteurs et leur rôle dans la mesure des paramètres climatiques pour une gestion rationnelle de l’eau en agriculture. Journées Internationales des Sciences et Technologies (JICT‘2007), Dec. 2004, Cadiz-Tanger.

Catfolis T., 1993. A method for Improving the Real-Time Recurrent Learning Algorithm. Neural Networks, 6(6): p. 807-821,

Chen D., Giles C. L., Sun G. Z., Chen H. H., Lee Y. C. and Goudreau M. W., 1993. Constructive Learning of Recurrent Neural Networks. Proc. IEEE ICNN, vol. III: p. 1196-1201, San Francisco,

Dreyfus G., Martinez J.-M., Samuelides M., Gordon M. B., Badran F., Thiria S. and Herault L.. 2002. Reseaux de neurones: Methodologie et applications. Ed. Eyrolles, Paris, ISBN: 2-212-11019-7.

Du H., Lam J. and Zhang N., 2006. Modelling of a magneto-rheological damper by evolving radial basis function networks. Engineering Applications of Artificial Intelligence, 19 p. 869–881.

Eddahhak A., Lachhab A., Ezzine L. and Bouchikhi B., 2005. Performance Evaluation of Low-Cost sensors and Instrumentation Conditioning Modules for the Control and Measuring Greenhouse Climate. International Conference on Modeling and Simulation, General Applications and Models in Engineering Science, 22-24 November 2005, Marrakech, Morocco.

Eddahhak A., Lachhab A., Ezzine L. and Bouchikhi B., 2007. Performance Evaluation of a Developing Greenhouse Climate Control with a Computer System. AMSE journal, Association for the Advancement of Modelling and Simulation Techniques in Enterprises, C, 68 (1) p. 53-64.

Ezzine L., Lachhab A., Eddahhak A., and Bouchikhi B., 2007. Statistical modelling of the inside temperature in greenhouse. Information and Communication Technologies International Symposium (ICTIS’07), p 540-543, 3-5 April, Fes, Morocco.

Ezzine L., Lachhab A., Eddahhak A.and Bouchikhi B., 2008. Identification of a Model of Regression of the Climatic Parameters under Greenhouse. Physical & Chemical news, Phys. Chem. News 39, p 43-51.

Fahlman S. E., Lebiere C., 1991. The Cascade- Correlation Learning Architecture. Rapport Technique, CMU-CS-90-100, août 1991.

Fahlman S. E., 1991. The Recurrent Cascade-Correlation Architecture. Rapport Technique, CMU-CS-91-100, mai 1991.

Haykin S., 1994. Neural Networks: A comprehensive foundation. Macmillan College Publishing Company, Inc., United States of America.

Lachhab A., Eddahhak A., Ezzine L. and Bouchikhi B., 2005. Strategy of Developing a Greenhouse Climate Control With a Computer System. International Conference on Modeling and Simulation , General Applications and Models in Engineering

Science,22-24 November 2005, Marrakech, Morocco.

Lachhab A., Eddahhak A., Didi S., Ezzine L., Salinas J.R., García-Lagos F., Atencia M., Joya G. and B. Bouchikhi, 2007. Mise au point d'un systeme de controle et de supervision du climat et de la fertirrigation goutte-a-goutte sous serre. Journées Internationales des Sciences et Technologies (JICT'2007).

Lachhab A., Ezzine L., Eddahhak A., Didi S., Salinas Vazquez J. R., García Lagos F., Atencia M., Joya Caparros G. and Bouchikhi B., 2008. Identification of greenhouse dynamic temperature model using statistical modeling. AMSE Journal, Association for the Advancement of Modelling and Simulation Techniques in Enterprises. 29 (2) p 38-48.

Lee J., Sankar R., 2007. Theoretical derivation of minimum mean square error of RBF based equalizer. Signal Processing, 87 p. 1613–1625.

Venkateswarlu Ch., Venkat Rao K., 2005. Dynamic recurrent radial basis function network model predictive control of unstable nonlinear processes. Chemical Engineering Science, 60, p. 6718 – 6732.

NON-ISOTHERMAL MODEL OF THE YEASTS GROWTH IN ALCOHOLIC FERMENTATIONS FOR HIGH QUALITY WINES

Pablo M. Aballay[(a)], Gustavo J.E. Scaglia[(a)], Martha D. Vallejo[(b)], Laura A. Rodríguez[(b)], Oscar A. Ortiz[(a)]

[(a)]Instituto de Ingeniería Química, Universidad Nacional de San Juan, Av. Libertador San Martín Oeste 1109, San Juan J5400ARL, Argentina
[(b)] Instituto de Biotecnología, Universidad Nacional de San Juan, Av. Libertador San Martín Oeste 1109, San Juan J5400ARL, Argentina

[(a)]paballay@unsj.edu.ar

ABSTRACT
Since, one of the most critical variables influencing the bioprocess in winemaking is temperature; a non-isothermal phenomenological model for yeast kinetics in winemaking fermentation was developed. The proposed model, based on a previous published by authors, considers a new expression for the maximum specific cellular growth rate and two more kinetic parameters depending on operation temperature. They are: specific cellular death rate and the carbon dioxide released at 85-95% of its maximum value. The developed model was validated by accurately predicting the cellular growth of own lab-scale fermentations and, it also verifies to follow the typical trend of literature experimental data. For such purpose, model performance between 10 to 40ºC was evaluated via simulations for constant and variable temperature predefined trajectories. Since obtained results are satisfactory, this model can be used to track complex temperature profiles to achieve high quality wines, as well as, in other control and optimization strategies.

Keywords: non isothermal operation, wine fermentation, phenomenological modelling, yeasts growth

1. INTRODUCTION

Argentina is the largest wine producer in South America. A range of fine wines has raised their incorporation in the most important international markets in the last years, and some of them are among the top rated wines in the world. The customers' increasing demand for high quality wines and its marked preferences for outstanding organoleptic properties of wine, presents new challenges for the winemaking technology.

The bioreactor bulk temperature is a well-known critical variable that determine the kinetics of the fermentation (Coleman, Fish, and Block 2007).
Temperature directly influences on microbial ecology of grape must and the biochemical reactions of yeasts (Fleet and Heard 1993). Moreover, it is known that *Saccharomyces cerevisiae* synthesizes aroma compounds during the winemaking fermentations. It is also stated that the production, quality, quantity and rate of yeast-derived aroma compounds is affected by the temperature used. Typically, temperatures ranging between 15ºC (for white wines) and 30ºC (for red wines) are used. Furthermore, most winemaking fermentations are not carried out at constant temperature. Experiments conducted at constant temperature, revealed that production of compounds related to fresh and fruity aromas is favoured at temperatures near 15°C, while flowery related aroma compounds are better produced at 28°C (Molina, Swiegers, Varela, Pretorius, and Agosin 2007).

In relation with some sensory-relevant flavour generation, it was suggested that higher temperatures, near 28 ºC, are only beneficial at the start of fermentation, and then lower temperatures will be advantageous due to the decrease of the volatility and removal of the aroma compounds formed (Fischer 2007).

It is evident that temperature strongly affects the quality of wine (Torija, Rozès, Poblet, Guillamón, and Mas 2003), and new technologies must include variable temperature trajectories throughout the fermentation.

The development of efficient control strategies for the main operation variables in fermentations such as pH, temperature, dissolved oxygen concentration; agitation speed, foam level, and others need accurate dynamic models (Morari and Zafiriou 1997, Henson 2003). Also, wine fermentation models are useful tools to assure wine quality and reproducibility among batches (Zenteno, Pérez-Correa, Gelmi, and Agosin 2010).

In previous reports, the authors have developed isothermal and non-isothermal first-principles and hybrid neural models, and an improved isothermal phenomenological model with satisfactory capability to approximate the wine fermentation profiles (Vallejo, Aballay, Toro, Vazquez, Suarez, and Ortiz 2005; Ortiz, Aballay, and Vallejo 2006; Aballay, Scaglia, Vallejo, and Ortiz 2008; Scaglia, Aballay, Mengual, Vallejo, and Ortiz 2009).

The objective of this work is to propose a non-isothermal phenomenological model for wine fermentation kinetics, able to predict with enough accuracy yeasts growth and track complex temperature profiles from 10 to 40ºC, to produce wines with high quality.

The proposed model couples mass and energy balances predicting the behaviour of the main state process variables: viable cells, substrate (total fermentable sugars) and ethanol concentrations, carbon dioxide released, and the bioreactor temperature. It is based on the one developed by Scaglia, Aballay, Mengual, Vallejo, and Ortiz (2009), that possesses a good performance for isothermal fermentations, and the one presented by Aballay, Scaglia, Vallejo, and Ortiz (2008) for non-isothermal fermentations. In the latter case, operating temperature ranges from 20 to 30ºC.

A set of ordinary differential equations (ODE), including the heat transferred between the reactor and its cooling jacket, constitute the present model. Balances have been coupled by means of the Arrhenius equation which describes the temperature influence on the cell growth (Aballay, Vallejo, and Ortiz 2006; Aballay, Scaglia, Vallejo, and Ortiz 2008) and death rates (Phisalaphong, Srirattana, and Tanthapanichakoon 2006).

Kinetic parameters of the model were adjusted using experimental data obtained from anaerobic lab-scale cultures of *Saccharomyces cerevisiae* (killer), and/or *Candida cantarelli* yeasts in Syrah must (red-grape juice), see Toro and Vazquez (2002). In the case of the specific parameters in Arrhenius expression, they were adjusted by the least-square method.

Since in practice, the temperature in the bioreactor must be maintained constant at a certain level to avoid the quality product decrease, or varied tracking a predefined trajectory to achieve a wine with particular organoleptic properties (Ortiz, Vallejo, Scaglia, Mengual, and Aballay 2009), the performance of model was tested via simulation to validate it. Results from model simulations and validation are shown. They state suitable agreement with own experimental and published data, predicting fermentation evolution without significant retards. The latter allows model application in advanced control strategies for the winemaking process.

The work is organised as follows. First, the lab-scale fermentation experiments carried out with variable temperature to validate the model to develop are described. Second, the non-isothermal kinetic modelling of the bioprocess from formerly developed isothermal and non-isothermal models is presented. Third, model simulation results are compared to: literature data to verify they well track cellular growth trends and, own experimental data for its validation. Fourth, a discussion on the appliance of the obtained model in complex control and optimization schemes in winemaking, and conclusions are exposed.

2. MATERIALS AND METHODS

Microorganism: *Saccharomyces cerevisiae*, (strain PM16, obtained in our laboratory[(b)]), maintained in agar-YEPD (yeast extract-peptone-dextrose), and propagated in red-grape must. Culture medium: concentrated red-grape must, properly diluted to obtain 23ºBrix at 23ºC, initial pH was set to 3.5, and sterilized at 121ºC during 20 minutes. Fermentations (FER3): 250 mL flasks containing 100 mL of sterile must was inoculated with $2x10^6$ yeast, capped with Muller's valves, and cultured in anaerobic conditions, at temperature following the sequence from 23ºC to 18ºC, presented in Fig. 4. Samples were taken each 6 hours during the first 7 days and then each day; yeasts were accounted by means a Neubauer chamber, the fermented must was centrifugated and the supernatant was maintained for analytical determinations.

3. MATHEMATICAL MODEL

In winemaking conditions, the main bio-reactions can be synthesised by the reductive pathway S ➔ X + P + CO_2, this reaction means that substrates (S, glucose and fructose and sucrose, after their hydrolysis as the limiting substrate), in anaerobic conditions, are metabolised to produce a yeast population (X), ethanol (P, mainly produced by yeast through the Embden-Meyerhof-Parnas metabolic pathway) and carbon dioxide (CO_2).

The ethanol-formation reaction from glucose is:

$$C_6H_{12}O_6 \rightarrow 2CH_3CH_2OH + 2CO_2 \qquad (1)$$

The metabolite accumulation in the extra-cellular medium has been modelled by a set of ODE based on mass balances on X, S, P and CO2 which change with time *t* [h] like in the isothermal model of Scaglia, Aballay, Mengual, Vallejo, and Ortiz (2009), which can be seen for further details, and it is summarised as Eqs. 2 through 5:

Viable cells:

$$\frac{dX}{dt} = \frac{e^{-(CO_2 - C0_{2(95)})}}{e^{(CO_2 - C0_{2(95)})} + e^{-(CO_2 - C0_{2(95)})}} A\mu_m \frac{S}{S + Ks\,B^a} \cdots$$
$$\cdots X\left(1 - \frac{X}{A\mu_m \dfrac{S}{(S + Ks\,B^a)\beta}}\right) + \qquad (2)$$
$$+\left[1 - \frac{e^{-(CO_2 - C0_{2(95)})}}{e^{(CO_2 - C0_{2(95)})} + e^{-(CO_2 - C0_{2(95)})}}\right]\left(CX\frac{dS}{dt} - K_d X\right)$$

Substrate:

$$\frac{dS}{dt} = \frac{1}{Y_{X/S}}\left[-X\left(\mu_m \frac{S}{S + Ks\,B^b} - E\mathrm{X}\right)\right] - \mathrm{FX} \qquad (3)$$

Carbon dioxide released:

$$\frac{dCO_2}{dt} = G\mu_m \frac{S}{S + Ks\,B^c} X + \\ + \frac{d}{dt}\left(H\,\mu_m \frac{S^2}{\left(S + Ks\,B^d\right)\left(S + Ks\,B^e\right)} X + I\,X \right) \quad (4)$$

Ethanol:

$$\frac{dP}{dt} = \frac{1}{Y_{CO_2/P}} \frac{dCO_2}{dt} \quad (5)$$

Numerical values of preceding model parameters and their description are shown in Table 1 in the Appendix.

Model assumptions are: other mass balance parameters of the model, including pH, are constant. Fermentation is not nitrogen source-limited; this is viable, based on information about the chemical composition of the local red-grape musts. Moreover, local winemakers only add nitrogen supplementation, in excess, to correct the white-grape musts. In the energy balance (Eq. 6): heat losses due to CO_2 evolution, water evaporation and ethanol and flavour losses are neglected; the average grape juice-wine density and specific heat, and all physical properties are uniform in the fermenting mass bulk. They are constant with the (bioreactor) temperature T [K] and time. Convective heat transfer coefficient of fermentation mass, implicitly included in Eq. (6), is constant (Colombié, Malherbe, and Sablayrolles 2007). In the cooling jacket: water properties variations and the fouling factor in jacket side are neglected. Heat transfers by radiation and conduction are negligible.

The non-isothermal kinetic model is constituted by mass balances of the before-mentioned model and the energy balance in the reactor and its cooling water jacket.

$$\frac{d\left(\rho_r \cdot V_r \cdot Cp_r \cdot T\right)}{dt} = Y_{H/CO_2} \cdot V_r \cdot \frac{dCO_2}{dt} - Q \quad (6)$$

V_r [m^3] is the volume. $Y_{H/CO2}$ [W·h produced/kg CO_2 released] is the energy due to the carbon dioxide released by the bio-reaction. It was obtained by stoichiometry (Eq. 1) from $Y_{H/S}$, the likely energetic yield on substrate consumed. Q [W] represents the exchanged heat between the fermenting mass and the cooling jacket (see details in Aballay, Scaglia, Vallejo, and Ortiz 2008). ρ_r [kg m^{-3}] and C_{pr} [W·h kg^{-1} K^{-1}] are density and specific heat of the fermenting mass.

Mass and energy balances are coupled by means of: Arrhenius' equation for maximum specific cellular growth and death rates, μ_m [h^{-1}] and K_d [h^{-1}] respectively, and polynomial regressions for dimensionless coefficients L within μ_m, and M within the parameter for estimation of the carbon dioxide released at 85-95% of its maximum value $CO_{2\,(95)}$. The above mentioned bioprocess variables progress in time and, temperature influence on them and their parameters can be expressed in a general way as: $\{dX/dt,\ dS/dt,\ dCO_2/dt \text{ and } dP/dt\} = ...$

$...f(X, S, CO_2, \mu_m(T), K_d(T), CO_{2(95)}(T))$.

The mathematical expressions for the three kinetic temperature-dependent parameters are given in Eqs. (7), (8) and (9):

$$\mu_m = \gamma . L . \frac{T \cdot e^{-\frac{E_a}{R \cdot T}}}{1 + e^{-\frac{\Delta G_d}{R \cdot T}}} \quad (7)$$

γ is the maximum cellular growth rate per Kelvin degree [$h^{-1}K^{-1}$], L is a dimensionless coefficient depending on the temperature (Eq. 10), E_a is the activation energy for cell growth [kJ $kmol^{-1}$] and ΔG_d [kJ $kmol^{-1}$] is Gibbs free energy change of the fermentation reaction. R is general gases constant [kJ $kmol^{-1}$ K^{-1}].

$$K_d = \begin{cases} K_{d,0} \cdot T \cdot e^{\frac{-E_d}{R \cdot T}} \ if\ T \le 304K \\ 0.0165\ Otherwise \end{cases} \quad (8)$$

K_d replaces parameter D in the model of Scaglia Aballay, Mengual, Vallejo, and Ortiz (2009). $K_{d,0}$ is the specific cellular death rate per Kelvin degree and E_d is the activation energy for cellular death [kJ $kmol^{-1}$].

Moreover, parameters E_a, ΔG_d, $K_{d,0}$, and E_d, were adjusted by the least-square method, using experimental data obtained from anaerobic lab-scale cultures of *Saccharomyces cerevisiae* (killer) and *Candida cantarelli* yeasts, with Syrah must in batch mode (Toro and Vazquez, 2002).

$$CO_{2(95)} = CO^*_{2(95)} \cdot M \quad (9)$$

$CO^*_{2\,(95)}$ is a carbon dioxide value, chosen between the 85% and 95% of the total carbon dioxide released at constant temperature (296K) and, M is a dimensionless coefficient depending on the temperature (Eq. 11).

$$L = f\,T^5 - g\,T^4 + h\,T^3 - i\,T^2 + j\,T - k \quad (10)$$

$$M = l\,T^5 - m\,T^4 + n\,T^3 - o\,T^2 + p\,T - q \quad (11)$$

Where f, g, h, i, j, k, l, m, n, o, p, and q are own coefficients of the model, see Table 2 in the Appendix.

Initial conditions and another parameters of the model used for simulating experimental fermentations from literature are described in Table 2 in the Appendix. Those fermentations are mentioned as: FERT, of Torija Rozès, Poblet, Guillamón, and Mas (2003), FER1 and FER2 (Toro and Vazquez 2002) and FER3 from own data. The latter was carried out to validate the present model. In addition, maximum values of viable cells concentration achieved during the fermentations are included in Table 2 (Appendix) as well.

4. SIMULATIONS

4.1. Results

The developed model was tested via simulations in similar conditions than experimental fermentations from literature. To carry out the simulations, the model was codified in Matlab™ software. Results are presented in this section.

Results are expressed on normalised yeast concentrations in order to allow comparisons between different yeast strains, having different masses.

Figure 1, represents the yeasts growth profiles attained by simulations at different constant temperatures ranging from 283K (10ºC) to 313K (40ºC) for the same initial conditions of substrate and yeasts concentration. It can be seen that yeast growth and the maximum cells concentration are favoured at temperatures between 290 and 300K. At lower temperatures than 290K, it is observed that the yeast growth is delayed and the maximum cells concentration achieved is lower than attained between 290 and 300K. For initial temperatures higher than 300K, not only the yeast growth is diminished but also the yeast death is anticipated. This situation may be due to the dual effect of temperature over the optimal growth conditions and the ethanol-tolerance.

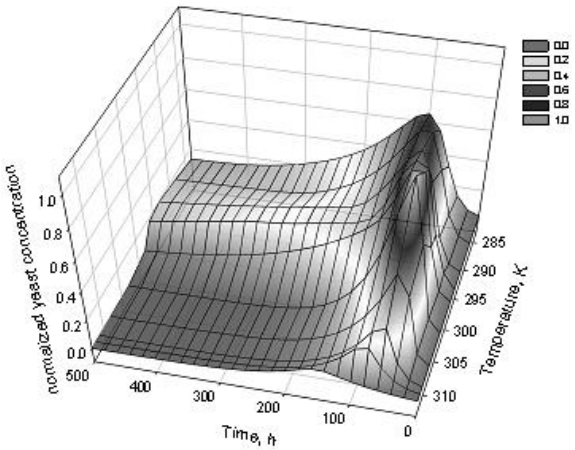

Figure 1: Normalised Viable Cells Profiles: Modelled Results at Different Temperatures (283-313K); Max. = $109.74 \cdot 10^6$ cfu mL^{-1} (Parameter Values from FER2)

In order to contrast the simulation results obtained with experimental data, it was constructed a 3D-mesh plot (Fig. 2), taking data from literature and reporting experiences of wine fermentations at different constant initial temperatures (Torija, Rozès, Poblet, Guillamón, and Mas 2003).

Comparing Figs. 1 and 2, it can be seen that the behaviour of the model approximates appropriately to the mentioned experimental data from literature. Even though, in the last case (Fig. 2), at low temperatures, the yeast growth seems to be more retarded than in Fig. 1. It is necessary to point out that yeast used by Torija, Rozès, Poblet, Guillamón, and Mas (2003), was not the same used to fit the model in Fig. 1. Thus, these yeasts may have similar performance but not exactly the same, because each strain has a proper behaviour pattern. Although, the comparison between Figs. 1 and 2 is promising, the model performance must be contrasted with experiences carried out at variable temperature profiles.

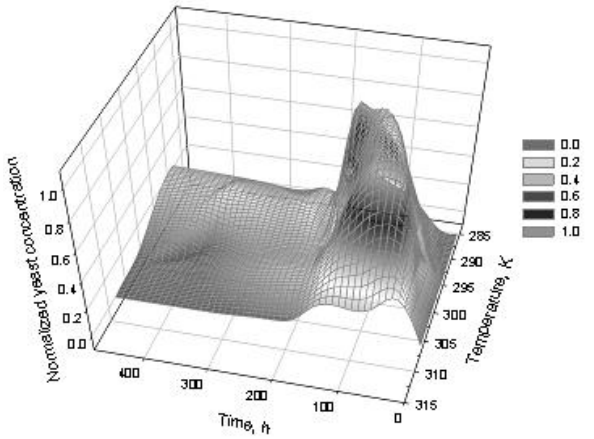

Figure 2: Normalised Viable Cells Profiles: Experimental Fermentations at Different Temperatures (288-308K) (Torija, Rozès, Poblet, Guillamón, and Mas 2003); Max.= $195 \cdot 10^6$cfu mL^{-1}

4.2. Model validation

The model validation was accomplished by simulation as well, using initial conditions of different own lab-scale experimental data sets at different constant and variable temperature profiles.

As Fig. 3 shows that for fermentations FER1 and 2 (both at constant 296±1K), the model proposed has an acceptable prediction with only up to 10 hours average in retard regarding experimental data.

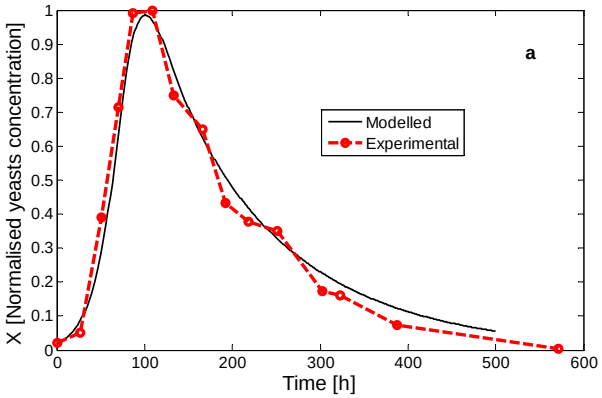

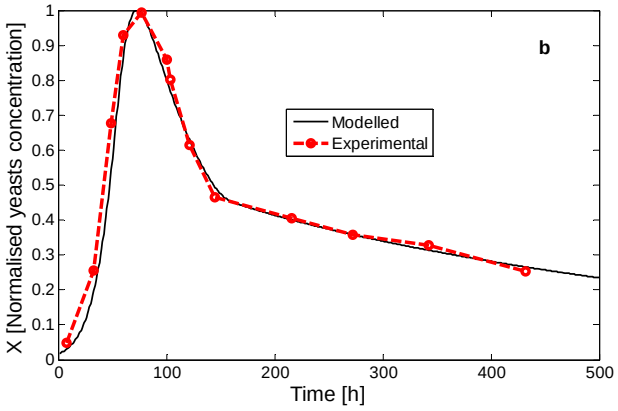

Figure 3: Normalised Viable Cells Profiles: Modelled and Experimental Fermentations: (**a**) FER1 (Max.= $92.3 \cdot 10^6$ cfu mL^{-1}) and (**b**) FER2 (Max.= $109.74 \cdot 10^6$ cfu mL^{-1}) both of them at 296±1K

Figure (4a), presents the model predictions and experimental results for fermentations performed at a predefined temperature profile, Fig. (4b), fixed from biochemical considerations on yeasts growth and yeast-related aroma compounds.

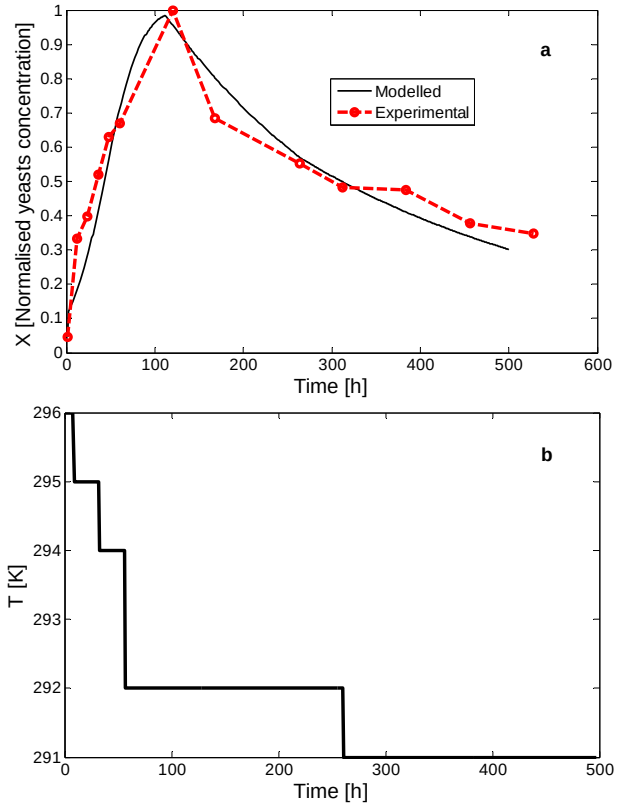

Figure 4: (**a**) Normalised Viable Cells Profiles: Modelled and Experimental Fermentation FER3 (Max.= $63.5 \cdot 10^6$ cfu mL^{-1}), at (**b**) a Specific fermentation temperature profile (296-291K)

Furthermore, results in Fig. 4, constitute the effective model validation since that it allows to predict the viable yeasts population when an optimal temperature profile is stated.

Table 1, illustrates a quantitative comparison of the obtained results in Figs. 3 and 4. According to Scaglia, Aballay, Mengual, Vallejo, and Ortiz (2009): firstly, it is used the mean absolute error (*MAE*, Eq. 12) that also has been used to predict biomass in this case,

$$MAE = \frac{\sum_{1}^{n} \left| X_{\text{mod}} - X_{\text{exp}} \right|}{n} \tag{12}$$

n is the number of experimental data, X_{mod} the predicted value of biomass (cells concentration) and, X_{exp} the experimental one.

Subsequently, the effectiveness of the presented model was assessed by means of the percentage mean error (*ME%*, Eq. 13) with respect to the experimental range of the variable expressed by its maximum value ($X_{\text{exp,max}}$); this, also regards the fermentation progress and its control (Malherbe, Fromion, Hilgert and Sablayrolles 2004).

$$ME\% = \frac{MAE}{X_{\text{exp, max}}} \cdot 100 \tag{13}$$

Lastly, in Table 1, it is exposed that both errors are into a typical maximum limit in biotechnology and process engineering of 10% with respect to data range of variable biomass, which is compensated with an experimental measurement error of about the similar value. Fundamentally, the predicted profiles do not show appreciable time retards with respect to the experimental data and achieves an enhanced precision by estimating biomass compared to own (Ortiz, Aballay, and Vallejo 2006), and other first-principles models like the ones of Coleman, Fish and Block (2007), and Phisalaphong, Srirattana, and Tanthapanichakoon (2006), respectively. This fact was attained with an additional critical variable as the temperature and the new parameters in the proposed model. Hence, it would be possible to apply it in control algorithms to track with proximity desired fermentation trajectories without significant delays in the control actions. Such characteristic is particularly essential during winemaking process, since a delayed control action on variables, such as temperature or pH, can generate a sluggish or stuck fermentation or the degradation in organoleptic properties of wine.

In addition, the model can be used at industrial scale with some adaptation, given that, other non-isothermal models developed from lab-scale alcoholic fermentations have been validated or tested with good performance, or highlighted their possible adaptation, taking into account scale-up effects (Phisalaphong Srirattana, and Tanthapanichakoon 2006; Colombié, Malherbe, and Sablayrolles 2007, Malherbe, Fromion, Hilgert and Sablayrolles 2004; Coleman, Fish, and Block 2007). In the work of Zenteno, Pérez-Correa, Gelmi, and Agosin (2010), the model was validated for a 10 m^3 industrial tank.

Table 1: Comparison between Simulated and Experimental Results for Viable Cells Concentration

Fermentation	MAE [10^6 cfu mL^{-1}]	ME%
FER1	0.4405	4.7722
FER2	0.232	2.1262
FER3	4.1527	6.5397

5. CONCLUSIONS

A first-principles model, for non-isothermal alcoholic fermentations in wider conditions of winemaking temperature, has been presented in this work. Since the bioprocess is strongly affected by temperature in aroma and flavour production, the final wine quality depends on monitoring and controlling on this variable. Therefore, the model obtained consist of mass balances, predicting state variables (viable cells, substrate and ethanol concentrations, and CO_2 released), coupled with an energy balance of the system. The latter is done by means of cellular growth and death parameters, and the $CO_{2\ (95)}$ parameter, all of them in function of temperature in an interval from 10 to 40°C.

The developed model has been satisfactorily validated via simulation with published and own experimental data, showing a proper behaviour to predict cellular growth kinetics at constant and variable predefined temperature profiles. This allows disposing of a reliable model to: approximate state variables trajectories and propose advanced control and optimization strategies.

The model validation reaches to lab-scale winemaking fermentations. It is possible to use it at industrial scale, in that case, it may be necessary include some aspects not considered such as: mixing of the fermentation mass and spatial concentration gradients, heat transfer, etc.

In addition, other topics will be included in next contributions, such as: to track other variables of the bioprocess as, substrate and ethanol concentrations, CO_2 released, density and/or pH; to show an extensive sensitivity study for model variables and parameters; to improve parameter estimation with artificial intelligence tools; to make efforts to reduce the winery cooling requirements even though the process demands specific cooling protocols to maintain low temperatures that protect the wine quality.

ACKNOWLEDGMENTS

We gratefully acknowledge the Universidad Nacional de San Juan and the National Council of Scientific and Technological Research (CONICET), Argentina, by the financial support to carry out this work.

APPENDIX

Table 1: Coefficients and parameters values from the isothermal fermentation model of Scaglia, Aballay, Mengual, Vallejo, and Ortiz (2009), used in the present non-isothermal model for three fermentations.

Description		Unit	Value*		
Fitting Coefficient					
			FERT	FER1	FER3
a	-	-	1.276	1.319	1.276
b	-	-	1.242	1.282	1.242
c	-	-	1.276	1.276	1.276
d	-	-	1.152	1.152	1.152
e	-	-	1.355	1.355	1.355
A	-	-	5.622	3.119	5.622
B	-	-	93.02	93.02	93.02
C	Volume of fermenting mass per substrate mass	$m^3\ kg^{-1}$	0.001	0.001	0.001
E	Volume of fermenting mass per formed cells and time	$m^3\ kg^{-1}\ hr^{-1}$	$1.01 \cdot 10^{-4}$	$1.65 \cdot 10^{-4}$	$1.01 \cdot 10^{-4}$
F	Specific rate of substrate consumption for cellular maintenance	$kg\ kg^{-1}\ hr^{-1}$	0.01	0.01	0.01
G	CO_2 released per formed cells	$kg\ kg^{-1}$	13.2	8.073	13.2
H	CO_2 released multiplied by time per formed cells	$kg\ hr\ kg^{-1}$	1440	880.7	1440
I	Similar to G	$kg\ kg^{-1}$	1.8	1.8	1.8
Kinetic and Yield Parameters					
Ks	Saturation coefficient in Monod's equation	$kg\ m^{-3}$	2.15		

β	Coefficient in Verlhurst's equation	m^3 kg^{-1} h^{-1}	$4.5 \cdot 10^{-3}$	$3.65 \cdot 10^{-3}$	$4.5 \cdot 10^{-3}$
$Y_{X/S}$	Formed cells per consumed substrate	kg kg^{-1}	0.04	0.061	0.04
$Y_{CO2/P}$	Carbon dioxide yield coefficient based on ethanol	kg kg^{-1}	0.775		

*Values for fermentation FER2 are not shown here.

Table 2: Initial conditions, coefficients and parameters used in the proposed non-isothermal model for three fermentations.

Description		Unit	Value*		
Initial Conditions					
			FERT	FER1	FER3
X(0)	Viable cells concentrat-ion (yeasts)	M-cfu m^{-3}**	$2 \cdot 10^6$		
S(0)	Substrate concentrat-ion	kg m^{-3}	200	208.5	226.2
$CO_2(0)$	Carbon dioxide evolution	kg m^{-3}	0		
P(0)	Ethanol concentrat-ion	kg m^{-3}	0		
T(0)	Bioreactor temperature	K	***	296	296
$t(0)$	Time	h	0		
$\mu_m(0)$	Maximum specific cellular growth rate	h^{-1}	$6.67 \cdot 10^{-2}$	$1.09 \cdot 10^{-1}$	$1.09 \cdot 10^{-1}$
$K_d(0)$	Specific cellular death rate per Kelvin degree	h^{-1}	$1.8 \cdot 10^{-3}$	$8.1 \cdot 10^{-3}$	$8.1 \cdot 10^{-3}$
$CO_{2,(95)}(0)$	CO_2 released between 85-95% of the maximum CO_2 released	kg m^{-3}	(*)	(*)	(*)
L(0)	-	-	1		
M(0)	-	-	1		
$Q(0)$	Exchanged heat between the fermenting mass and the cooling jacket	W	1.25	1.18	(**)
Maximum Value Achieved					
X_{max}	Viable cells concentrat-ion (yeasts)	M-cfu m^{-3}	$195 \cdot 10^6$	$92.3 \cdot 10^6$	$63.5 \cdot 10^6$
Fitting Coefficients					
f	-	-	$4.23 \cdot 10^{-7}$		
g	-	-	$6.41 \cdot 10^{-4}$		
h	-	-	0.3873		
i	-	-	116.9		
j	-	-	17631		
k	-	-	$1.06 \cdot 10^6$		
l	-	-	$2.7 \cdot 10^{-7}$		
m	-	-	$4.1 \cdot 10^{-4}$		
n	-	-	0.2479		
o	-	-	74.89		
p	-	-	11299		
q	-	-	$6.81 \cdot 10^5$		
Physical-chemical and Kinetic Parameters					
ρ_r	Density of the fermenting mass	kg m^{-3}	998.204		
C_{pr}	Specific heat of the fermenting mass	W·h kg^{-1} K^{-1}	1.01684		
V_r	Volume of the fermenting mass	m^3	0.003		
$Y_{H/CO2}$	Energy due to the carbon dioxide released by the bio-reaction	W·h produc-ed/kg of CO_2 releas-ed	310.3748		
γ	Maximum cellular growth rate per Kelvin degree	$h^{-1}K^{-1}$	1.08	1.66	0.83
ΔG_d	Gibbs free energy change of the fermentatio n reaction	kJ $kmol^{-1}$	1916.9		
E_a	Activation energy for cell growth	kJ $kmol^{-1}$	1928.37		

E_d	Activation energy for cell death	kJ $kmol^{-1}$	1.7 $\cdot 10^5$	1.7 $\cdot 10^5$	1.789 $\cdot 10^5$
$K_{d,0}$	Specific cellular death rate per Kelvin degree	h^{-1}	3.1 $\cdot 10^{26}$	1.2 $\cdot 10^{27}$	1.2 $\cdot 10^{27}$
$CO^*_{2(95)}$	CO_2 released between 85-95% of the maximum CO_2 released at constant temperature	kg m^{-3}	94	97.5	97.5
R	General gases constant	kJ $kmol^{-1}$ K^{-1}	8.309		

*Values for fermentation FER2 are not shown here.

**Millions of Colony Forming Units per cubic meter.

***Different constant temperatures: 288, 293, 298, 303 and 308K.

(*) Idem to $CO^*_{2(95)}$ values.

(**) Values according to temperature trajectory required.

REFERENCES

Aballay, P.M., Vallejo, M.D., Ortiz, O.A., 2006. Temperature control system for high quality wines using a hybrid model and a neural control system. *Proceedings of the XVI Congresso Brasileiro de Engenharia Química-COBEQ 2006,* pp. 1153-2429. 24-27 September, Santos (Brazil).

Aballay, P.M., Scaglia, G.J.E., Vallejo, M.D., Ortiz, O.A., 2008. Non isothermal phenomenological model of an enological fermentation: modelling and performance analysis. *Proceedings of the 10th International Chemical and Biological Engineering Conference - CHEMPOR 2008*, pp. 4-6 September, Braga (Portugal).

Coleman, M.C., Fish, R., Block, D.E., 2007. Temperature-dependent kinetic model for nitrogen-limited wine fermentations. *Applied and Environmental Microbiology,* 73 (18), 5875–5884.

Colombié, S., Malherbe, S., Sablayrolles, J.M., 2007. Modeling of heat transfer in tanks during wine-making fermentation. *Food Control*, 18, 953–960.

Fischer, U., 2007. Wine Aroma. In: Berger, R. G. , ed. *Flavours and Fragrances, Chemistry, Bioprocessing and Sustainability.* Berlin Heidelberg: Springer, 241-267.

Fleet, G.H., Heard, G.M., 1993. Yeasts: growth during fermentation. In: Fleet, G.M., ed. *Wine Microbiology and Biotechnology.* Chur (Switzerland): Harwood Academic Publishers, 27–54.

Henson, M. A., 2003. Dynamic modeling and control of yeast cell populations in continuous biochemical reactors. *Computers and Chemical Engineering*, 27 (8-9), 1185-1199.

Malherbe, S., Fromion, V., Hilgert, N., Sablayrolles, J.M., 2004. Modeling the effects of assimilable nitrogen and temperature on fermentation kinetics in enological conditions. *Biotechnology and Bioengineering,* 86 (3), 261–272.

Matlab™, 2004. *Version 7.0.1. Release 14. User guide*. Natick (Massachusetts, USA): The MathWorks, Inc.

Molina, A.M., Swiegers, J.H., Varela, C., Pretorius, I.S., Agosin, E., 2007. Influence of wine fermentation temperature on the synthesis of yeast-derived volatile aroma compounds, *Applied Microbiology & Biotechnology,* 77, 675–687.

Morari, M., and Zafiriou, E., 1997. *Robust Process Control.* UK: Pearson Education.

Ortiz, O.A., Aballay, P.M., Vallejo, M.D., 2006. Modelling of the killer yeasts growth in an enological fermentation by means of a hybrid model. *Proceedings of the XXII Interamerican Congress of Chemical Engineering and V Argentinian Congress of Chemical Engineering. Innovation and Management for Sustainable Development,* A. 13b-224, pp. 451-452. 1-4 October, Buenos Aires (Argentina).

Ortiz, O.A., Vallejo, M.D., Scaglia, G.J.E., Mengual, C.A., Aballay, P.M., 2009. Advanced Temperature Tracking Control for High Quality Wines using a Phenomenological Model. In: de Brito Alves, R.M., Oller do Nascimento, C.A., and Chalbaud Biscaia Jr., E., eds. *10th International Symposium on Process Systems Engineering - PSE2009, 27, Part A, Computer Aided Chemical Engineering - Series*. Amsterdam (The Netherlands): Elsevier B.V., 1389-1394.

Phisalaphong, M., Srirattana, N., Tanthapanichakoon, W., 2006. Mathematical modeling to investigate temperature effect on kinetic parameters of ethanol fermentation. *Biochemical Engineering Journal,* 28, 36–43.

Scaglia, G.J.E., Aballay, P.M., Mengual, C.A., Vallejo, M.D., Ortiz, O.A., 2009. Improved phenomenological model for an isothermal winemaking fermentation. *Food Control,* 20, 887–895.

Torija, M.J., Rozès N., Poblet M., Guillamón J. M., Mas A., 2003. Effects of fermentation temperature on the strain population of *Saccharomyces cerevisiae*. *International Journal of Food Microbiology,* 80, 47-53.

Toro, M.E., Vazquez, F., 2002. Fermentation behavior of controlled mixed and sequential cultures of *Candida cantarellii* and *Saccharomyces cerevisiae* wine yeasts. *World Journal of Microbiology & Biotechnology,* 18, 347- 354.

Vallejo, M. D, Aballay, P. M., Toro, M. E., Vazquez, F., Suarez, G. I., Ortiz, O. A., 2005. Hybrid

Modeling and Neural Prediction of the Wild Killer Yeast Fermentation Performance in a Winemaking Process. *Proceedings of the 2nd Mercosur Congress on Chemical Engineering and 4th Mercosur Congress on Process Systems Engineering*, Paper code 230, pp. 1-10. 14-18 August, Rio de Janeiro (Brazil).

Zenteno, M.I, Pérez-Correa, J.R., Gelmi, C.A., Agosin, E., 2010. Modeling temperature gradients in wine fermentation tanks. *Journal of Food Engineering*, 99, 40–48.

Authors Index

Aballay	Pablo M.	143
Amouri	Achour	45
Askour	Rachid	129
Basbous	Tammam	73
Basualdo	Marta	93
Belhadj	Jamel	67
Belkoura	Lotfi	135
Ben Rhouma	Amine	67
Benhadj Braiek	Naceur	37
Bouchikhi	Benachir	135
Bououlid	Badr	99, 129
Bouyekhf	Rachid	115
Chalal	Lamine	61
Chibani	Abdelhakim	45
Colas	Frederic	61
Dauphin-Tanguy	Geneviève	61
Degliuomini	Lucas Nieto	93
Deshayes	Laurant	107
Dhifaoui	Rachid	121
Dieulot	Jean-Yves	61
Djouani	Karim	53
Ed-dahhak	Abdelali	135
El Afou	Youssef	135
EL Moudni	Abdellah	115
Ezzine	Latifa	135
Feroldi	Diego	93
Fuchiwaki	Masaki	21
Guerbaoui	Mohamed	135
Guillaud	Xavier	37
Ilinca	Adrian	73
J.E. Scaglia	Gustavo	143
Jain	S. C.	1, 11
Junco	Sergio	27
Khadraoui	Ammar	53
Khezami	Nadhira	37
Kouiss	Khalid	107
Krishnan	V. L.	11
Lachhab	Abdeslam	135
Mahfoudi	Chawki	45, 53
Mimouni	Mohamed Faouzi	121
Mkhida	Abdelhak	99
Motawej	Fadi	115
Nacusse	Matías	27
Ortiz	Oscar A.	143
Outbib	Rachid	83,93
Paris	Jean Luc	107
Pathak	P. M.	1, 11
Patolia	Haresh	1
Perron	Jean	73
Poulet	Philippe	83
Roboam	Xavier	67
Rodríguez	Laura A.	143
Saadi	Janah	107
Sardana	Lokesh	11
Sekkat	Souhail	107
Shimizu	Fumio	21
Suzuki	Katsuya	21
Tanaka	Kazuhiro	21
Thiriet	Jean Marc	99
Vallejo	Martha D.	143
Yahia	Hedi	121
Yamakawa	Sho	21
Younes	Rafic	73
Zaatri	Abdelouahab	45, 53
Zumoffen	David	93